

Editorial corner – a personal view

Insights into carcinogenic potential of micro(nano)plastics

Kalappa Prashantha^{a*}, Krishnappa Amita^b

^aCentre for Research and Innovation, Adichunchanagiri School of Natural Sciences, Adichunchanagiri University, B.G. Nagara, Mandya District-571448 Karnataka, India

^bDepartment of Pathology, Adichunchanagiri Institute of Medical Sciences, Adichunchanagiri University, B.G. Nagara, Mandya District-571448 Karnataka, India

The term microplastics (MPs) has been the subject of research for a while, but nanoplastics (NPs) are a relatively new concept. Microplastics (<https://doi.org/10.1016/j.marpolbul.2018.11.022>), are any synthetic solid particle or polymeric matrix, with size ranging from 1 μm to 5 mm, of either primary or secondary manufacturing origin, which are insoluble in water. Nanoplastics (<https://doi.org/10.1016/j.envpol.2018.01.024>) present colloidal properties in aqueous system with size less than 1 μm and result from the degradation of industrial plastic objects. Micro(nano)plastics (MNPs) is relative new term used to discuss both micro- and nanoplastics, are plastic fragments, ubiquitously found within the environment and living organisms including human tissue. Human beings are being exposed to micro(nano)plastics (MNPs) predominantly through ingestion and inhalation. MNPs are complex materials composed of polymer matrix with additives such as flame retardants, UV-stabilizers, colorants and surface finishers among others. These additives are added to polymers during the compounding process and most of them are typically not chemically linked to polymers. As a result, these additives can leach to external medium easily. MNPs have a very large surface to volume ratio which leads to high leaching rate. Hence, once MNPs accumulate in living organisms, their additives and monomer residues can easily penetrate into tissues and organs leading to a localized toxicity by inducing or enhancing an immune response. Recently, many research groups reported the presence of monomers and constituents of MNPs in human

tissues such as the liver, stomach, kidney, spleen, lungs *etc.*

Direct evidence of the role of MNPs in carcinogenesis has not been reported to date. However, recently, MNPs have been detected in human cancer tissue, suggesting (<https://doi.org/10.21203/rs.3.rs-1315103/v1>) its role in causing cancer. It has been observed that oxidative stress and chronic irritation due to MNPs (<https://doi.org/10.1016/j.scitotenv.2020.143872>) leads to the production of pro-inflammatory mediators that may induce angiogenesis. Angiogenesis is a well-established attribute of cancer progression. Likewise, endocrine disruptive chemicals (EDCs) present in the MNPs can mimic oestrogen, which may lead to DNA damage and promote breast cancer. There are also reports that EDCs can affect intestinal microorganisms influencing cancer risk. EDCs with recognized estrogenic activity have also been found to increase the risk of extrahepatic biliary tract cancer. Furthermore, organochlorine compounds present in some MNPs modulate K-RAS activation (K-RAS is an oncogene which when mutated leads a normal cell to transform to cancerous state) leading to exocrine pancreatic cancer (<https://doi.org/10.3390/cancers14194637>). In latest research, (<https://doi.org/10.1016/j.scitotenv.2022.159306>) molecular mechanism of MNPs in the induction of cancer signalling pathways in the kidney and testis has been reported using a microfluidic platform for the first time.

Despite this, risk posed by MNPs is uncertain and the evidence is weak. Discrepancies in the physical characteristics of the MNPs studied, bias introduced

*Corresponding author, e-mail: prashantha.k@gmail.com

© BME-PT

by the additives and pollutants carried by MNPs, as well as the robustness of the study designs, renders the generalization of study results to humans ambiguous. Demonstration of the actual potential of MNPs on carcinogenesis requires extensive and trans-disciplinary research with robust

study design to establish a cause-effect relationship. This demands for further research on the exact molecular mechanism deciphering signalling pathways to be elucidated in order to provide the evidence on the carcinogenic potential of micro(nano)plastics.



Dr. Kalappa Prashantha
Member of the International Advisory Board



Dr. Krishnappa Amita

Review article

Recent progress in sulfur-containing technical lignin-based polymer composites

Shritama Mukherjee[✉], Samrat Mukhopadhyay^{*✉}

Department of Textile and Fiber Engineering, Indian Institute of Technology, Hauz Khaz, 110016 New Delhi, India

Received 10 May 2022; accepted in revised form 26 August 2022

Abstract. The aromatic biopolymer lignin, present in lignocellulosic material, can act as an antioxidant and has antimicrobial and UV blocking properties due to the presence of aromatic ring and phenolic hydroxyl groups with aliphatic hydroxyl, carboxyl, methoxy groups. It is produced in huge amounts as a by-product during the delignification process in the paper and pulp industries. Lignin-based polymer composites with advantageous properties can fulfill the growing demand for lightweight polymer composites. Incorporating lignin as reinforcement in polymer composite can make it more environmentally friendly. Among four technical lignin, kraft lignin and liginosulfonate have a unique molecular structure that includes sulfur and can be extracted from black liquor and spent liquor, respectively. Moreover, the negatively charged sulfite groups in liginosulfonate can have an electrostatic attraction to a wide range of positively charged polymers and materials, making it an ideal additive for the adsorbent material. The main intention of this review is to increase the knowledge on the use of cheap and widely available kraft lignin and liginosulfonate as reinforcement in polymer composites and to find the shortcomings to advance further research on the application of technical lignin. The article mainly focuses on advancements in kraft lignin and liginosulfonate polymer composites.

Keywords: biopolymers, lignin fractionation, phenolic hydroxyl group, kraft lignin and liginosulfonate-based composite, polyanion

1. Introduction

The word ‘Lignin’ was first used by a Swiss botanist, A.P. Candolle, in 1813. It is derived from the word ‘lignum’ or wood. It is a highly complex and cross-linked amorphous aromatic heteropolymer. The demand for lightweight polymer composite material has increased dramatically due to its high strength, tailored properties, and wide applications. Along with this, there is also a growing environmental concern for developing suitable polymer composites with renewable, biodegradable biopolymers to reduce the use of non-biodegradable petroleum-based plastics. One promising candidate is lignin, with properties such as antimicrobial, antioxidant, and UV blocking ability due to the presence of aromatic structure.

Lignin is generally present in the cell wall of woody biomass along with cellulose and hemicellulose. Together they are often termed lignocellulosic biomass, which is 30–50% cellulose, 20–35% hemicellulose, and 15–20% lignin [1–5]. Lignin acts as an adhesive that gives lignocellulosic biomass its resistance, rigidity, and structural integrity and protects cell walls from outside stresses [6]. An open network is created by hemicellulose-coated cellulose fibrils, and the empty places are mainly filled with lignin which is described in Figure 1 [7, 8]. It is covalently bonded with hemicellulose by different bonds, such as benzyl ether, γ -ester, and phenyl glycoside bonds [9]. Lignocellulosic biomass is also the main source of lignin which represents nearly 30% of all organic carbon in the biosphere which can be extracted from

*Corresponding author, e-mail: samrat@textile.iitd.ac.in
© BME-PT

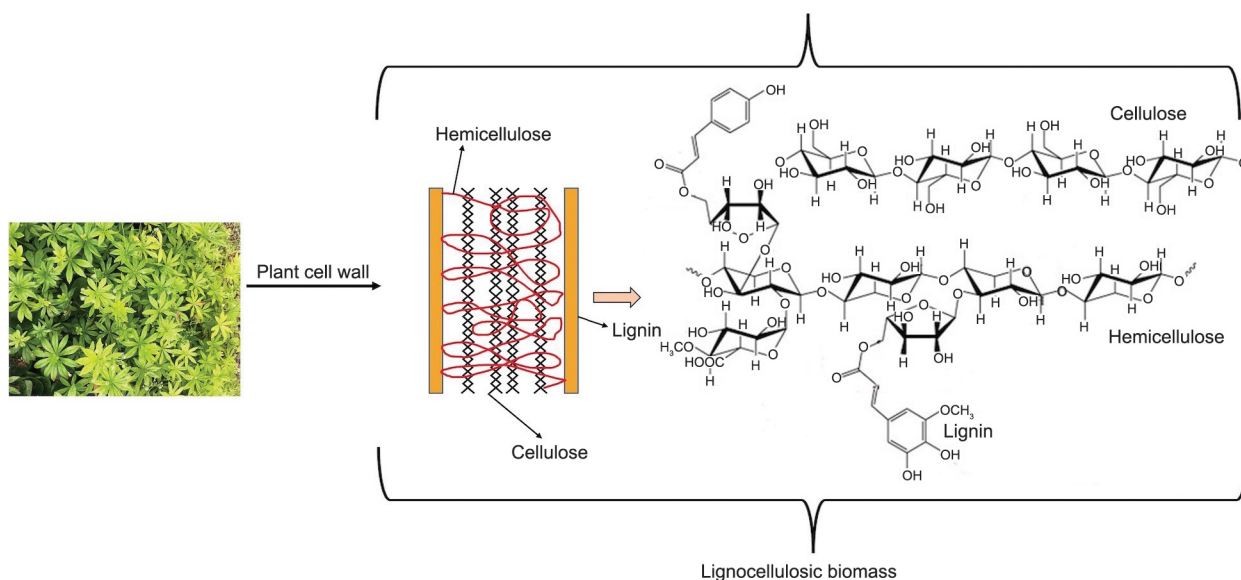


Figure 1. Lignocellulosic biomass and interaction between lignin, hemicellulose and cellulose [7].

the biomass by breaking the bonds between cellulose, lignin, and hemicellulose using strong acids or bases [2].

Lignin consists of three types of phenylpropane monomeric unit, *i.e.*, *p*-coumaryl alcohol (4-hydroxy phenyl (H)), coniferyl alcohol (guaiacyl (G)), and sinapyl alcohol (syringyl (S)) and it is described in Figure 2. In Figure 3, lignin from poplar has been represented with its monomeric unit. G, S, and H units can be bonded by different linkages such as β -aryl

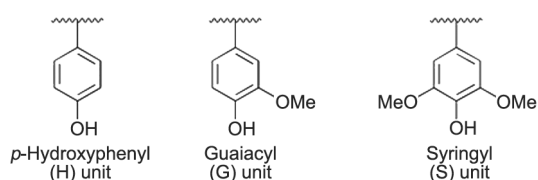


Figure 2. Three types of lignin’s monomeric unit [7].

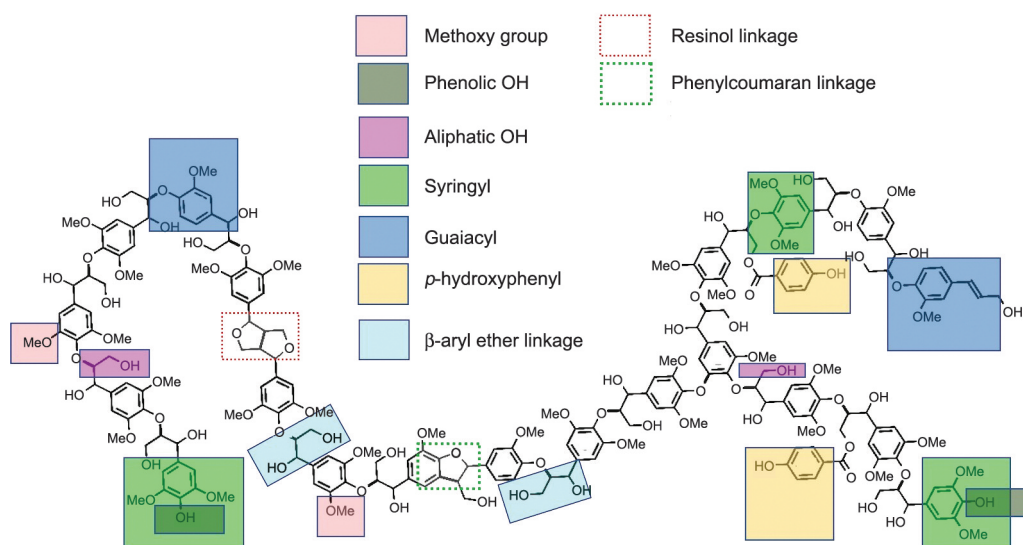


Figure 3. Lignin macromolecular structure from poplar [10]. By permission of Oxford University Press.

ether (β -O-4'), phenylcoumaran (β -5), resinol (β - β), *etc.* [10]. It has many functional groups, such as aliphatic hydroxyl, phenolic hydroxyl, methoxy, *etc.* Its structure is highly variable, and the amounts of lignin monomers can vary depending on the origin of the plant and parts of the plant, such as different organs, and tissues. Lignin isolated from different plants has different amounts of monomeric units as well as different linkages and this is displayed in Table 1. Yuan *et al.* [11] isolated lignin from poplar by three different methods, *i.e.*, by the milling process, using cellulolytic enzymes, and by the alkaline process. Lignin isolated by these three methods has different S/G ratios as listed in Table 1. Lignin isolated from bamboo stem and pith contains different amounts of G, S, and H units, as reported by Wen *et al.* [12].

Table 1. Compositional analysis of lignin isolated from different plant and different parts of plant by different methods.

Plant species	Parts of the plant	Lignin interunit linkage [%]			<i>p</i> -hydroxyphenyl unit (H) [%]	Guaiacyl unit (G) [%]	Syringyl unit (S) [%]	References	
		(β -O-4') β -aryl ether	(β -5') Phenylcoumarans	(β - β') Resinols					
<i>Cocos nucifera</i>	Coir fiber	82	13	4	4	78	18	[13]	
<i>Corchorus capsularis</i>	Jute fiber	72	4	16	2	33	65	[14]	
<i>Dendrocalamus sinicus</i> (Milled wood lignin from bamboo)	–	79.5	5.6	7.2	9	35	56	[15]	
<i>Miscanthus</i> \times <i>giganteus</i> (Ethanol organosolv lignin)	–	–	–	–	4	52	44	[16]	
<i>Paulownia fortune</i> (milled wood lignin)	–	62	11	12	0	60	40	[17]	
<i>Phyllostachys pubescens</i> (bamboo)	Stem (Milled wood lignin)	–	69.7	6.3	10.5	2	31	67	[12]
	Pith (Milled wood lignin)	–	75	4.7	6	1	21	78	
<i>Quercus suber L.</i> (Oak)	Cork	68	20	4	2	85	13	[18]	
	Phloem	71	13	7	1	58	41		
	Xylem	77	9	8	1	45	55		
<i>Populus tomentosa</i> (Poplar tree)	Milled wood lignin	–	83.2	2.6	12.7	S/G ratio		[11]	
	Cellulolytic enzyme lignin	–	84.5	2.1	12.2	1.43			
	Alkaline lignin	–	81.1	2.1	16.4	2.29			
<i>E. urophylla</i> \times <i>E. grandis</i> (Eucalyptus) (Milled than enzymatic hydrolysis)	Heartwood	–	62.1	0.2	11.6	2.83		[19]	
	Sapwood	–	62.4	0.4	7.7	2.74			
	Barkwood	–	69.0	1	2.9	2.91			
Softwood kraft lignin (acid precipitation followed by solvent fraction)	Acetone insoluble	–	12.7	2.6	3.5	–		[20]	
	Acetone/hexane soluble 1 (H300)	–	4.4	1.8	2.4	–			
	Acetone/hexane soluble 2 (H500)	–	4.6	1.8	2.9	–			
	Acetone/hexane soluble 3 (H900)	–	2.5	0.90	1.7	–			
	Acetone/hexane soluble 4 (H1500)	–	1.4	0.4	1.6	–			

During pulping process, lignocellulosic biomass is subjected to delignification for the separation of cellulose and hemicellulose. Mainly four methods are used in the industrial pulping process, which are kraft, sulfite, soda, and organosolv. Lignin is produced

as by-product of all these processes. The annual production of lignin from the chemical pulping industry is more than 50 million tons. This lignin can be extracted from pulping effluent by different methods such as using membrane technology, precipitation,

ion exchange membrane, *etc.*, and it is often termed technical lignin.

At a low price, the most common technical lignin available in the market is lignin isolated from the kraft process (kraft lignin) and lignin isolated from the sulfite process (lignosulfonate), followed by lignin isolated from soda and organosolv process. Differences between kraft, lignosulfonate, soda, and organosolv lignin in molecular weight, sulfur content, and solubility in water and the organic solvent is shown in Table 2. Kraft lignin and lignosulfonates are structurally different from soda and organosolv lignin. Both kraft lignin and lignosulfonate contain sulfur due to using sulfur-containing materials during pulping. As it is listed in Table 2, the amount of sulfur groups in the kraft lignin structure is around 1–3% by weight. This lignin also has a higher amount of aliphatic thiol groups and is primarily hydrophobic [23, 24]. On the other hand, lignosulfonate acts like polyanion due to the presence of negatively charged sulfonate groups (Table 2). For this reason, lignosulfonate can attract different cationic materials by electrostatic interaction. This property is extensively used by researchers to prepare polymer composite with polycation by electrostatic interaction. Lignosulfonates are also water-soluble at a wide range of pH, which is very advantageous for the preparation of hydrogel [25]. Moreover, lignin has antioxidant and antimicrobial properties due to the abundant presence of phenolic groups in its macromolecular structure. It is also highly resistant to biological attacks due to its highly complex structure [1, 3, 26]. Often waste technical lignin is used as fuel, and sulfur present in kraft and lignosulfonate can cause secondary pollution in the form of sulfur dioxide [27, 28]. Thus, kraft lignin and lignosulfonate have been widely used in different polymer composite materials for diverse applications. The main scope of this review is on the use of kraft lignin and lignosulfonate in different polymer composites as reinforcement for different applications. For better understanding, a brief discussion about the extraction of kraft lignin and

lignosulfonate from black liquor and spent liquor, respectively, has also been included in this review.

2. Lignin extraction process

Depending on the amount of lignin production, two kinds of lignin extraction methods exist. The first is analytical scale extraction, and the second is industrial scale extraction [1]. The analytical process is mainly used for small-scale production of lignin to isolate more precise structure or pure form of native lignin. Technical lignin is primarily produced as a by-product in the paper and pulp industry in the delignification process. Strong acids or base and vigorous mechanical treatment are used to separate lignin from carbohydrates which leads to the fragmentation of lignin macromolecules. The soda process, organosolv process, sulfite process, and kraft process are the major industrial processes. These processes are described in Figure 4 with the structure of isolated lignin. The different process used for industrial scale and laboratory scale extraction of lignin from lignocellulosic material has been discussed in recent review articles [1, 29]. However, for better understanding and as the extraction process has a significant effect on the properties of extracted kraft lignin and lignosulfonate, a summary of the extraction of kraft lignin from black liquor and lignosulfonate from spent liquor has been discussed in the next section.

2.1. Kraft lignin

German chemist Carl Ferdinand in Gdansk invented the kraft process for separating lignin from cellulose and hemicellulose. The Kraft extraction process is a widely used method in the paper and pulp industry due to its high yield. This process utilizes sodium hydroxide (NaOH) and sodium sulfide (Na₂S) in a solution with the former in a higher percentage as described in Figure 4. This process is also termed as the sulfate process due to the use of Na₂S. After the final stage, more than 90% of lignin is extracted in the form of black liquor. Black liquor has lignin along with NaOH, Na₂S, and other materials from the wood.

Table 2. Properties of technical lignin [21, 22].

Technical lignin	Molecular weight [kDa]	Sulfur content [wt%/wt%]	Solubility
Kraft lignin	1.5–5.0 (up to 25)	1.0–3.0	Alkali, organic solvent <i>i.e.</i> , dimethylformamide (DMF), pyridine, dimethyl sulfoxide (DMSO)
Lignosulfonate	1.0–50.0 (up to 150)	3.5–8.0	Water
Soda lignin	0.8–3.0 (up to 15)	0	Alkali
Organosolv	0.5–5.0	0	Different organic solvent

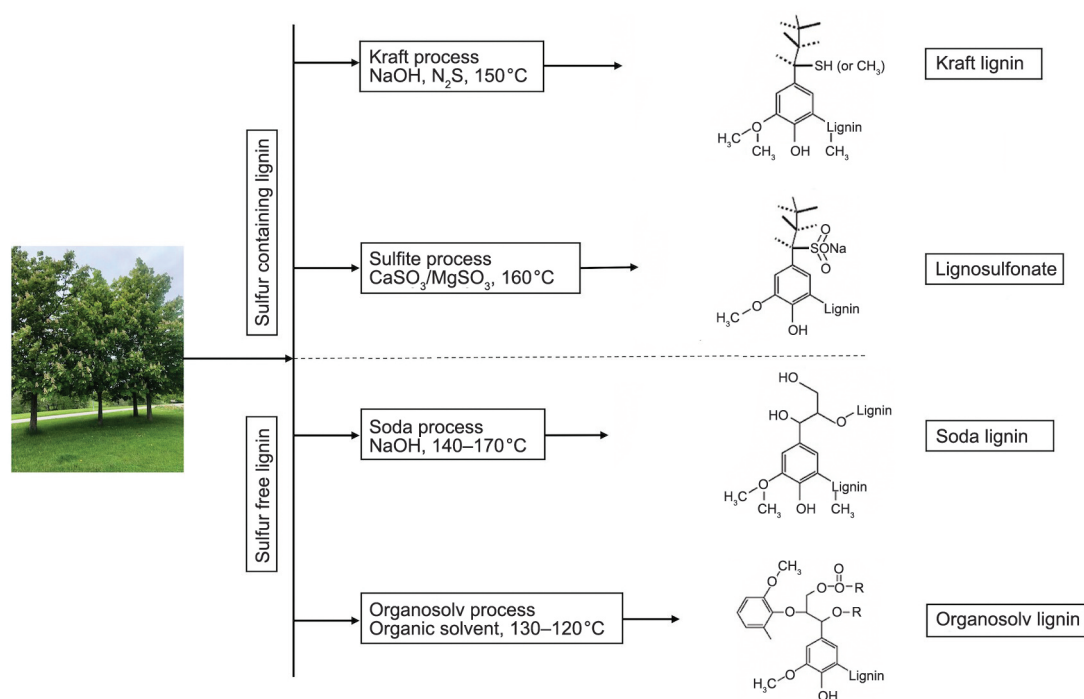


Figure 4. Technical lignin and their structure.

This liquor is highly alkalic, viscous, and black or brown due to its high lignin content [29, 30]. Lignin produced during the kraft process is termed as kraft lignin (KL). Several studies are currently being conducted to develop cost-effective methods for isolating lignin from black liquor. Generally, a cost-effective and more sophisticated method involves a combination of acid precipitation and membrane filtration, such as microfiltration (MF), ultrafiltration (UF), and nanofiltration (NF).

It is predicted that high molecular weight lignin molecules remain in colloidal form in black liquor. During precipitation, lignin self-aggregates due to the instability of its molecular structure. The stability of lignin molecules in an aqueous solution is resulted due to interplay between forces such as van der Waals forces, electrostatic forces, and other hydrophobic forces. According to Rudatin *et al.* [31], the equilibrium of these forces mainly depends on the functional groups present in the lignin molecule, conditions such as pH, temperature, *etc.* of the solution and concentration of lignin in that solution. In black liquor, under alkaline pH, lignin remains as negatively charged due to the dissociation of phenolic and carboxyl groups. Lignin molecules remain associated with sodium as a counter ion. In this stage, negatively charged lignin molecules repel each other due to electrostatic forces, and as a result, these molecules remain stable and dissolve in an aqueous solution. For this reason, KL is soluble in an aqueous solution

at alkaline pH. Lignin molecules become neutral when pH of the black liquor is reduced due to the interaction of hydrogen ions with negatively charged functional groups and the replacement of sodium ions with hydrogen ions (protonation). Consequently, neutral lignin molecules do not repel each other by electrostatic forces and start to attract each other by hydrophobic forces, which results in self-aggregation followed by precipitation. The whole mechanism of KL precipitation is described in Figure 5. At pH value the same or below the pK_a value of phenolic groups (9, 4–10), functional groups of lignin are protonated, which results in further instability of lignin molecules and resulted in precipitation of lignin. Usually, pH value of the solution is kept below pK_a value of lignin. A pH of less than 2 is preferable as it facilitates complete protonation of hydroxyl and carboxyl groups to form sodium-free hydrogen lignite. According to Norgren *et al.* [32], high molecular weight lignin molecule has higher pK_a values than lower molecular weight fraction. Therefore, larger lignin molecules with higher pK_a values are more unstable even in highly alkalic black liquor. This is why self-aggregation and precipitation occur first in the case of larger molecules, followed by smaller lignin molecules [33].

Sulphuric acid, carbon dioxide, or chlorine dioxide is usually used to reduce the pH of the black liquor to 5–7. Subsequently, precipitated lignin is separated by membrane filtration. The molecular weight of KL

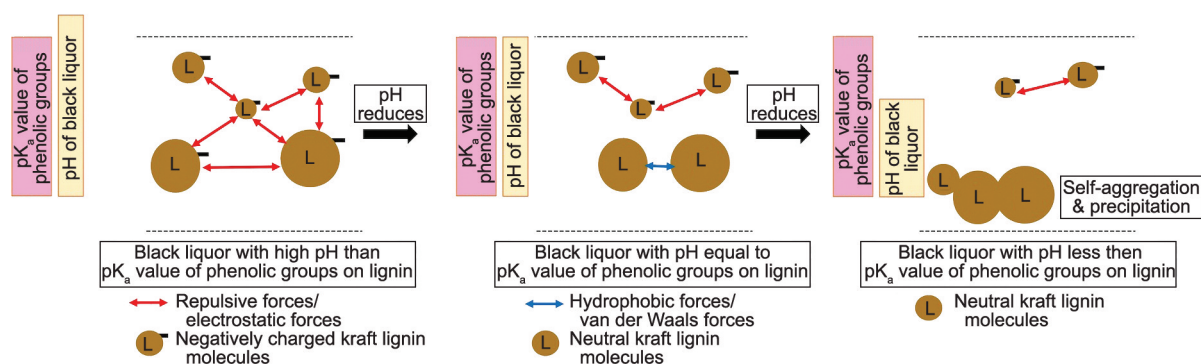


Figure 5. Mechanisms of kraft lignin precipitation from black liquor by acidification.

can vary between 1000 to 3000 Da and can go up to 15 000 Da. Due to lignin molecules' wide molecular weight distribution, flux decline is a significant obstacle for membrane filtration. However, membrane technology is a very energy-efficient and cheap alternative. Between polymeric and ceramic membranes, ceramic ones are reported to be the most efficient for membrane filtration as they can tolerate the high pH of black liquor [34, 35]. Membrane filtration of KL has been reviewed in detail recently by Humpert *et al.* [34]. In addition to these methods, electrochemical methods and liquid-liquid extraction methods have also been used by researchers to isolate lignin from black liquor [33].

Lignin can be isolated from black liquor by using electrolysis and electrodialysis. In these processes, lignin is precipitated at the anode, and at the cathode, hydrogen is produced. During electrolysis, the anode chamber has the black liquor, and in the cathode chamber, a diluted solution of NaOH is kept. A cation exchange membrane separates the anode chamber and cathode chamber. During the electrolysis, Na⁺ ions from black liquor move towards the cathode chamber through a membrane because of the application of the electrical field. In the cathode chamber, these sodium ions react with OH ions formed due to the cathodic reduction of water, subsequently leading to NaOH formation. In the anode chamber, hydrogen ions are formed due to anodic oxidation of water which is resulted in acidic pH. These two reactions led to the formation of acidified black liquor in the anode chamber and NaOH in the cathode chamber as main outlet streams. These hydrogen ions replace the sodium ions present in the lignin molecules, which convert negatively charged lignin molecules into neutral lignin molecules. Then self-aggregation and precipitation of KL occur following the same principle of acid precipitation. Subsequently,

lignin is deposited on the surface of the anode. In this process, platinum and nickel have proven to be good anode materials [36–38]. Haddad *et al.* [37] studied KL precipitation from black liquor by electrodialysis, where charged membranes such as cation exchange and bipolar membranes were used for ion transport. Electrodes only functioned as electrical terminals [37, 39]. In a recent study by Chen *et al.* [40], a microbial biomass recovery cell was used to isolate lignin by electrolysis. Anaerobic sludge acts as the anode that produces H⁺ ions [40, 41].

Many researchers used solvent fractionation to separate lignin from black liquor. Alcohol and calcium solution [42], acetone [43], and ethyl acetate [44] are common organic solvents that have been used as an organic solvent for KL fractionation. Ropponen *et al.* [43] reported that a low molecular weight fraction of KL has higher phenolic hydroxyl groups. Moreover, It has a higher amount of S units and has a low glass transition temperature (T_g).

Dominguez-Robels *et al.* [45] used two different concentrations of acetone for KL fractionation. First, KL extracted by acid precipitation was mixed with a 60% aqueous solution of acetone, and insoluble lignin was separated at this stage. The concentration of the solution was subsequently decreased to 40% and the insoluble fraction was isolated. Molecular structure KL, extracted from black liquor by different methods, has various amounts of functional groups which is shown in Table 3. Acetone soluble fraction had the lowest molecular weight with the highest phenolic hydroxyl groups (Table 3).

Wang *et al.* [54] used hexane, diethyl ether, methylene chloride, methanol, and dioxane with increasing hydrogen bonding capacity. It was observed that the average molecular weight of KL increases with the increasing hydrogen bonding capacity of the solvents. A higher molecular weight fraction is reported to have

Table 3. Amounts of aliphatic-OH, phenolic OH, COOH groups, average molecular weight, and T_g of KL, extracted by different methods.

Extraction process		Aliphatic-OH [mmol/g]	Phenolic-OH [mmol/g]	COOH [mmol/g]	M_w [Da]	T_g [°C]	References
Ceramic membrane	Initial: lignoboost lignin	1.97±0.07	4.27±0.04	0.45±0.01	–	–	[46]
	Final: filtered fraction	0.43±0.02	3.8±0.27	1.00±0.08	1600–400		
Ultrafiltration	Fraction 1: >10 kDa	2.62	2.81	0.52	33 500	170	[47]
	Fraction 2:>5 kDa	2.33	2.95	0.49	28 200	159	
	Fraction 3: 5–10 kDa	1.88	3.87	0.49	4 900	140	
	Fraction 4: 1–5 kDa	1.37	3.7	0.35	4 700	94	
	Fraction 5: 0–5 kDa	1.42	3.61	0.46	4 100	82	
	Fraction 6: 0–1 kDa	1.25	4.11	0.38	2 700	70	
LLE (acetone/water)	Fraction SKL (Softwood kraft lignin)	1.72	3.57	0.44	4 130	–	[45]
	Fraction SKL insoluble	1.75	2.10	0.19	11 230	–	
	Fraction SKL precipitation	1.79	4.38	0.42	5 600	–	
	Fraction SKL soluble	1.70	5.91	0.54	2 260	–	
LLE	Initial KL	1.17	2.76	0.28	4 100	–	[48]
	Ethanol 80% insoluble	1.85	3.43	0.33	7 600	–	
	Ethanol 70% precipitate	1.50	2.75	0.20	5 300	–	
	Ethanol 60% precipitate	1.40	2.53	0.23	4 300	–	
	Ethanol 50% precipitate	1.29	2.82	0.29	3 300	–	
	Ethanol 40% precipitate	1.37	3.01	0.37	2 800	–	
	Ethanol 30% precipitate	2.09	2.94	0.40	2 200	–	
	Ethanol 10% soluble	2.22	4.05	0.71	1 500	–	
	Acetone 50% precipitate	1.28	2.62	0.26	6 000	–	
	Acetone 40% precipitate	1.13	2.94	0.32	3 500	–	
	Acetone 30% precipitate	1.06	2.87	0.33	2 700	–	
	Acetone 10% soluble	2.25	4.04	0.63	1 600	–	
	PGME 50% precipitate	1.97	2.33	0.20	6 700	–	
	PGME 40% precipitate	1.86	2.63	0.24	3 900	–	
	PGME 30% precipitate	1.88	2.74	0.29	2 800	–	
PGME 10% soluble	1.89	3.95	0.56	1 700	–		
Solvent fractionation	KL	2.24	4.25	0.42	6 300	153	[49]
	Acetone soluble fraction	1.63	5.76	0.57	3 500	112	
	Acetone insoluble fraction	2.74	3.08	0.35	14 000	173	
Sequential solvent fractionation	SKL	2.07	4.19	–	–	138	[50]
	Acetone soluble	1.59	5.03	–	–	118	
	Acetone insoluble	1.72	3.69	–	–	146	
	Acetone insoluble, methanol soluble	1.96	4.48	–	–	173	
	Acetone insoluble, methanol insoluble	2.08	4.06	–	–	174	
	Methanol soluble	2.08	4.83	–	–	170	
	Methanol insoluble	1.95	3.94	–	–	175	
	Acetone soluble (by dialysis)	1.57	4.69	–	–	112	
	Acetone insoluble, methanol soluble (by dialysis)	1.63	4.08	–	–	131	
Acetone insoluble, methanol insoluble (by dialysis)	2.34	2.87	–	–	169		
Softwood kraft lignin (acid precipitation followed by solvent fraction)	Acetone insoluble	3.00	3.50	0.50	12 200	–	[20]
	Acetone/hexane soluble 1, (H300)	2.40	5.20	0.60	3 300	–	
	Acetone/hexane soluble 2, (H500)	2.10	5.30	0.70	2 000	–	
	Acetone/hexane soluble 3, (H900)	2.00	5.50	0.80	1 300	–	
	Acetone/hexane soluble 4, (H1500)	1.70	5.70	0.60	1 000	–	

Table 3. Continuously.

Extraction process		Aliphatic-OH [mmol/g]	Phenolic-OH [mmol/g]	COOH [mmol/g]	M_w [Da]	T_g [°C]	References
Kraft lignin	Kraft lignin	3.13	3.09	0.14	5410	162	[51]
	5 kDa	4.11	2.97	0.12	7010	–	
	3 kDa trapped	2.43	3.87	0.15	3540	149	
	3 kDa permeate	1.51	4.21	0.16	1890	117	
Lignin	Softwood kraft lignin	3.48	4.61	0.79	–	–	[52]
	Hardwood soda lignin	2.12	4.04	0.97	–	–	
Lignin	Kraft lignin	1.89	3.97	0.46	–	–	[53]
	KL treated with 0.25 pyrrolidine	0.06	1.07	0.40	–	–	
	KL treated with 1.5 pyrrolidine	0.37	3.07	0.62	–	–	

higher branching as well as higher thermal stability. It was also observed that a higher molecular weight fraction has a higher amount of β -aryl ether bond (β -O-4). In another study by Passoni *et al.* [55], tetrahydrofuran, methanol and 2-butanone were used for kraft lignin fractionation. It was observed that the 2-butanone soluble fraction was low molecular weight while the methanol soluble fraction was higher. This can be due to the strong ability of methanol to form a hydrogen bond with longer OH-rich macromolecular lignin molecules than 2-butanone. However, the main challenge of using solvent fractionation is the use of costly and toxic solvents. Jääskeläinen *et al.* [48] used less toxic chemicals such as ethanol, acetone, and propylene glycol monomethyl ether to extract KL. The soluble fraction of KL had the lowest molecular weight and higher phenolic hydroxyl content. This drawback can also be overcome by using ionic liquids. Ionic liquids are organic salts with low melting points ($<100^\circ\text{C}$). Usually, they are liquid at room temperature and consist of anions and cations entirely. Moreover, they are non-flammable, have lower toxicity, and have scalable physicochemical properties. Pu *et al.* [56] reported that KL is soluble in certain ionic liquids, such as [hmim][CF₃SO₃], [mmim][MeSO₄], [bmim][MeSO₄]. However, the solubility of lignin mainly depends on the types of anions present in ionic liquids. For example, anions such as [PF₄]⁻ and [BF₆]⁻ negatively affect the solubilization of lignin [56, 57]. The industry mainly uses four methods for the isolation of lignin from black liquor. These methods are WestVaco, LignoForce, LignoBoost, and SLRP [33].

2.2. Lignosulfonates

Lignin produced by the sulfite process is often termed as lignosulfonates. In this pulping process, lignocellulosic biomass reacts with a metallic sulfite, usually

calcium sulfite (CaSO₃) or magnesium sulfite (MgSO₃) and sulfur dioxide (SO₂). The reaction mainly involves a series of reactions, including sulfonation, hydrolysis, and condensation. The introduction of sulfonic groups leads to the formation of relatively soluble lignosulfonates with cations such as Mg, Na, or NH⁴⁺. By forming lignosulfonates, subsequent fragmentation of the lignin molecule occurs through its hydrolysis and dissolution with cellulose. The sulfite process is carried out at pH ranging from 1.5 to 2 at reaction temperatures ranging from 140 to 160 °C [23, 30].

The spent liquor from the sulfite process mainly consists of lignosulfonates (50–80 wt%), and hemicellulose (30 wt%) with different residual pulping chemicals. Lignosulfonates mainly contain two types of ionizing groups, *i.e.*, sulfonates whose pK_a is around 2 and phenolic groups whose pK_a is around 10. For this reason, it is soluble in water over the entire pH range and cannot be precipitated. Techniques such as membrane filtration, liquid-liquid extraction, ion exchange, and amine extraction have been utilized to isolate lignosulfonates from spent liquor [23, 29, 30, 58].

Lignosulfonates have molecular weights ranging from 1000 to 50000 Da. Its molecular weight is higher than the other component of the spent solution, such as hemicellulose and other chemicals. For that reason, membrane filtration is a practical method to separate lignosulfonate from the spent solution. Ultrafiltration (UF) was first employed to separate lignosulfonates which was produced in the calcium bisulfite (Ca(HSO₃)₂) pulping process in 1981 in Norway. The purity of the isolated lignosulfonates was 95% by using polysulfone membrane of molecular weight cut off (MWCO) value of 20000 Da [59]. Polysulfone, cellulose acetate, and fluoropolymer

membrane with MWCO values of 1, 5, 10, 20, 50, and 100 kDa [60], regenerated cellulose NF membrane of 0.5 kDa MWCO value [61], cellulose films [62] were used for extraction of lignosulfonate.

Lignosulfonate is extracted as calcium salt in the commercial lignosulfonate extraction method termed as the ‘Howard method’. In this method, in the first step, adding calcium oxide leads to the precipitation of calcium sulfite present in the spent liquor at pH 8.5, which is then filtered and removed. In the second step, the addition of calcium oxide leads to the formation of calcium lignosulfonates which are solid at pH 12. This can be isolated by filtration and recovery of lignosulfonates in this form; this method can be more than 90% [23, 63]. Another method used for the extraction of lignosulfonates is amine extraction. This method converts lignosulfonates into water-insoluble, lignosulfonic acid-amine adducts using amines such as long chain aliphatic amine, tri-n-hexyl-amine, and poly ethyleneimine. Then water insoluble adducts are extracted by liquid-liquid extraction. However, the main drawbacks of this method are the removal of amines from the solution, the formation of salt (NaCl) during re-extraction as well as the formation of foam, problems regarding emulsion, etc. [64, 65].

Chakrabarty *et al.* [66], used a liquid membrane for the separation of lignosulfonate from spent solution. A liquid membrane is a liquid barrier between two aqueous phases of different compositions, termed as feed phase and strip phase. Components can flow through the liquid membrane by using a diffusional process because of their own concentration gradient. The liquid membrane can be supported or non-supported such as bulk and emulsion liquid membrane. Chakrabarty *et al.* [66] used a bulk liquid membrane of dichloroethane as solvent and trioctylamine (TOA) as a carrier for the separation of lignosulfonate. They also used a supported liquid membrane which is a hydrophobic porous membrane with an organic phase with a carrier phase. One of the important factors affecting the optimal use of a liquid membrane is its stability; the reported stability of the membrane was up to 10 hours. Maximum lignosulfonate recovery was observed in the case of PA 6.6, as a hydrophobic porous membrane at 4% TOA concentration with 0.5 M NaOH as strip [67]. The amount increased significantly when surfactant such as polyethylene glycol was added to the liquid membrane system. The number of optimum lignosulfonates was 85%,

in this case [68]. Sunflower oil was mixed with TOA by Kumar *et al.* [69], for the separation of lignosulfonates by liquid membrane.

In a study by Kontturi and Sundholm, lignosulfonate was extracted using different aliphatic long chain amines-organic solvent systems. Amines used in this process are dodecyl amine, dioctyl amine, and trioctyl amine dissolved in 1-butanol, 1-pentanol, methyl isobutyl ketone, 1,2-dichloroethane, or cyclohexane. Lignosulfonates were extracted according to their molecular weight in this method [70].

3. Kraft lignin-based polymer composite

3.1. Kraft Lignin-based Polymer composites with synthetic polymer matrix

KL was used as reinforcement with polyolefins as a polymer matrix by researchers. Table 4 describes the application of KL as reinforcement in different polymer matrices, chemical modifications of KL for better dispersion, and improvement of properties of end composites. Lignin is a polar polymer with, on average, 1 or 2 hydroxyl groups per monomer as described in Figure 2, and Polyolefins are highly hydrophobic as well as non-polar without any polar groups. So, for better dispersion of lignin in the polymer matrix, alkylation or different types of chemical modifications are required. Chemical modifications are also needed to increase the loading of reinforcements in the polymer matrix. The lower molecular weight fraction of softwood KL has a higher amount of phenolic hydroxy group content, which makes it suitable for such chemical modifications. Aliphatic hydroxyl groups present in lignin was chemically modified by acetylation, esterification *etc.* to reduce its hydrophilicity as it is described in Figures 6 and 7.

Chen *et al.* [71] used alkylated KL for the development of polypropylene-lignin composite. It was reported that with an increase in the amount of alkylated KL in polypropylene, tensile modulus, and strength of the composite decreased. This negative effect can be due to a reduction in crosslink density of the matrix as alkylated KL act as a plasticizer, and this phenomenon can lead to a reduction in matrix integrity. However, an increase in impact strength was observed up to 10% alkylated KL loading in polypropylene which is due to better compatibility of alkylated KL with polypropylene. Acetylation, where phenolic hydroxyl groups of lignin are replaced with acetate groups, can make lignin more compatible with hydrophobic synthetic polymers.

Table 4. Different kraft lignin-based polymer composite.

	Types	Polymer type	Chemical modification of KL	Application of KL	Reference
Kraft lignin	Polymer composite	Polypropylene	Alkylation, acetylation, Aminolysis, Hybrid with SiO ₂ , hybrid with ZnO	Flame retardant, Improvement of mechanical properties, coupling agent, oil absorption,	[53, 71–90]
		Polyethylene	Methylation Esterification, hybrid with MgO, hybrid with ZnO, lignin reverse micelle	Antioxidant, improvement of thermal stability and mechanical properties, UV protection, antimicrobial,	[49, 51, 91–107]
		Polystyrene	Esterification,	Adsorbent, antioxidant, improvement of mechanical properties,	[108–113]
		PET	Acetylated	Antioxidant, improvement of mechanical properties	[114, 115]
		PVA	–	Adsorbent, antibacterial, antibiofilm, UV protection, antioxidant	[116–119]
		PBAT	Methylation & maleic anhydride grafting with PBAT	Cheap packing material	[120]
		PVC	Hybrid filler with Mg(OH) ₂ , hybrid filler with silica,	Oil rejection, improvement of mechanical properties	[121–123]
		Polyaniline	–	Dopant, adsorbent	[124, 125]
		Starch	–	Improvement of mechanical properties and hydrophobicity, gas separation	[126–128]
		PLA	Acetylation, acidified and methylated,	Improvement of mechanical and water absorption, antioxidant	[129–136]
		CNF	Colloidal lignin particle	UV protection, improvement of mechanical and water absorption, antioxidant	[137, 138]
		MCC	Propargylated	Semitransparent, flexible, UV blocking properties	[139]
		Chitosan	–	Antibacterial, antioxidant, adsorbent, UV protection, improvement of mechanical properties	[140–145]
		PHB	–	Antioxidant, improvement of mechanical properties	[146]
Natural rubber	Hydroxymethylation	Antioxidant, improvement of mechanical properties	[147, 148]		

This chemical modification can also increase thermal stability, which is advantageous for the thermal processing of lignin, such as compression molding. Jeong *et al.* [72] used acetylated softwood KL to develop polypropylene, low-density polyethylene

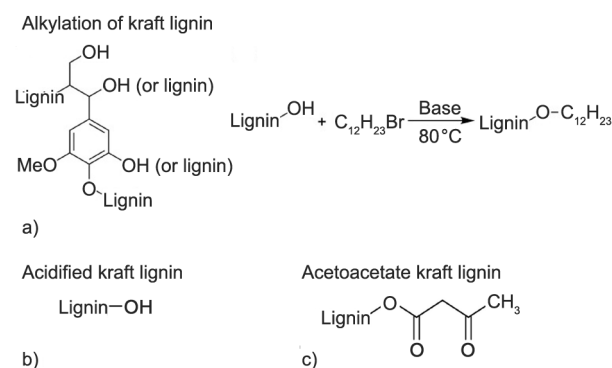


Figure 6. Different chemical modification of kraft lignin for better dispersion in polymer matrix, a) alkylation of kraft lignin, b) acidified kraft lignin, c) acetoacetate kraft lignin [71, 133, 148]. With permission from John Wiley and sons.

(LDPE), polystyrene, and polyethylene terephthalate (PET)-based composite material by melt blending and compression molding. All the composites exhibited a slight increase in the young modulus up to 37% loading of acetylated KL. Improvements in toughness were observed up to a specific loading of KL. With higher percentage of KL loading, resultant composites with all four synthetic polymers showed diminished mechanical properties and became brittle. In the case of esterification, it was reported that with increasing ester carbon chains from C2 to C4, the distribution of KL became more homogenous in the polyethylene matrix. A sharp increase in the Young modulus was observed with increasing loading of KL [94, 99]. Most of the chemical modification of KL was performed to increase hydrophobicity and decrease surface tension. This was done using polymer-surfactant adsorption. Alkenyl succinic acid anhydride or alkyl ketene dimer (AKD) is hydrophobic surface reagent that was used by Atifi *et al.*

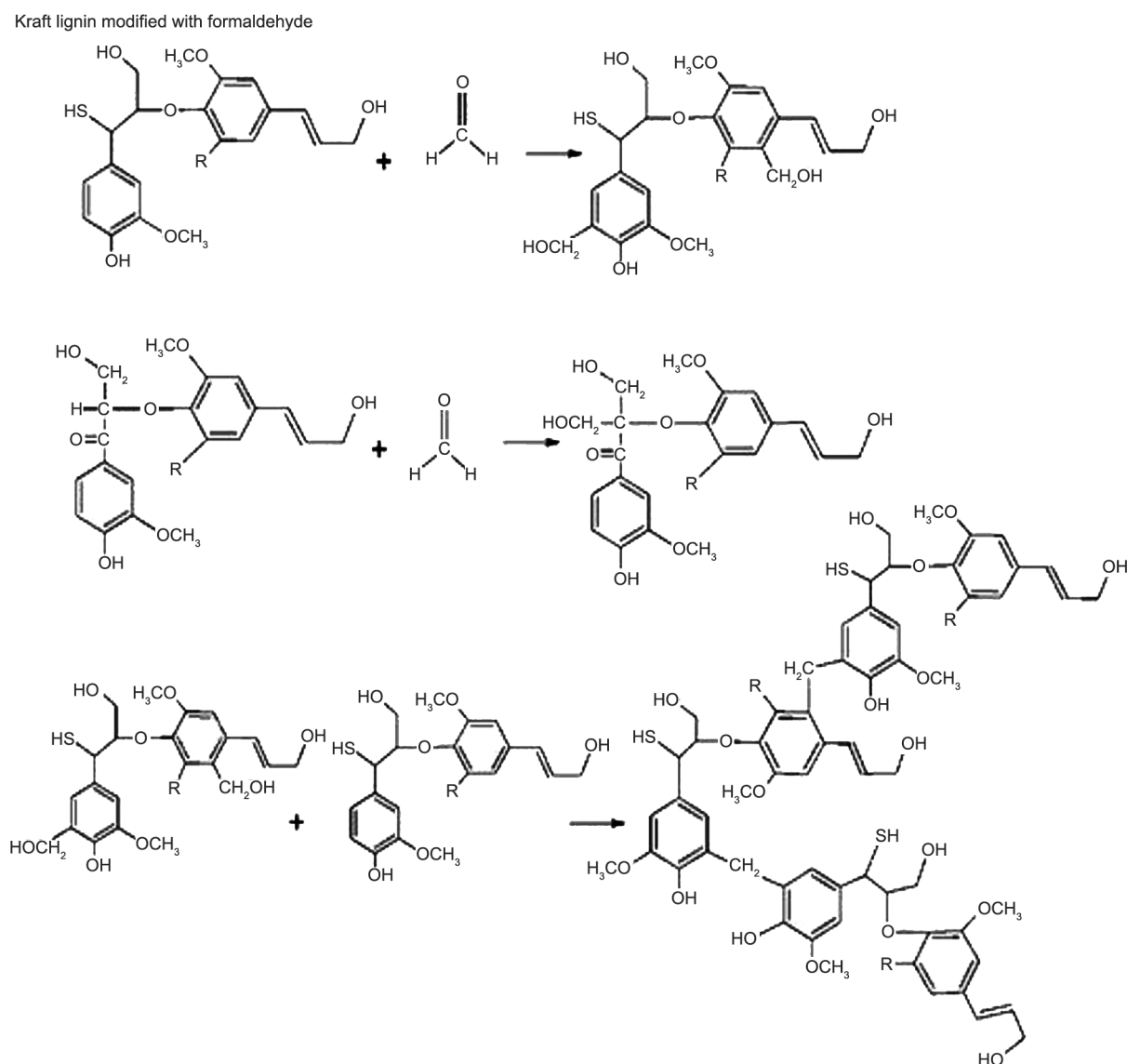


Figure 7. Different chemical modification of kraft lignin by using formaldehyde [148].

[149] to modify KL. Other hydrophobic materials such as polyethylene oxide (PEO), polyethylene-block-poly(ethylene glycol) (PE-*b*-PEG), cetrimonium bromide (CTAB), and dodecyl succinic anhydride (DDSA) were also used to modify KL. Treatment of KL with AKD and PE-*b*-PEG showed the best results with the highest hydrophobicity of lignin particles. This resulted in increased young modulus due to better dispersion in the case of AKD-KL/polypropylene and PE-*b*-PEG-KL/polypropylene composite.

Without chemical modification, the incorporation of KL in polyethylene composites resulted in a decrease in mechanical strength [93]. However, it was reported that a low molecular weight fraction of KL, with higher phenolic hydroxyl groups and lower double bonds, had better compatibility with the polyethylene matrix. Better dispersion of KL in polyethylene matrix caused

an increase in young modulus in the case of KL/polyethylene composite [92]. Fractionalization of KL was performed to have different molecular weight fractions with different phenolic hydroxyl group content by Huang *et al.* [51], as described in Figure 8 and listed in Table 3. In Figure 8c, it can be clearly observed that the tensile strength of the composites increased with decreasing molecular weight of KL due to better dispersion of lower molecular weight fraction with a higher amount of phenolic hydroxyl group. Compatibilizer was used to increase the interaction between polyethylene and KL. For better dispersion of KL in KL/polyolefin composites, coupling agents such as poly(styrene-*co*-ethylene-*co*-butylene-*co*-styrene) (SEBS) modified as SEBS-NH₂, maleic anhydride grafted with polyethylene (MAPE) [95], Organic peroxide such as dicumyl

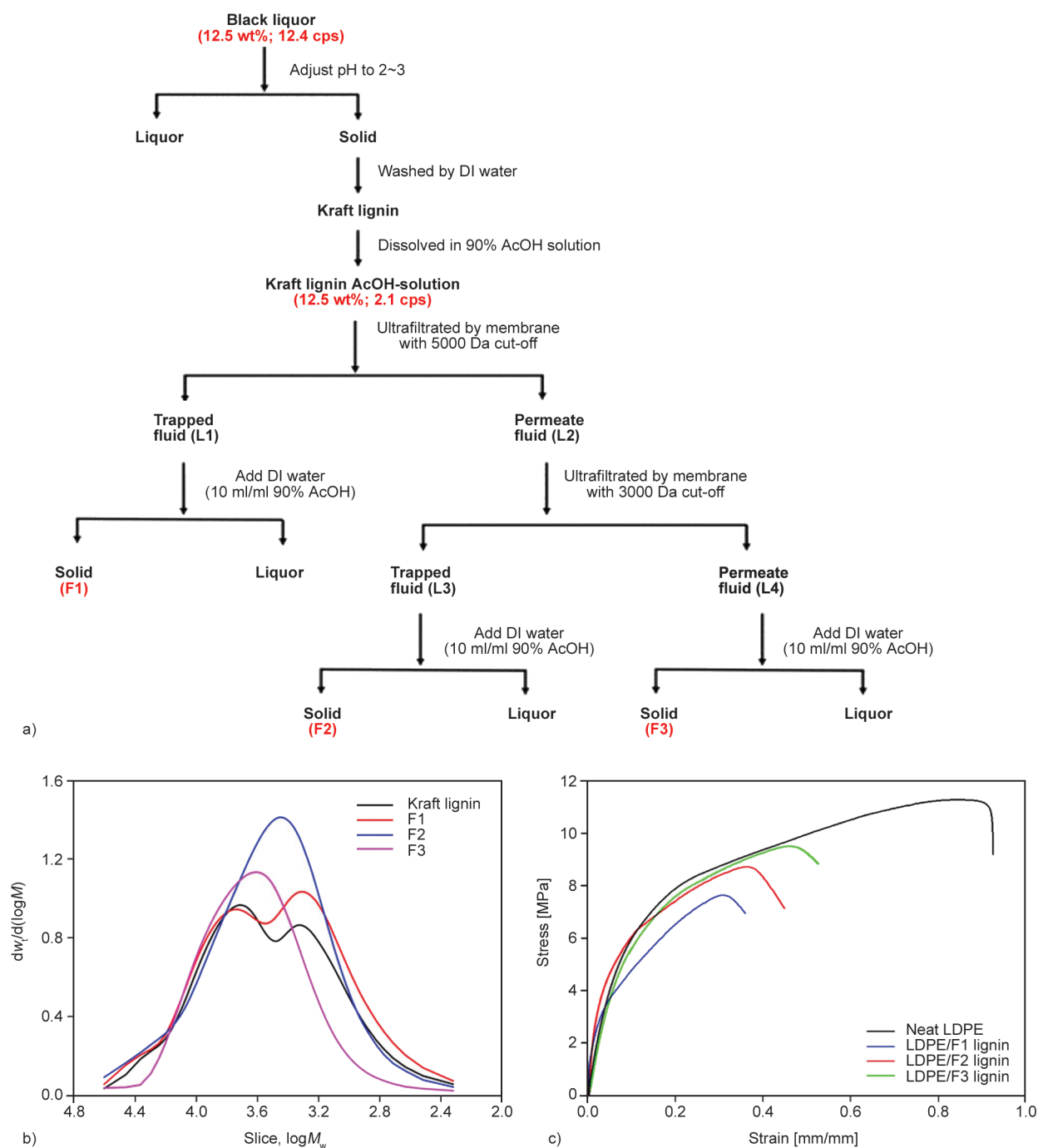


Figure 8. a) Process used for sequential ultrafiltration of KL using membrane with different MWCO, b) Gel permeation chromatography (GPC) chromatograms of KL and fractionated lignin of different molecular weight, c) stress vs. strain curve of LDPE/lignin composites with 20 wt% KL and fractionated lignin [51]. Copyright 2017 American Chemical society.

peroxide (DCP) [51, 89, 92, 93, 98, 150], Polyethylene oxide (PEO) along with boric acid and DCP [52], Silane coupling agent bis (3-triethoxysilyl propyl) tetrasulfide (TESPT) [151], maleated polypropylene in combination with ethylene butyl acrylate glycidyl methacrylate (EBGMA) [90], copper (II) sulfate pentahydrate ($\text{CuSO}_4 \cdot 5\text{H}_2\text{O}$) [152] were used. When SEBS- NH_2 was used as a compatibilizer, a sharp

increase in the young modulus of polyethylene/KL composite was observed. Due to the presence of aromatic molecules in SEBS- NH_2 , the compound is partially miscible in polyethylene matrix and interacts with KL via hydrogen bonding as well as π -stacking forces [95].

Apart from conventional thermal processing techniques, polymerization in the presence of lignin was

also used by researchers to develop lignin-based polymer composites. Modified KL with methacrylic anhydride was used for co-polymerization with styrene and methyl methacrylate to develop a polymer composite of polystyrene and poly(methyl methacrylate) (PMMA) in a study by Goliszek *et al.* [153]. Polymer composites with low levels of modified lignin had slower degradation rates under accelerated aging because of their polymer networks. However, with a concentration of modified lignin above 20 wt%, the polymer composites became more heterogeneous and showed higher degradation in the case of PMMA. The polymer composite of modified lignin and polystyrene showed better resistance toward accelerated aging. Polymerization was used for the preparation of polyethylene/lignin composite by anchoring lignin into vanadium-based Ziegler-Natta catalyst VOCl_3 [105, 109–111]. Industrial process such as solid-state shear pulverization (SSSP) was used by Iyer and Torkelson, and they reported that composites prepared by the SSSP method showed better lignin dispersion in polyolefin matrix than in the conventional melt mixing process. Materials are subjected to extraordinarily large compressive and shear forces during solid state processing, which can be responsible for such better dispersion of lignin [154].

KL was used along with different inorganic oxide fillers, such as MgO , ZnO , SiO_2 , *etc.*, in polymer composites to have different properties, usually for specific application-based properties [155, 156]. Bula *et al.* [96] used MgO -KL for the preparation of polyethylene composite which can have application as packaging material. Although composite film with MgO -lignin showed lower gas and water vapor permeability, this film exhibited excellent UV protection compared to neat LDPE, which can be used as UV screening films. It was reported that hydroxyl groups, double bonds, and aromatic rings present in lignin molecules are mainly responsible for the absorption of UV light [119]. Lignin also has antimicrobial properties. Phenolic hydroxyl groups present in lignin was reported to be primarily responsible for causing damage to the bacterial cell membrane, thereby having antimicrobial properties [119]. For this reason, KL along with ZnO in polyethylene composite [102], and poly(vinyl alcohol) (PVA) PVA/gelatin/KL [118] composite were developed with antimicrobial properties for food packaging applications. Composites with KL was studied for application as adsorbent for metals and other chemicals. Monoliths

were developed from polypropylene and lignin by Alassod *et al.* [87] for thermally induced phase separation techniques for application as oil absorbents. KL-incorporated polystyrene (KL-PS) exhibited better adsorption efficiency for copper ions due to the presence of different functional groups in lignin, which resulted in higher solid surface energy than polystyrene and improved interaction with copper ions [109]. KL/PVA composite was prepared as adsorbents for bisphenol A and erythromycin. The composite was microporous flow permeable material with binding sites of lignin available on the surface. However, during desorption, leakage of lignin along with adsorbed chemicals was reported by Ivanov *et al.* [117].

In a study by Widsten *et al.* [157], KL, acetylated KL and KL were treated with urea and formaldehyde to have higher N_2 , which were then used as a flame retardant in polypropylene composite. KL treated with urea and formaldehyde exhibited similar properties as of pentaerythritol (PER) which is an extensively used flame retardant along with ammonium polyphosphate (APP). The good performance of KL treated with urea and formaldehyde was due to the presence of a higher amount of N_2 , which resulted in the production of poorly burning gases such as ammonia.

Antioxidant properties of KL were reported in polyethylene at a very low concentration, below 2 wt%, due to the presence of phenolic groups in lignin [85]. Moreover, commercial antioxidant was reported to have a higher leaching rate than lignin due to the highly crosslinked structure of lignin, which inhibits its solubilization and consequently reduces its diffusion in the polymer matrix [158]. The thermal antioxidant property of lignin was reported to be dependent on the total content of phenolic and aliphatic hydroxyl groups [159]. The lower amount of phenolic hydroxyl group can reduce the overall anti-oxidative property of lignin. The study by Sedeghifar *et al.* [49] demonstrated that higher phenolic hydroxyl content of the acetone soluble fraction of KL resulted in 55% better anti-oxidant activity. In a study by Ye *et al.* [53], acetylated lignin was subjected to selective aminolysis to have a higher number of phenolic hydroxyl groups with higher numbers of aliphatic hydroxyl groups blocked (Table 3). Polypropylene/KL and polypropylene/modified KL both showed an increase in oxidative thermal stability of the polymer. It is predicted that phenolic hydroxyl groups of

untreated and modified KL capture the radicals generated from the tertiary proton in the polypropylene macromolecular chain. However, superior mechanical properties were observed in the case of polypropylene/modified KL due to better dispersion as blocking of aliphatic hydroxyl groups made modified KL more hydrophobic. So, modified KL was more compatible with polypropylene structure than untreated KL. Subsequently, it was concluded that in the case of thermooxidative stability, the main factor is the number of phenolic hydroxyl groups present in the lignin molecule, not the degree of dispersion of lignin in the polymer matrix. So, selective aminolysis of acetylated KL was concluded to be a better option for having improved mechanical properties, better dispersion in polymer matrix due to the presence of a lower number of aliphatic hydroxyl groups, and improved thermal oxidative stability due to the presence of a higher number of phenolic hydroxyl groups. Similarly, butylated KL using *n*-butyric anhydride in polypropylene could also be advantageous [84]. Moreover, KL can reduce the harmful effects of radiation on the mechanical and thermal properties of the polymer as reported by Sugano-Segura *et al.* [78].

Lignin can also be used as a coupling agent in hybrid polymer composite to increase adhesion between second reinforcements and polymer matrix [79]. Luo *et al.* [80] used different concentrations of KL as a natural compatibilizer in wood flour/polypropylene composite. In the case of lower concentration of KL (0.5 and 1.0 wt%) in wood flour/polypropylene composite, reduced water absorption and improved mechanical properties were observed. However, in the case of a higher concentration, an increase in water absorption and a decrease in mechanical properties were reported. Superior properties in the case of lower concentration were due to better interfacial adhesion between wood flour and polypropylene in the presence of 0.5 and 1.0 wt% KL. Similarly, esterified KL was used as a coupling agent in a bark/ polyethylene composite [103]. Due to lignin's aromatic structure, it is compatible with carbon fiber and alkylation; on the other hand, it can increase the compatibility of lignin with polypropylene. For this reason, Sakai *et al.* [88] used alkylated lignin as a compatibilizing agent in polypropylene/carbon fiber composite. Moreover, another important aspect of this study is the use of ionic liquid 1-ethyl-3-methylimidazolium acetate or [Emim][OAc] for alkylation treatment.

3.2. Kraft lignin-based polymer composites with natural polymer matrix

Lignin was used as reinforcements in bio-polymer composite using starch, cellulose, natural rubber, chitosan, poly lactic acid (PLA), collagen, *etc.*, as polymer matrix (Table 4).

Starch, another abundant biopolymer like lignin, was used extensively by the researcher to develop polymer composite with superior thermal and mechanical properties. In a study by de Freitas *et al.* [126], the incorporation of KL made the composite film more hydrophobic, more thermally stable than native starch and with superior mechanical properties. The developed composite with 4% KL was able to adsorb methyl orange due to the presence of different functional groups in lignin. Zhao *et al.* [127] reported that a lower molecular weight fraction of lignin was a more suitable candidate for improving the mechanical properties of starch composite films than a higher molecular weight fraction with lower G + S unit content.

Farooq *et al.* [137] prepared cellulose nanofibril (CNF) nanocomposite with KL as colloidal lignin particles (CLPs) which are easily dispersed in aqueous media. The authors used an easy and simple method to prepare lignin nanoparticles by dissolving KL into an aqueous solution of acetone. This method can be used for the preparation of lignin nanoparticle-reinforced polymer composites. The prepared composite film with 10% CLP exhibited almost double toughness as the film of only CNF. The authors concluded that at 10% concentration, CLP acted as ball bearing lubricating agent, which could transfer stress and enhance the toughness of the composite film. Moreover, the prepared film had antioxidant, and UV-blocking properties with reduced water sorption. The interaction between CNF and CLP is mainly by hydrogen bonding and electrostatic interaction.

The polymer composite of KL with polylactic acid or PLA is extensively studied by researchers. In recent years, numerous works have been done to develop efficient PLA/KL polymer composite, mainly for food packaging applications and as 3D printing material. Without any chemical modification and coupling agent, PLA/KL composite has shown poor mechanical as well as thermal properties due to poor dispersion of filler in the polymer matrix [160–162]. In work by Kim *et al.* [131], hydrophilic hydroxyl groups of KL were acetylated to improve the compatibility of

lignin. The prepared composite film had UV protection. Both tensile strength and elongation were improved with the addition of modified KL with young modulus remaining unchanged. Other modifications of KL such as grafting of two bio-based monomer lauryl methacrylate (LMA) and tetrahydrofurfuryl methacrylate (THFMA) with KL by free radical polymerization [132], modification to have acetoacetate functional group [133] were also explored to increase the compatibility with PLA. Compatibilizer such as polymeric diphenylmethane diisocyanate (PMDI) [130] was also used to increase the dispersion of lignin in the PLA matrix.

KL was also used as reinforcement in natural rubber or NR. It is reported that the thiol group present in KL can interact with unsaturated chains of the polymer matrix by forming carbon-sulfur covalent bonds, which is subsequently resulted in stronger filler-polymer interaction [163]. However, due to aggregation formation by lignin molecule, contact surface between filler and polymer matrix can be reduced, which leads to poor dispersion. Datta and Parcheta used glycerolysate and naphthenic oil as plasticizing agents for KL/natural rubber composite to have better dispersion of the filler [147, 164]. In work by Aini *et al.* [148], KL was hydroxymethylated for better dispersion in the rubber matrix. Often carbon black was used along with lignin for better dispersion due to the synergistic reinforcing effect. In this study, better crosslinking between hydroxymethylated KL and rubber matrix was observed.

Hybrid polymer composite is a class of polymer composite where two or more reinforcements are used to improve the original properties of the polymer matrix or to introduce new properties. Such hybrid polymer biocomposite was prepared by using starch as polymer matrix and cellulose nano fiber or CNF and KL as reinforcements. The prepared composite was used as a gas separation membrane, and the incorporation of lignin in the composite films improved gas selectivity as well as mechanical properties [128]. In another study, where 2-hydroxyethyl cellulose and KL were used in gellan gum as a polymer matrix, lignin improved the hydrophobicity of the composite film, gave protection under UV, and acted as an antioxidant [165]. Hydroxypropyl methylcellulose (HPMC)/KL/chitosan composite film with the antimicrobial and antioxidant composite film was also prepared [140].

da Rosa *et al.* [135] used KL powder in sludge fiber waste/ PLA composite as a coupling agent. It was reported that incorporation of KL, resulted in improved compatibility between fiber and PLA, which is observed as improved mechanical properties, improved thermal stability as well as reduced water absorption. Reduced water absorption can be due to favorable interaction between aromatic functional groups of lignin with cellulosic fiber. KL was also used as a compatibilizer in PLA/reduced graphene oxide (rGO), where lignin promoted homogenous dispersion by creating weak interaction with PLA and rGO [166].

The composite film of carrageenan/KL had improved mechanical strength and antimicrobial properties. Moreover, lignin made the film more thermally stable due to antioxidant properties and gave protection under UV. Improved hydrophobicity as well as lower water vapor permeability (WVP) was also observed [167]. Poly(3-hydroxybutyrate-co-3-hydroxyvalerate) (PHBV) is a biopolymer produced by different bacteria. Native PHBV has poor thermooxidative stability and lower gas permeability. However, PHBV/KL biopolymer composite exhibited improved thermooxidative stability and gas permeability [168]. However, it was also reported that unmodified lignin was found to be poorly miscible in PHBV polymer matrix and can have a limited effect on the resultant composite's properties due to phase separation and non-interaction between two biopolymers. Luo *et al.* [169] used compatibilization by free radical grafting during extrusion of KL and PHBV by using dicumyl peroxide (DCP). The main aim of using compatibilization during melt blending was to have continuous interphase, which can subsequently result in better dispersion of KL in PHBV. Poly(3-hydroxybutyrate) (PHB) is a similar kind of biopolymer to PHBV and is produced by different bacteria. Improved thermal stability, as well as improved mechanical properties, were observed due to strong interfacial interaction between lignin and PHB via hydrogen bond in the case of PHB/KL composite film. It was also reported that pickering emulsion technique could be useful for having uniform dispersion of lignin particles in PHB polymer matrix [146]. Chitosan was also used for preparing polymer composite. In a recent work by Izaguirre *et al.* [141], sequentially solvent extracted KL was used for preparing polymer composite with chitosan. Polymer

composite with lignin fraction obtained from ethanol fraction exhibited improved mechanical strength as well as UV blocking properties. Masilompane *et al.* [143] prepared a nanocomposite from chitosan, KL and TiO₂ for adsorbent of synthetic dyes by electrostatic interaction. Nanocomposites was in powder form, which resulted in higher adsorption due to a larger surface area with more active sites. Duan *et al.* [145] used ionic liquid 1-butyl-3-methylimidazolium acetate and γ -valerolactone for the preparation of composite film with chitin and KL. The prepared film was studied as an adsorbent for heavy metal ions. Moreover, film showed excellent stability and flexibility in the aqueous solution, making it more suitable for wastewater treatment.

4. Lignosulfonate-based polymer composite

Lignosulfonate salt can be made of calcium, sodium, magnesium, and ammonium, depending on the type of base or metallic sulfite used during the pulping process. With many advantageous structural and chemical properties, it is also very cheap form of lignin that can have useful applications in polymer composites. In this section, different studies exploring the use of lignosulfonates as filler in polymer composites are discussed in detail.

4.1. Lignosulphonate-based synthetic polymer composite

Lignosulfonates, like KL, are also immiscible in non-polar polyolefins, such as polyethylene and polypropylene. Due to weak interaction between non-polar polymer and lignin molecules, the latter tend to interact with each other, forming aggregation followed by very poor dispersion. Miscibility can be improved either by chemical modifications or by using a coupling agent. Table 5 shows the use of lignosulfonate in different polymer composites, improvement of the properties after inclusion of

lignosulfonate, and application of resultant polymer composites.

Lignosulfonate was chemically modified by using hydrotalcite or layered double hydroxide (LDH) for incorporation into polypropylene. Layered double hydroxide, is a well-known flame retardant that is used widely with other polymers. However, due to its hydrophilic nature, LDH is poorly dispersed in a non-polar polymer such as polypropylene, resulting in poor flame retardant properties. LDH has positively charged layers that can be used for modification with negatively charged organic molecules by surface adsorption and anion exchange. Lignosulfonates are polyanions and Wu *et al.* [173] prepared LDH-lignosulfonate for incorporation in polymer composites with polypropylene. The addition of lignosulfonates in LDH resulted in increased hydrophobicity and subsequently improved dispersion in the polypropylene matrix. Due to better dispersion, and synergistic flame retardancy between LDH and lignosulfonate, the prepared composite with LDH-LS (lignosulfonate) exhibited minimum heat release rate, total heat release, and total smoke production. LDH and lignosulfonate form a continuous and higher amount of char residues due to the uniform dispersion of filler in the polymer matrix. Hydrophilic and water-soluble lignosulfonate is a polyanionic molecule. It can adsorb heavy metal ions in water, dyes and alcohols, and this property is advantageous for use as a nanofiltration membrane. Moreover, abundant carboxyl and hydroxyl groups present in lignin molecules are also useful as adsorption sites. Polyethyleneimine (PEI)/lignosulfonate thin film was prepared on polysulfone ultrafiltration membrane by the layer-by-layer assembly and crosslinking technology where PEI was polycation. The prepared membrane had amino and hydroxyl groups on the surface and showed improved adsorption efficiency towards heavy metal ions [202].

Table 5. Different lignosulfonate-based polymer composite.

Lignosulfonates	Types	Polymers	Application of lignosulfonates	References
	Polymer composite	Polypropylene	Flame retardant, antioxidant, improvement of mechanical properties	[170–173]
	PVA	Lowering of melting point, improvement of mechanical properties, antioxidant	[174–176, 205]	
	PANI	Dopant, adsorbent	[177–181]	
	Polypyrrole	Dopant, adsorbent	[182, 183]	
	PEDOT	Dopant	[184, 185]	
	PLA	UV protection, antioxidant, improvement of mechanical properties	[160, 186–189]	
	Chitosan	Adsorbent, antimicrobial, improvement of mechanical properties, antioxidant, antibiofilm	[190–201]	

Szabó *et al.* [203] used different polymer matrices to understand which polymer is best suited for uniform dispersion of lignosulfonates without any chemical modification or incorporation of a coupling agent. They used polypropylene and aromatic polymers such as polystyrene, polycarbonate and glycol-modified poly(ethylene terephthalate) (PET). Lignin molecules mainly interact with other polymers via hydrogen bond and aromatic π electron interaction, as reported in previous studies. Therefore, all three aromatic polymers showed better interaction with lignosulfonate via π interaction than the polypropylene/lignosulfonate composite. However, the interaction between lignosulfonate and polystyrene was weaker among the three as the aromatic ring in polystyrene does not have any functional groups, and interaction is only via π interaction. In glycol-modified PET, the aromatic ring has two carbonyl groups which can form hydrogen bonds with different functional groups present in lignosulfonates and this, combined with π interaction, lignosulfonate/glycol modified PET exhibited strong interaction. From this study, it can be concluded that polymers with aromatic rings and different functional groups in the repeating unit was found to be a more suitable choice of polymers for the preparation of polymer composites with lignosulfonate. Better dispersion of lignosulfonate was also observed in another aromatic polymer (PBAT) polybutylene adipate terephthalate. However, lignosulfonate used in this study was modified by maleic anhydride. π interaction and chemical modifications can be resulted in better miscibility [204].

Polyaniline (PANI) is also an aromatic polymer that was used with lignosulfonate for the preparation of composite with a different range of applications. Lignosulfonate is rich in phenylpropane groups with hydrophilic sulfonic groups and electroactive methoxy phenol groups. These phenols groups can be converted to quinone/hydroquinone groups which make lignosulfonate a quinone-based redox polymer undergoing fast proton-coupled reversible redox transitions over a wide pH range. Moreover, these quinone groups can further be utilized for electrochemical energy storage. Being polyanionic and water soluble, lignosulfonate has become a popular, cost-effective and environmentally friendly polyanionic dopant that is added to increase electrical conductivity of conducting polymers. However, lignin molecules are electronically insulating. Therefore, for the successful use of the quinone group converted

from phenol groups in lignin as energy storage, it is required to choose a polymer material of good electronic and ionic conductivity [180]. Rebis and Milczarek prepared a composite with lignosulfonate using three different conducting polymers *i.e.*, PANI, polypyrrole and poly(3,4-ethylene dioxythiophene) (PEDOT). It was observed that methoxy phenol groups of lignosulfonates were converted to quinones during the preparation of PANI/lignosulfonate and PEDOT/lignosulfonate composite. However, in the case of polypyrrole/lignosulfonate, methoxy phenol groups remained in their native form and were converted to quinone by post-polymerization oxidation. All three composites showed improved redox electroactivity and increased charge storage. Moreover, PANI/lignosulfonate exhibited optimal electroactivity in pH 7 to 9. This is a usual characteristic of PANI polymerized in the presence of polyanionic structures; in this case, the polyanion is lignosulfonate [180]. To improve electrical conductivity, Qian *et al.* [185] prepared PEDOT/lignosulfonate composite by emulsion polymerization and then prepared composite was again subjected to pickering emulsion polymerization using 3,4-ethylene-dioxythiophene (EDOT) monomer. It was reported that the final composite was much more conductive than the initial materials due to the high content of PEDOT in the core structure. Xu *et al.* [177] used $(\text{NH}_4)_2\text{S}_2\text{O}_8$ as an oxidizing agent for the preparation of PANI/ lignosulfonate and phenol groups were converted to quinone by oxidation during polymerization. Zhang *et al.* [179] used laccase, a lignin-degrading enzyme for polymerization of PANI-Emeraldine salt (PANI-ES)/lignosulfonate composite, using atmospheric oxygen as an oxidizing agent. The prepared composite can be used on the surface of the cotton fabric to make it electrically conductive. PANI/lignosulfonate composite was also used as expanders in a lead-acid battery. Expanders are usually used to reduce the degree of compaction within negative plates and to provide more ionically transport channels within plates during the charge/discharge process. Although lignosulfonates are mainly used as expanders for their 3D structure, it is electrically insulating, and this limits their application in the battery. However, PANI/lignosulfonate composite exhibited more advantageous properties than lignosulfonate due to the optimal combination of electronically conductive PANI and ionically conductive lignosulfonate with 3D structure. Moreover, this composite

made the battery's lifecycle longer as reported in this study [181]. PANI/lignosulfonate [178], Polypyrrole/lignosulfonate [183] composite were used as adsorbents for textile dyes and heavy metals via electrostatic interaction, hydrogen bond and intermolecular interaction. Lignosulfonate was used to improve the bonding strength of polypyrrole/cellulose fiber composite. Incorporation of lignosulfonate improved the bonding strength due to formation of more hydrogen bonds. However, the electrical conductivity of the prepared composite was reduced due to the non-conducting properties of lignosulfonate [182]. PVA is widely used in the food packaging industry for its water soluble, low cost, and excellent gas barrier properties. Thermal processing, such as extrusion, compression molding *etc.*, are industrial processing techniques used for thermoplastics. Due to the presence of strong inter- and intermolecular hydrogen bonding, PVA has a very narrow thermal processing window which makes thermal processing of this polymer challenging. Usually, the plasticizer is incorporated to lower its melting point, which can have a negative effect on the application as food packaging materials, as plasticizers are often toxic in nature. Lignin molecules are safe and reported to have lower cytotoxicity. Ye *et al.* [175] prepared a polymer composite with calcium lignosulfonate/PVA. Polymer composite exhibited a reduction of the melting temperature from 226.1 to 212.8 °C with increasing loading of lignosulfonates. In PVA, this reduction of melting temperature is caused by disruption of the crystalline region due to strong interactions between lignosulfonates and the polymer [175]. Moreover, improved mechanical properties were also observed in the case of polymer composites with increasing loading of lignosulfonates. Lignosulfonates, like PVA, are water soluble, which is advantageous for the preparation of polymer composite by a simple solvent casting method [175, 176]. To improve interaction between PVA and lignosulfonates, the latter was grafted with acrylic acid. The grafted lignosulfonate had better interaction with PVA via hydrogen bonding than unmodified lignosulfonate. A reduced melting temperature of 214 °C was observed with only 35% of grafted lignosulfonates when similar reduction was observed with 60% unmodified lignosulfonate. Moreover, improved mechanical strength and thermal stability were observed in acrylic acid grafted lignosulfonate/PVA composite [174].

Lignosulfonate was used as a compatibilizer. In a study by Wang *et al.* [206], jute fibers were coated with sodium lignosulfonate, which interacted with fiber via hydrogen bond and dipole bond. Improved mechanical properties were observed in the case of jute fiber coated with lignosulfonate/polypropylene composite than jute fiber/polypropylene composite due to increased interfacial binding between filler and polymer matrix. Methacrylated lignosulfonate was used as a compatibilizer in the flax fiber/polyester matrix. Flax fibers were treated with methacrylated lignosulfonate and this treatment enhanced the interaction between fiber and the polymer matrix [207].

4.2. Lignosulphonate-based natural polymer composite

Different natural polymers were used with lignosulfonate for the preparation of bio-composite. Chitosan, PLA, and CNF have extensively studied polymers. Unlike KL, very limited work has been performed on starch/lignosulfonate composite (Table 5) [208].

A composite film was prepared from α -cellulose/ZnCl₂/CaCl₂ along with lignosulfonate by crosslinking via intermolecular hydrogen bond and using succinic anhydride and triethanolamine as linkage bridge. The prepared film had improved mechanical strength, hydrophobicity, antibacterial properties, thermal stability as well as UV blocking properties [209]. A similar composite film was prepared from carboxylated cellulose nanofiber (CNF) and lignosulfonate. The prepared film showed elastic properties due to the uniform dispersion of CNF resulting from electrostatic repulsion by lignosulfonates [138]. Moreover, CNF/lignosulfonate/CaCl₂ film exhibited flame retardancy and high electrical resistance [210]. Sodium ion of lignosulfonate was modified by using ionic liquid tris-[2-(2-methoxy ethoxy)ethyl]amine (TrisEG). Modified lignosulfonate with ethylene glycol functionality was used as a dispersant for cellulose/gluten composites. The prepared composite had improved mechanical strength than the composite containing unmodified lignosulfonate [211]. Bacterial cellulose (BC) is a nano form of cellulose. Lignosulfonate/BC membrane has been prepared for application ion exchange membrane in a fuel cell with improved thermal stability and mechanical properties [212].

Chitosan is a natural biopolymer with high content of hydrophilic hydroxyl and amino functional groups

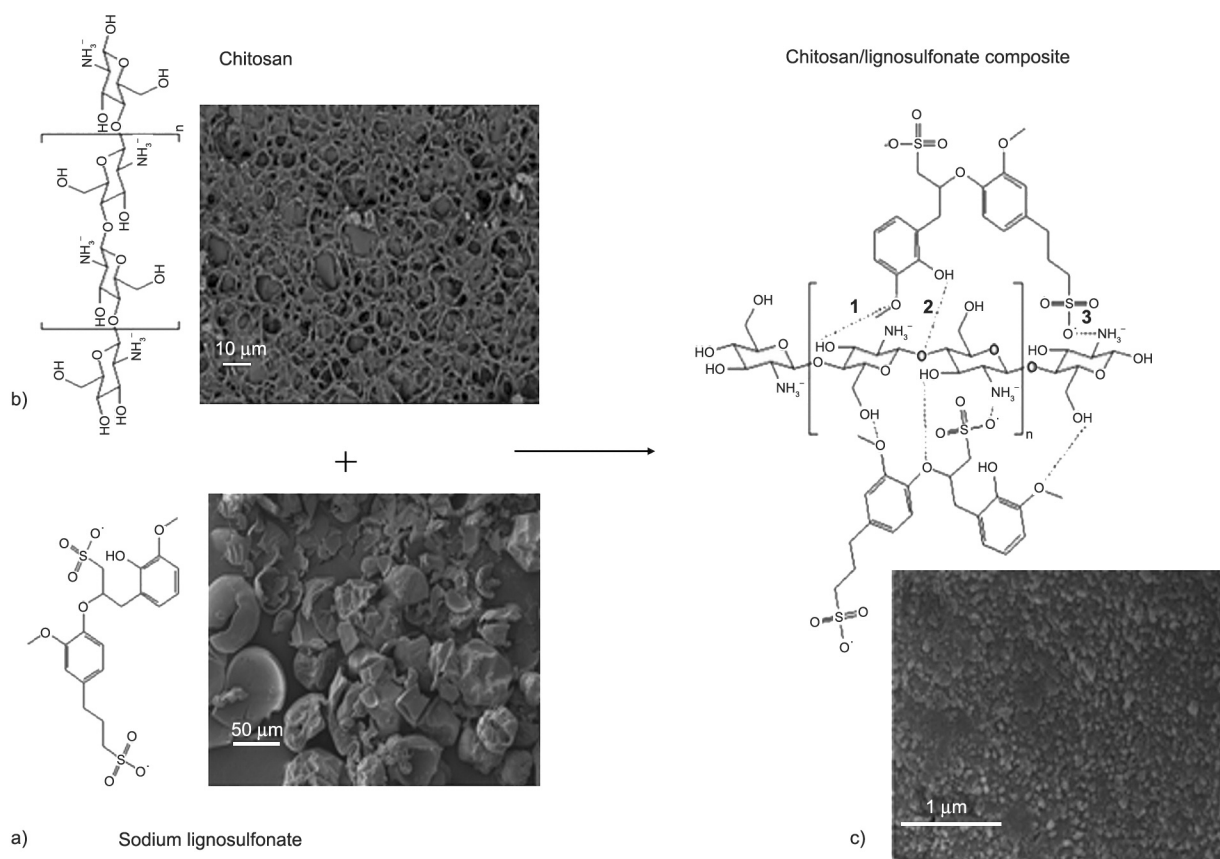


Figure 9. a) Chitosan, b) sodium lignosulfonate, c) chitosan/lignosulfonate composite and SEM image [201]. Copyright 2019 American chemical society.

i.e. primary, secondary, and acetylamino groups [198]. Chitosan with a positively charged amino group can be crosslinked with lignosulfonate with a negatively charged sulfonate group, as described in Figure 9. For their effective and strong interaction, the chitosan/lignosulfonate composite is extensively studied by the researcher. Gu *et al.* [201] prepared chitosan/lignosulfonate composite in powder form for adsorption of textile dyes. Two polymers interact with each other by electrostatic interaction between the amino group and the sulfonate group. Moreover, a weak hydrogen bond has also been formed between the hydroxyl group of chitosan and the methoxy group of lignosulfonates. Phenolic hydroxyl group also can interact with β -1,4-glycosidic oxygen of chitosan. The composite has strong adsorption efficiency towards congo red, rhodamine B and Cr (VI). Adsorption was due to electrostatic interaction between cations and anions of the composite and respected materials. Due to effective electrostatic and chemical adsorption, chitosan/lignosulfonate composite was also used for adsorption of other heavy metals like Pb (II) [194, 199], Cu (II), Co (II) [200], Hg (II) [198], methylene blue [197].

Often, other materials are also incorporated into the composite to enhance their effective adsorption of specific toxic chemicals. One such element is graphene oxide (GO). Chitosan treated with Fe_3O_4 was used in this study to give the composite magnetic properties, which can be used for the collection of adsorbents, after use, by using a magnet. Moreover, other than electrostatic interaction and weak hydrogen bonding, π - π stacking interaction can be involved during the adsorption process, as it was reported in this study [197]. In another study, Zhang *et al.* [194] prepared chitosan/lignosulfonate composite by free radical polymerization in the presence of *N,N*-methylene bisacrylamide and potassium persulfate. The prepared composite had 3D structural network and good mechanical strength due to which the adsorbent can be reused repeatedly after adsorption of Pb (II) ions followed by desorption at lower pH. Chitosan/lignosulfonate composite was prepared as a nanosphere with antimicrobial properties [193]. The antibacterial property of the composite was used to protect carbon steel from different sulfate-reducing bacteria-induced corrosion by Rasheed *et al.* [192]. Authors concluded that chitosan/lignosulfonate could

be used commercially in oil and gas industry pipelines to prevent microbial-induced corrosion [191]. Chitosan/lignosulfonate was used as flame retardants on cotton fabric. Due to the presence of the amino group, a higher amount of non-combustible product has been formed, which resulted in good flame retardancy properties of chitosan/lignosulfonate [190].

Like KL, lignosulfonate is also a suitable choice for preparing polymer composite material with PLA for different applications, mainly for the food packaging industry. Different properties of PLA were enhanced by the addition of lignosulfonate. The incorporation of lignosulfonate has improved antioxidant properties, UV light adsorption capacities of the prepared composite. However, the sulfonic group present in lignosulfonate is highly hydrophilic, due to which PLA/lignosulfonate usually has increased water absorption and accelerated biodegradation. To make PLA/lignosulfonate composite more hydrophobic, Ye *et al.* [186] subjected lignosulfonate to desulfonation to reduce hydrophilic group content. PLA/desulfonated lignosulfonate showed improved thermal stability than PLA/lignosulfonate, which can be due to better compatibility between PLA and desulfonated lignosulfonate. However, mechanical properties and UV absorption properties of both types of composites remained almost similar. PLA has dielectric properties and can be used as an electrically insulating material for different purposes. For better interaction and dispersion, lignosulfonate was modified with oleic acid, lactic acid, butyric acid and butyrolactone by radio frequency cold plasma method. PLA/modified lignosulfonate exhibited improved dielectric properties, mechanical strength, and hydrophilicity. Chemical modification improved the dispersion of filler in the PLA matrix [187]. PLA also has poor fire retardancy properties. For that purpose, Tawiah *et al.* [188] prepared azo-boron coupled with 4,4'-sulfonoyldiphenol-(((1E,1'E)-(sulfonyl-bis(6-hydroxy-3,1-phenylene))bis(diazene-2,1-diyl))bis(3,1-phenylene)) diboronic acid (SBDA). Composite material was prepared from PLA with SBDA and calcium lignosulfonate to reduce fire retardancy of PLA. PLA with 10 wt% lignosulfonate and 5 wt% SBDA exhibited improved fire retardancy as well as a lowered melting point for easier thermal processing. It was reported that the presence of the boron-hydroxyl group along with calcium lignosulfonate had produced an increasing amount of glassy carbonaceous char during combustion, which was mainly responsible

for increasing fire retardancy. PLA/lignosulfonate also exhibited antimicrobial and improved biodegradability than pure PLA films [189]. Mimini *et al.* [160] prepared PLA composite with KL, organosolv lignin and lignosulfonate to understand the effects of different types of lignin on composite's properties. It was reported that PLA/lignosulfonate exhibited lower melting point and higher mechanical strength than PLA/KL and PLA/organosolv lignin. Moreover, PLA/lignosulfonate is a better choice for the application of 3D printing. This advantageous effect of lignosulfonate over KL and organosolv lignin is mainly due to the presence of sulfonic groups, which give the lignin molecule net negative charge along with high surface activity, stabilizing and dispersing properties [160].

Lignosulfonate/polypropylene composite was used as a compatibilizer for PLA/coffee grounds composite. The amount of polypropylene and lignosulfonate has been 9 and 2–5%, respectively. Better mechanical properties, as well as better thermal stability, were observed in case of PLA/coffee ground composite with lignosulfonate and polypropylene than PLA/coffee ground/polypropylene and PLA/coffee ground/lignosulfonate due to the synergistic effect of lignosulfonate/polypropylene as compatibilizer [213]. The incorporation of ammonium lignosulfonate has as compatibilizer enhanced mechanical properties and improved internal bonding between PLA and wood fiber. However, due to higher hydrophilicity, the prepared composite had higher hydrophilicity and water swelling properties [214].

5. Conclusions and perspective

In this review, recent progress and challenges regarding the extraction of kraft lignin and lignosulfonates from black liquor and spent liquor, respectively, were discussed in detail. Recent progress in polymer composite with KL and lignosulfonate with synthetic and natural polymers are summarized. The final properties of the composites, as well as their different application, were also discussed. The review outlines various chemical modifications and extraction methods of KL and lignosulfonate and suggests recommendations for modification strategies in polymer matrices to enhance dispersion and compatibility. Based on the review, some of the areas worth exploring are detailed below:

- KL is more hydrophobic in nature and more compatible with polyolefin, such as polypropylene,

polyethylene, *etc.* than lignosulfonate. Chemical modifications such as esterification, alkylation, acetylation of KL, and addition of coupling agents are advantageous for better dispersion in a polyolefin matrix. The fractionation of KL by organic solvent to have a lower molecular weight fraction with high amounts of phenolic hydroxyl groups also improves its compatibility with polyolefins. The biodegradability of the polyolefin/KL composite needs to be explored to understand whether KL affects polyolefin biodegradability.

- Aromatic polymers such as PET, PS, and PANI are more compatible with KL and lignosulfonate than polyethylene, polypropylene, *etc.* Lignin can interact with aromatic polymers via π - π interaction, which is resulted in better dispersion of lignin in a polymer matrix. Moreover, aromatic polymers with functional groups such as phenolic hydroxyl group are the most suitable choice of polymer matrix for lignin-based polymer composites. Polymers can also be modified for better dispersion of lignin. This field merits further study.
- In the case of polyolefins, several studies report an increase in young's modulus with the addition of KL. Hence, kraft lignin can be further explored as a component in composite materials where a high modulus is desired.
- Colloidal lignin particle (CLP) has a very strong positive effect on thermal oxidative stability, mechanical properties, and on UV protection. However, CLP is only used with CNF for the preparation of polymer composites. To gain a deeper understanding of their effects, it is crucial to understand how they interact with different polymers.
- Lignosulfonate is a unique form of lignin molecule with a net negative charge and affinity towards different chemicals from aqueous solution by electrostatic interaction and hydrogen bonding. Lignosulfonate is soluble in water in a wide range of pH. For this reason, lignosulfonate has been studied extensively as a component for the preparation of many effective adsorbents. The availability and low price of lignosulfonate make it a feasible candidate for industrial use in water treatment.
- Lignosulfonate is also successfully used for doping electrically conductive material. In applications, these materials may effectively increase the

electrical conductivity of electrically conducting materials and energy storage.

- Many researchers have reported the amphiphilic nature of lignosulfonate, which can be used as a coupling agent or compatibilizer in hybrid composite to improve the interaction between filler and polymer. This area, however, is hardly explored by researchers. More insight is needed to explore the full potential of lignosulfonate as a coupling agent.

References

- [1] Duval A., Lawoko M.: A review on lignin-based polymeric, micro- and nano-structured materials. *Reactive and Functional Polymers*, **85**, 78–96 (2014).
<https://doi.org/10.1016/j.reactfunctpolym.2014.09.017>
- [2] Bajwa D. S., Pourhashem G., Ullah A. H., Bajwa S. G.: A concise review of current lignin production, applications, products and their environmental impact. *Industrial Crops and Products*, **139**, 111526 (2019).
<https://doi.org/10.1016/j.indcrop.2019.111526>
- [3] Thakur V. K., Thakur M. K.: Recent advances in green hydrogels from lignin: A review. *International Journal of Biological Macromolecules*, **72**, 834–847 (2015).
<https://doi.org/10.1016/j.ijbiomac.2014.09.044>
- [4] Thakur V. K., Thakur M. K., Raghavan P., Kessler M. R.: Progress in green polymer composites from lignin for multifunctional applications: A review. *ACS Sustainable Chemistry and Engineering*, **2**, 1072–1092 (2014).
<https://doi.org/10.1021/sc500087z>
- [5] Upton B. M., Kasko A. M.: Strategies for the conversion of lignin to high-value polymeric materials: Review and perspective. *Chemical Reviews*, **116**, 2275–2306 (2016).
<https://doi.org/10.1021/acs.chemrev.5b00345>
- [6] Liao J. J., Latif N. H. A., Trache D., Brosse N., Hussin M. H.: Current advancement on the isolation, characterization and application of lignin. *International Journal of Biological Macromolecules*, **162**, 985–1024 (2020).
<https://doi.org/10.1016/j.ijbiomac.2020.06.168>
- [7] Lee H. V., Hamid S. B. A., Zain S. K.: Conversion of lignocellulosic biomass to nanocellulose: Structure and chemical process. *The Scientific World Journal*, **2014**, 631013 (2014).
<https://doi.org/10.1155/2014/631013>
- [8] Schutyser W., Renders T., van den Bosch S., Koelewijn S-F., Beckham G. T., Sels B. F.: Chemicals from lignin: An interplay of lignocellulose fractionation, depolymerisation, and upgrading. *Chemical Society Reviews*, **47**, 852–908 (2018).
<https://doi.org/10.1039/C7CS00566K>

- [9] Katahira R., Elder T. J., Beckham G. T.: A brief introduction to lignin structure. in ‘Lignin valorization: Emerging approaches’ (ed.: Beckham G. T.) Royal Society of Chemistry, Cambridge, 1–20 (2018).
<https://doi.org/10.1039/9781788010351-00001>
- [10] Vanholme R., Demedts B., Morreel K., Ralph J., Boerjan W.: Lignin biosynthesis and structure. *Plant Physiology*, **153**, 895–905 (2010).
<https://doi.org/10.1104/pp.110.155119>
- [11] Yuan T-Q., Sun S-N., Xu F., Sun R-C.: Structural characterization of lignin from triploid of *Populus tomentosa* carr. *Journal of Agricultural and Food Chemistry*, **59**, 6605–6615 (2011).
<https://doi.org/10.1021/jf2003865>
- [12] Wen J-L., Sun S-L., Xue B-L., Sun R-C.: Quantitative structural characterization of the lignins from the stem and pith of bamboo (*Phyllostachys pubescens*). *Holzforchung*, **67**, 613–627 (2013).
<https://doi.org/10.1515/hf-2012-0162>
- [13] Rencoret J., Ralph J., Marques G., Gutiérrez A., Martínez Á. T., del Río J. C.: Structural characterization of lignin isolated from coconut (*Cocos nucifera*) coir fibers. *Journal of Agricultural and Food Chemistry*, **61**, 2434–2445 (2013).
<https://doi.org/10.1021/jf304686x>
- [14] del Río J. C., Rencoret J., Marques G., Li J., Gellerstedt G., Jiménez-Barbero J., Martínez Á. T., Gutiérrez A.: Structural characterization of the lignin from jute (*Cochorus capsularis*) fibers. *Journal of Agricultural and Food Chemistry*, **57**, 10271–10281 (2009).
<https://doi.org/10.1021/jf900815x>
- [15] Shi Z., Xu G., Deng J., Dong M., Murugadoss V., Liu C., Shao Q., Wu S., Guo Z.: Structural characterization of lignin from *D. sinicus* by FTIR and NMR techniques. *Green Chemistry Letters and Reviews*, **12**, 235–243 (2019).
<https://doi.org/10.1080/17518253.2019.1627428>
- [16] El Hage R., Brosse N., Chrusciel L., Sanchez C., Sannigrahi P., Ragauskas A.: Characterization of milled wood lignin and ethanol organosolv lignin from miscanthus. *Polymer Degradation and Stability*, **94**, 1632–1638 (2009).
<https://doi.org/10.1016/j.polyimdegradstab.2009.07.007>
- [17] Rencoret J., Marques G., Gutiérrez A., Nieto L., Jiménez-Barbero J., Martínez Á. T., del Río J. C.: Isolation and structural characterization of the milled-wood lignin from *Paulownia fortunei* wood. *Industrial Crops and Products*, **30**, 137–143 (2009).
<https://doi.org/10.1016/j.indcrop.2009.03.004>
- [18] Lourenço A., Rencoret J., Chemetova C., Gominho J., Gutiérrez A., del Río J. C., Pereira H.: Lignin composition and structure differs between xylem, phloem and phellem in *Quercus suber* L. *Frontiers in Plant Science*, **7**, 1612 (2016).
<https://doi.org/10.3389/fpls.2016.01612>
- [19] Xiao M-Z., Chen W-J., Hong S., Pang B., Cao X-F., Wang Y-Y., Yuan T-Q., Sun R-C.: Structural characterization of lignin in heartwood, sapwood, and bark of eucalyptus. *International Journal of Biological Macromolecules*, **138**, 519–527 (2019).
<https://doi.org/10.1016/j.ijbiomac.2019.07.137>
- [20] Crestini C., Lange H., Sette M., Argyropoulos D. S.: On the structure of softwood kraft lignin. *Green Chemistry*, **19**, 4104–4121 (2017).
<https://doi.org/10.1039/C7GC01812F>
- [21] Kai D., Tan M. J., Chee P. L., Chua Y. K., Yap Y. L., Loh X. J.: Towards lignin-based functional materials in a sustainable world. *Green Chemistry*, **18**, 1175–1200 (2016).
<https://doi.org/10.1039/C5GC02616D>
- [22] Kazzaz A. E., Fatehi P.: Technical lignin and its potential modification routes: A mini-review. *Industrial Crops and Products*, **154**, 112732 (2020).
<https://doi.org/10.1016/j.indcrop.2020.112732>
- [23] Aro T., Fatehi P.: Production and application of ligno-sulfonates and sulfonated lignin. *ChemSusChem*, **10**, 1861–1877 (2017).
<https://doi.org/10.1002/cssc.201700082>
- [24] Aini N. A. M., Othman N., Hussin M. H., Sahakaro K., Hayeemasae N.: Effect of extraction methods on the molecular structure and thermal stability of kenaf (*Hibiscus cannabinus* core) biomass as an alternative bio-filler for rubber composites. *International Journal of Biological Macromolecules*, **154**, 1255–1264 (2020).
<https://doi.org/10.1016/j.ijbiomac.2019.10.280>
- [25] Yang D., Li H., Qin Y., Zhong R., Bai M., Qiu X.: Structure and properties of sodium lignosulfonate with different molecular weight used as dye dispersant. *Journal of Dispersion Science and Technology*, **36**, 532–539 (2015).
<https://doi.org/10.1080/01932691.2014.916221>
- [26] Chio C., Sain M., Qin W.: Lignin utilization: A review of lignin depolymerization from various aspects. *Renewable and Sustainable Energy Reviews*, **107**, 232–249 (2019).
<https://doi.org/10.1016/j.rser.2019.03.008>
- [27] Saleh T. A.: Global trends in technologies and nanomaterials for removal of sulfur organic compounds: Clean energy and green environment. *Journal of Molecular Liquids*, **359**, 119340 (2022).
<https://doi.org/10.1016/j.molliq.2022.119340>
- [28] Saleh T. A.: Characterization, determination and elimination technologies for sulfur from petroleum: Toward cleaner fuel and a safe environment. *Trends in Environmental Analytical Chemistry*, **25**, e00080 (2020).
<https://doi.org/10.1016/j.teac.2020.e00080>
- [29] Lobato-Peralta D. R., Duque-Brito E., Villafán-Vidales H. I., Longoria A., Sebastian P. J., Cuentas-Gallegos A. K., Arancibia-Bulnes C. A., Okoye P. U.: A review on trends in lignin extraction and valorization of lignocellulosic biomass for energy applications. *Journal of Cleaner Production*, **293**, 126123 (2021).
<https://doi.org/10.1016/j.jclepro.2021.126123>

- [30] Doherty W. O. S., Mousaviou P., Fellows C. M.: Value-adding to cellulose ethanol: Lignin polymers. *Industrial Crops and Products*, **33**, 259–276 (2011).
<https://doi.org/10.1016/j.indcrop.2010.10.022>
- [31] Rudatin S., Sen Y. L., Woerner D. L.: Association of kraft lignin in aqueous solution. in ‘Lignin’ (eds.: Glasser W. G., Sarkanen S.) ACS Symposium Series, Washington, Vol. 397, 144–154 (1989).
<https://doi.org/10.1021/bk-1989-0397.ch011>
- [32] Norgren M., Edlund H., Wågberg L., Lindström B., Annergren G.: Aggregation of kraft lignin derivatives under conditions relevant to the process, part I: Phase behaviour. *Colloids and Surfaces A: Physicochemical and Engineering Aspects*, **194**, 85–96 (2001).
[https://doi.org/10.1016/S0927-7757\(01\)00753-1](https://doi.org/10.1016/S0927-7757(01)00753-1)
- [33] Kienberger M., Maitz S., Pichler T., Demmelmayr P.: Systematic review on isolation processes for technical lignin. *Processes*, **9**, 804 (2021).
<https://doi.org/10.3390/pr9050804>
- [34] Humpert D., Ebrahimi M., Czermak P.: Membrane technology for the recovery of lignin: A review. *Membranes*, **6**, 42 (2016).
<https://doi.org/10.3390/membranes6030042>
- [35] Figueiredo P., Lintinen K., Hirvonen J. T., Kostianen M. A., Santos H. A.: Properties and chemical modifications of lignin: Towards lignin-based nanomaterials for biomedical applications. *Progress in Materials Science*, **93**, 233–269 (2018).
<https://doi.org/10.1016/j.pmatsci.2017.12.001>
- [36] Jin W., Tolba R., Wen J., Li K., Chen A.: Efficient extraction of lignin from black liquor *via* a novel membrane-assisted electrochemical approach. *Electrochimica Acta*, **107**, 611–618 (2013).
<https://doi.org/10.1016/j.electacta.2013.06.031>
- [37] Haddad M., Bazinet L., Savadogo O., Paris J.: A feasibility study of a novel electro-membrane based process to acidify Kraft black liquor and extract lignin. *Process Safety and Environmental Protection*, **106**, 68–75 (2017).
<https://doi.org/10.1016/j.psep.2016.10.003>
- [38] Oliveira R. C. P., Mateus M., Santos D. M. F.: Black liquor electrolysis for hydrogen and lignin extraction. *ECS Transactions*, **72**, 43–53 (2016).
<https://doi.org/10.1149/07222.0043ecst>
- [39] Bazinet L., Lamarche F., Ippersiel D.: Bipolar-membrane electrodialysis: Applications of electrodialysis in the food industry. *Trends in Food Science and Technology*, **9**, 107–113 (1998).
[https://doi.org/10.1016/S0924-2244\(98\)00026-0](https://doi.org/10.1016/S0924-2244(98)00026-0)
- [40] Chen X., Katahira R., Ge Z., Lu L., Hou D., Peterson D. J., Tucker M. P., Chen X., Ren Z. J.: Microbial electrochemical treatment of biorefinery black liquor and resource recovery. *Green Chemistry*, **21**, 1258–1266 (2019).
<https://doi.org/10.1039/C8GC02909A>
- [41] Du X., Zhang H., Sullivan K. P., Gogoi P., Deng Y.: Electrochemical lignin conversion. *ChemSusChem*, **13**, 4318–4343 (2020).
<https://doi.org/10.1002/cssc.202001187>
- [42] Villar J. C., Caperos A., García-Ochoa F.: Precipitation of kraft black liquors by alcohol-calcium solutions. *Separation Science and Technology*, **31**, 1721–1739 (1996).
<https://doi.org/10.1080/01496399608000722>
- [43] Ropponen J., Räsänen L., Rovio S., Ohra-Aho T., Liitiä T., Mikkonen H., van de Pas D., Tamminen T.: Solvent extraction as a means of preparing homogeneous lignin fractions. *Holzforschung*, **65**, 543–549 (2011).
<https://doi.org/10.1515/HF.2011.089>
- [44] Faustino H., Gil N., Baptista C., Duarte A. P.: Antioxidant activity of lignin phenolic compounds extracted from kraft and sulphite black liquors. *Molecules*, **15**, 9308–9322 (2010).
<https://doi.org/10.3390/molecules15129308>
- [45] Domínguez-Robles J., Tamminen T., Liitiä T., Peresin M. S., Rodríguez A., Jääskeläinen A-S.: Aqueous acetone fractionation of kraft, organosolv and soda lignins. *International Journal of Biological Macromolecules*, **106**, 979–987 (2018).
<https://doi.org/10.1016/j.ijbiomac.2017.08.102>
- [46] Aminzadeh S., Lauberts M., Dobe G., Ponomarenko J., Mattsson T., Lindström M. E., Sevastyanova O.: Membrane filtration of kraft lignin: Structural characteristics and antioxidant activity of the low-molecular-weight fraction. *Industrial Crops and Products*, **112**, 200–209 (2018).
<https://doi.org/10.1016/j.indcrop.2017.11.042>
- [47] Sevastyanova O., Helander M., Chowdhury S., Lange H., Wedin H., Zhang L., Ek M., Kadla J. F., Crestini C., Lindström M. E.: Tailoring the molecular and thermo-mechanical properties of kraft lignin by ultrafiltration. *Journal of Applied Polymer Science*, **131**, 40799 (2014).
<https://doi.org/10.1002/app.40799>
- [48] Jääskeläinen A-S., Liitiä T., Mikkelsen A., Tamminen T.: Aqueous organic solvent fractionation as means to improve lignin homogeneity and purity. *Industrial Crops and Products*, **103**, 51–58 (2017).
<https://doi.org/10.1016/j.indcrop.2017.03.039>
- [49] Sadeghifar H., Argyropoulos D. S.: Correlations of the antioxidant properties of softwood kraft lignin fractions with the thermal stability of its blends with polyethylene. *ACS Sustainable Chemistry and Engineering*, **3**, 349–356 (2015).
<https://doi.org/10.1021/sc500756n>
- [50] Majdar R. E., Ghasemian A., Resalati H., Saraeian A., Crestini C., Lange H.: Case study in kraft lignin fractionation: ‘Structurally purified’ lignin fractions – The role of solvent H-bonding affinity. *ACS Sustainable Chemistry and Engineering*, **8**, 16803–16813 (2020).
<https://doi.org/10.1021/acssuschemeng.0c05364>

- [51] Huang C., He J., Narron R., Wang Y., Yong Q.: Characterization of kraft lignin fractions obtained by sequential ultrafiltration and their potential application as a biobased component in blends with polyethylene. *ACS Sustainable Chemistry and Engineering*, **5**, 11770–11779 (2017).
<https://doi.org/10.1021/acssuschemeng.7b03415>
- [52] Bova T., Tran C. D., Balakshin M. Y., Chen J., Capanema E. A., Naskar A. K.: An approach towards tailoring interfacial structures and properties of multiphase renewable thermoplastics from lignin–nitrile rubber. *Green Chemistry*, **18**, 5423–5437 (2016).
<https://doi.org/10.1039/C6GC01067A>
- [53] Ye D., Kong J., Gu S., Zhou Y., Huang C., Xu W., Zhang X.: Selective aminolysis of acetylated lignin: Toward simultaneously improving thermal-oxidative stability and maintaining mechanical properties of polypropylene. *International Journal of Biological Macromolecules*, **108**, 775–781 (2018).
<https://doi.org/10.1016/j.ijbiomac.2017.10.168>
- [54] Wang K., Xu F., Sun R.: Molecular characteristics of Kraft-AQ pulping lignin fractionated by sequential organic solvent extraction. *International Journal of Molecular Sciences*, **11**, 2988–3001 (2010).
<https://doi.org/10.3390/ijms11082988>
- [55] Passoni V., Scarica C., Levi M., Turri S., Griffini G.: Fractionation of industrial softwood kraft lignin: Solvent selection as a tool for tailored material properties. *ACS Sustainable Chemistry and Engineering*, **4**, 2232–2242 (2016).
<https://doi.org/10.1021/acssuschemeng.5b01722>
- [56] Pu Y., Jiang N., Ragauskas A. J.: Ionic liquid as a green solvent for lignin. *Journal of Wood Chemistry and Technology*, **27**, 23–33 (2007).
<https://doi.org/10.1080/02773810701282330>
- [57] Bokhary A., Leitch M., Liao B. Q.: Liquid–liquid extraction technology for resource recovery: Applications, potential, and perspectives. *Journal of Water Process Engineering*, **40**, 101762 (2021).
<https://doi.org/10.1016/j.jwpe.2020.101762>
- [58] Fatehi P., Chen J.: Extraction of technical lignins from pulping spent liquors, challenges and opportunities. in ‘Production of biofuels and chemicals from lignin’ (eds.: Fang Z., Smith R. L.) Springer, Singapore, 35–54 (2016).
https://doi.org/10.1007/978-981-10-1965-4_2
- [59] Pabby A. K., Rizvi S. S. H., Sastre A. M.: *Handbook of membrane separations*. CRC Press, Boca Raton (2015).
- [60] Bhattacharya P. K., Todi R. K., Tiwari M., Bhattacharjee C., Bhattacharjee S., Datta S.: Studies on ultrafiltration of spent sulfite liquor using various membranes for the recovery of lignosulphonates. *Desalination*, **174**, 287–297 (2005).
<https://doi.org/10.1016/j.desal.2004.09.017>
- [61] Pateraki C., Ladakis D., Stragier L., Verstraete W., Kookos I., Papanikolaou S., Koutinas A.: Pretreatment of spent sulphite liquor *via* ultrafiltration and nanofiltration for bio-based succinic acid production. *Journal of Biotechnology*, **233**, 95–105 (2016).
<https://doi.org/10.1016/j.jbiotec.2016.06.027>
- [62] Kienberger M., Demmelmayer P., Weißl M., Zankl A., Spirk S.: Biobased support layers for the fractionation and selective extraction of lignosulfonates. *Solvent Extraction and Ion Exchange*, **38**, 132–141 (2020).
<https://doi.org/10.1080/07366299.2019.1691764>
- [63] Qureshi N., Hodge D. B., Vertès A.: *Biorefineries: Integrated biochemical processes for liquid biofuels*. Elsevier, Amsterdam (2014).
- [64] Ringena O., Saake B., Lehnen R.: Isolation and fractionation of lignosulfonates by amine extraction and ultrafiltration: A comparative study. *Holzforschung*, **59**, 405–412 (2005).
<https://doi.org/10.1515/HF.2005.066>
- [65] Fatehi P., Chen J.: *Production of biofuels and chemicals from lignin*. Springer, Singapore (2016).
- [66] Chakrabarty K., Krishna K. V., Saha P., Ghoshal A. K.: Extraction and recovery of lignosulfonate from its aqueous solution using bulk liquid membrane. *Journal of Membrane Science*, **330**, 135–144 (2009).
<https://doi.org/10.1016/j.memsci.2008.12.069>
- [67] Chakrabarty K., Saha P., Ghoshal A. K.: Separation of lignosulfonate from its aqueous solution using supported liquid membrane. *Journal of Membrane Science*, **340**, 84–91 (2009).
<https://doi.org/10.1016/j.memsci.2009.05.016>
- [68] Chakrabarty K., Saha P., Ghoshal A. K.: Separation of lignosulfonate from its aqueous solution using emulsion liquid membrane. *Journal of Membrane Science*, **360**, 34–39 (2010).
<https://doi.org/10.1016/j.memsci.2010.04.043>
- [69] Kumar V., Singh R. K., Chowdhury P.: Efficient extraction and recovery of lignosulfonate using sunflower oil as green solvent in liquid membrane transport: Equilibrium and kinetic study. *Journal of Industrial and Engineering Chemistry*, **67**, 109–122 (2018).
<https://doi.org/10.1016/j.jiec.2018.06.021>
- [70] Kontturi A.-K., Sundholm G.: The extraction and fractionation of lignosulfonates with long chain aliphatic amines. *Acta Chemica Scandinavica*, **40**, 121–125 (1986).
<https://doi.org/10.3891/acta.chem.scand.40a-0121>
- [71] Chen F., Dai H., Dong X., Yang J., Zhong M.: Physical properties of lignin-based polypropylene blends. *Polymer Composites*, **32**, 1019–1025 (2011).
<https://doi.org/10.1002/pc.21087>
- [72] Jeong H., Park J., Kim S., Lee J., Cho J. W.: Use of acetylated softwood kraft lignin as filler in synthetic polymers. *Fibers and Polymers*, **13**, 1310–1318 (2012).
<https://doi.org/10.1007/s12221-012-1310-6>

- [73] Klapiszewski Ł., Bula K., Sobczak M., Jesionowski T.: Influence of processing conditions on the thermal stability and mechanical properties of PP/silica-lignin composites. *International Journal of Polymer Science*, **2016**, 1627258 (2016).
<https://doi.org/10.1155/2016/1627258>
- [74] Bula K., Klapiszewski Ł., Jesionowski T.: A novel functional silica/lignin hybrid material as a potential bio-based polypropylene filler. *Polymer Composites*, **36**, 913–922 (2015).
<https://doi.org/10.1002/pc.23011>
- [75] Borysiak S., Klapiszewski Ł., Bula K., Jesionowski T.: Nucleation ability of advanced functional silica/lignin hybrid fillers in polypropylene composites. *Journal of Thermal Analysis and Calorimetry*, **126**, 251–262 (2016).
<https://doi.org/10.1007/s10973-016-5390-1>
- [76] Klapiszewski Ł., Grzabka-Zasadzińska A., Borysiak S., Jesionowski T.: Preparation and characterization of polypropylene composites reinforced by functional ZnO/lignin hybrid materials. *Polymer Testing*, **79**, 106058 (2019).
<https://doi.org/10.1016/j.polymertesting.2019.106058>
- [77] de Sousa Junior R. R., Gouveia J. R., Nacas A. M., Tavares L. B., Ito N. M., de Moura E. N., Gaia F. A., Pereira R. F., dos Santos D. J.: Improvement of polypropylene adhesion by kraft lignin incorporation. *Materials Research*, **22**, e20180123 (2019).
<https://doi.org/10.1590/1980-5373-mr-2018-0123>
- [78] Sugano-Segura A. T. R., Tavares L. B., Rizzi J. G. F., Rosa D. S., Salvadori M. C., dos Santos D. J.: Mechanical and thermal properties of electron beam-irradiated polypropylene reinforced with Kraft lignin. *Radiation Physics and Chemistry*, **139**, 5–10 (2017).
<https://doi.org/10.1016/j.radphyschem.2017.05.016>
- [79] Lourençon T. V., Santilli B. V., Magalhães W. L. E., Muniz G. I. B.: Thermal stabilization of wood/polypropylene composites through addition of unmodified, low-cost kraft lignin. *Waste and Biomass Valorization*, **11**, 1555–1563 (2020).
<https://doi.org/10.1007/s12649-018-0484-6>
- [80] Luo S., Cao J., Sun W.: Evaluation of Kraft lignin as natural compatibilizer in wood flour/polypropylene composites. *Polymer Composites*, **38**, 2387–2394 (2017).
<https://doi.org/10.1002/pc.23821>
- [81] Saffian H. A., Talib M. A., Lee S. H., Md Tahir P., Lee C. H., Ariffin H., Asa'ari A. Z. M.: Mechanical strength, thermal conductivity and electrical breakdown of kenaf core fiber/lignin/polypropylene biocomposite. *Polymers*, **12**, 1833 (2020).
<https://doi.org/10.3390/polym12081833>
- [82] Dias O. A. T., Sain M., Cesarino I., Leão A. L.: Development of high bio-content polypropylene composites with different industrial lignins. *Polymers for Advanced Technologies*, **30**, 70–78 (2019).
<https://doi.org/10.1002/pat.4444>
- [83] Maldhure A. V., Ekhe J. D.: Effect of modifications of lignin on thermal, structural, and mechanical properties of polypropylene/modified lignin blends. *Journal of Thermoplastic Composite Materials*, **30**, 625–645 (2017).
<https://doi.org/10.1177/0892705715610402>
- [84] Ye D., Li S., Lu X., Zhang X., Rojas O. J.: Antioxidant and thermal stabilization of polypropylene by addition of butylated lignin at low loadings. *ACS Sustainable Chemistry and Engineering*, **4**, 5248–5257 (2016).
<https://doi.org/10.1021/acssuschemeng.6b01241>
- [85] Chen F., Liu W., Seyed Shahabadi S. I., Xu J., Lu X.: Sheet-like lignin particles as multifunctional fillers in polypropylene. *ACS Sustainable Chemistry and Engineering*, **4**, 4997–5004 (2016).
<https://doi.org/10.1021/acssuschemeng.6b01369>
- [86] Luo S., Cao J., McDonald A. G.: Esterification of industrial lignin and its effect on the resulting poly(3-hydroxybutyrate-co-3-hydroxyvalerate) or polypropylene blends. *Industrial Crops and Products*, **97**, 281–291 (2017).
<https://doi.org/10.1016/j.indcrop.2016.12.024>
- [87] Alassod A., Gibril M., Islam S. R., Huang W., Xu G.: Polypropylene/lignin blend monoliths used as sorbent in oil spill cleanup. *Heliyon*, **6**, e04591 (2020).
<https://doi.org/10.1016/j.heliyon.2020.e04591>
- [88] Sakai H., Kuroda K., Muroyama S., Tsukegi T., Kakuchi R., Takada K., Hata A., Kojima R., Ogoshi T., Omichi M., Ninomiya K., Takahashi K.: Alkylated alkali lignin for compatibilizing agents of carbon fiber-reinforced plastics with polypropylene. *Polymer Journal*, **50**, 281–284 (2018).
<https://doi.org/10.1038/s41428-017-0009-3>
- [89] Triwulandari E., Ghozali M., Sondari D., Septiyanti M., Sampora Y., Meliana Y., Fahmiati S., Restu W. K., Haryono A.: Effect of lignin on mechanical, biodegradability, morphology, and thermal properties of polypropylene/polylactic acid/lignin biocomposite. *Plastics, Rubber and Composites*, **48**, 82–92 (2019).
<https://doi.org/10.1080/14658011.2018.1562746>
- [90] Abdelwahab M. A., Misra M., Mohanty A. K.: Injection molded biocomposites from polypropylene and lignin: Effect of compatibilizers on interfacial adhesion and performance. *Industrial Crops and Products*, **132**, 497–510 (2019).
<https://doi.org/10.1016/j.indcrop.2019.02.026>
- [91] Sadeghifar H., Argyropoulos D. S.: Macroscopic behavior of kraft lignin fractions: Melt stability considerations for lignin–polyethylene blends. *ACS Sustainable Chemistry and Engineering*, **4**, 5160–5166 (2016).
<https://doi.org/10.1021/acssuschemeng.6b00636>
- [92] Alekhina M., Erdmann J., Ebert A., Stepan A. M., Sixta H.: Physico-chemical properties of fractionated softwood kraft lignin and its potential use as a bio-based component in blends with polyethylene. *Journal of Materials Science*, **50**, 6395–6406 (2015).
<https://doi.org/10.1007/s10853-015-9192-9>

- [93] Hu L., Stevanovic T., Rodrigue D.: Unmodified and esterified Kraft lignin-filled polyethylene composites: Compatibilization by free-radical grafting. *Journal of Applied Polymer Science*, **132**, 41484 (2015).
<https://doi.org/10.1002/app.41484>
- [94] Dehne L., Vila C., Saake B., Schwarz K. U.: Esterification of Kraft lignin as a method to improve structural and mechanical properties of lignin-polyethylene blends. *Journal of Applied Polymer Science*, **134**, 44582 (2017).
<https://doi.org/10.1002/app.44582>
- [95] Hu L., Stevanovic T., Rodrigue D.: Compatibilization of kraft lignin-polyethylene composites using unreactive compatibilizers. *Journal of Applied Polymer Science*, **131**, 41040 (2014).
<https://doi.org/10.1002/app.41040>
- [96] Bula K., Klapiszewski Ł., Piasecki A., Jesionowski T.: The role of inorganic-organic bio-fillers containing kraft lignin in improvement in functional properties of polyethylene. *Materials*, **14**, 2114 (2021).
<https://doi.org/10.3390/ma14092114>
- [97] Bula K., Kubicki G., Jesionowski T., Klapiszewski Ł.: MgO-Lignin dual phase filler as an effective modifier of polyethylene film properties. *Materials*, **13**, 809 (2020).
<https://doi.org/10.3390/ma13030809>
- [98] Rojas-Lema S., Ivorra-Martinez J., Lascano D., Garcia-Garcia D., Balart R.: Improved performance of environmentally friendly blends of biobased polyethylene and kraft lignin compatibilized by reactive extrusion with dicumyl peroxide. *Macromolecular Materials and Engineering*, **306**, 2100196 (2021).
<https://doi.org/10.1002/mame.202100196>
- [99] Dehne L., Babarro C. V., Saake B., Schwarz K. U.: Influence of lignin source and esterification on properties of lignin-polyethylene blends. *Industrial Crops and Products*, **86**, 320–328 (2016).
<https://doi.org/10.1016/j.indcrop.2016.04.005>
- [100] Tang Y., Ye Z., Jean M.: Influence of lignin accessibility on chemical and biological decomposition of lignin/polyethylene composite thermoplastics. *The Canadian Journal of Chemical Engineering*, **98**, 104–118 (2020).
<https://doi.org/10.1002/cjce.23623>
- [101] Kabir A. S., Li H., Yuan H., Kuboki T., Xu C.: Effects of de-polymerized lignin content on thermo-oxidative and thermal stability of polyethylene. *Journal of Analytical and Applied Pyrolysis*, **140**, 413–422 (2019).
<https://doi.org/10.1016/j.jaap.2019.04.023>
- [102] Klapiszewski Ł., Bula K., Dobrowolska A., Czaczyk K., Jesionowski T.: A high-density polyethylene container based on ZnO/lignin dual fillers with potential antimicrobial activity. *Polymer Testing*, **73**, 51–59 (2019).
<https://doi.org/10.1016/j.polymertesting.2018.11.018>
- [103] Mariotti N., Wang X. M., Rodrigue D., Stevanovic T.: Combination of esterified kraft lignin and MAPE as coupling agent for bark/HDPE composites. *Journal of Materials Science Research*, **3**, 8–22 (2013).
<https://doi.org/10.5539/jmsr.v3n2p8>
- [104] Chiappero L. R., Bartolomei S. S., Estenoz D. A., Moura E. A. B., Nicolau V. V.: Lignin-based polyethylene films with enhanced thermal, opacity and biodegradability properties for agricultural mulch applications. *Journal of Polymers and the Environment*, **29**, 450–459 (2021).
<https://doi.org/10.1007/s10924-020-01886-6>
- [105] Wang S., Feng N., Zheng J., Yoon K-B., Lee D., Qu M., Zhang X., Zhang H.: Preparation of polyethylene/lignin nanocomposites from hollow spherical lignin-supported vanadium-based Ziegler–Natta catalyst. *Polymers for Advanced Technologies*, **27**, 1351–1354 (2016).
<https://doi.org/10.1002/pat.3803>
- [106] Qian Y., Qiu X., Zhong X., Zhang D., Deng Y., Yang D., Zhu S.: Lignin reverse micelles for UV-absorbing and high mechanical performance thermoplastics. *Industrial and Engineering Chemistry Research*, **54**, 12025–12030 (2015).
<https://doi.org/10.1021/acs.iecr.5b03360>
- [107] Orebom A., Di Francesco D., Shakari P., Samec J. S. M., Pierrou C.: Thermal and mechanical properties of esterified lignin in various polymer blends. *Molecules*, **26**, 3219 (2021).
<https://doi.org/10.3390/molecules26113219>
- [108] Pérez-Guerrero P., Lisperguer J., Navarrete J., Rodrigue D.: Effect of modified *Eucalyptus nitens* lignin on the morphology and thermo-mechanical properties of recycled polystyrene. *BioResources*, **9**, 6514–6526 (2014).
<https://doi.org/10.15376/biores.9.4.6514-6526>
- [109] Ghavidel N., Fatehi P.: Synergistic effect of lignin incorporation into polystyrene for producing sustainable superadsorbent. *RSC Advances*, **9**, 17639–17652 (2019).
<https://doi.org/10.1039/C9RA02526J>
- [110] Zhang Z., Mulyadi A., Kuang X., Liu W., Li V., Gogoi P., Liu X., Deng Y.: Lignin-polystyrene composite foams through high internal phase emulsion polymerization. *Polymer Engineering and Science*, **59**, 964–972 (2019).
<https://doi.org/10.1002/pen.25046>
- [111] Kim Y. S., Youe W-J., Kim S. J., Lee O-K., Lee S-S.: Preparation of a thermoplastic lignin-based biomaterial through atom transfer radical polymerization. *Journal of Wood Chemistry and Technology*, **35**, 251–259 (2015).
<https://doi.org/10.1080/02773813.2014.937006>
- [112] Schorr D., Rodrigue D., Diouf P., Stevanovic T.: Recycled polystyrene composites reinforced with esterified and non-esterified kraft lignins. *Journal of Materials Science Research*, **4**, 63 (2015).
<https://doi.org/10.5539/jmsr.v4n1p63>

- [113] Victor P. A., Gonçalves S. B., Machado F.: Styrene/lignin-based polymeric composites obtained through a sequential mass-suspension polymerization process. *Journal of Polymers and the Environment*, **26**, 1755–1774 (2018).
<https://doi.org/10.1007/s10924-017-1078-2>
- [114] Luiz F. N., Scremin F. R., Werncke E., de Oliveira Basso R. L., Possan E., Bittencourt P. R. S.: Thermal evaluation by DSC and tensile strength of extruded blends from polyethylene terephthalate and kraft lignin. *Waste and Biomass Valorization*, **11**, 367–373 (2020).
<https://doi.org/10.1007/s12649-018-0367-x>
- [115] Lazzari L., Domingos E., Silva L., Kuznetsov A., Romão W., Araujo J.: Kraft lignin and polyethylene terephthalate blends: Effect on thermal and mechanical properties. *Polimeros*, **29**, e2019055 (2019).
<https://doi.org/10.1590/0104-1428.06618>
- [116] Rejmontová P., Kovalčík A., Humpolíček P., Capáková Z., Wrzecionko E., Sába P.: The use of fractionated Kraft lignin to improve the mechanical and biological properties of PVA-based scaffolds. *RSC Advances*, **9**, 12346–12353 (2019).
<https://doi.org/10.1039/C8RA09757G>
- [117] Ivanov A. E., Halthur T., Ljunggren L.: Flow permeable composites of lignin and poly(vinyl alcohol): Towards removal of bisphenol A and erythromycin from water. *Journal of Environmental Chemical Engineering*, **4**, 1432–1441 (2016).
<https://doi.org/10.1016/j.jece.2016.02.026>
- [118] El-Nemr K. F., Mohamed H. R., Ali M. A., Fathy R. M., Dhmees A. S.: Polyvinyl alcohol/gelatin irradiated blends filled by lignin as green filler for antimicrobial packaging materials. *International Journal of Environmental Analytical Chemistry*, **100**, 1578–1602 (2020).
<https://doi.org/10.1080/03067319.2019.1657108>
- [119] Monteiro V. A. C., da Silva K. T., da Silva L. R. R., Mattos A. L. A., de Freitas R. M., Mazzetto S. E., Lomonaco D., Avelino F.: Selective acid precipitation of Kraft lignin: A tool for tailored biobased additives for enhancing PVA films properties for packaging applications. *Reactive and Functional Polymers*, **166**, 104980 (2021).
<https://doi.org/10.1016/j.reactfunctpolym.2021.104980>
- [120] Xiong S-J., Pang B., Zhou S-J., Li M-K., Yang S., Wang Y-Y., Shi Q., Wang S-F., Yuan T-Q., Sun R-C.: Economically competitive biodegradable PBAT/lignin composites: Effect of lignin methylation and compatibilizer. *ACS Sustainable Chemistry and Engineering*, **8**, 5338–5346 (2020).
<https://doi.org/10.1021/acssuschemeng.0c00789>
- [121] Yong M., Zhang Y., Sun S., Liu W.: Properties of polyvinyl chloride (PVC) ultrafiltration membrane improved by lignin: Hydrophilicity and antifouling. *Journal of Membrane Science*, **575**, 50–59 (2019).
<https://doi.org/10.1016/j.memsci.2019.01.005>
- [122] Tomaszewska J., Kłapiszewski L., Skórczewska K., Szalaty T. J., Jesionowski T.: Advanced organic-inorganic hybrid fillers as functional additives for poly(vinyl chloride). *Polimery*, **62**, 19–26 (2017).
<https://doi.org/10.14314/polimery.2017.019>
- [123] Kłapiszewski Ł., Tomaszewska J., Skórczewska K., Jesionowski T.: Preparation and characterization of eco-friendly Mg(OH)₂/lignin hybrid material and its use as a functional filler for poly(vinyl chloride). *Polymers*, **9**, 258 (2017).
<https://doi.org/10.3390/polym9070258>
- [124] Seo J. H., Choi C. S., Bae J. H., Jeong H., Lee S-H., Kim Y. S.: Preparation of a lignin/polyaniline composite and its application in Cr(VI) removal from aqueous solutions. *BioResources*, **14**, 9169–9182 (2019).
<https://doi.org/10.15376/biores.14.4.9169-9182>
- [125] Wang L., Li X., Xu H., Wang G.: Construction of polyaniline/lignin composite with interpenetrating fibrous networks and its improved electrochemical capacitance performances. *Synthetic Metals*, **249**, 40–46 (2019).
<https://doi.org/10.1016/j.synthmet.2019.01.016>
- [126] de S. M. de Freitas A., Rodrigues J. S., Maciel C. C., Pires A. A. F., Lemes A. P., Ferreira M., Botaro V. R.: Improvements in thermal and mechanical properties of composites based on thermoplastic starch and kraft lignin. *International Journal of Biological Macromolecules*, **184**, 863–873 (2021).
<https://doi.org/10.1016/j.ijbiomac.2021.06.153>
- [127] Zhao Y., Tagami A., Dobele G., Lindström M. E., Sevastyanova O.: The impact of lignin structural diversity on performance of cellulose nanofiber (CNF)-starch composite films. *Polymers*, **11**, 538 (2019).
<https://doi.org/10.3390/polym11030538>
- [128] Pylypchuk I., Selyanchyn R., Budnyak T., Zhao Y., Lindström M., Fujikawa S., Sevastyanova O.: ‘Artificial wood’ lignocellulosic membranes: Influence of kraft lignin on the properties and gas transport in tunicate-based nanocellulose composites. *Membranes*, **11**, 204 (2021).
<https://doi.org/10.3390/membranes11030204>
- [129] Gordobil O., Delucis R., Egüés I., Labidi J.: Kraft lignin as filler in PLA to improve ductility and thermal properties. *Industrial Crops and Products*, **72**, 46–53 (2015).
<https://doi.org/10.1016/j.indcrop.2015.01.055>
- [130] Park C-W., Youe W-J., Kim S-J., Han S-Y., Park J-S., Lee E-A., Kwon G-J., Kim Y-S., Kim N-H., Lee S-H.: Effect of lignin plasticization on physico-mechanical properties of lignin/poly(lactic acid) composites. *Polymers*, **11**, 2089 (2019).
<https://doi.org/10.3390/polym11122089>
- [131] Kim Y., Suhr J., Seo H-W., Sun H., Kim S., Park I-K., Kim S-H., Lee Y., Kim K-J., Nam J-D.: All biomass and UV protective composite composed of compatibilized lignin and poly(lactic-acid). *Scientific Reports*, **7**, 43596 (2017).
<https://doi.org/10.1038/srep43596>

- [132] Sun Y., Ma Z., Xu X., Liu X., Liu L., Huang G., Liu L., Wang H., Song P.: Grafting lignin with bioderived polyacrylates for low-cost, ductile, and fully biobased poly(lactic acid) composites. *ACS Sustainable Chemistry and Engineering*, **8**, 2267–2276 (2020).
<https://doi.org/10.1021/acssuschemeng.9b06593>
- [133] Guo J., Chen X., Wang J., He Y., Xie H., Zheng Q.: The influence of compatibility on the structure and properties of PLA/lignin biocomposites by chemical modification. *Polymers*, **12**, 56 (2020).
<https://doi.org/10.3390/polym12010056>
- [134] Domínguez-Robles J., Martín N. K., Fong M. L., Stewart S. A., Irwin N. J., Rial-Hermida M. I., Donnelly R. F., Larrañeta E.: Antioxidant PLA composites containing lignin for 3D printing applications: A potential material for healthcare applications. *Pharmaceutics*, **11**, 165 (2019).
<https://doi.org/10.3390/pharmaceutics11040165>
- [135] da Rosa T. S., Trianoski R., Michaud F., Yamashita F., Iwakiri S.: Sludge fiber waste and kraft lignin powder as fillers in polylactic acid biocomposites: Physical, mechanical, and thermal properties. *Polymers*, **13**, 672 (2021).
<https://doi.org/10.3390/polym13050672>
- [136] Grzabka-Zasadzińska A., Kłapiszewski Ł., Bula K., Jesionowski T., Borysiak S.: Supermolecular structure and nucleation ability of polylactide-based composites with silica/lignin hybrid fillers. *Journal of Thermal Analysis and Calorimetry*, **126**, 263–275 (2016).
<https://doi.org/10.1007/s10973-016-5311-3>
- [137] Farooq M., Zou T., Riviere G., Sipponen M. H., Österberg M.: Strong, ductile, and waterproof cellulose nanofibril composite films with colloidal lignin particles. *Biomacromolecules*, **20**, 693–704 (2019).
<https://doi.org/10.1021/acs.biomac.8b01364>
- [138] Liu Y.: Strong and flexible nanocomposites of carboxylated cellulose nanofibril dispersed by industrial lignin. *ACS Sustainable Chemistry and Engineering*, **6**, 5524–5532 (2018).
<https://doi.org/10.1021/acssuschemeng.8b00402>
- [139] Sadeghifar H., Venditti R., Jur J., Gorga R. E., Pawlak J. J.: Cellulose-lignin biodegradable and flexible UV protection film. *ACS Sustainable Chemistry and Engineering*, **5**, 625–631 (2017).
<https://doi.org/10.1021/acssuschemeng.6b02003>
- [140] Alzageem A., Klein S. E., Bergs M., Do X. T., Korte I., Dohlen S., Hüwe C., Kreyenschmidt J., Kamm B., Larkins M., Schulze M.: Antimicrobial activity of lignin and lignin-derived cellulose and chitosan composites against selected pathogenic and spoilage microorganisms. *Polymers*, **11**, 670 (2019).
<https://doi.org/10.3390/polym11040670>
- [141] Izaguirre N., Gordobil O., Robles E., Labidi J.: Enhancement of UV absorbance and mechanical properties of chitosan films by the incorporation of solvolytically fractionated lignins. *International Journal of Biological Macromolecules*, **155**, 447–455 (2020).
<https://doi.org/10.1016/j.ijbiomac.2020.03.162>
- [142] Kopania E., Wiśniewska-Wrona M.: Biopolymer composites based on lignin and microcrystalline chitosan. *Progress on Chemistry and Application of Chitin and its Derivatives*, **21**, 122–134 (2016).
<https://doi.org/10.15259/PCACD.21.13>
- [143] Masilompane T. M., Chaukura N., Mishra S. B., Mishra A. K.: Chitosan-lignin-titania nanocomposites for the removal of brilliant black dye from aqueous solution. *International Journal of Biological Macromolecules*, **120**, 1659–1666 (2018).
<https://doi.org/10.1016/j.ijbiomac.2018.09.129>
- [144] Wawrzekiewicz M., Bartczak P., Jesionowski T.: Enhanced removal of hazardous dye from aqueous solutions and real textile wastewater using bifunctional chitin/lignin biosorbent. *International Journal of Biological Macromolecules*, **99**, 754–764 (2017).
<https://doi.org/10.1016/j.ijbiomac.2017.03.023>
- [145] Duan Y., Freyburger A., Kunz W., Zollfrank C.: Lignin/chitin films and their adsorption characteristics for heavy metal ions. *ACS Sustainable Chemistry and Engineering*, **6**, 6965–6973 (2018).
<https://doi.org/10.1021/acssuschemeng.8b00805>
- [146] Lugoloobi I., Li X., Zhang Y., Mao Z., Wang B., Sui X., Feng X.: Fabrication of lignin/poly(3-hydroxybutyrate) nanocomposites with enhanced properties via a Pickering emulsion approach. *International Journal of Biological Macromolecules*, **165**, 3078–3087 (2020).
<https://doi.org/10.1016/j.ijbiomac.2020.10.156>
- [147] Datta J., Parcheta P.: A comparative study on selective properties of Kraft lignin–natural rubber composites containing different plasticizers. *Iranian Polymer Journal*, **26**, 453–466 (2017).
<https://doi.org/10.1007/s13726-017-0534-0>
- [148] Aini N. A. M., Othman N., Hussin M. H., Sahakaro K., Hayeemasae N.: Hydroxymethylation-modified lignin and its effectiveness as a filler in rubber composites. *Processes*, **7**, 315 (2019).
<https://doi.org/10.3390/pr7050315>
- [149] Atifi S., Miao C., Hamad W. Y.: Surface modification of lignin for applications in polypropylene blends. *Journal of Applied Polymer Science*, **134**, 45103 (2017).
<https://doi.org/10.1002/app.45103>
- [150] Hu L., Stevanovic T., Rodrigue D.: Comparative study of polyethylene composites containing industrial lignins. *Polymers and Polymer Composites*, **23**, 369–374 (2015).
<https://doi.org/10.1177/096739111502300602>
- [151] Hait S., De D., Ghosh A. K., Al Aiti M., Ghosh P., Chanda J., Mukhopadhyay R., Dasgupta S., Wiefner S., Heinrich G., Das A.: Treasuring waste lignin as superior reinforcing filler in high cis-polybutadiene rubber: A direct comparative study with standard reinforcing silica and carbon black. *Journal of Cleaner Production*, **299**, 126841 (2021).
<https://doi.org/10.1016/j.jclepro.2021.126841>

- [152] Diop A., Mijiyawa F., Koffi D., Kokta B. V., Montplaisir D.: Study of lignin dispersion in low-density polyethylene. *Journal of Thermoplastic Composite Materials*, **28**, 1662–1674 (2015).
<https://doi.org/10.1177/0892705714556829>
- [153] Goliszek M., Podkościelna B., Sevastyanova O., Fila K., Chabros A., Paçzkowski P.: Investigation of accelerated aging of lignin-containing polymer materials. *International Journal of Biological Macromolecules*, **123**, 910–922 (2019).
<https://doi.org/10.1016/j.ijbiomac.2018.11.141>
- [154] Iyer K. A., Torkelson J. M.: Sustainable green hybrids of polyolefins and lignin yield major improvements in mechanical properties when prepared *via* solid-state shear pulverization. *ACS Sustainable Chemistry and Engineering*, **3**, 959–968 (2015).
<https://doi.org/10.1021/acssuschemeng.5b00099>
- [155] Grzabka-Zasadzińska A., Klapiszewski Ł., Jesionowski T., Borysiak S.: Functional MgO–lignin hybrids and their application as fillers for polypropylene composites. *Molecules*, **25**, 864 (2020).
<https://doi.org/10.3390/molecules25040864>
- [156] Klapiszewski Ł., Pawlak F., Tomaszewska J., Jesionowski T.: Preparation and characterization of novel PVC/silica–lignin composites. *Polymers*, **7**, 1767–1788 (2015).
<https://doi.org/10.3390/polym7091482>
- [157] Widsten P., Tamminen T., Paajanen A., Hakkarainen T., Liitiä T.: Modified and unmodified technical lignins as flame retardants for polypropylene. *Holzforchung*, **75**, 584–590 (2021).
<https://doi.org/10.1515/hf-2020-0147>
- [158] Gadioli R., Waldman W. R., de Paoli M. A.: Lignin as a green primary antioxidant for polypropylene. *Journal of Applied Polymer Science*, **133**, 43558 (2016).
<https://doi.org/10.1002/app.43558>
- [159] Chen K., Ye D., Gu S., Zhou Y.: Thermal-oxidative effect of Kraft lignin antioxidant in polypropylene: Uncovering the key factor using correlation analysis model. *International Journal of Biological Macromolecules*, **107**, 478–485 (2018).
<https://doi.org/10.1016/j.ijbiomac.2017.09.016>
- [160] Mimini V., Sykacek E., Hashim S. N. A. S., Holzweber J., Hettegger H., Fackler K., Potthast A., Mundigler N., Rosenau T.: Compatibility of kraft lignin, organosolv lignin and liginosulfonate with PLA in 3D printing. *Journal of Wood Chemistry and Technology*, **39**, 14–30 (2019).
<https://doi.org/10.1080/02773813.2018.1488875>
- [161] Črešnar K. P., Klonos P. A., Zamboulis A., Terzopoulou Z., Xanthopoulou E., Papadopoulos L., Kyritsis A., Kuzmič K., Zemljíč L. F., Bikiaris D. N.: Structure-properties relationships in renewable composites based on polylactide filled with tannin and kraft lignin – Crystallization and molecular mobility. *Thermochimica Acta*, **703**, 178998 (2021).
<https://doi.org/10.1016/j.tca.2021.178998>
- [162] Anwer M. A. S., Naguib H. E., Celzard A., Fierro V.: Comparison of the thermal, dynamic mechanical and morphological properties of PLA-lignin & PLA-tannin particulate green composites. *Composites Part B: Engineering*, **82**, 92–99 (2015).
<https://doi.org/10.1016/j.compositesb.2015.08.028>
- [163] Barana D., Ali S. D., Salanti A., Orlandi M., Castellani L., Hanel T., Zoia L.: Influence of lignin features on thermal stability and mechanical properties of natural rubber compounds. *ACS Sustainable Chemistry and Engineering*, **4**, 5258–5267 (2016).
<https://doi.org/10.1021/acssuschemeng.6b00774>
- [164] Datta J., Parcheta P., Surówka J.: Softwood-lignin/natural rubber composites containing novel plasticizing agent: Preparation and characterization. *Industrial Crops and Products*, **95**, 675–685 (2017).
<https://doi.org/10.1016/j.indcrop.2016.11.036>
- [165] Rukmanikrishnan B., Ramalingam S., Rajasekharan S. K., Lee J., Lee J.: Binary and ternary sustainable composites of gellan gum, hydroxyethyl cellulose and lignin for food packaging applications: Biocompatibility, antioxidant activity, UV and water barrier properties. *International Journal of Biological Macromolecules*, **153**, 55–62 (2020).
<https://doi.org/10.1016/j.ijbiomac.2020.03.016>
- [166] Patanair B., Saiter-Fourcin A., Thomas S., Thomas M. G., Pundarikashan P. P., Nair K. G., Kumar V. K., Maria H. J., Delpouve N.: Promoting interfacial interactions with the addition of lignin in poly(lactic acid) hybrid nanocomposites. *Polymers*, **13**, 272 (2021).
<https://doi.org/10.3390/polym13020272>
- [167] Rukmanikrishnan B., Rajasekharan S. K., Lee J., Ramalingam S., Lee J.: K-carrageenan/lignin composite films: Biofilm inhibition, antioxidant activity, cytocompatibility, UV and water barrier properties. *Materials Today Communications*, **24**, 101346 (2020).
<https://doi.org/10.1016/j.mtcomm.2020.101346>
- [168] Kovalcik A., Machovsky M., Kozakova Z., Koller M.: Designing packaging materials with viscoelastic and gas barrier properties by optimized processing of poly(3-hydroxybutyrate-co-3-hydroxyvalerate) with lignin. *Reactive and Functional Polymers*, **94**, 25–34 (2015).
<https://doi.org/10.1016/j.reactfunctpolym.2015.07.001>
- [169] Luo S., Cao J., McDonald A. G.: Interfacial improvements in a green biopolymer alloy of poly(3-hydroxybutyrate-co-3-hydroxyvalerate) and lignin *via in situ* reactive extrusion. *ACS Sustainable Chemistry and Engineering*, **4**, 3465–3476 (2016).
<https://doi.org/10.1021/acssuschemeng.6b00495>
- [170] Bozsódi B., Romhányi V., Pataki P., Kun D., Renner K., Pukánszky B.: Modification of interactions in polypropylene/liginosulfonate blends. *Materials and Design*, **103**, 32–39 (2016).
<https://doi.org/10.1016/j.matdes.2016.04.061>

- [171] Gou R., Guo M.: Effects of different ammonium lignosulfonate contents on the crystallization, rheological behaviors, and thermal and mechanical properties of ethylene propylene diene monomer/polypropylene/ammonium lignosulfonate composites. *Tappi Journal*, **19**, 9–17 (2020).
<https://doi.org/10.32964/tj19.1.9>
- [172] Schneider M., Finimundi N., Podzorova M., Pantyukhov P., Poletto M.: Assessment of morphological, physical, thermal, and thermal conductivity properties of polypropylene/lignosulfonate blends. *Materials*, **14**, 543 (2021).
<https://doi.org/10.3390/ma14030543>
- [173] Wu K., Xu S., Tian X-Y., Zeng H-Y., Hu J., Guo Y-H., Jian J.: Renewable lignin-based surfactant modified layered double hydroxide and its application in polypropylene as flame retardant and smoke suppression. *International Journal of Biological Macromolecules*, **178**, 580–590 (2021).
<https://doi.org/10.1016/j.ijbiomac.2021.02.148>
- [174] Hu X-Q., Ye D-Z., Tang J-B., Zhang L-J., Zhang X.: From waste to functional additives: Thermal stabilization and toughening of PVA with lignin. *RSC Advances*, **6**, 13797–13802 (2016).
<https://doi.org/10.1039/C5RA26385A>
- [175] Ye D-Z., Jiang L., Hu X., Zhang M-H., Zhang X.: Lignosulfonate as reinforcement in polyvinyl alcohol film: Mechanical properties and interaction analysis. *International Journal of Biological Macromolecules*, **83**, 209–215 (2016).
<https://doi.org/10.1016/j.ijbiomac.2015.11.064>
- [176] Ye D-Z., Zhang X., Gu S., Zhou Y., Xu W.: Non-isothermal crystallization kinetics of eucalyptus lignosulfonate/polyvinyl alcohol composite. *International Journal of Biological Macromolecules*, **97**, 249–257 (2017).
<https://doi.org/10.1016/j.ijbiomac.2017.01.010>
- [177] Xu H., Jiang H., Li X., Wang G.: Synthesis and electrochemical capacitance performance of polyaniline doped with lignosulfonate. *RSC Advances*, **5**, 76116–76121 (2015).
<https://doi.org/10.1039/C5RA12292A>
- [178] Xu W., Chen Y., Kang J., Li B.: Synthesis of polyaniline/lignosulfonate for highly efficient removal of acid red 94 from aqueous solution. *Polymer Bulletin*, **76**, 4103–4116 (2019).
<https://doi.org/10.1007/s00289-018-2586-5>
- [179] Zhang Y., Dong A., Fan X., Wang Q., Zhang Y., Yu Y., Cavaco-Paulo A.: Laccase-catalyzed synthesis of conducting polyaniline-lignosulfonate composite. *Journal of Applied Polymer Science*, **133**, 42941 (2016).
<https://doi.org/10.1002/app.42941>
- [180] Rebiś T., Milczarek G.: A comparative study on the preparation of redox active bioorganic thin films based on lignosulfonate and conducting polymers. *Electrochimica Acta*, **204**, 108–117 (2016).
<https://doi.org/10.1016/j.electacta.2016.04.061>
- [181] Chen C., Liu Y., Chen Y., Li X., Cheng J., Chen S., Lin J., Zhang X., Zhang Y.: Effect of polyaniline-modified lignosulfonate added to the negative active material on the performance of lead-acid battery. *Electrochimica Acta*, **338**, 135859 (2020).
<https://doi.org/10.1016/j.electacta.2020.135859>
- [182] Mao H., Dong Y., Qian X., An X.: Enhancement of bonding strength of polypyrrole/cellulose fiber (PPy/CF) hybrid through lignosulfonate doping. *Cellulose*, **24**, 2255–2263 (2017).
<https://doi.org/10.1007/s10570-017-1242-9>
- [183] Luo J-J., Lü Q-F.: Controllable preparation and heavy-metal-ion adsorption of lignosulfonate-polypyrrole composite nanosorbent. *Polymer Composites*, **36**, 1546–1556 (2015).
<https://doi.org/10.1002/pc.23062>
- [184] Che C., Vagin M., Ail U., Gueskine V., Phopase J., Brooke R., Gabrielsson R., Jonsson M. P., Mak W. C., Berggren M., Crispin X.: Twinning lignosulfonate with a conducting polymer *via* counter-ion exchange for large-scale electrical storage. *Advanced Sustainable Systems*, **3**, 1900039 (2019).
<https://doi.org/10.1002/advsu.201900039>
- [185] Qian Y., Wang T., Qiu X., Zhao D., Liu D., Deng Y.: Conductivity enhancement of poly(3,4-ethylenedioxythiophene)/lignosulfonate acid complexes *via* pickering emulsion polymerization. *ACS Sustainable Chemistry and Engineering*, **4**, 7193–7199 (2016).
<https://doi.org/10.1021/acssuschemeng.6b02135>
- [186] Ye H., Zhang Y., Yu Z.: Effect of desulfonation of lignosulfonate on the properties of poly(lactic acid)/lignin composites. *BioResources*, **12**, 4810–4829 (2017).
<https://doi.org/10.15376/biores.12.3.4810-4829>
- [187] Cazacu G., Darie-Nita R. N., Chirila O., Totolin M., Asandulesa M., Ciolacu D. E., Ludwiczak J., Vasile C.: Environmentally friendly polylactic acid/modified lignosulfonate biocomposites. *Journal of Polymers and the Environment*, **25**, 884–902 (2017).
<https://doi.org/10.1007/s10924-016-0868-2>
- [188] Tawiah B., Yu B., Yang W., Yuen R. K. K., Fei B.: Flame retardant poly (lactic acid) biocomposites based on azo-boron coupled 4,4'-sulfonyldiphenol and its combination with calcium lignosulfonate – Crystalline and mechanical properties. *Polymers for Advanced Technologies*, **30**, 2207–2220 (2019).
<https://doi.org/10.1002/pat.4649>
- [189] Chaubey A., Aadil K. R., Jha H.: Synthesis and characterization of lignin-poly lactic acid film as active food packaging material. *Materials Technology*, **36**, 585–593 (2021).
<https://doi.org/10.1080/10667857.2020.1782060>
- [190] Li P., Liu C., Xu Y-J., Jiang Z-M., Liu Y., Zhu P.: Novel and eco-friendly flame-retardant cotton fabrics with lignosulfonate and chitosan through LbL: Flame retardancy, smoke suppression and flame-retardant mechanism. *Polymer Degradation and Stability*, **181**, 109302 (2020).
<https://doi.org/10.1016/j.polymdegradstab.2020.109302>

- [191] Rasheed P. A., Alfantazi A., Jabbar K. A., Mahmoud K. A.: Inhibition of microbially influenced corrosion by chitosan@lignosulfonate nanospheres under dynamic flow conditions. *Journal of Bio- and Tribo-Corrosion*, **7**, 103 (2021).
<https://doi.org/10.1007/s40735-021-00539-y>
- [192] Rasheed P. A., Pandey R. P., Jabbar K. A., Samara A., Abdullah A. M., Mahmoud K. A.: Chitosan/lignosulfonate nanospheres as ‘green’ biocide for controlling the microbiologically influenced corrosion of carbon steel. *Materials*, **13**, 2484 (2020).
<https://doi.org/10.3390/ma13112484>
- [193] Pandey R. P., Rasool K., Rasheed P. A., Gomez T., Pasha M., Mansour S. A., Lee O-S., Mahmoud K. A.: One-step synthesis of an antimicrobial framework based on covalently cross-linked chitosan/lignosulfonate (CS@LS) nanospheres. *Green Chemistry*, **22**, 678–687 (2020).
<https://doi.org/10.1039/C9GC03461G>
- [194] Zhang F., Wang B., Jie P., Zhu J., Cheng F.: Preparation of chitosan/lignosulfonate for effectively removing Pb(II) in water. *Polymer*, **228**, 123878 (2021).
<https://doi.org/10.1016/j.polymer.2021.123878>
- [195] Lou T., Cui G., Xun J., Wang X., Feng N., Zhang J.: Synthesis of a terpolymer based on chitosan and lignin as an effective flocculant for dye removal. *Colloids and Surfaces A: Physicochemical and Engineering Aspects*, **537**, 149–154 (2018).
<https://doi.org/10.1016/j.colsurfa.2017.10.012>
- [196] Yan M., Huang W., Li Z.: Chitosan cross-linked graphene oxide/lignosulfonate composite aerogel for enhanced adsorption of methylene blue in water. *International Journal of Biological Macromolecules*, **136**, 927–935 (2019).
<https://doi.org/10.1016/j.ijbiomac.2019.06.144>
- [197] Zeng W., Liu Y-G., Hu X-J., Liu S-B., Zeng G-M., Zheng B-H., Jiang L-H., Guo F-Y., Ding Y., Xu Y.: Decontamination of methylene blue from aqueous solution by magnetic chitosan lignosulfonate grafted with graphene oxide: Effects of environmental conditions and surfactant. *RSC Advances*, **6**, 19298–19307 (2016).
<https://doi.org/10.1039/C5RA27657H>
- [198] Zhang D., Wang L., Zeng H., Rhimi B., Wang C.: Novel polyethyleneimine functionalized chitosan–lignin composite sponge with nanowall-network structures for fast and efficient removal of Hg(II) ions from aqueous solution. *Environmental Science: Nano*, **7**, 793–802 (2020).
<https://doi.org/10.1039/C9EN01368G>
- [199] Pan J., Zhu J., Cheng F.: Preparation of sodium lignosulfonate/chitosan adsorbent and application of Pb²⁺ treatment in water. *Sustainability*, **13**, 2997 (2021).
<https://doi.org/10.3390/su13052997>
- [200] Mu R., Liu B., Chen X., Wang N., Yang J.: Adsorption of Cu (II) and Co (II) from aqueous solution using lignosulfonate/chitosan adsorbent. *International Journal of Biological Macromolecules*, **163**, 120–127 (2020).
<https://doi.org/10.1016/j.ijbiomac.2020.06.260>
- [201] Gu F., Geng J., Li M., Chang J., Cui Y.: Synthesis of chitosan–lignosulfonate composite as an adsorbent for dyes and metal ions removal from wastewater. *ACS Omega*, **4**, 21421–21430 (2019).
<https://doi.org/10.1021/acsomega.9b03128>
- [202] Xie M-Y., Wang J., Wu Q-Y.: Nanofiltration membranes *via* layer-by-layer assembly and cross-linking of polyethyleneimine/sodium lignosulfonate for heavy metal removal. *Chinese Journal of Polymer Science*, **38**, 965–972 (2020).
<https://doi.org/10.1007/s10118-020-2422-x>
- [203] Szabó G., Romhányi V., Kun D., Renner K., Pukánszky B.: Competitive interactions in aromatic polymer/lignosulfonate blends. *ACS Sustainable Chemistry and Engineering*, **5**, 410–419 (2017).
<https://doi.org/10.1021/acssuschemeng.6b01785>
- [204] Yang X., Zhong S.: Properties of maleic anhydride-modified lignin nanoparticles/polybutylene adipate-co-terephthalate composites. *Journal of Applied Polymer Science*, **137**, 49025 (2020).
<https://doi.org/10.1002/app.49025>
- [205] Nouh S. A., Abou Elfadl A., Benthani K., Gupta R., Keshk S. M. A. S.: Optical and structural properties of polyvinyl alcohol loaded with different concentrations of lignosulfonate. *Journal of Vinyl and Additive Technology*, **25**, 85–90 (2019).
<https://doi.org/10.1002/vnl.21677>
- [206] Wang Q., Wang J., Liang W., Cui Z., Si J.: Improved mechanical properties of jute fiber/polypropylene composite with interface modified by sodium lignosulfonate. *Journal of Biobased Materials and Bioenergy*, **14**, 186–194 (2019).
<https://doi.org/10.1166/jbmb.2020.1957>
- [207] Xu Y., Adekunle K., Ramamoorthy S. K., Skrifvars M., Hakkarainen M.: Methacrylated lignosulfonate as compatibilizer for flax fiber reinforced biocomposites with soybean-derived polyester matrix. *Composites Communications*, **22**, 100536 (2020).
<https://doi.org/10.1016/j.coco.2020.100536>
- [208] Shi R., Li B.: Preparation and characterization of corn starch and lignosulfonate blend film with a high content of lignosulfonate. *BioResources*, **11**, 8860–8874 (2016).
- [209] Lu X., Que H., Guo H., Ding C., Liu X., Qin Y., Robin H. M., Xu C., Gu X.: α -cellulose-based films: Effect of sodium lignosulfonate (SLS) incorporation on physicochemical and antibacterial performance. *Cellulose*, **28**, 7243–7256 (2021).
<https://doi.org/10.1007/s10570-021-03949-w>
- [210] Jančić U., Bračić M., Ojstršek A., Božič M., Mohan T., Gorgieva S.: Consolidation of cellulose nanofibrils with lignosulphonate bio-waste into excellent flame retardant and UV blocking membranes. *Carbohydrate Polymers*, **251**, 117126 (2021).
<https://doi.org/10.1016/j.carbpol.2020.117126>

- [211] Guterman R., Molinari V., Josef E.: Ionic liquid lignosulfonate: Dispersant and binder for preparation of biocomposite materials. *Angewandte Chemie International Edition*, **58**, 13044–13050 (2019).
<https://doi.org/10.1002/anie.201907385>
- [212] Vilela C., Morais J. D., Silva A. C. Q., Muñoz-Gil D., Figueiredo F. M. L., Silvestre A. J. D., Freire C. S. R.: Flexible nanocellulose/lignosulfonates ion-conducting separators for polymer electrolyte fuel cells. *Nanomaterials*, **10**, 1713 (2020).
<https://doi.org/10.3390/nano10091713>
- [213] Lee H. J., Lee H. K., Lim E., Song Y. S.: Synergistic effect of lignin/polypropylene as a compatibilizer in multiphase eco-composites. *Composites Science and Technology*, **118**, 193–197 (2015).
<https://doi.org/10.1016/j.compscitech.2015.08.018>
- [214] Hu J-P., Guo M-H.: Influence of ammonium lignosulfonate on the mechanical and dimensional properties of wood fiber biocomposites reinforced with polylactic acid. *Industrial Crops and Products*, **78**, 48–57 (2015).
<https://doi.org/10.1016/j.indcrop.2015.09.075>

Research article

Comparative assessment of cutting processes in the mechanical behavior of basalt fiber/poly(lactic acid) matrix composites

Varikkadinmel Binaz^{ID}, Kaushik Deepak^{ID}, Inderdeep Singh^{*ID}

Mechanical and Industrial Engineering Department, Indian Institute of Technology Roorkee, Uttarakhand, India

Received 5 June 2022; accepted in revised form 29 August 2022

Abstract. To be used in semi-structural applications, the components of sustainable composites must have good mechanical properties and excellent dimensional/geometrical integrity, both of which are influenced by secondary processing techniques. Less emphasis has been placed on the development, mechanical/microstructural characterization, and secondary processing of sustainable basalt fiber/poly(lactic acid) composites (BFPLA), which can be an excellent choice for semi-structural applications. The present investigation aims to determine the best cutting process to create samples from BFPLA, as well as to experimentally evaluate the effect of different cutting processes (scroll sawing, computer numerical control (CNC) milling, water jet cutting, and abrasive water jet cutting (AWJ)) on the tensile and flexural properties of samples. Stereomicroscopy and field-emission scanning electron microscope (FE-SEM) are used to assess and correlate the influence of surface defects caused by cutting methods with mechanical behavior. AWJ machining consistently generated uniform surface profiles across all specimens, with minimum thermal degradation and fiber roll-out. Compared to the tensile strength values of unidirectional longitudinal, transversal, and bidirectional samples cut using milling, AWJ specimens exhibited a percentage increase of 27.9, 70.2, and 54.4%, respectively. It has been concluded that the choice of cutting technique has a significant impact on the strength of cut samples.

Keywords: biodegradable polymers, mechanical properties, material testing, machining processes, basalt fiber

1. Introduction

The ever-growing global plastic usage and contamination issues, added with the increased consumption of single-use plastics during the pandemic, have necessitated the development of sustainable and green solutions and their expanded applications [1]. That is where the employment of sustainable/compostable plastics and their composites, especially the ones where the reinforcements are natural fibers, plays a vital role in mitigating this global issue. Green composite materials are already being embraced as an essential part of future manufacturing approaches [2, 3]. Sustainable composites are currently being used in applications where minor structural requirements are

needed, like packaging industries and skin tissue engineering [4, 5]. In order to broaden their employment in semi-structural applications, as in the fields of automobile, transportation, and medical equipment, the parts produced must have acceptable mechanical properties and should be of a better dimensional and geometrical quality [6]. Appropriate material selection and primary processing techniques mainly influence the mechanical properties, whereas proper secondary processing/machining can determine the product's final dimensional and geometric stability [7, 8]. Among the available biodegradable polymers, extensive studies concerning the usage of poly(lactic acid) (PLA) as the matrix material for

*Corresponding author, e-mail: inderdeep.singh@me.iitr.ac.in
© BME-PT

sustainable composites are being carried out. These compostable thermoplastic polymers (as they emanate from potato, corn, and beet sugar) possess good mechanical properties comparable to synthetic polymers [9, 10] and hence are being investigated in this study as the matrix material.

Determining the optimal fiber reinforcement from biopolymers, like PLA, in order to fabricate eco-friendly and economically admissible functional composites is a critical task. Mahajan *et al.* [11] have employed a hybrid consolidated structure comprising various multi-criteria decision-making techniques to select the most acceptable fiber from the available natural fiber pool. The authors inferred that basalt fiber is the preferred choice by all techniques to deliver sustainable-green composites with mechanical properties appropriate for semi-structural utilization. Basalt fiber, classified as an eco-friendly natural fiber, has a 16% higher modulus, stronger alkaline resistance, similar tensile strength, increased interfacial adhesion, and is commercially available when compared to glass fiber. Also, basalt fibers are bio-inert, and their deformation at break is more than that of carbon fibers [12]. Although much literature has systematically documented the mechanical performance of different PLA-natural fiber composites, there is less attention on the systematic investigation of the development, and mechanical/microstructural characterization of basalt fiber reinforced PLA (BFPLA) composites.

Liu *et al.* [12] used a twin-screw extruder to prepare BFPLA composites with various concentrations of basalt fibers. The outcomes indicated that basalt fiber had a strong reinforcing and toughening influence than glass fiber. The same extrusion-injection molding method was also followed by Tábi *et al.* [13] and Deák and Czigány [14]. It was demonstrated that a renewable and sustainable composite with superior mechanical properties, eligible for engineering applications could be fabricated using basalt fiber reinforcement through injection molding. They have suggested that BFPLA composites could be utilized to produce technical parts with extreme precision, intricate design, and 3D shape. It was explained that by drying the materials properly, composites with higher mechanical properties might be produced. Deák and Czigány [14] also suggested that 30 wt% short basalt fiber reinforced PLA composite exhibited an impressive tensile and flexural strength, that were respectively 119.7 and 180.0 MPa. Unlike

other authors, Chatiras *et al.* [15] used basalt woven fabric for hot pressing/compression molding (film stacking method). This processing technique led to better mechanical properties as it avoided high shearing and fiber breakage, which occurs during extrusion and injection molding. This method provided composites with better fiber orientation and good fiber-matrix adhesion, and their tensile, flexural, and impact strength values were comparable with glass fiber mat composites. All these available studies suggest superior mechanical properties of BFPLA composites, making them an excellent sustainable alternative to glass/carbon fibers reinforced composites for specific applications. BFPLA composites are hence proved to be a good competitor for medium load applications, including laptop panels, two-wheeler visors, wheel hub covers on automobiles, *etc.*

Because of its convenience and simplicity, compression moulding is a popular cost-saving process for the primary manufacturing of composites. The fibre degradation caused by the intense thermomechanical processing that occurs during injection and extrusion moulding is avoided through the film stacking method, which also results in better-aligned fibres. As the result of this technique is in the form of laminate, cutting specimens for testing and further examination is substantial work.

The investigations to uncover the best sample cutting method from a laminate plate are given less attention in the literature. Researchers have tried to find the effect of edge trimming of the plates on their mechanical properties, primarily based on glass and carbon fiber reinforced polymer composites using different machining processes. Ghidossi *et al.* [16] examined the effect of cutting variables on the extent of damage and mechanical performance of off-axis glass/epoxy unidirectional specimens machined by side milling. The results showed that the machining parameters used to prepare the specimens significantly impacted their mechanical performance. The graphite/epoxy laminates were machined using three different cutting processes by Arola and Ramula [17], and it was found that the machined surface quality varied depending on the cutting method employed. However, there was no discernible difference in the laminate's bulk strength when subjected to bending loads. The stiffness of the graphite/bismaleimide laminate decreased with the magnitude of its surface roughness under fatigue loading [18].

In a flax-reinforced polymer composite, the dependency of the cutting tool and the method employed on delamination behavior was established [19]. The effect of defects produced by different machining techniques on the mechanical behavior of carbon fibre reinforced polymer composites was investigated, and it was concluded that the type and mode of mechanical loading affect composite mechanical response and favor a specific machining process [20]. Experiments were carried out to determine the effect of cutting methods on the mechanical properties of glass epoxy composites, and a correlation was established [21]. All these studies suggest the dependency of surface damage/delamination and mechanical properties on machining processes and various cutting tools. It is also crucial to note that fewer studies concerning sample preparation were available, and specifically, no examinations were based on sustainable composites.

The current experimental investigation is influenced by the requirement for cutting the samples from BFPLA laminates. The need to make the best samples with excellent mechanical properties motivated the authors to identify the best cutting method available. The present study hence aims to find out the best cutting process for sample making from a BFPLA laminate and to experimentally evaluate the effect of four different cutting tools/mechanisms (scroll saw, CNC milling machine, two-dimensional water jet cutting, and abrasive water jet cutting machine) on the tensile and flexural properties of the specimen. A comparative study has also been performed with BFPLA composites prepared from unidirectional and bidirectional basalt fabric mats. Furthermore, the results have been validated and substantiated through stereomicroscope analysis and microstructure examination using a field emission scanning electron microscope (FE-SEM).

2. Experimental procedure

2.1. Materials

PLA, which is used as the matrix material (3052-D, Natur-tec, Minnesota, USA), possesses a density of

$1.24 \text{ g}\cdot\text{cm}^{-3}$ and a melt temperature of 147°C , is 100% compostable, and meets ASTM D6400 and EN 13432 standards. The bi-directional basalt fabric consists of woven unstitched yarns (600-114, GBF Basalt Fiber Co. Ltd., Zhejiang, China) and uni-directional basalt fabrics (600-112, GBF Basalt Fiber Co. Ltd., Zhejiang, China) are employed to fabricate two types of BFPLA laminates. The complete properties of the selected basalt fibers (taken from the technical data sheet) are given in Table 1.

2.2. Processing of BFPLA laminates

Before the processing of laminates, the basalt fabric is cut into rectangular shapes ($25 \text{ cm} \times 24 \text{ cm}$) and dried in a hot air oven at 90°C for 24 hours. PLA granules are dried for 6 hours at 60°C to remove the majority of the absorbed humidity. The optimum parameters for processing individual PLA sheets and composites were identified through pilot experiments.

Individual thin PLA sheets with an average thickness of 1 mm are manufactured by hot compression molding at 150°C . The pressure is applied periodically, starting with 0.5 MPa for 3 minutes of contact time, then increasing to 4 MPa at a steady temperature for the next two minutes. At 60°C , the sheets are cooled under pressure and removed.

In order to manufacture laminates, basalt fabric mats and polymer sheets are stacked one on top of the other in a metallic mold. The complete assembly is hot-pressed at 180°C for 8 minutes with an initial pressure of 4 MPa. The pressure is then increased to 6 MPa for 2 minutes, followed by cooling of laminate under pressure. Laminates with an average thickness of 4 mm are ejected from the mold at a temperature of 60°C . This method avoids fiber breakage caused by shear stresses induced by the melt-mixing procedure while simultaneously optimizing fiber orientation. One BFPLA laminate is developed using 5 PLA sheets and 4 basalt fiber mats. The same method is used to process both bidirectional and uni-directional laminates. The fiber weight fraction of

Table 1. Properties of the basalt fabric used.

	Weft & Warp yarn specification [Tex]	Weft & Warp picks [ends/10 mm]	Woven pattern	Thickness [mm]	Tensile strength [MPa]	Areal density [$\text{g}\cdot\text{m}^{-2}$]
Bidirectional basalt fabric	132	5×5	Twill	0.45	2100	480
Unidirectional basalt fabric	300	5	Unidirection	0.39	2100	400

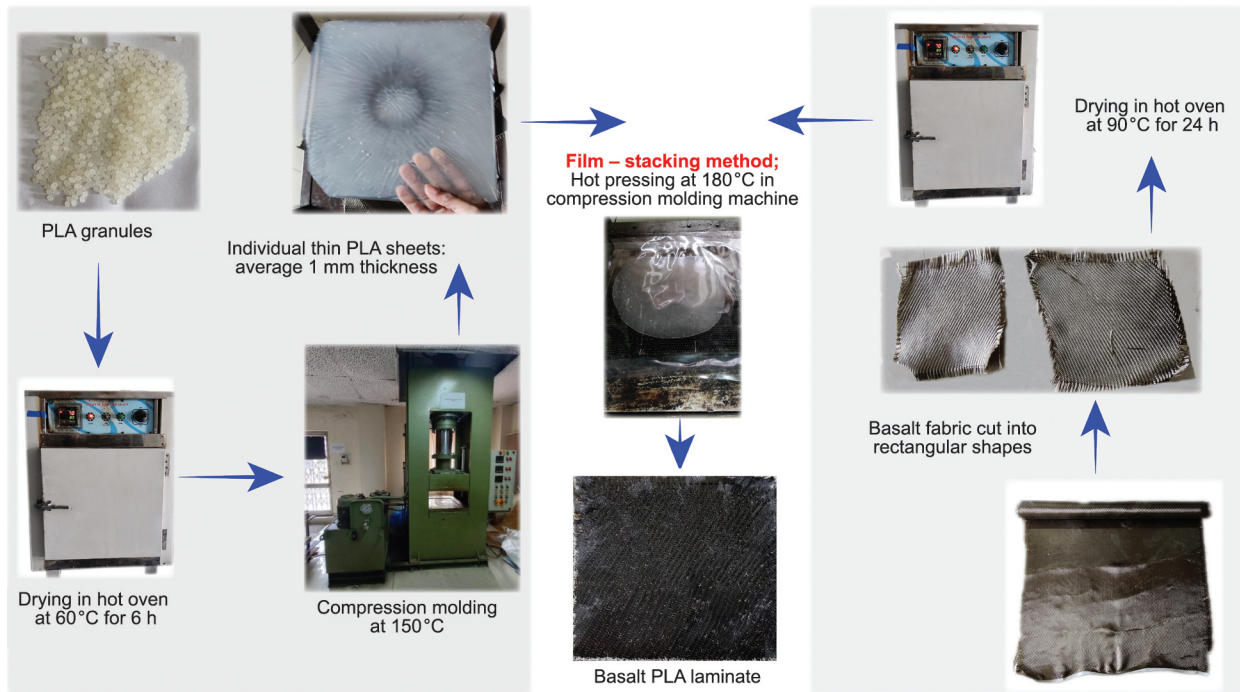


Figure 1. Primary processing of BFPLA laminates.

unidirectional laminates is kept constant at 21% and that of bidirectional composites at 26%. The complete procedure is schematically shown in Figure 1.

2.3. Cutting processes

Four alternative procedures are used to cut samples from laminates (Figure 2). The specifications of the



Figure 2. Machines used for cutting samples. (a) MAKITA SJ401 variable speed scroll saw, (b) 5 inch scroll saw blade (c) Carvey CNC milling machine (d) Milling machine spindle (e) Solid carbide single flute upcut end mill (f) KMT waterjet system (g) Ultra-high pressure pump (h) Abrasive cutting head.

machine used and machining settings are explained in the following sections.

2.3.1. Scroll sawing

The variable speed scroll saw (SJ401, Makita, Aichi, Japan) with a throat depth of 406 mm and a stroke length of 18 mm is employed. All samples are cut using a 5 inch saw blade with 70 teeth per inch (TPI) and a stroke per minute (SPM) of 1200.

2.3.2. CNC milling

A CNC milling machine (Model: Carvey 3D, Inventables Inc., Chicago, USA) equipped with a solid carbide single flute upcut end mill (cutting diameter: 1/8 inch) is used for cutting BFPLA laminates. EASEL software is used to make the 3D design and input the feed rate and cutting depth. Feed rate, depth per pass, and plunge rate are set to the standard values of 1016 mm/min, 0.8 mm, and 304.8 mm/min, respectively.

2.3.3. The water jet and abrasive water jet cutting

The water jet and abrasive water jet cutting are done on a 45 kW Streamline Pro-III model (KMT waterjet systems, Auf der Laukert, Germany) having ultra-high pressure intensifier pumps of 6200 bar. All waterjet machining experiments were done with the abrasive waterjet nozzle to eliminate the impact of nozzle configuration on machining. Abrasive is added to the waterjet in the mixing chamber, and during waterjet operations, the abrasive entrance of the nozzle was blocked to prevent air from entering the jet and reduce cutting efficiency. The following standard cutting parameters were established for all specimens: feed rate of 1000 mm/min, stand-off distance of 3 mm, traverse rate of 250 mm/min, garnet abrasive materials, the abrasive flow rate of 200 gm/min during piercing, the abrasive flow rate of 150 gm/min while cutting, and a waterjet nozzle orifice diameter of 75 microns.

2.4. Mechanical testing

The mechanical properties (tensile and flexural) of the cut BFPLA specimens were evaluated and examined in terms of strength and modulus on a Universal Testing Machine (UTM) (Instron: 5982, USA) in accordance with ASTM D3039 and ASTM D7264 standards. A loading rate of 2 mm/min and a gauge length of 50 mm was set for tensile testing, while a span

length of 60 mm was set for the flexural test, which was carried out using a 3 point bending fixture. To determine the failure process, the testing procedure was also recorded using a 1080p video camera at 60 fps (with 6 part lens quality and 64MP).

2.5. Stereomicroscope and microstructural analysis

The BFPLA specimens cut using various machining methods are observed under a stereomicroscope (Model: SMZ-745T, Nikon). Also, to depict the morphology of the surface and the topographical trends, microstructure analysis of the machined area is performed using a Field Emission-Scanning Electron Microscope (FE-SEM) (Model: Sigma 500, Zeiss Ultra Plus, Jena, Germany). Before micrographs were taken, a thin layer of gold was applied to the specimen using a sputter coater (BAL-TEC-SCD-005) to enhance its conductivity. This study can help determine and correlate the effect of surface defects with different cutting processes on the mechanical behavior of developed biocomposites.

The complete methodology followed for this study is shown in [Figure 3](#). The nomenclature used to name and identify the different specimens machined using the various cutting processes is given in [Table 2](#).

3. Results and discussion

3.1. Cutting of specimens and microstructural analysis

3.1.1. Scroll saw

A reciprocating pin end (hardened, high carbon steel) 5 inch blade with 70 TPI, with small round gullets and a lower feed rate, is used to reduce the burning effect and provide a comparatively better surface finish. The images of UDLS, UDTS, and BDS specimens and their magnified view captured using a stereomicroscope are shown in [Figures 4a–4c](#), respectively. As the scroll saw threads the sharp reciprocating blade through the workpiece, the energy of the cut is converted into heat. Because the laminates are cut along the fiber direction in UDLS specimens, less force was required to cut the specimen than in other specimens. Cutting deformation and friction resulted from the blade's reciprocating movement, the material's limited thermal conductivity, and the lack of coolant resulted in increased heat generation during the cutting operation. This has led to a greater impact effect between the workpiece and the sawblade, as well as increased cutting resistance and cutting vibration.

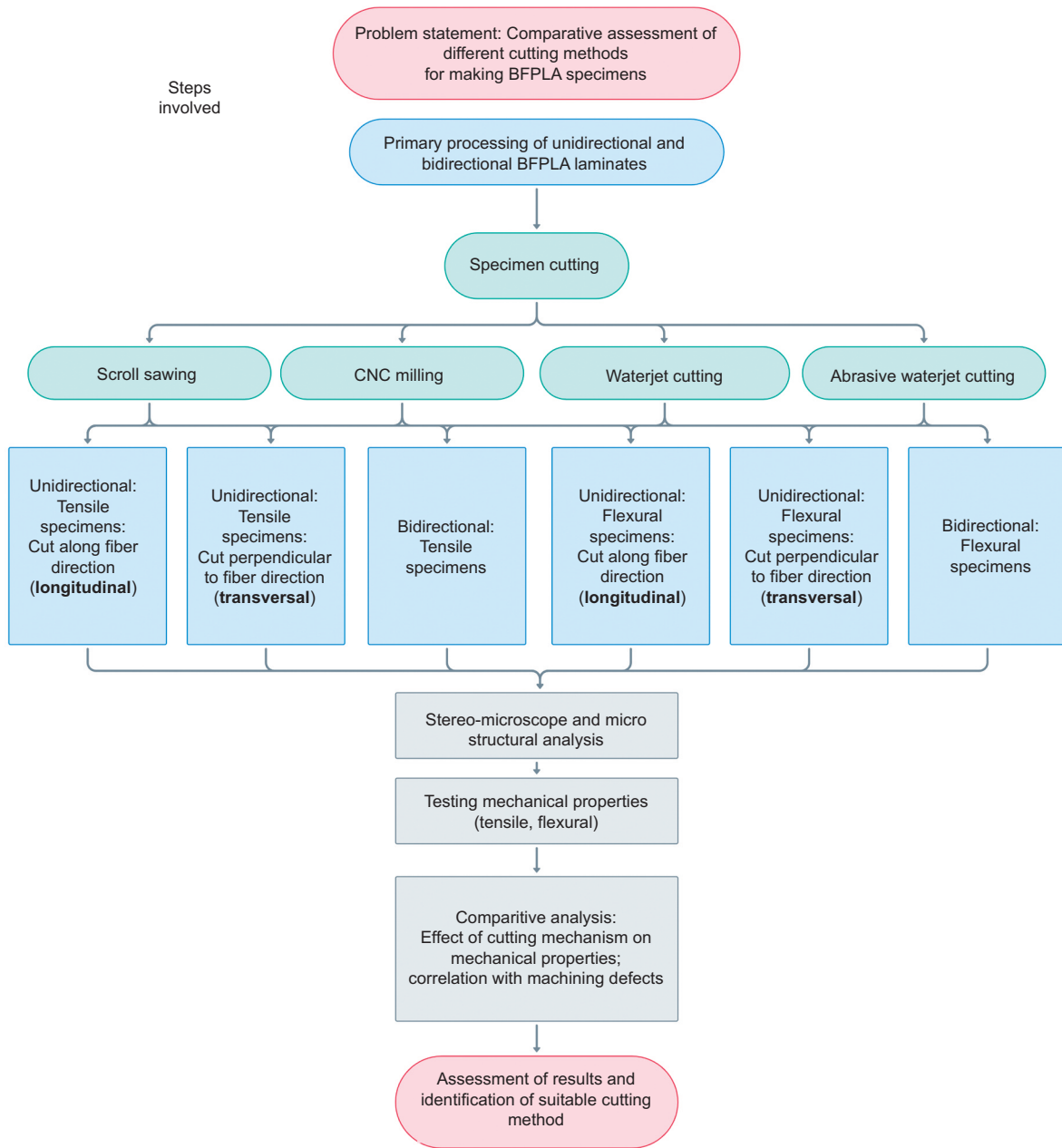


Figure 3. Research methodology employed.

Table 2. Nomenclature used for specimens machined using various cutting processes.

Nomenclature	Details
UDLS	Unidirectional laminate specimen cut along the fiber direction (longitudinal) using scroll saw
UDTS	Unidirectional laminate specimen cut perpendicular to fiber direction (transversal) using scroll saw
BDS	Bidirectional laminate specimen cut using a scroll saw
UDLM	Unidirectional laminate specimen cut along the fiber direction (longitudinal) using a milling machine
UDTM	Unidirectional laminate specimen cut perpendicular to fiber direction (transversal) using a milling machine
BDM	Bidirectional laminate specimen cut using a milling machine
UDLW	Unidirectional laminate specimen cut along the fiber direction (longitudinal) using waterjet
UDTW	Unidirectional laminate specimen cut perpendicular to fiber direction (transversal) using waterjet
BDW	Bidirectional laminate specimen cut using waterjet
UDLAW	Unidirectional laminate specimen cut along the fiber direction (longitudinal) using abrasive waterjet,
UDTAW	Unidirectional laminate specimen cut perpendicular to fiber direction (transversal) using abrasive waterjet
BDAW	Bidirectional laminate specimen cut using abrasive waterjet

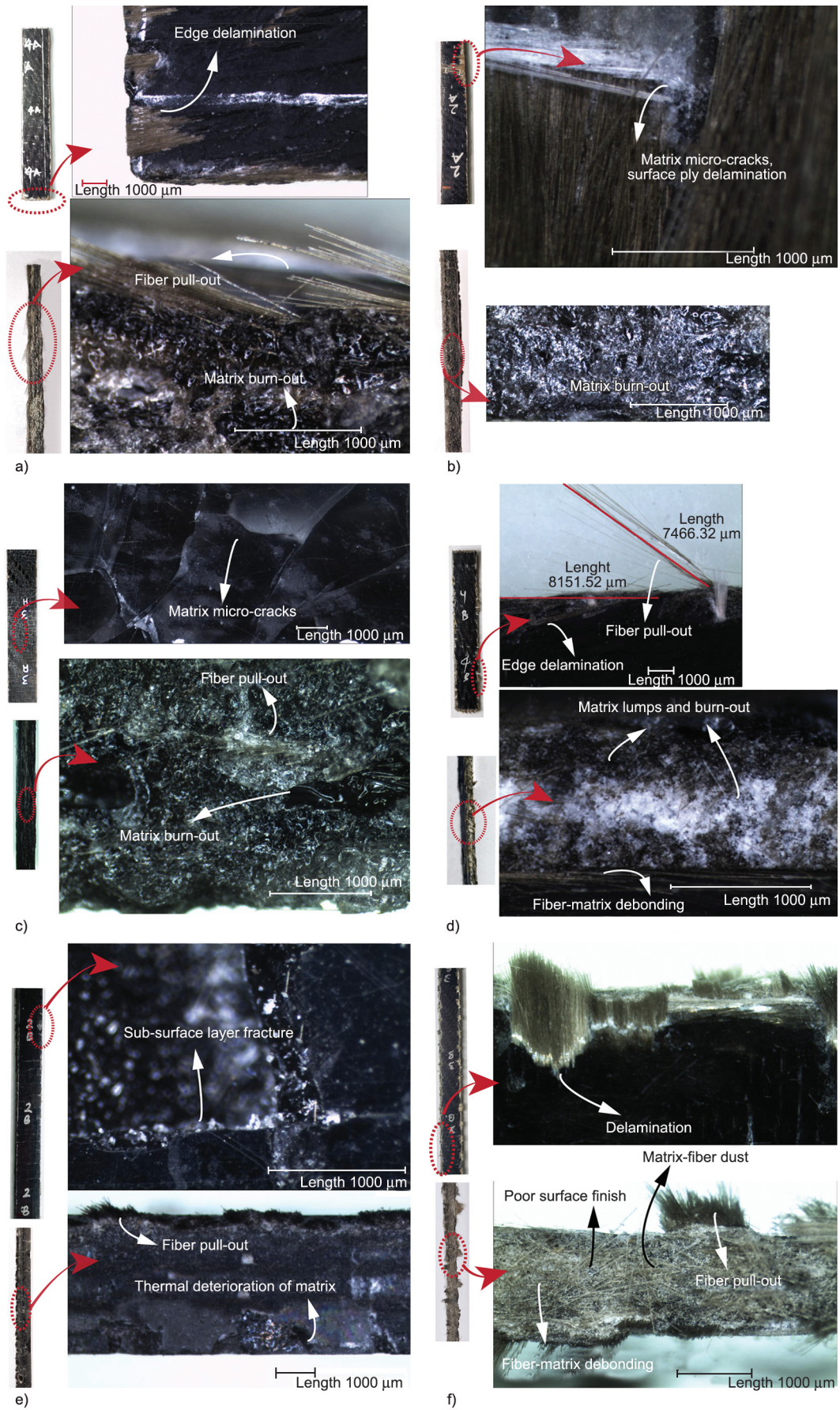


Figure 4. Specimens stereomicroscopy images cut by scroll saw and milling machine: (a) UDLS (b) UDTS (c) BDS (d) UDLM (e) UDTM (f) BDM.

Based on the magnified images of UDTS and BDS specimens, significant matrix burn-out and micro-cracks may be seen. Surface ply delamination is common for all three types of specimens. Fiber pull-out is significant in UDLS and has led to a visually poor surface finish.

Another critical observation during cutting using a scroll saw is that the PLA matrix melts and solidifies during the cutting process and leaves a glossy texture on the machined face. This can be observed clearly in the FE-SEM micrograph of BDS at 250× magnification. (Figure 6a). The melted PLA matrix sticks onto the sawblade pulling out fibers, resulting in voids, matrix fiber debonding, and reduced tool life. This is found prominent in cutting BDS samples and has resulted in cracked surfaces of the top matrix (PLA) layer.

3.1.2. CNC milling

A solid carbide single flute upcut end mill bit is employed, which assists in high-speed milling and high-volume removal of work material while creating a substantially better surface finish than two and three flute bits. The pictures of UDLM, UDTM, and BDM specimens and their magnified view obtained using a stereomicroscope are presented in Figures 4d–4f, respectively. When the bit first enters the laminate during the milling operation, friction at the start of the cut generates an excessively work-hardened layer in the workpiece. Fiber–matrix debonding, edge delamination, fiber disintegration, and pull-out of fibers are frequent forms of defects observed during the evaluation of all milled specimens. FE-SEM analysis of BDM (Figure 6b) also confirms the fibre damage in the form of breaking, bending, and cluster formation. The abrasive characteristics of the basalt fibers have produced substantial wear on tools contributing to subsurface damage in the specimens. For the BDM specimen, the micro-flaws, subsurface layer fractures, and increased surface roughness attributable to fiber/matrix dust linked with machining resulted in poor surface quality. The generation of elevated temperatures while machining has led to the softening and thermal deterioration of PLA. The burning of the matrix is more evident in UDTM specimens, whereas UDLM specimens reveal lumped matrix on the machined surface. Also, the UDLM specimens displayed a reduced rough surface as compared to the UDTM and BDM specimens.

3.1.3. Waterjet cutting

The images of UDLW, UDTW, and BDW specimens and their magnified view captured using stereomicroscope are shown in Figures 5a–5c, respectively. The developed heat from the machining micro-zone is swiftly dispersed since the water may function as a coolant in addition to its machining operation. This leads to the decreased build-up of heat, and consequently, thermal degradation of the matrix is negligible in all the waterjet cut specimens. This also leads to decreased delamination and inhibition of fiber debonding to some degree. UDLW exhibits minute cracks in the matrix top layer at a few spots, though not as much as in the longitudinal specimens cut using a scroll saw and CNC milling.

The machined surfaces are usually striated, consisting of crevices marking the erosion track of the water jet, which is very much evident on UDLW and UDTW specimens. UDTW displays a unique machined surface with micro matrix lumps found around the cut fibers. This may be attributed to the heat created when performing a transverse cut of fibers resulting in the quick melting and cooling of the PLA matrix. Small matrix lumps are also observed on BDW specimens but do not follow a patterned structure as seen on UDTW specimens. The FE-SEM micrographs of the BDW specimen (Figure 6c) reveal a substantially improved surface quality, with laminate layers clearly visible and distinguishable. Micrographs also demonstrate the minimal fiber pull-out and suppression of fiber disintegration, however, the waviness pattern caused by the jet deflection route is noticeable. Fiber roll-out damage is observed in the UDLW specimens. The term ‘roll-out’ refers to the final separation of fibers from their matrix area [22]. This may be generated by high-pressure jet stresses acting on the bare fibers within the machined zone. The fibres that have been broken or partially de-bonded from the matrix may be dislodged by incident jet pressures [23]. Bare fibers are also visible in BDW specimens, which resulted from the erosion of the enclosing matrix material. Micrographs show the fracture of fibers caused by the elevated water jet pressure on fibers. Hence the predominant material removal process visible in water jet cutting of BFPLA laminate, which is also confirmed by FE-SEM characterization, is the material failure associated with fibre breakage and matrix erosion.

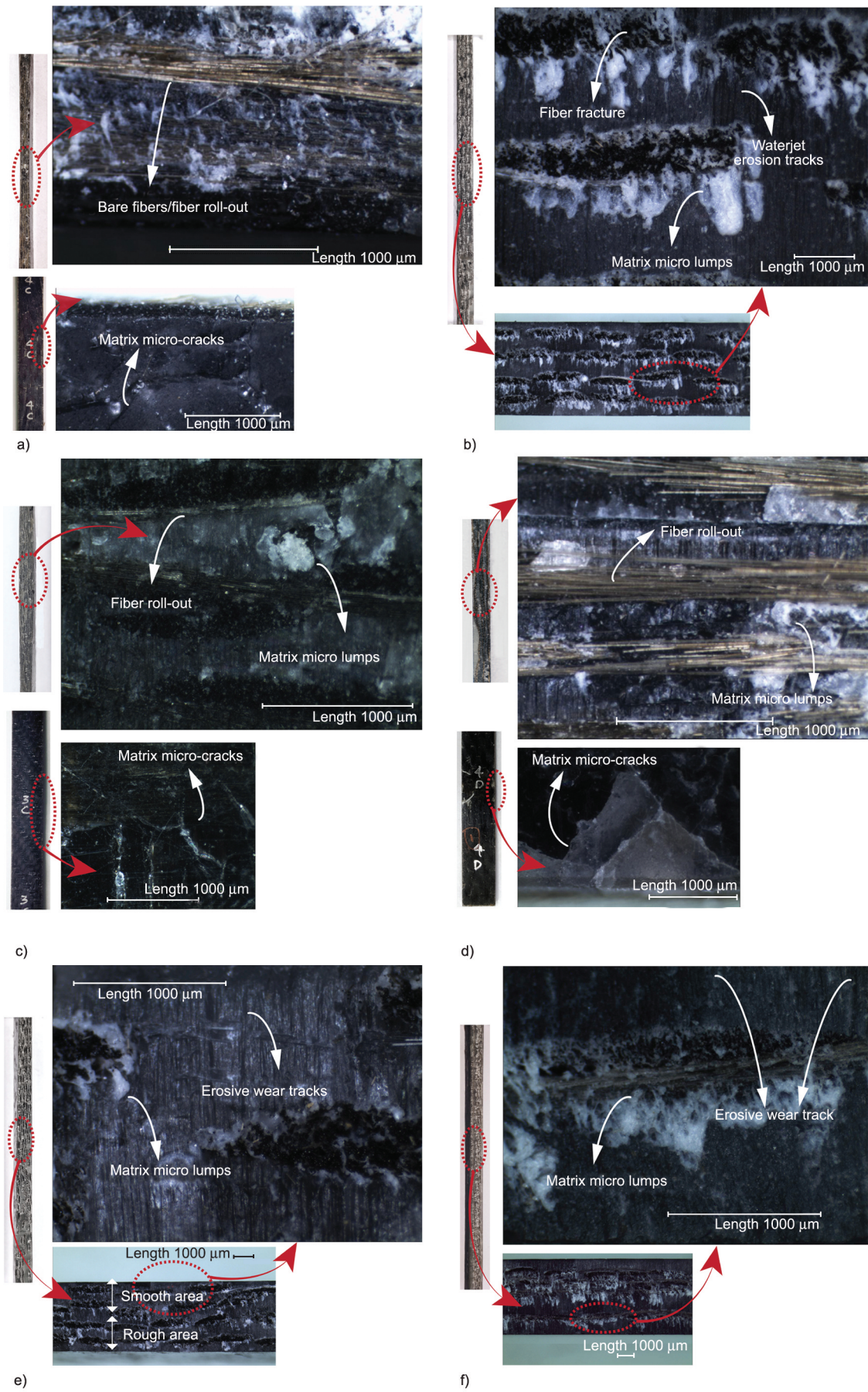


Figure 5. Specimens stereomicroscopy images cut from BFPLA laminate: (a) UDLW (b) UDTW (c) BDW (d) UDLOW (e) UDTAW (f) BDAW.

3.1.4. Abrasive waterjet cutting

The principal material removal technique in abrasive waterjet cutting is erosion by solid abrasive particles. Micro-cutting (cutting deformation or ploughing deformation), brittle fracture, melting, and fatigue are four subprocesses outlined by Meng *et al.* [24] that act concurrently and whose supremacy is governed by process parameters.

The images of UDLAW, UDTAW, and BDAW specimens and their microscopic view are shown in Figures 5d–5f, respectively. For all the specimens, the cutting front observations reveal the erosive wear tracks in the top zone of the cutting region and the formation of material lips towards the end of the tracks. Errant abrasive particles catapulting through the periphery of the coherent jet create these wear grooves. Also, the upper section displays a zone of smooth surface, and the bottom part indicates a comparably rougher area.

3.1.5. Microstructural analysis of the BDS, BDM, BDW, and BDAW specimens

Nonetheless, for all the specimens, regardless of fiber type and cutting direction, abrasive waterjet machining delivered consistently better and uniform surface profiles than all of the other machining methods employed, and the machined area is reasonably smooth, with no texture unevenness across the specimen depth. Although shallow abrasive wear tracks can be spotted on the FE-SEM micrographs of the BDAW specimen (Figure 6d), the waviness patterns as found on the BDW specimen were missing here. Minor levels of fibre pull-outs are also identified, although the degree of damage found is much lower than that observed with the other three processes.

Like in waterjet cutting, matrix burning and thermal damage are negligible in abrasive waterjet specimens as well. One notable feature discovered in abrasive water jet specimens is that a damage zone/matrix

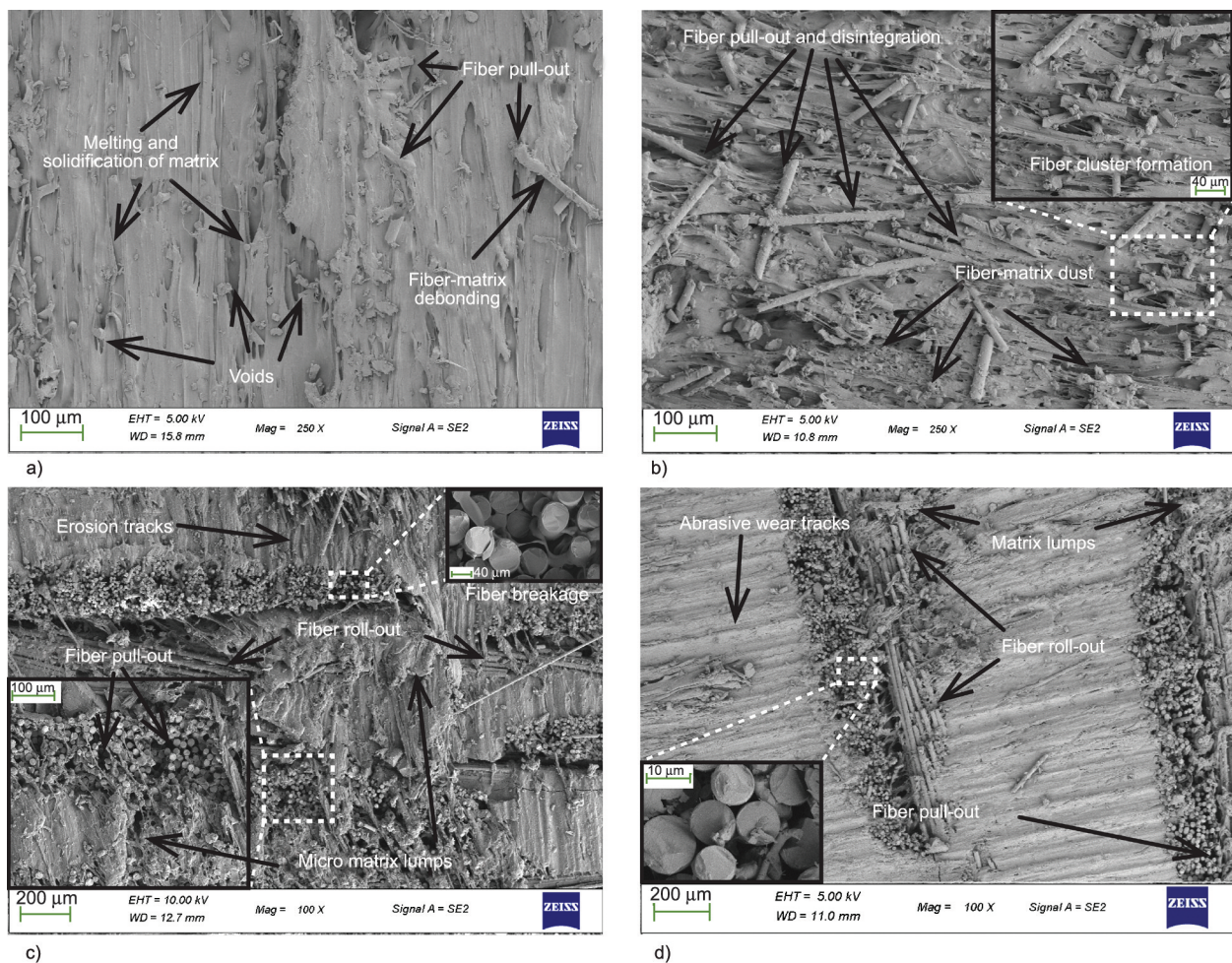


Figure 6. FE-SEM micrographs of the machined region of specimens: (a) BDS (b) BDM (c) BDW (d) BDAW.

fracture is present at the top layer margins and is much more evident on the UDLOW samples, which may be due to the impact of high-energy abrasives on laminate. Evidently, these were not so dominant in water jet specimens. In UDLOW specimens, little fiber roll-out is observed, although the frequency and degree of roll-out are much lower than what is observed in waterjet machined specimens. The decreased magnitude of the force acting on the machining zone is reflected in the lower amount of fiber roll-out. FE-SEM analysis suggests that the micro-machining effects of abrasives and consequent matrix erosion are the dominating material removal process. These material removal mechanisms also assist towards a more consistent surface with reduced roughness and variability than the waterjet machined area. Interestingly like the UDTW samples, tiny matrix lumps are seen surrounding the cut fibers in BDAW specimens. Whereas the UDTAW samples demonstrate no/fewer lumps formation, much of the matrix around the fibers on the machined area is still intact. In comparison to other cutting processes,

abrasive waterjet samples did not show significant material degradation to either the fiber or matrix.

3.2. Tensile and flexural testing

All specimens are tested to obtain strength and modulus under tensile and flexural loading conditions at room temperature. The results obtained are plotted and shown in the Figure 7. The specimens show a specific trend in strength values. Clearly, the abrasive waterjet specimen showed the highest tensile strength value for all unidirectional (longitudinal), unidirectional (transversal), and bidirectional variants and the specimens obtained using CNC, while milling showed the least. Water jet specimens displayed the second-highest value, followed by the scroll saw specimens. The same trend is followed for flexural strength as well.

The abrasive water jet cut specimens showed a percentage increase of 27.9, 70.2, and 54.4% for the tensile strength values of unidirectional longitudinal, transversal and bidirectional, respectively, compared to the tensile strength values of specimens cut through

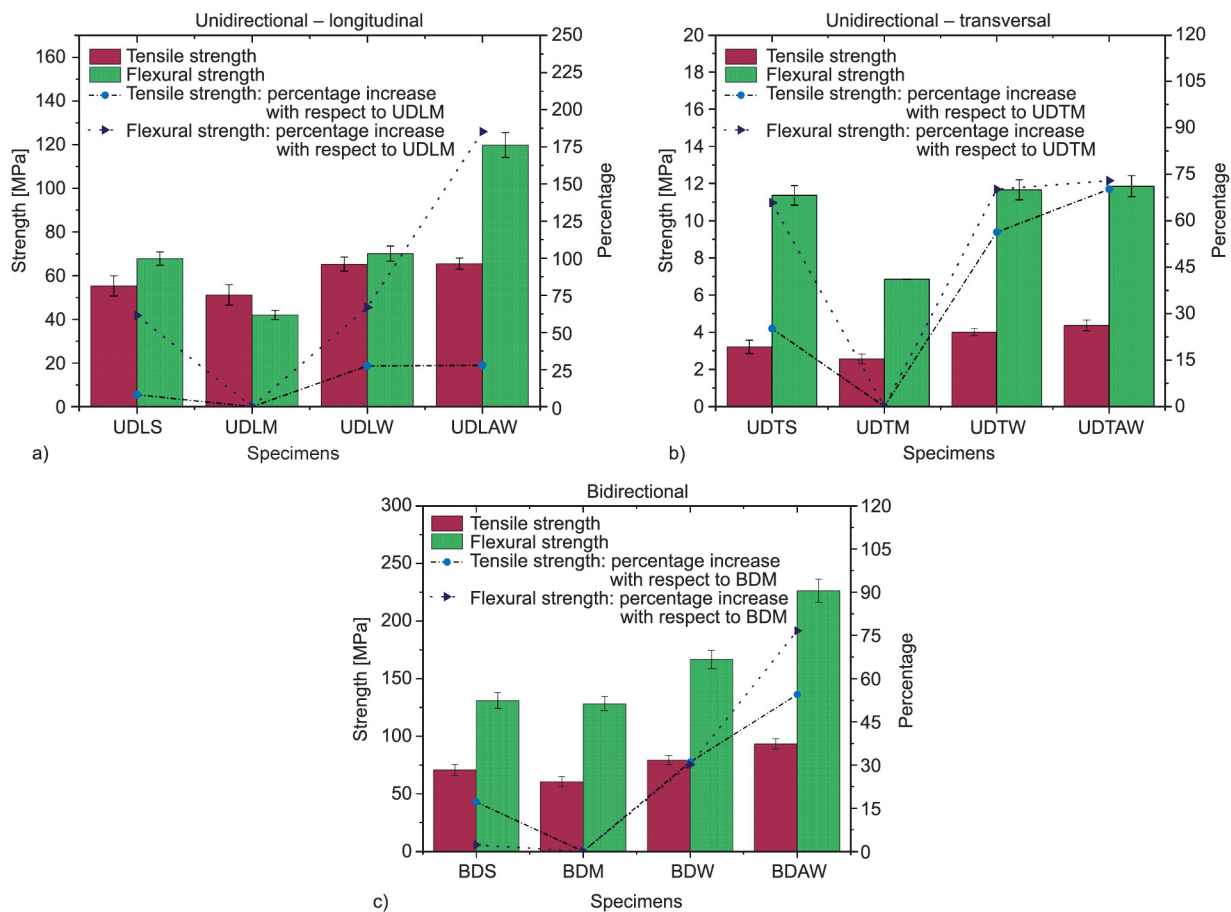


Figure 7. Tensile and flexural strength values of (a) unidirectional – longitudinal specimens (b) unidirectional – transversal specimens (c) bidirectional specimens.

CNC milling. Furthermore, when flexural strength values of unidirectional longitudinal, transversal and bidirectional specimens were compared to those of CNC milled specimens, the abrasive water jet cut specimens exhibited a percentage increase of 185.2, 72.9, and 76.6, respectively. The bidirectional specimen exhibited the maximum improvement of 17.9% when the tensile strength of specimens cut using abrasive waterjet was compared to the waterjet cut specimen, while the unidirectional longitudinal specimen showed the least improvement with only a 0.3% gain. In contrast, the abrasive waterjet cut unidirectional longitudinal specimen displayed a 70.9% rise in results when compared to the waterjet cut specimen for flexural strength.

The FESEM analysis and microscopy studies of milled specimens revealed the generation of elevated temperatures and matrix burning on milling cut specimens. This might have resulted in the fiber-matrix debonding in specimens, resulting in a reduction in strength and deterioration of the structural integrity. This may impair the tensile strength of specimens as well. Also, it was evident from the micrographs that the scroll saw cut specimens showed extensive fiber pull-out and matrix-fiber debonding. This machining-induced damage might have resulted in reduced mechanical properties. The matrix burning and thermal damage were negligible in abrasive waterjet and waterjet cut specimens. Also, on abrasive waterjet specimens, the degree of fiber pull-out was much lower than what was seen in waterjet machined specimens, which might have resulted in their better mechanical strength.

According to the mechanical characteristics of PLA-based composites reported in the literature, the flexural strength of the flax fiber (50 wt%) reinforced PLA laminate was 215 MPa, while the tensile strength of the banana (40 wt%)/ PLA biocomposites was 78.6 MPa [25]. The PLA/glass laminates offered tensile and flexural strengths of 108.2 and 99.4 MPa, respectively [15]. Flexural strength of 180.0 MPa was obtained for the PLA composite with 30% short basalt fiber reinforcement [14]. In this study, the bidirectional sample specimens cut with an abrasive waterjet yielded the highest tensile and flexural strength values of 93.28 and 226.2 MPa, respectively, which are better than those found in the literature. It is now evident that the abrasive water jet cut samples exhibit the key characteristics of a material removal method for use in composites, particularly BFPLA laminates.

The tensile and flexural modulus values followed a similar trend as the strength values as shown in Figure 8. Abrasive water jet cut specimens showed better elasticity than the rest of the specimens. Also, it was found that the unidirectional longitudinal cut specimens showed better stiffness (tensile modulus of 3017.5 MPa and flexural modulus of 17237 MPa) than bidirectional laminates. Prior work has documented the dependence of modulus values with regard to machining. According to Abidi *et al.* [26], the delamination defects and cut specimen surface quality caused Young’s modulus values of carbon fiber reinforced polymer laminate to vary with respect to the machining processes. Sjögren *et al.* [27] demonstrated that defects, particularly fiber breakages,

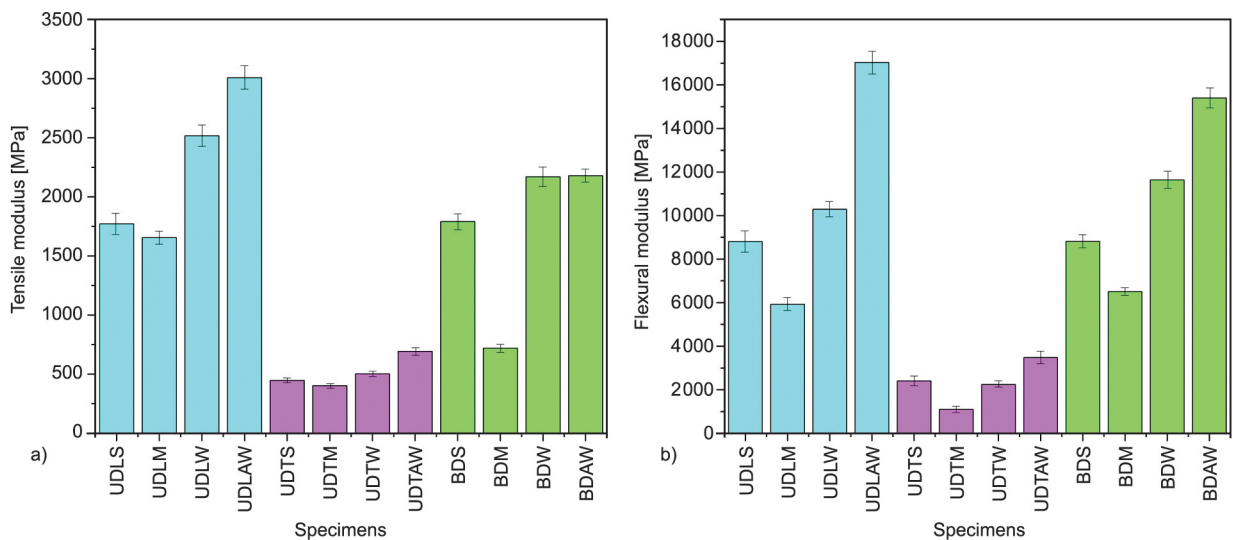


Figure 8. (a) Tensile modulus of tested specimens (b) flexural modulus of tested specimens.

influence the elastic modulus of an impact-damaged composite laminate. Cutting end-surface roughness and microcracks have been connected to changes in a material's loading stiffness and modulus values [28, 29]. A greater elastic modulus indicates a stiffer and typically more brittle material, which is less malleable and this suggests that bidirectional samples have comparatively better ductile properties along with higher ultimate strength values than other variants, particularly abrasive waterjet machined samples.

3.3. Failure analysis

The stress-strain curves of specimens machined using an abrasive waterjet are shown in Figure 9. The failure process at the macroscopic laminate level is explained via images from the captured film.

Fracture is the full breakdown of the laminate's continuity, and it always begins with the commencement of a crack, followed by crack propagation. Figures 10a–10h demonstrate the tensile testing stages of the bidirectional specimen. As the load reached about 41 MPa, the top and bottom matrix layers formed additional microcracks, along with the initial cracks developed during machining. At the stress value of 45 MPa, the number of cracks began to increase, and minor fiber breakages (which are aligned in the transverse direction) emerged. As loading progressed, the concentration of these microcracks grew, and as the stress reached about 70 MPa, the matrix fractures coalesced, followed by fiber-matrix debonding, resulting in more fiber pull-outs. When the matrix breaks, the basalt fibers carry the stress, resulting in little dip and rise on the illustrated curve.

As one can see, the failure of one layer affects the stiffness and residual strength of the laminate but

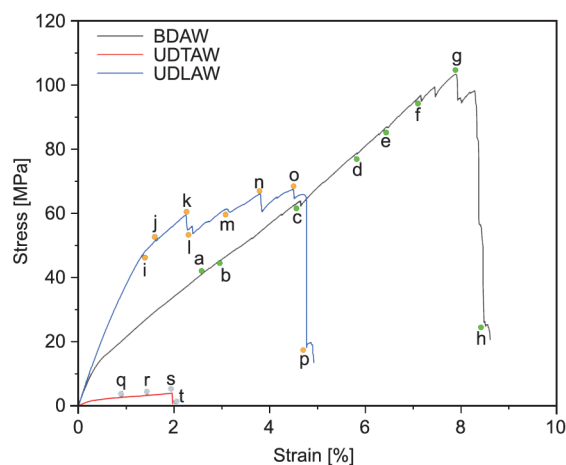


Figure 9. Stress-strain curves of abrasive waterjet machined specimens.

does not always result in total failure. This type of failure may occur due to a low interlaminar shear strength; cracks in one layer will turn along these interfaces, isolating the initially cracked layer from the other laminae, and the laminate will proceed to carry the load with slightly reduced stiffness and residual strength. Furthermore, Dharan [30] proposed that the original matrix crack might leave the fiber intact via crack bridging for brittle fibers in a brittle matrix. When both the matrix and the fiber are brittle, the fibers stay intact while the matrix fracture propagates around them, as in a glass-epoxy composite. At 84 MPa, the matrix completely fails. Interply failures (delamination) tend to predominate at about 94 MPa, combined with fiber breakage, resulting in total laminate failure at 103 MPa. The final failed specimen is depicted in Figures 10u and 10v.

Figures 10i–10p depict the failure process in a unidirectional longitudinal specimen machined using an abrasive water jet. At about 45 MPa, the initial failure appears in the form of a fiber break, which is accompanied by a failure of the surrounding matrix by transverse cracking that extends up to the neighboring fibers and fiber debonding. The size of these failure spots stays essentially the same as the load increases, but their number increases throughout the specimen, causing additional weakening. As the load rises to 58 MPa, the number of isolated fractures increases, providing a weaker route for fracture on the specimen's sides. With increasing stress, fiber failures accelerate, eventually resulting in the coalescence of fiber breaks through transverse cracking followed by interfacial shearing at 66 MPa. Figures 10w and 10x exhibit the UDLAW specimen that failed.

The failure process of unidirectional transversal specimen cut using abrasive waterjet is shown in Figures 10q–10t. UDTAW specimens exhibited typical brittle fracture behavior, with nearly constant stress (3.67 MPa) during cracking, rapid crack propagation, and negligible deformation. This might be because, when the specimen was pulled in the direction normal to the fiber, the Poisson effect in the matrix causes significant shear stress at the fiber ends, causing the bond to break. The matrix has fractured in a cleavage mode, as seen in Figures 10y, 10z₁, and 10z₂, while the fibers have remained almost intact. Another interesting data to be noted is that the tensile and flexural strength, as well as the elastic modulus values of transverse cut specimens, show a considerable reduction compared to the longitudinal ones.

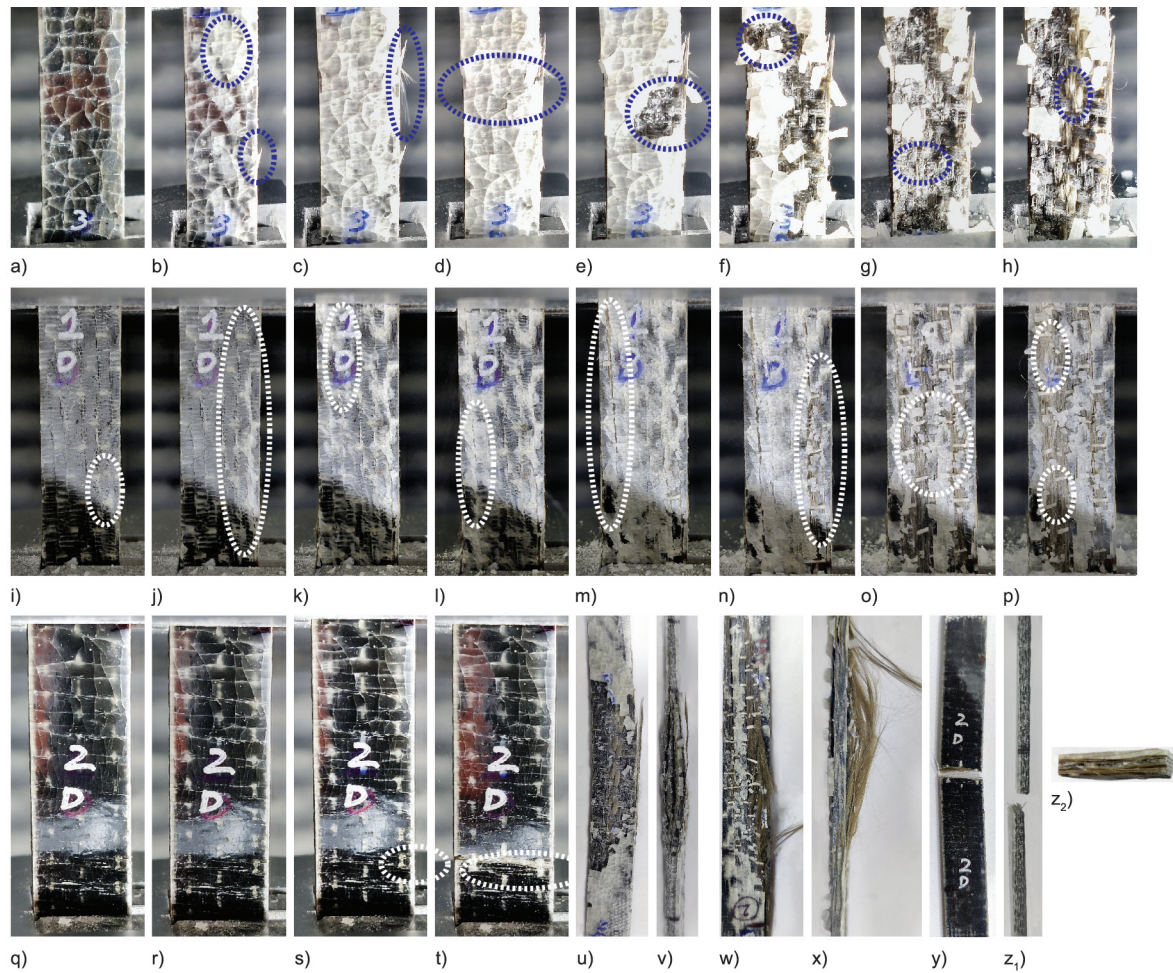


Figure 10. The tensile testing stages of abrasive waterjet machined specimens, (a to h) failure process of BDAW, (i to p) failure process of UDLaw, (q to t) failure process of UDTAW, (u, v) top view and side view of failed BDAW, (w, x) top view and side view of failed UDLaw, (y–z₂) top view and side view of failed UDTAW.

Patel and Dave [31] reported a decrease in tensile strength of specimens with higher fiber orientation angle/cutting direction (45°) and a better tensile strength for specimens (longitudinal) with 0° fiber orientation angle. Ramulu and Arola [22] have observed a 97% reduction in strength values, and Cordin *et al.* [32] have reported an 88% decrease for specimens cut at 90° to the fiber orientation. In our experiments, the transversal specimens showed an average of 94% reduction in tensile strength and 85% reduction in flexural strength values compared to the longitudinal ones. This shows that changes in the fiber orientation angle can lead to a considerable weakening of the material. Despite significant improvements in mechanical characteristics along the fiber direction, the strength values in the transverse direction are inferior to those of pure PLA material. This also supports the anisotropic behavior of the processed BFPLA. The elastic modulus of unidirectional laminates can be theoretically calculated by

the rule of mixtures. A modified micromechanical model [33, 34] for the prediction of elastic modulus is given below (Equation (1)):

$$E_c = \kappa \eta_d \eta_l \eta_0 V_f E_f + V_m E_m \quad (1)$$

where κ is the fiber area correction factor, η_d is the fibre diameter distribution factor, η_l is the fibre length distribution factor, η_0 is the fibre orientation distribution factor, E_x is the elastic modulus, V_x is the volume fraction with the subscript *c*, *f* and *m* being composite, matrix, and fiber, respectively. According to Equation (1), the parameter η_0 quantifies the impact of fiber alignment with respect to the load applied. It is calculated using the equation given below (Equation (2)):

$$\eta_0 = \sum_n a_n \cos^4 \theta_n \quad (2)$$

This clearly illustrates that if the cutting direction is 90° , $\cos\theta$ will be zero, implying that basalt fibres will make no contribution to the stiffness of the laminate. Furthermore, the reinforcing fibres in the 90° orientation reduce the rigidity of the laminate, which may be justified by the ease with which basalt and PLA debond, leading to significantly lower strength and modulus values.

4. Conclusions

The current experimental investigation aims to determine the optimal cutting process for cutting specimens from a BFPLA laminate. Additionally, a comparative assessment is reported for composites with unidirectional and bidirectional basalt fabric mats. The following are the primary conclusions of the present research endeavor.

- The abrasive nature of basalt fibers resulted in significant tool wear, resulting in subsurface damage and increased surface roughness, according to the stereomicroscope and FE-SEM analysis of milled specimens. The high-temperature values and matrix burning resulted in matrix-fiber debonding in milled specimens, reducing strength and structural integrity.
- Microscopy and microstructural analysis revealed considerable fiber pull-out and matrix-fiber debonding in the scroll saw cut specimens. Thermal deterioration of the matrix is minimized in all waterjet cut specimens, resulting in decreased delamination and mitigation of fiber debonding to a certain extent. Material failure owing to fiber fracture and matrix erosion is the principal mechanism of material loss in water jet cutting of BFPLA laminates.
- Abrasive waterjet machining consistently generated significantly uniform surface profiles as compared to other methods across all specimens, independent of the fiber type or cutting direction. The machined area was generally smooth, with no texture unevenness over the specimen depth. Matrix burning, thermal degradation, and fiber roll-out were reduced due to the minimal force exerted in the machining zone. The primary material removal mechanisms seem to be abrasive micromachining and matrix erosion.
- In all unidirectional (longitudinal), unidirectional (transversal), and bidirectional variants, the abrasive waterjet specimen provided the highest tensile

strength, while the CNC machined specimen had the lowest. Water jet specimens had the second-highest value, followed by scroll saw specimens. A similar trend exists for flexural strength values.

- The abrasive waterjet cutting effectively generated bidirectional BFPLA specimens with the highest tensile and flexural strengths of 93.28 and 226.2 MPa.

It is concluded that the choice of cutting technique has a substantial influence on the strength of cut samples, and abrasive water jet cutting is the best approach for producing better quality BFPLA samples with smooth, uniform surface profiles, fewer defects, and improved mechanical properties. Future research may focus on quantifying machining damages on a sustainable composite and expanding the evaluation of the impacts of machining damages on fatigue and impact strength. A correction criteria index may also be generated for predicting the actual strength of laminates produced when samples are cut using traditional cutting methods.

Acknowledgements

The authors would like to acknowledge the financial support provided by the Ministry of Education (MoE), Government of India.

References

- [1] Silva A. L. P., Prata J. C., Walker T. R., Campos D., Duarte A. C., Soares A., Barcelò D., Rocha-Santos T.: Rethinking and optimising plastic waste management under COVID-19 pandemic: Policy solutions based on redesign and reduction of single-use plastics and personal protective equipment. *Science of the Total Environment*, **742**, 140565 (2020).
<https://doi.org/10.1016/j.scitotenv.2020.140565>
- [2] Mohanty A. K., Vivekanandhan S., Pin J-M., Misra M.: Composites from renewable and sustainable resources: Challenges and innovations. *Science*, **362**, 536–542 (2018).
<https://doi.org/10.1126/science.aat9072>
- [3] Mohd-Ishak Z. A., Ahmad-Thirmizir M. Z.: Producing green composites via polymer blending. *Express Polymer Letters*, **15**, 910–911 (2021).
<https://doi.org/10.3144/expresspolymlett.2021.73>
- [4] Verma N., Pramanik K., Sing A. K., Biswas A.: Design of magnesium oxide nanoparticle incorporated carboxy methyl cellulose/poly vinyl alcohol composite film with novel composition for skin tissue engineering. *Materials Technology*, **37**, 706–716 (2021).
<https://doi.org/10.1080/10667857.2021.1873634>

- [5] Arrieta M. P., Beltran F., Abarca de las Muelas S. S., Gaspar G., Sanchez Hernandez R., de la Orden M. U., Urreaga J. M.: Development of tri-layer antioxidant packaging systems based on recycled PLA/sodium caseinate/recycled PLA reinforced with lignocellulosic nanoparticles extracted from yerba mate waste. *Express Polymer Letters*, **16**, 881–900 (2022).
<https://doi.org/10.3144/expresspolymlett.2022.64>
- [6] Jani S. P., Kumar A. S., Khan M. A., Kumar M. U.: Machinability of hybrid natural fiber composite with and without filler as reinforcement. *Materials and Manufacturing Processes*, **31**, 1393–1399 (2016).
<https://doi.org/10.1080/10426914.2015.1117633>
- [7] Jaeschke P., Kern M., Stute U., Haferkamp H., Peters C., Herrmann A. S.: Investigation on interlaminar shear strength properties of disc laser machined consolidated CF-PPS laminates. *Express Polymer Letters*, **5**, 238–245 (2011).
<https://doi.org/10.3144/expresspolymlett.2011.23>
- [8] Komanduri R.: Machining of fiber-reinforced composites. *Machining Science and Technology*, **1**, 113–152 (2007).
<https://doi.org/10.1080/10940349708945641>
- [9] Akintayo O. S., Olajide J. L., Betiku O. T., Egoh A. J., Adegbesan O. O., Daramola O. O., Sadiku E. R., Desai D. A.: Poly(lactic acid)-silkworm silk fibre/fibroin biocomposites: A review of their processing, properties, and nascent applications. *Express Polymer Letters*, **14**, 924–951 (2020).
<https://doi.org/10.3144/expresspolymlett.2020.76>
- [10] Wang F. Y., Dai L., Ge T. T., Yue C. B., Song Y. M.: α -methylstyrene-assisted maleic anhydride grafted poly(lactic acid) as an effective compatibilizer affecting properties of microcrystalline cellulose/poly(lactic acid) composites. *Express Polymer Letters*, **14**, 530–541 (2020).
<https://doi.org/10.3144/expresspolymlett.2020.43>
- [11] Mahajan A., Binaz V., Singh I., Arora N.: Selection of natural fiber for sustainable composites using hybrid multi criteria decision making techniques. *Composites Part C: Open Access*, **7**, 100224 (2022).
<https://doi.org/10.1016/j.jcomc.2021.100224>
- [12] Liu T., Yu F., Yu X., Zhao X., Lu A., Wang J.: Basalt fiber reinforced and elastomer toughened polylactide composites: Mechanical properties, rheology, crystallization, and morphology. *Journal of Applied Polymer Science*, **125**, 1292–1301 (2012).
<https://doi.org/10.1002/app.34995>
- [13] Tábi T., Tamás P., Kovács J. G.: Chopped basalt fibres: A new perspective in reinforcing poly(lactic acid) to produce injection moulded engineering composites from renewable and natural resources. *Express Polymer Letters*, **7**, 107–119 (2013).
<https://doi.org/10.3144/expresspolymlett.2013.11>
- [14] Deák T., Czigány T.: Chemical composition and mechanical properties of basalt and glass fibers: A comparison. *Textile Research Journal*, **79**, 645–651 (2009).
<https://doi.org/10.1177/0040517508095597>
- [15] Chatiras N., Georgiopoulos P., Christopoulos A., Kontou E.: Thermomechanical characterization of basalt fiber reinforced biodegradable polymers. *Polymer Composites*, **40**, 4340–4350 (2019).
<https://doi.org/10.1002/pc.25295>
- [16] Ghidossi P., El-Mansori M., Pierron F.: Influence of specimen preparation by machining on the failure of polymer matrix off-axis tensile coupons. *Composites Science and Technology*, **66**, 1857–1872 (2006).
<https://doi.org/10.1016/j.compscitech.2005.10.009>
- [17] Arola D., Ramula M.: Machining-induced surface texture effects on the flexural properties of a graphite/epoxy laminate. *Composites*, **25**, 822–834 (1994).
[https://doi.org/10.1016/0010-4361\(94\)90143-0](https://doi.org/10.1016/0010-4361(94)90143-0)
- [18] Arola D., Williams C. L.: Surface texture, fatigue, and the reduction in stiffness of fiber reinforced plastics. *Journal of Engineering Materials and Technology*, **124**, 160–166 (2002).
<https://doi.org/10.1115/1.1416479>
- [19] Slamani M., Karabibene N., Chatelain J-F., Beauchamp Y.: Edge trimming of flax fibers and glass fibers reinforced polymers composite – An experimental comparative evaluation. *International Journal of Material Forming*, **14**, 1497–1510 (2021).
<https://doi.org/10.1007/s12289-021-01644-6>
- [20] Haddad M., Zitoune R., Eyma F., Castanié B.: Influence of machining process and machining induced surface roughness on mechanical properties of continuous fiber composites. *Experimental Mechanics*, **55**, 519–528 (2015).
<https://doi.org/10.1007/s11340-014-9967-y>
- [21] Matur M. S., Kori S. A., Rao R. M. V. G. K.: Comparative analysis of cutting effect on mechanical properties and microstructural behavior of glass epoxy composites. *AIP Conference Proceedings*, **2057**, 020061 (2019).
<https://doi.org/10.1063/1.5085632>
- [22] Ramulu M., Arola D.: Water jet and abrasive water jet cutting of unidirectional graphite/epoxy composite. *Composites*, **24**, 299–308 (1993).
[https://doi.org/10.1016/0010-4361\(93\)90040-f](https://doi.org/10.1016/0010-4361(93)90040-f)
- [23] Sheikh-Ahmad J. Y.: Nontraditional machining of FRPs. in ‘Machining of polymer composites’ (ed.: Sheikh-Ahmad J. Y.) Springer, Boston, 237–291 (2009).
https://doi.org/10.1007/978-0-387-68619-6_6
- [24] Meng H. C., Ludema K. C.: Wear models and predictive equations: Their form and content. *Wear*, **181**, 443–457 (1995).
[https://doi.org/10.1016/0043-1648\(95\)90158-2](https://doi.org/10.1016/0043-1648(95)90158-2)
- [25] Ranakoti L., Gangil B., Mishra S. K., Singh T., Sharma S., Ilyas R. A., El-Khatib S.: Critical review on polylactic acid: Properties, structure, processing, biocomposites, and nanocomposites. *Materials*, **15**, 4312 (2022).
<https://doi.org/10.3390/ma15124312>

- [26] Abidi A., Salem S. B., Bezazi A., Boumediri H.: A comparative study on the effect of milling and abrasive water jet cutting technologies on the tensile behavior of composite carbon/epoxy laminates. *Mechanics of Composite Materials*, **57**, 539–550 (2021).
<https://doi.org/10.1007/s11029-021-09978-7>
- [27] Sjögren A., Krasnikovs A., Varna J.: Experimental determination of elastic properties of impact damage in carbon fibre/epoxy laminates. *Composites Part A: Applied Science and Manufacturing*, **32**, 1237–1242 (2001).
[https://doi.org/10.1016/s1359-835x\(01\)00058-6](https://doi.org/10.1016/s1359-835x(01)00058-6)
- [28] Meng K. P., Chai C. G., Sun Y. L., Wang W., Wang Q. Y., Li Q. M.: Cutting-induced end surface effect on compressive behaviour of aluminium foams. *European Journal of Mechanics - A/Solids*, **75**, 410–418 (2019).
<https://doi.org/10.1016/j.euromechsol.2019.02.015>
- [29] Cooper R. C., Bruno G., Onel Y., Lange A., Watkins T. R., Shyam A.: Young's modulus and Poisson's ratio changes due to machining in porous microcracked cordierite. *Journal of Materials Science*, **51**, 9749–9760 (2016).
<https://doi.org/10.1007/s10853-016-0209-9>
- [30] Dharan C. K. H.: Fracture mechanics of composite materials. *Journal of Engineering Materials and Technology*, **100**, 233–247 (1978).
<https://doi.org/10.1115/1.3443485>
- [31] Patel H. V., Dave H. K.: Effect of fiber orientation on tensile strength of thin composites. *Materials Today: Proceedings*, **46**, 8634–8638 (2021).
<https://doi.org/10.1016/j.matpr.2021.03.598>
- [32] Cordin M., Bechtold T., Pham T.: Effect of fibre orientation on the mechanical properties of polypropylene–lyocell composites. *Cellulose*, **25**, 7197–7210 (2018).
<https://doi.org/10.1007/s10570-018-2079-6>
- [33] Virk A. S., Hall W., Summerscales J.: Modulus and strength prediction for natural fibre composites. *Materials Science and Technology*, **28**, 864–871 (2013).
<https://doi.org/10.1179/1743284712y.0000000022>
- [34] Cullen R. K., Singh M. M., Summerscales J.: Characterisation of natural fibre reinforcements and composites. *Journal of Composites*, **2013**, 416501 (2013).
<https://doi.org/10.1155/2013/416501>

Research article

Increased processing temperature assisted reactive toughening of poly(lactic acid)

Nóra Lukács¹, Kata Enikő Decsov¹, Béla Molnár², Ferenc Ronkay^{2,3},
Katalin Bordácsné Bocz¹

¹Department of Organic Chemistry and Technology, Faculty of Chemical Technology and Biotechnology, Budapest University of Technology and Economics, Műegyetem rkp. 3., H-1111 Budapest, Hungary

²Imsys Ltd, Material Testing Laboratory, Mozaik utca 14/A., H-1033 Budapest, Hungary

³Department of Polymer Engineering, Faculty of Mechanical Engineering, Budapest University of Technology and Economics, Műegyetem rkp. 3., H-1111 Budapest, Hungary

Received 4 July 2022; accepted in revised form 29 August 2022

Abstract. Toughening efficiency of poly(ethylene-*n*-butylene-acrylate-*co*-glycidyl methacrylate) (EBA-GMA) in poly(lactic acid) (PLA) matrix has been found to significantly increase at elevated blending temperature. In the case of PLA/EBA-GMA blends having 10.0 or 12.5 wt% EBA-GMA contents, the accelerated PLA degradation at raised processing temperature resulted in reduced mechanical performance. At 15.0 wt% EBA-GMA ratio, however, increased elongation and by 250% improved notched Izod impact strength was achieved when the blending temperature was raised from 240 to 260 °C. This beneficial effect is attributed to the accelerated compatibilization reactions between the components in the presence of short-chain PLA molecules, which allow the rapid formation of a toughening enhancer interphase (TEI) during melt processing. As a result, the brittle-ductile transition can be reached at lower elastomer content than expected. Decreased melt flow index (MFI) values besides stabilized blend morphology indicated efficient PLA–EBA-GMA compatibilization at elevated processing temperature. Accordingly, enhanced nucleation ability of the PLA/EBA-GMA interphase and hindered chain crystallization of PLA were found by differential scanning calorimetry (DSC) analyses. In association with the intensified compatibilization reactions cross-linking of the terpolymer was also revealed using the thermally stimulated depolarization current (TSDC) technique.

Keywords: biopolymers, biocomposites, processing technologies, mechanical properties, thermal properties

1. Introduction

Nowadays, there is a shift in the focus toward developing and applying environmentally friendly polymers. Commonly used non-biodegradable plastics, accumulating in massive landfills, are dangerous for human health and cause depletion in soil fertility [1]. The aim is to produce materials that, when released into the environment, naturally degrade into non-toxic substances. Among the few commercially available biobased thermoplastic polymers, poly(lactic acid) (PLA) has undergone the most investigation [2]. PLA is a biodegradable aliphatic thermoplastic

polyester derived from renewable sources. It has many excellent mechanical properties (such as strength and stiffness), making it suitable for industrial applications [3].

In comparison with similar biopolymers, such as polyhydroxyalkanoates (PHAs), poly(ethylene glycol) (PEG), and poly(caprolactone) (PCL), PLA has better thermal processibility [4]. On the other hand, PLA's poor toughness significantly hinders its application in many fields [2]. Although the tensile strength and Young's modulus of PLA are comparable with those of polystyrene (PS) and poly(ethylene

*Corresponding author, e-mail: boczkatalin@gmail.com

© BME-PT

terephthalate) (PET), due to its brittleness, PLA has limitations in electric, electronic, and other industrial applications [4–6]. In order to widen the application possibilities of PLA, its toughness needs to be improved, which can be achieved by modifications. Various toughening strategies have been used to overcome this drawback [7], such as copolymerization [8], plasticization [9], the addition of organic/inorganic fillers [10], and melt blending [11, 12].

Melt blending with flexible polymers is one of the most industrially feasible and economic solutions for improving the impact resistance of an inherently rigid polymer [6]. The elastomer blended with the brittle polymer effectively dissipates the stress so that the material shows ductility and plastic deformation. The disadvantage of this toughening method is that the dispersed particles often have poor compatibility with the matrix and are prone to aggregate, resulting in insufficient dispersion. The interfacial tension can be reduced by improving the compatibility between the components, which allows for better mechanical properties [6, 13]. In contrast, the dispersion can be improved by changing the proportions of the compounds, their viscosity ratios, or the production parameters, for example, blending temperature or shear rate.

Since PLA has poor miscibility with the majority of polymer modifiers, to increase miscibility and interfacial adhesion, reactive blending has been demonstrated to be an effective and convenient way to achieve high-impact-resistant PLA materials [14]. The most frequently used modifiers are functionalized copolymers. Glycidyl methacrylate-containing elastomers may be suitable for this purpose, as their functional groups allow reactive compatibilization [15]. It is generally accepted that the carboxyl and/or hydroxyl group of PLA reacts with the epoxide group of the reactive elastomer [16, 17]. Nevertheless, it has to be noted that while the reactive interfacial compatibilization between PLA and the other (mostly petroleum-based) rubbery polymer generally largely improves the toughening efficiency, it sacrifices the biodegradability of PLA adversely [18].

Oyama [19] used poly(ethylene-glycidyl methacrylate) (EGMA) for reactive blending with PLA, while the effects of crystallinity and annealing treatment on the properties of the compound were investigated. Using differential scanning calorimeter (DSC) measurements, they found that the crystallinity of

PLA/EGMA (80/20) blends increased from 6 to 40% after annealing the blend at 90 °C for 2.5 hours. Also, the impact strength increased by approximately 50 times, in which a remarkable role was attributed to crystallinity.

The blending temperature also has a significant effect on the efficiency of the toughening mechanism. Increasing the temperature can promote compatibility and the possibility of elastomer cross-linking, while at lower processing temperatures, the number of PLA-elastomer compatibilization bonds tends to be much lower [20]. Yuryev *et al.* [3] applied poly(ethylene-*n*-butylene-acrylate-*co*-glycidyl methacrylate) (EBA-GMA) as a reactive compatibilizer for PLA. They used elevated temperatures (up to 270 °C), which are not typical for PLA, to show the effects on bonding and interfacial adhesion. To reduce the role of degradation, they used chain extenders (CEs) in blends that created bonds between PLA chains. They found that with the help of the CE, degradation was not as significant as before; moreover, the interfacial compatibilization has improved.

Liu *et al.* [21] investigated the effect of zinc ionomer of ethylene/methacrylic acid copolymer (EMAA-Zn) in PLA/EBA-GMA/EMAA-Zn blends manufactured at different blending temperatures ranging between 185 and 240 °C. In order to show the effect of the functional group of EBA-GMA, in one case, they replaced it with poly(ethylene-butylene-acrylate) (EBA). The impact strength and tensile strength significantly decreased in this case. Rheological studies showed that the addition of EMMA-Zn catalyst promoted the cross-linking reactions of the elastomer and helped the interfacial compatibilization as well. The greater the mixing temperature was, the more noticeable the toughening effect was.

In the present investigation, our aim was to show that EBA-GMA can be used as a reactive toughening agent for PLA and that the effectiveness of the reactive compatibilization can be noticeably improved by using optimized processing conditions. The elevated melt blending temperature (*i.e.*, higher than 200 °C, commonly used in the case of PLA) is expected to promote the reactive compatibilization, and elastomer cross-linking but accelerate the PLA degradation during processing at the same time [22]. Therefore, in this study, the effect of blending temperature and composition was optimized in terms of the mechanical properties of the PLA/EBA-GMA

blends, while corresponding changes in the crystalline structure, phase morphology, and rheology were explored.

2. Experimental

2.1. Materials

In this work, Ingeo™ Biopolymer 3100HP PLA (NatureWorks LLC Minnetonka, MN, USA), with a D-lactide content of 0.5%, glass transition temperature (T_g) in the range of 55–60 °C, and melting temperature (T_m) in the range of 170–190 °C, was used. The melt flow index of this PLA grade is in the range of 22–24 g/10 min (at 210 °C, with a 2.16 kg load). As an impact modifier, EBA-GMA was used. For that, Elvaloy PTW was provided by DuPont Co. (Wilmington, USA) with 28% acrylate monomer content.

Sample preparation

Compounding was performed using an LTE 26-44 (Labtech Scientific, Muang, Samutprakarn, Thailand) type twin-screw extruder. Before processing, the PLA materials were dried at 80 °C for 12 hours. Extrusions were performed by setting three different end zone temperatures; 220, 240, and 260 °C, respectively (Table 1). It has to be noted that since no CE was used in the blends, a significant drop in the processibility occurred at blending temperatures exceeding 260 °C due to a drastic decrease in melt viscosity and noticeable degradation of PLA. The screw speed was 60 rpm in all cases. After being pelletized and dried at 80 °C for 12 hours, all pellets were injection molded into a dumbbell shape at 200 °C, while the mold temperature was 40 °C. The holding pressure was 60 MPa, and the back pressure was 3 MPa.

2.2. Methods

Izod impact test

Izod impact tests were performed using a 5113.100/01 type (Zwick, Ulm, Germany) impact tester, with an

Izod impact hammer of 2.75 J at room temperature, according to ISO 180 standard. Ten notched (Type A) specimens were tested in each case.

Tensile test

Tensile tests were carried out by L3369 (Instron, Norwood MA, USA) universal mechanical tester according to ISO 527-2 standard. A crosshead speed of 1 mm/min was used to determine modulus; 20 mm/min was applied for tensile tests. For each investigation, 5 specimens were tested at room temperature.

Torque rheology

Torque measurements during melt mixing were performed in a Brabender Plasti-Corder Lab-Station type (Brabender GmbH & Co. KG, Duisburg, Germany) internal mixer equipped with a W 50 EHT 3Z kneading chamber. In one case, a given amount of pre-dried PLA pellets had been weighted according to the compositions and then added into the 50 cm³ mixing chamber and mixed at 260 °C with rotors rotating at 50 rpm for 4 min. At this time point, the required amount of EBA-GMA pellets (PLA and EBA-GMA together added up to 60 g in each case) were added and mixed for an additional 2 min. In the other case, equally 51 g of pre-dried PLA pellets had added in the mixing chamber set to 220, 240, or 260 °C, respectively, and mixed at 50 rpm for 4 min. At this time point, equally 9 g of EBA-GMA pellets were added and mixed for an additional 2 min. The variation of torque moment during melt mixing was continuously recorded.

Melt flow index (MFI)

Melt flow rate measurements were conducted by LMI-5000 (Dynisco, Franklin MA, USA) tester. Before the investigation, PLA pellets were dried at 80 °C for 2 hours. The applied temperature was 190 °C, the applied mass was 2.16 kg, and the cutting time was 10 s.

Scanning electron microscopy (SEM)

The morphology of PLA/EBA GMA blends was observed by EVO MA10 (Zeiss, Oberkochen, Germany) scanning electron microscope. Samples were embedded in epoxy resin, then the rubber phase of the samples was selectively extracted with toluene (1 hour immersion at room temperature). The applied gold

Table 1. Zone temperatures during extrusion.

	Zone temperatures during extrusion [°C]				Die
	1–3. zone	4–6. zone	7–9. zone	10–11. zone	
220 °C end zone	205	210	215	220	220
240 °C end zone	225	230	235	240	240
260 °C end zone	245	250	255	260	260

coating was 5 nm, and the accelerating voltage was 15.75 kV.

Differential scanning calorimetry (DSC)

Investigations of the crystalline phase were carried out by DSC131 EVO (Setaram, Lyon, France) DSC. Heat-cool-heat cycle was applied at heating and cooling rates of 10 °C/min under a nitrogen atmosphere, in the temperature range of 30–200 °C. 5–8 mg samples were taken from the same part of the injection-molded specimens each time. The crystallinity of PLA was calculated from the first heating scan with the help of Equation (1):

$$X_c [\%] = \frac{\Delta H_m - \Delta H_{cc}}{\Delta H_f \cdot (1 - \alpha)} \quad (1)$$

where ΔH_m [J/g] is the enthalpy of melting, ΔH_{cc} [J/g] is the enthalpy of cold crystallization, ΔH_f [J/g] is the enthalpy of 100% crystalline PLA, and α [–] is the ratio of the EBA-GMA additive.

Thermally stimulated depolarization current (TSDC)

The glass transition temperature of EBA-GMA was determined by TSC II (Setaram, Lyon, France) equipment using the thermally stimulated depolarization current (TSDC) technique. This method allows the temperature-dependent characteristics of the polymers, namely their phase transitions and molecular mobility, to be studied with high sensitivity. Therefore, it is also suitable for examining small relaxations in multi-component systems [23, 24].

0.5 mm thick specimens were analyzed, obtained from the center of the neck area of the 4 mm thick injection molded dumbbell-shaped samples. The two 1.75 mm thick edge layers were removed using an LS Twin (Remet, Italy) polisher.

During all measurements, the sample was polarised at 0 °C (T_p) with 300 V (U_p) polarisation voltage for 5 minutes (t_p). Then a cooling step followed with a 10 °C/min (r_c) cooling rate to the -80 °C freezing temperature (T_0) while the electric field was still present. The holding time at T_0 was 1 minute (t_0), and the polarisation was turned off in this step. In the next step, a 5 °C/min heating rate was used to reach the final temperature ($T_f = 0$ °C), while the depolarisation current was recorded as a function of the temperature.

3. Results and discussion

3.1. Effects of blending temperature and EBA-GMA content on the toughening of PLA

In general, higher loadings of 20–25 wt% of EBA-GMA type reactive terpolymer are necessitated to reach the brittle-ductile transition in polyesters [25–29]. Yuryev *et al.* [3] demonstrated a distinct temperature dependence in the toughness of PLA/EBA-GMA blends having over 20 wt% EBA-GMA content and containing CE as well. In this work, the experiments were designed with the aim to analyse the hypothesis that low-molecular-weight PLA chains, forming *in situ* during high-temperature processing, may enhance the rate of compatibilization reactions on the PLA/EBA-GMA interface and, consequently, the brittle-ductile transition may be reached at lowered terpolymer content. Therefore, two-component blends were prepared from PLA and EBA-GMA, and without using CE, with the blending ratio of the elastomer ranging from 10.0 to 15.0 wt% with 2.5 wt% ranging steps. The PLA/EBA-GMA blends were extrusion processed at 220, 240, and 260 °C, respectively, and then comprehensively analyzed.

Figure 1 illustrates the result of Izod impact tests performed on notched injection-molded specimens. The notched Izod impact strength of neat PLA was measured to be 3.4±0.2 kJ/m². It can be seen that the elevated blending temperature was not effective at lower EBA GMA contents; however, at a 15.0 wt% EBA-GMA ratio significant increase in the impact strength can be observed for the blend prepared at

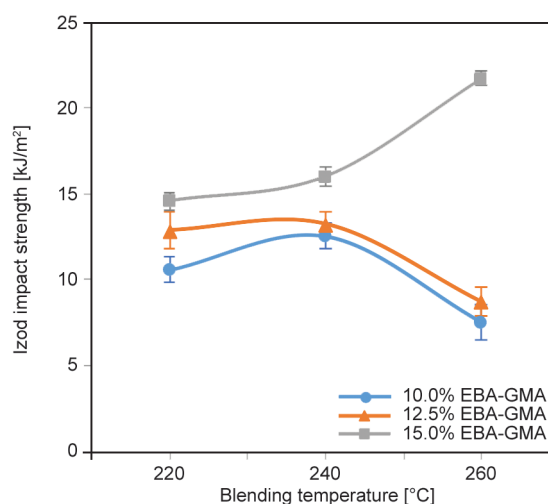


Figure 1. Notched Izod impact strength of the PLA/EBA-GMA blends.

260 °C. Despite the identical elastomer content of 15.0 wt%, at elevated blending temperature, 30% higher impact strength was achieved compared to the blends prepared at 240 °C or lower. It is claimed that the high processing temperature of 260 °C accelerates the degradation of PLA, but also the compatibilization reactions between PLA and the epoxy functionalized elastomer [3]. Since no CE was used in the blends that could compensate for the molecular weight decrease, the harmful effect of thermal degradation of PLA is clearly manifested by the noticeable (about 35–40%) decrease of the impact resistance of the blends with 10.0 and 12.5 wt% EBA-GMA contents. At 15.0 wt% of EBA-GMA, however, the degree of PLA/EBA-GMA interface bonding increases, so it can compensate for thermal degradation effects. Nevertheless, it is proposed that the compatibilization reactions are increasingly facilitated in the presence of the short-chain PLA molecules formed *in situ* during processing at 260 °C. As a result, the brittle-ductile transition is reached at lower (15.0 wt%) EBA-GMA content than expected based on previous research studies [19, 25]. This conclusion is analogous to our earlier findings, where the low-molecular-weight PET fractions, whether from waste [25] or formed *in situ* during melt processing [29], were successfully utilized to enhance the efficiency of the reactive impact modifier in PET/EBA-GMA blends. Tensile tests were performed to examine the quasi-static mechanical properties of the PLA/EBA GMA blends prepared at different processing temperatures. As a reference, tensile strength, Young's modulus, and elongation at break values for neat PLA were measured to be 61.9±1.3 MPa, 3262±70 MPa and 3.1±0.4%, respectively. Figure 2 shows the testing results obtained for the blends. The tensile strength of the blends containing 10.0 wt% EBA-GMA remained unchanged as extrusion temperature increased, while at higher EBA-GMA contents, a slightly decreasing trend can be observed (Figure 2a). Tensile modulus values changed similarly to the tensile strength; however, at 10.0 wt% EBA-GMA ratio, the stiffness of the blends even slightly increased with increasing blending temperature (Figure 2b). This may be attributed to the increasing crystalline ratio of PLA in the blends due to the easier arranging of shorter molecular chains, which are likely formed at increased processing temperatures. The observed decrease in strength and modulus at 12.5 and 15.0 wt% EBA-GMA as a function of

increasing blending temperature is likely associated with the reduction in PLA molecular weight that obviously occurs at elevated processing temperatures. (Unfortunately, the determination of the molecular weight of PLA in the blends is rather difficult due to the EBA-GMA yielding insoluble fractions.) But as the effect of thermal degradation is less pronounced at lower (10.0 wt%) EBA-GMA content, it suggests that the decrease in molecular weight is not detrimental even at 260 °C. It is assumed that viscosity may also be an important factor in the mechanical performance of the blends. Namely, under the same processing conditions, at a lower EBA-GMA ratio, droplets of smaller size are formed, and thus finer dispersion can be achieved. The mechanical performance of such a fine dispersion is less sensitive to the smaller defects of the matrix material. Nevertheless, it is claimed that the changes in the tensile strength and moduli are not significant in the examined temperature range.

Since elongation at break is more sensitive to morphology and interfacial bonding, this parameter showed noticeable changes both with composition and blending temperature (Figure 2c). The elongation of the blends with EBA-GMA ratios of 12.5 and 10.0 wt% showed decreasing tendency with increasing processing temperature, likely due to increasingly intense degradation of PLA and insufficient interfacial bonding. However, the blends containing 15.0 wt% EBA-GMA showed increasing elongation as a function of increasing blending temperature, indicating a significant degree of chemical bonding between the PLA matrix and the toughening phase. Toughness and elongation of the blends followed similar tendencies, and the blend with 15.0 wt% EBA-GMA and prepared at 260 °C showed the best performance in both respects. These results further reinforce the assumption that the presence of highly reactive short-chain fractions, formed during processing at high temperature, boosts the reactive toughening of PLA by forming a toughening enhancer interphase (TEI) [25]. In former research studies, catalysts were added with the aim of lowering the activation energy of reactive compatibilization on the PLA/EBA-GMA interface [21, 30]. Our results suggest that the low-molecular-weight PLA chains, being present in the blends that are produced at higher temperatures, due to their increased mobility and higher number of functional end groups, can also enhance the rate of compatibilization reactions on the

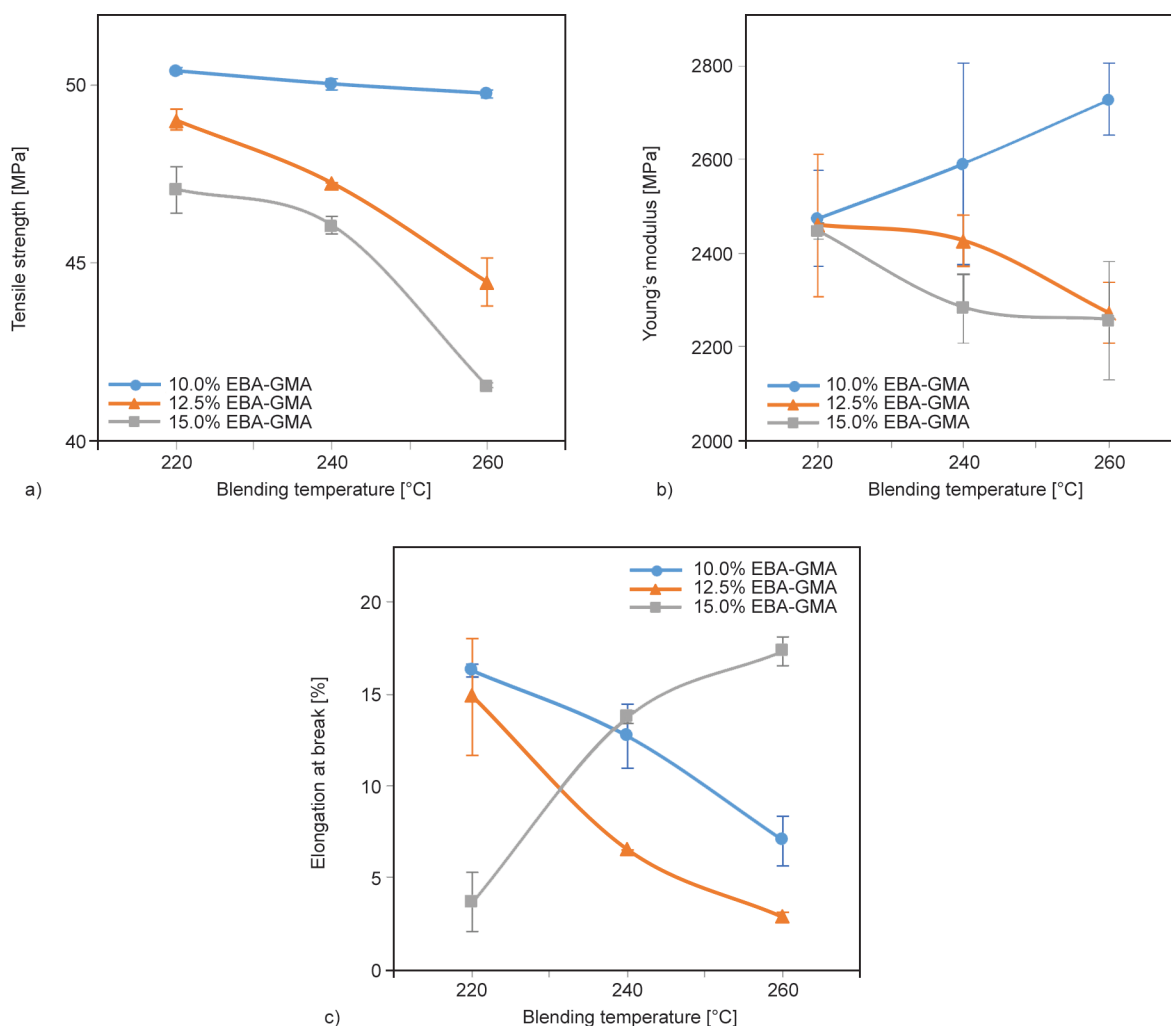


Figure 2. a) Tensile strength, b) tensile modulus, and c) elongation at break of the PLA/EBA-GMA blends.

PLA/EBA-GMA interface. Consequently, noticeable improvement in toughness can be achieved at a reduced terpolymer ratio by optimizing (increasing) the blending temperature.

3.2. Rheology of the PLA/EBA-GMA blends

In order to detect the chemical reactions, including degradation and cross-linking, during melt-processing, torque values were recorded during melt-mixing of the blend components. The torque change was continuously recorded as a function of mixing time during melt-mixing of PLA either with an increasing amount of EBA-GMA (Figure 3a) or with identical 15.0 wt% EBA-GMA content but by applying increasing mixing temperature (Figure 3b). As can be seen in Figure 3a, both the peak of the torque response after EBA-GMA addition and the equilibrium torque value at 6 min increase when the EBA-GMA proportion is increased. These results indicate

increasing viscosity of the PLA blends with increasing EBA-GMA content, likely due to the increasing occurrence of compatibilization reactions taking place between the components. As can be seen in Figure 3b, the viscosity-related equilibrium torque values, recorded either after complete melting of the PLA pellets or after blend formation with EBA-GMA, are highly dependent on the processing temperature. Based on the torque curves recorded during melt-mixing, the relative change in the equilibrium torque value, which occurred as a result of 15 wt% EBA-GMA addition, can be evaluated at each applied processing temperature. In Figure 4, the thus determined relative torque difference (as a percentage) is presented for each examined PLA/EBA-GMA blend. The relative torque difference was found to increase with EBA-GMA content and processing temperature as well. Accordingly, both factors are supposed to increase the occurrence of compatibilization reactions.

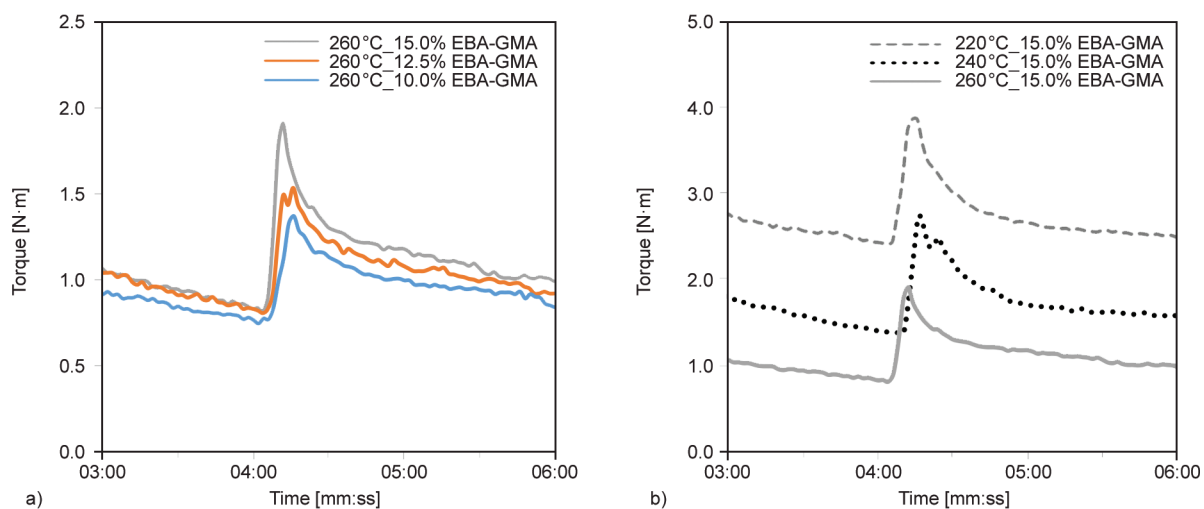


Figure 3. The torque responses as a function of mixing time during melt-mixing with a) increasing amount of EBA-GMA (at 260 °C); b) increasing mixing temperature (at 15.0 wt% EBA-GMA content).

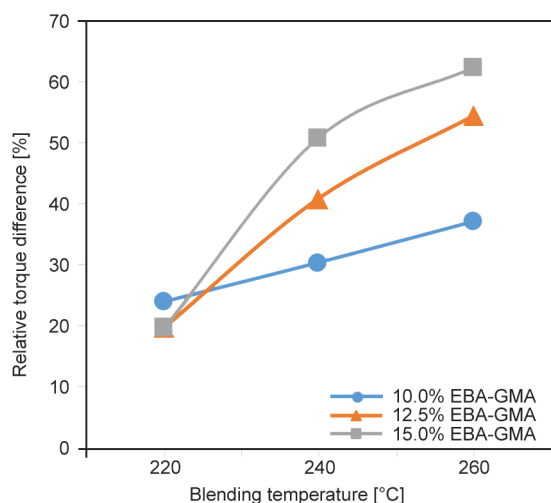


Figure 4. Relative torque difference determined for the PLA/EBA-GMA blends.

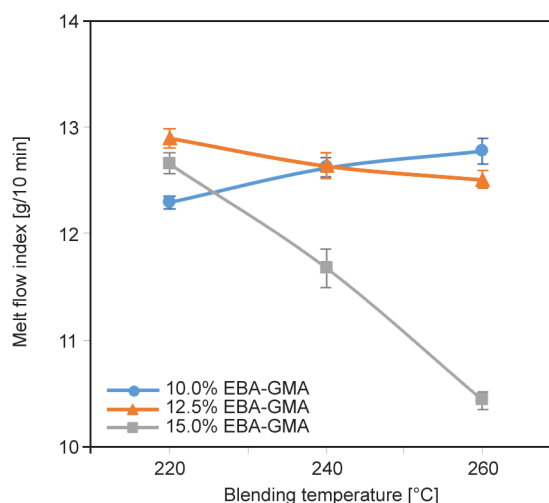


Figure 5. Melt flow index of the PLA/EBA-GMA blends (190 °C, 2.16 kg).

3.3. MFI of the PLA/EBA-GMA blends

With the help of the melt flow index measurements, the rate of degradation during production and the reactions between the components can be indirectly deduced. Figure 5 shows the MFI values of the PLA blends differing in EBA-GMA contents and processing temperatures. The MFI values were determined at 190 °C in all cases, so it is proposed that the viscosity did not change noticeably during measurement, but it is mainly determined by the structure formed during extrusion processing. At 190 °C, closely identical MFI values of 12.8 ± 0.4 g/10 min and 12.7 ± 0.5 g/10 min were measured for the EBA-GMA additive and the additive-free PLA (after extrusion processing), respectively. It can be seen in Figure 5 that the MFI values measured for the PLA/EBA-GMA blends, after extrusion processing at 220 °C,

vary in the same MFI range of 12–13 g/10 min as those of the starting components, indicating a minimal rate of chemical reactions taking place between the components at this relative low processing temperature. The slight increase in the melt flow rate of the 10.0 wt% EBA-GMA-containing blends as a function of raising blending temperature is associated with accelerated PLA degradation and indicates an insufficient rate of PLA/EBA-GMA compatibilization. At higher EBA-GMA content of 12.5 wt%, however, a decreasing melt flowability can be observed with elevating blending temperatures suggesting increasingly effective compatibilization reactions between the components, which compensate for the decrease in melt viscosity due to thermal degradation. At an even higher EBA-GMA ratio of 15.0 wt%, the increased degree of reactive compatibilization

exceeds the level of thermal degradation effects and results in appreciable reductions in melt flow rates. The noticeably increased resistance to flow when the melt is processed at an elevated blending temperature of 260 °C supports the assumption that reactions between the components occur that seem more determinative with the increase of blending temperature. It can also be concluded that a sufficient amount of epoxy functionalized elastomer is needed to achieve considerable structural change in the system and thus reach the brittle-ductile transition zone.

3.4. Phase morphology of the EBA-GMA blends

The morphology of the blends was investigated by scanning electron microscopy (SEM). Figure 6 shows the SEM micrographs of PLA/EBA-GMA blends taken after the selective dissolution of the EBA-GMA phase. With the increasing amount of EBA-GMA, the size of the dispersed particles increases at each set temperature. When considering the effect of the processing temperature at a given EBA-GMA ratio, the particle size of the elastomer

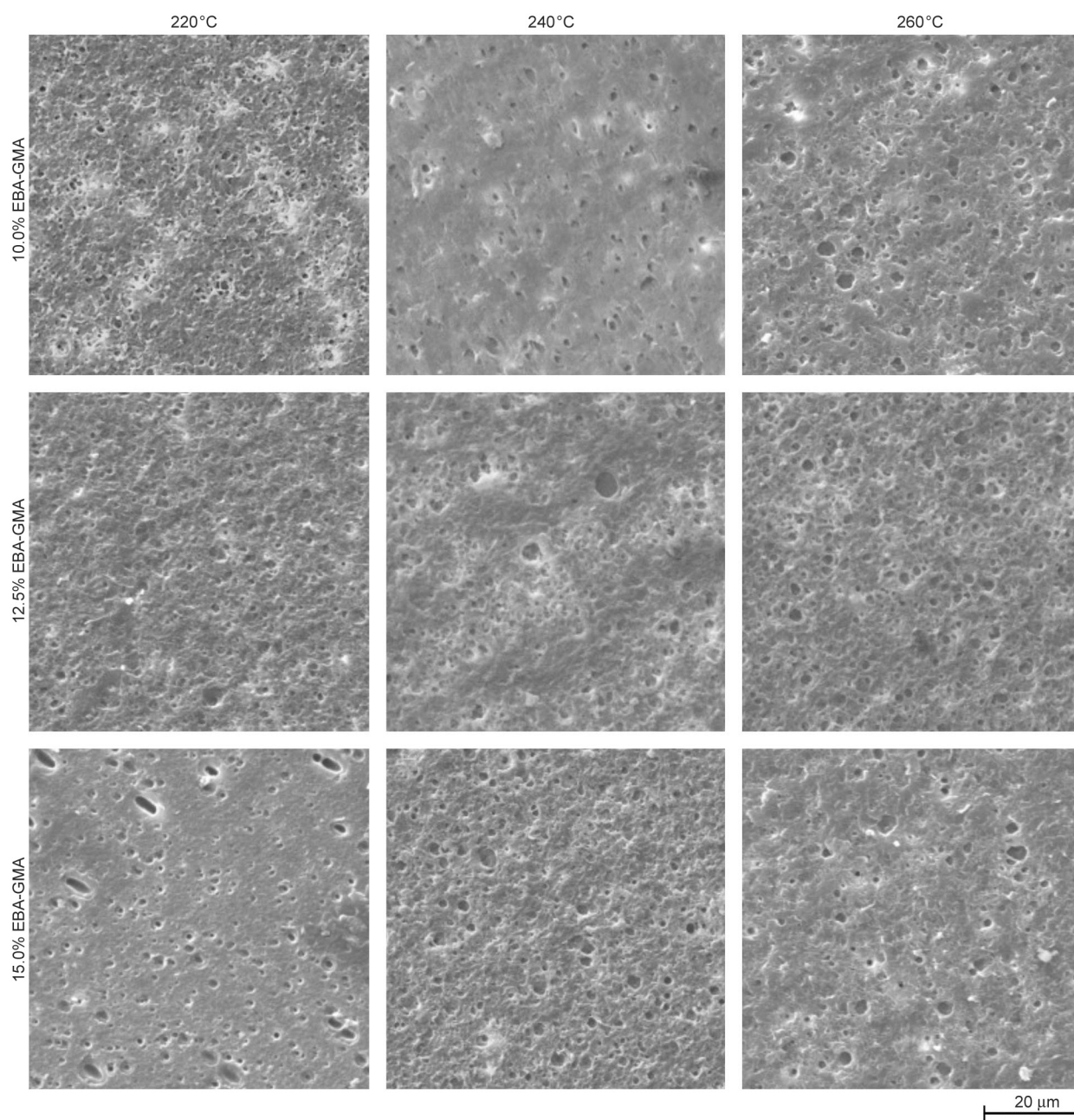


Figure 6. SEM micrographs of PLA/EBA-GMA blends after selective extraction of the terpolymer.

droplets does not show any definite trend. Generally, the smaller droplet size results in greater interfacial boundary, favoring compatibilization. Superior impact resistance was observed for the blend with 15.0 wt% of EBA-GMA when prepared at 260 °C; which blend, however, does not show a distinct morphology. It was therefore concluded that the increased impact strength could not be explained only by morphological effects (*i.e.*, size and dispersion of the droplets), but it must depend on the nature of the interactive phases and their interfacial interaction.

3.5. Crystalline structure and crystallization of the PLA matrix

The thermal characteristics and crystalline structure of PLA in the blends were investigated by DSC measurements. The obtained DSC thermograms are presented in Figure 7, while corresponding thermal characteristics are shown in Table 2. It can be seen in Table 2 that the glass transition temperature (T_{g1}) and melting temperature (T_{m1}) do not show any definite trend with the change of blending temperature or composition; they range between 60.9–63.4 and 175.8–176.8 °C, respectively. Based on the crystallinity (X_{c1}) of the PLA/EBA-GMA blends, as determined from the first heating scan, it was concluded that, in the examined range, the blending temperature does not significantly affect the crystallinity of the injection molded products; similarly to the findings of Liu *et al.* [20]. In contrast with the conclusions of Oyama, here, the difference in crystallinity phase structure does not have a clear relation with impact strength [19].

In order to examine the crystallization behavior of PLA in the blends, relative crystallinity (X_{c2}) was determined from the second heating cycle (*i.e.*, crystals formed from the cooling cycle were examined). It can be seen in Figure 8 that the relative crystallinity

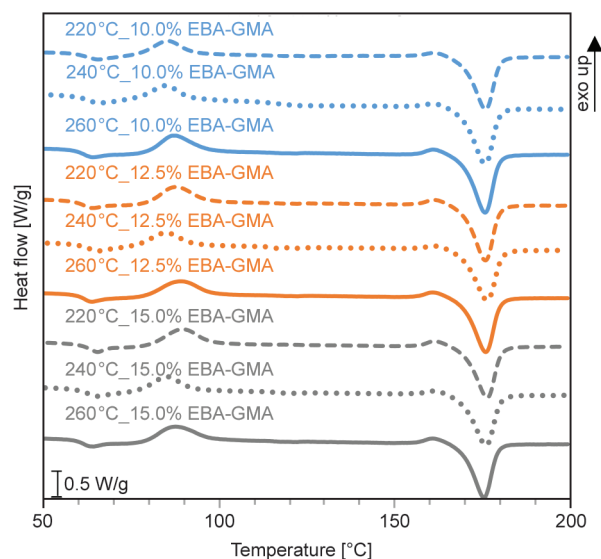


Figure 7. DSC curves of the PLA/EBA-GMA blends.

(X_{c2}) shows a maximum curve as a function of increasing blending temperature suggesting two opposing effects that affect the crystallization of PLA. The increase in the crystalline ratio when the processing temperature is increased from 220 to 240 °C is associated with the decreasing molecular weight of PLA due to accelerated degradation. Further increase in the blending temperature to 260 °C leads, however, to noticeably lower crystallinity. At this elevated temperature, crystallization of PLA chains is assumed to be restricted by the facilitated compatibilization reactions between the carboxyl or hydroxyl end groups of the PLA chains and the epoxy groups of EBA-GMA.

The trends observed in the cold crystallization temperatures (T_{cc1}) (derived from the first heating cycle) and in the temperatures of crystallization (T_c) during cooling also support this theory. It can be seen in Table 2 that at 15.0 wt% EBA-GMA content and an elevated processing temperature of 240 °C, the T_{cc1} of the blends shifts to a lower temperature while the

Table 2. Results of DSC analyses.

Blending temperature [°C]	EBA-GMA content [wt%]	T_{g1} [°C]	T_{m1} [°C]	T_{cc1} [°C]	X_{c1} [%]	T_c [°C]
220	10.0	61.0±0.8	175.8±0.1	87.1±2.2	34.4±1.1	93.9±0.3
	12.5	62.1±1.3	176.1±0.3	87.5±0.7	28.2±3.1	93.0±0.1
	15.0	61.8±1.0	176.8±0.5	88.8±0.9	25.2±0.8	93.3±0.2
240	10.0	61.3±0.6	175.8±0.2	85.9±1.3	36.2±3.0	94.4±0.5
	12.5	61.2±0.5	176.5±0.6	86.5±0.7	27.1±1.2	93.3±0.4
	15.0	63.4±0.2	175.8±0.3	85.2±0.3	35.4±3.4	95.0±0.1
260	10.0	61.7±0.2	175.8±0.2	87.3±0.9	28.3±0.8	93.3±0.2
	12.5	62.3±0.9	176.3±0.4	87.7±2.2	25.9±2.2	93.3±0.7
	15.0	60.9±0.8	176.1±0.9	87.2±0.6	26.6±1.2	93.2±0.2

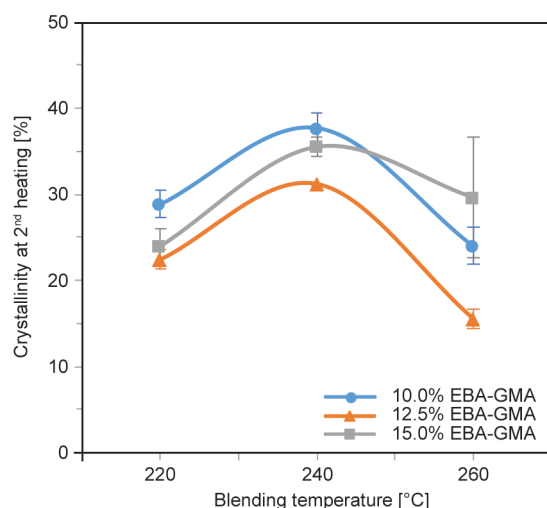


Figure 8. Relative crystallinity (X_{c2}) of the PLA/EBA-GMA blends derived from DSC second heating curves.

T_c shifts to a higher temperature, both indicating increased nucleation efficiency of the PLA/EBA-GMA interphase [3, 31]. At a higher processing temperature of 260 °C, however, T_{cc1} and T_c fall back to similar values as measured for the blends processed at 220 °C. It is proposed that even though the short polymer chains can form crystals more readily than long chains, due to the intensified PLA–EBA–GMA compatibilization reactions at 260 °C, the motion of these shorter PET chains becomes increasingly restricted, accompanied by increasing T_{cc1} and decreasing T_c values [3, 31].

The DSC results further reinforce the assumption that the outstanding impact strength of the 15.0 wt% EBA-GMA containing blend, when processed at 260 °C, is mainly related to the intensified PLA–EBA–GMA compatibilization reactions that allow excellent toughening efficiency.

3.6. Structure of the EBA-GMA phase

Compatibilization reactions are almost always associated with cross-linking of the terpolymer, and in the case of cross-linking, an increase in the glass transition temperature (T_g) of the elastomer can be expected [25]. The thermally stimulated depolarization current (TSDC) method was used to determine the T_g of the EBA-GMA phase in the blends produced at different blending temperatures. The obtained results are shown in Figure 9. The T_g of the elastomer shows a minimum curve as a function of blending temperature, likely as a result of two effects. The changes in T_g are, on the one hand, related to the particle size of the dispersed phase; the finer

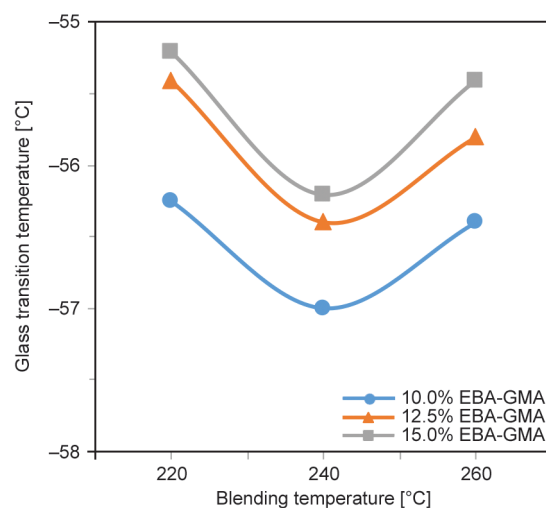


Figure 9. Glass transition temperature (T_g) of the EBA-GMA phase in the PLA/EBA-GMA blends derived from TSDC curves.

dispersion results in depression of the T_g [32]. On the other hand, the T_g of the elastomer increases with the degree of cross-linking.

It can be seen in Figure 9 that at a given blending temperature, the T_g increases with increasing EBA-GMA ratio parallel as the particle size increases, as also observed by SEM imaging (Figure 6). When the blending temperature was increased from 240 to 260 °C, the T_g increased at all EBA-GMA ratios, suggesting the formation of cross-links in all cases. The results of the TSDC study confirmed our hypothesis that increasing the compounding temperature improves interfacial compatibility and parallels the cross-linking of the elastomer. Consequently, a significant increase in impact strength can be achieved, but only when the interparticle distance can be reduced below the critical value. The latter can be reached by increasing the EBA-GMA content or by improving the dispersion of the elastomer phase.

4. Conclusions

Toughening of PLA by EBA-GMA was found to be increasingly efficient when the blends were processed at elevated temperatures. The notched Izod impact resistance and elongation at break of the PLA/EBA-GMA blend significantly improve, even though the harmful effects of accelerated thermal and hydrolytic degradation of PLA at elevated processing temperature have not been compensated by CE addition. On the contrary, it is proposed that the short-chain PLA molecules formed *in situ* during high-temperature thermomechanical processing play a key role in

enhanced toughening efficiency. Namely, low-molecular-weight PLA chains have a higher number of functional end groups and increased mobility which allows the rapid formation of toughening enhancer interphase between the PLA and the reactive elastomer, which provides a significant improvement in the impact strength. According to this theory, a similar beneficial effect on the toughening efficiency can be expected when the processing-induced PLA degradation is accelerated in the presence of humidity, *e.g.*, by omitting the drying step of PLA pellets before melt processing.

At EBA-GMA contents lower than 15.0 wt%, the intense PLA degradation during high-temperature blending resulted in reduced mechanical performance, *i.e.*, decreased impact strength, tensile strength and modulus. At 15.0 wt% EBA-GMA, however, the elongation at break increased, and the notched Izod impact resistance improved by approx. 250% only by applying a high blending temperature of 260 °C instead of 240 °C or below. Decreased flowability (MFI) of the melt accompanied by stabilized dispersed droplet size (as observed during SEM examination) indicated intensified compatibilization reactions between the components. Facilitated interphase nucleation accompanied by restricted crystallization ability (as obtained from DSC analyses) and increased degree of elastomer cross-linking (as found by TSDC measurements) provided further evidence for efficient reactive compatibilization on the PLA/EBA-GMA interphase. As a result, raising the blending temperature allows the production of high-impact-resistant ($a > 20 \text{ kJ/m}^2$) PLA blends at reduced (15.0 wt%) elastomer content, *i.e.*, at a lower cost. This recognition may contribute to the widening of the application fields of this biopolymer.

Acknowledgements

The project was funded by the National Research, Development and Innovation Fund of Hungary in the frame of the 2018-1.3.1-VKE-2018-00017, 2019-1.3.1-KK-2019-00004 and GINOP_PLUSZ-2.1.1-21-2022-00041 projects. The research was funded by the Hungarian Scientific Research Fund, grant number FK128352. The research reported in this paper and carried out at the Budapest University of Technology and Economics has been supported by the National Research Development and Innovation Fund (TKP2020 Institution Excellence Subprogram, Grant No. BME-IE-NAT) based on the charter of bolster issued by the National Research Development and Innovation Office under the auspices

of the Ministry for Innovation and Technology. K. Decsov was supported by the ÚNKP-21-3-II-BME-290 New National Excellence Program of the Ministry for Innovation and Technology from the source of the National Research, Development and Innovation Fund.

References

- [1] Geyer R., Jambeck J. R., Law K. L.: Production, use, and fate of all plastics ever made. *Science Advances*, **3**, e1700782 (2017).
<https://doi.org/10.1126/sciadv.1700782>
- [2] Liu H., Zhang J.: Research progress in toughening modification of poly(lactic acid). *Journal of Polymer Science Part B: Polymer Physics*, **49**, 1051–1083 (2011).
<https://doi.org/10.1002/polb.22283>
- [3] Yuryev Y., Mohanty A. K., Misra M.: A new approach to supertough poly(lactic acid): A high temperature reactive blending. *Macromolecular Materials and Engineering*, **301**, 1443–1453 (2016).
<https://doi.org/10.1002/mame.201600242>
- [4] Rasal R. M., Janorkar A. V., Hirt D. E.: Poly(lactic acid) modifications. *Progress in Polymer Science*, **35**, 338–356 (2010).
<https://doi.org/10.1016/j.progpolymsci.2009.12.003>
- [5] Kovačević Z., Bischof S., Vujasinović E., Fan M.: The potential of nanoclay modified *Spartium junceum L.* fibres used as reinforcement in PLA matrix composites for automotive applications. *International Journal of Nanotechnology*, **15**, 695–700 (2018).
<https://doi.org/10.1504/IJNT.2018.098436>
- [6] Zhao X., Hu H., Wang X., Yu X., Zhou W., Peng S.: Super tough poly(lactic acid) blends: A comprehensive review. *RSC Advances*, **10**, 13316–13368 (2020).
<https://doi.org/10.1039/D0RA01801E>
- [7] Tábi T., Ageyeva T., Kovács J. G.: Improving the ductility and heat deflection temperature of injection molded poly(lactic acid) products: A comprehensive review. *Polymer Testing*, **101**, 107282 (2021).
<https://doi.org/10.1016/j.polymertesting.2021.107282>
- [8] Grijpma D. W., Nijenhuis A. J., van Wijk P. G. T., Pennings A. J.: High impact strength as-polymerized PLLA. *Polymer Bulletin*, **29**, 571–578 (1992).
<https://doi.org/10.1007/BF00296720>
- [9] Tee Y. B., Talib R. A., Abdan K., Chin N. L., Basha R. K., Yunus K. F. M.: Toughening poly(lactic acid) and aiding the melt-compounding with bio-sourced plasticizers. *Agriculture and Agricultural Science Procedia*, **2**, 289–295 (2014).
<https://doi.org/10.1016/j.aaspro.2014.11.041>
- [10] Jiang L., Zhang J., Wolcott M. P.: Comparison of polylactide/nano-sized calcium carbonate and polylactide/montmorillonite composites: Reinforcing effects and toughening mechanisms. *Polymer*, **48**, 7632–7644 (2007).
<https://doi.org/10.1016/j.polymer.2007.11.001>

- [11] Bocz K., Domonkos M., Igricz T., Kmetty Á., Bárány T., Marosi G.: Flame retarded self-reinforced poly(lactic acid) composites of outstanding impact resistance. *Composites Part A: Applied Science and Manufacturing*, **70**, 27–34 (2015).
<https://doi.org/10.1016/j.compositesa.2014.12.005>
- [12] Baouz T., Rezgui F., Yilmazer U.: Ethylene-methyl acrylate-glycidyl methacrylate toughened poly(lactic acid) nanocomposites. *Journal of Applied Polymer Science*, **128**, 3193–3204 (2013).
<https://doi.org/10.1002/app.38529>
- [13] Kaynak C., Meyva Y.: Use of maleic anhydride compatibilization to improve toughness and other properties of polylactide blended with thermoplastic elastomers. *Polymers for Advanced Technologies*, **25**, 1622–1632 (2014).
<https://doi.org/10.1002/pat.3415>
- [14] Rasal R. M., Hirt D. E.: Toughness decrease of PLA-PHBHHx blend films upon surface-confined photopolymerization. *Journal of Biomedical Materials Research Part A*, **88**, 1079–1086 (2009).
<https://doi.org/10.1002/jbm.a.32009>
- [15] Andrzejewski J., Nowakowski M.: Development of toughened flax fiber reinforced composites. Modification of poly(lactic acid)/poly(butylene adipate-co-terephthalate) blends by reactive extrusion process. *Materials*, **14**, 1523 (2021).
<https://doi.org/10.3390/ma14061523>
- [16] Lee P.-C., Kuo W.-F., Chang F.-C.: *In situ* compatibilization of PBT/ABS blends through reactive copolymers. *Polymer*, **35**, 5641–5650 (1994).
[https://doi.org/10.1016/S0032-3861\(05\)80038-2](https://doi.org/10.1016/S0032-3861(05)80038-2)
- [17] Kim Y. F., Choi C. N., Kim Y. D., Lee K. Y., Lee M. S.: Compatibilization of immiscible poly(L-lactide) and low density polyethylene blends. *Fibers and Polymers*, **5**, 270–274 (2004).
<https://doi.org/10.1007/BF02875524>
- [18] Wu F., Misra M., Mohanty A. K.: Super toughened poly(lactic acid)-based ternary blends via enhancing interfacial compatibility. *ACS Omega*, **4**, 1955–1968 (2019).
<https://doi.org/10.1021/acsomega.8b02587>
- [19] Oyama H. T.: Super-tough poly(lactic acid) materials: Reactive blending with ethylene copolymer. *Polymer*, **50**, 747–751 (2009).
<https://doi.org/10.1016/j.polymer.2008.12.025>
- [20] Liu H., Chen F., Liu B., Estep G., Zhang J.: Super toughened poly(lactic acid) ternary blends by simultaneous dynamic vulcanization and interfacial compatibilization. *Macromolecules*, **43**, 6058–6066 (2010).
<https://doi.org/10.1021/ma101108g>
- [21] Liu H., Guo X., Song W., Zhang J.: Effects of metal ion type on ionomer-assisted reactive toughening of poly(lactic acid). *Industrial and Engineering Chemistry Research*, **52**, 4787–4793 (2013).
<https://doi.org/10.1021/ie303317k>
- [22] Jamshidi K., Hyon S.-H., Ikada Y.: Thermal characterization of polylactides. *Polymer*, **29**, 2229–2234 (1988).
[https://doi.org/10.1016/0032-3861\(88\)90116-4](https://doi.org/10.1016/0032-3861(88)90116-4)
- [23] Shmeis R. A., Wang Z., Krill S. L.: A mechanistic investigation of an amorphous pharmaceutical and its solid dispersions, Part I: A comparative analysis by thermally stimulated depolarization current and differential scanning calorimetry. *Pharmaceutical Research*, **21**, 2025–2030 (2004).
<https://doi.org/10.1023/B:PHAM.0000048193.94922.09>
- [24] Sedita J. S., O'Reilly J. M.: A thermally stimulated depolarization current study of polymers in the glass transition region. *Polymer Engineering and Science*, **41**, 15–22 (2001).
<https://doi.org/10.1002/pen.10704>
- [25] Bocz K., Ronkay F., Decsov K. E., Molnár B., Marosi G.: Application of low-grade recycle to enhance reactive toughening of poly(ethylene terephthalate). *Polymer Degradation and Stability*, **185**, 109505 (2021).
<https://doi.org/10.1016/j.polymdegradstab.2021.109505>
- [26] Loyens W., Groeninckx G.: Ultimate mechanical properties of rubber toughened semicrystalline PET at room temperature. *Polymer*, **43**, 5679–5691 (2002).
[https://doi.org/10.1016/S0032-3861\(02\)00472-X](https://doi.org/10.1016/S0032-3861(02)00472-X)
- [27] Loyens W., Groeninckx G.: Deformation mechanisms in rubber toughened semicrystalline polyethylene terephthalate. *Polymer*, **44**, 4929–4941 (2003).
[https://doi.org/10.1016/S0032-3861\(03\)00478-6](https://doi.org/10.1016/S0032-3861(03)00478-6)
- [28] Zong Y., Cheng Y., Dai G.: The relationship between rheological behavior and toughening mechanism of toughened poly(ethylene terephthalate). *Journal of Composite Materials*, **42**, 1571–1585 (2008).
<https://doi.org/10.1177/0021998308090829>
- [29] Ronkay F., Molnár B., Szabó E., Marosi G., Bocz K.: Water boosts reactive toughening of PET. *Polymer Degradation and Stability*, **203**, 110052 (2022).
<https://doi.org/10.1016/j.polymdegradstab.2022.110052>
- [30] Liu H., Song W., Chen F., Guo L., Zhang J.: Interaction of microstructure and interfacial adhesion on impact performance of polylactide (PLA) ternary blends. *Macromolecules*, **44**, 1513–1522 (2011).
<https://doi.org/10.1021/ma1026934>
- [31] Ojijo V., Ray S. S.: Super toughened biodegradable polylactide blends with non-linear copolymer interfacial architecture obtained *via facile in-situ* reactive compatibilization. *Polymer*, **80**, 1–17 (2015).
<https://doi.org/10.1016/j.polymer.2015.10.038>
- [32] Yousefi A. A.: Composition-dependent depression of the glass transition temperature of the rubber phase in a PE-SBR blend. *e-Polymers*, **15**, 393–399 (2015).
<https://doi.org/10.1515/epoly-2015-0063>

Research article

Influence of different vulcanizing agents on structures and properties of sepiolite-filled natural rubber composites

Nabil Hayeemasae^{1,2}, Siriwat Soontaranon³, Abdulhakim Masa^{2,4*}

¹Department of Rubber Technology and Polymer Science, Faculty of Science and Technology, Prince of Songkla University, Pattani Campus, 94000 Pattani, Thailand

²Research Unit of Advanced Elastomeric Materials and Innovations for BCG Economy (AEMI), Faculty of Science and Technology, Prince of Songkla University, Pattani Campus, 94000 Pattani, Thailand

³Synchrotron Light Research Institute, Muang District, 30000 Nakhon Ratchasima, Thailand

⁴Rubber Engineering & Technology Program, International College, Prince of Songkla University, Hat Yai, 90110 Songkhla, Thailand

Received 30 May 2022; accepted in revised form 10 September 2022

Abstract. This study aimed to explore the best cross-link agent for preparing natural rubber (NR) composites containing sepiolite as filler. Three types of vulcanizing agents, namely, sulfur, peroxide, and phenolic resin, were employed, and their effects on the thermomechanical and mechanical properties and microstructures were investigated. Compared to other vulcanizing agents, the greatest thermomechanical and mechanical properties improvement was achieved by using phenolic resin as a crosslinker. The highest tensile stress and tensile strength improvement were also achieved from the phenolic resin system. Tensile strength was improved by approximately 78%, nearly twice as much as that in the sulfur system. Such drastic improvement was attributed to the combined effect of homogeneity dispersion and strong adhesion between rubber and filler, as revealed by Fourier-transform infrared spectroscopy, facilitating the strain-induced crystallization process in NR. The phenolic resin was the best vulcanizing agent for preparing NR/sepiolite composites.

Keywords: polymer composites, rubber, vulcanizing agents, sepiolite filler

1. Introduction

Natural rubber (NR) is not used as an engineering product unless it is cross-linked and reinforced with fillers. Aside from achieving appropriate performance characteristics for end-use applications, incorporating a filler is a simple, effective, and generally inexpensive method for enhancing the properties of rubber products [1–4]. Various types of filler have been applied in rubber composites, with carbon black and silica being the most widely used fillers in the rubber industries [1, 2].

Recently, the use of sepiolite as filler in rubber composites has been the subject of research due to the unique structure of sepiolite, allowing for the

enhancement of mechanical, thermal, and barrier performance of composites [5–7]. Sepiolite, a naturally occurring material, is a hydrous magnesium silicate with the conceptual unit cell formula of $\text{Si}_{12}\text{Mg}_8\text{O}_{30}(\text{OH},\text{F})_4\cdot(\text{H}_2\text{O})_4\cdot 8\text{H}_2\text{O}$. It is a 2:1 phyllosilicate structural family having a fibrous morphology with a length of about 0.2–4 μm . The structure of the sepiolite has a tunnel-like micropore channel and has silanol groups (Si–OH) at the edges of the tunnel, allowing for effective adsorption and improved interaction with the rubber matrix [8, 9].

It has been reported that incorporating sepiolite by milling technique enhanced the properties of the composites, such as curing, mechanical, thermal,

*Corresponding author, e-mail: abdulhakim.m@psu.ac.th
© BME-PT

swelling, flammability, and morphological properties [5]. Di Credico *et al.* [10] have prepared NR/sepiolite composites by using the latex-compounding technique and found that this approach provided more uniformity of sepiolite distribution in the rubber matrix. The dynamic mechanical properties of NR/sepiolites were greater than those of composites prepared using the conventional milling approach. However, the mechanical properties, *i.e.*, tensile and curing properties, were not reported. Recently, Hayemasae *et al.* [7] have investigated the effect of sepiolite addition procedures (mill and latex mixing approaches) on the properties of the NR/sepiolite composites. They have discovered that the conventional milling method improved composite properties due to better rubber–filler interactions attributed to the nature of sepiolite, which does not swell in water like other types of clay.

To our best knowledge, the effect of vulcanizing agents on the properties of NR/sepiolite composites has not been reported. Since the sepiolite contained Si–OH groups on its surface, determining the best vulcanizing agents for this composite is of interest. In this study, the NR/sepiolite composites containing three different vulcanizing agents, namely, sulfur, peroxide, and phenolic resin, were prepared. Thermomechanical and tensile properties were investigated using temperature scanning stress relaxation (TSSR) and tensile test. The microstructure changes were investigated using small-angle and wide-angle X-ray diffraction (SAXS, WAXS). The dispersion of sepiolite filler was examined by using a scanning electron microscope (SEM), and Fourier-transform infrared spectroscopy (FTIR) was used to clarify the interaction between NR and filler. The possibility of properties enhancement for various composites was discussed.

2. Experimental setup

2.1. Materials

NR-graded STR 5L was supplied by Chalong Concentrated Natural Rubber Latex Industry Co., Ltd., Songkhla, Thailand. Zinc oxide (ZnO, 99%) was purchased from Global Chemical Co., Ltd., Samut Prakan, Thailand. Stearic acid was purchased from Imperial Chemical Co., Ltd., Bangkok, Thailand. Sepiolite clay, having the main compositions of [wt%]; SiO₂ (55%), Al₂O₃ (15%), Fe₂O₃ (3%) with traces of water, was produced by Guangzhou Billion Peak Chemical Technology Co., Ltd., Guangzhou, China.

The sulfur (S, 99%) cross-link agent and its accelerator, dibenzothiazole disulfide (MBTS, 96%), were supplied by Siam Chemical Co., Ltd., Samut Prakarn, Thailand, and Shanghai Rokem Industrial Co., Ltd., Shanghai, China, respectively. Dicumyl peroxide (DCP, 40%) crosslinker and its coagent, triallyl isocyanurate, (TAIC, 98%), were purchased from Wuzhou International Co., Ltd., Shenzhen, China, and Sigma-Aldrich, Inc., Missouri, USA, respectively. Phenolic resin cross-link agent containing methylol content of 6.0–9.0% (HRJ-10518) and its catalyst, stannous chloride (SnCl₂, 98%), were supplied by Schenectady International Inc., New York, USA, and KemAus, New South Wales, Australia, respectively.

2.2. Rubber composite preparation

NR and NR/sepiolite composites with various vulcanizing agents, including sulfur (S), peroxide (P), and phenolic resin (Ph), were prepared using a laboratory-size internal mixer (Plastograph EC, Brabender GmbH & Co., Duisburg, Germany) with a mixing chamber of 55 cm³. The chemical ingredients listed in Table 1 were added in the order shown in Figure 1. The NR with and without stearic acid and ZnO were initially mixed for 3 min in an internal mixer at a rotor speed of 60 rpm and 40 °C of mixer temperature. It should be noted here that stearic acid and ZnO were used as activators for the S cross-link system. After that, the sepiolite filler was added to the mixture and mixed for 5 min. Next, the curing promoter (MBTS, TAIC, or SnCl₂) was fed to the mixing chamber and allowed to mix for 1 min. Finally, a curing agent (S, DCP, or Ph) was added to the mixture and mixed for 1 min. After completion of the mixing with a total mixing time of 10 min, the

Table 1. Compound formulations for NR and its composite compounds.

Chemicals	Quantity [phr]		
	S-Sep 10	P-Sep 10	Ph-Sep 10
NR	100	100	100
Stearic acid	1		
ZnO	3		
Sepiolite clay	0 and 10	0 and 10	0 and 10
MBTS	1.5		
S	1.5		
TAIC		1.5	
DCP		1.5	
SnCl ₂			1
Phenolic resin			10

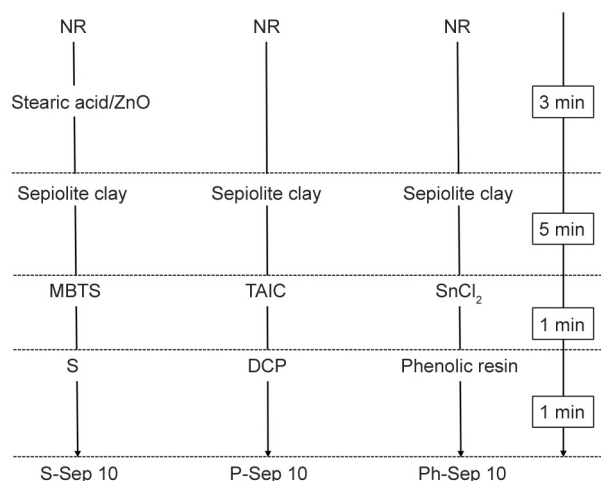


Figure 1. Sequence of chemical addition.

rubber compounds were then cross-linked through compression molding (SLLP-50, Siam Lab, Nonthaburi, Thailand) at 160 °C, following their respective curing times (t_{90}) to obtain 1 mm thick cross-linked sheets. The NR composite containing 10 phr sepiolite samples cross-linked with sulfur, peroxide, and phenolic resin systems were noted as S-Sep 10, P-Sep 10, and Ph-Sep 10, respectively, while their unfilled counterparts were indicated as S, P, and Ph, respectively.

2.3. Rubber composite characterization

2.3.1. Curing properties

The curing characteristics of rubber compounds were determined using a moving die rheometer (MDR 3000 Basic, Montech, Buchen, Germany) at 160 °C. The minimum torque (M_L), maximum torque (M_H), torque difference ($M_H - M_L$), scorch time (t_{S1}), and cure time (t_{90}) parameters were reported.

2.3.2. Fourier-transform infrared spectroscopy (FTIR)

Attenuated total reflectance–Fourier-transform infrared (ATR-FTIR) spectra of all samples were characterized using a Spotlight 200i spectrometer (Perkin Elmer, Inc., Massachusetts, USA). Each spectrum was recorded with resolutions of 4 cm^{-1} from 4000 to 400 cm^{-1} .

2.3.3. Thermomechanical properties and cross-link density

The thermomechanical properties and cross-link density of NR and its composites were measured using the temperature scanning stress relaxation (TSSR) meter, (Brabender, Duisburg, Germany). The

dumbbell-shaped test specimens (ISO 527, type 5A) of NR composites and neat NR were placed in the heating chamber and stretched for 50% at 23 °C. After 2 hours, the specimens were subjected to a nonisothermal test at a heating rate of 2 °C/min until the specimens were ruptured.

The apparent cross-link density (ν) can be estimated from the maximum slope in the initial part of the stress temperature curve using the Equation (1) [11]:

$$\nu = \frac{\kappa}{R(\lambda - \lambda^{-2})} \quad (1)$$

where R is the universal gas constant, λ is the nominal strain ratio, and κ is the temperature coefficient of stress which can be defined as the derivative of mechanical stress (σ) as a function of temperature (T) as Equation (2) [11]:

$$\kappa = \left(\frac{\partial \sigma}{\partial T} \right)_{\lambda, p} \quad (2)$$

where, from the theory of rubber elasticity, the σ is directly proportional to the absolute T , and this relationship can be shown as Equation (3) [11]:

$$\sigma = \frac{\rho RT}{M_c} (\lambda - \lambda^{-2}) \quad (3)$$

where, ρ denotes the mass density, R is the universal gas constant, λ signifies the extension ratio ($\lambda = L/L_0$, where L and L_0 are the final and initial length of the sample, respectively), and M_c is the average molar weight of the elastically active network chains, which is inversely proportional to the ν of the networks according to the following correlations (Equation (4)):

$$M_c = \frac{\rho}{\nu} \quad (4)$$

By combining Equations (2) and (3), the value of ν at constant strain can be finally calculated from the slope of stress versus temperature as previously expressed in Equation (1).

2.3.4. Tensile properties

The tensile properties, including stress at 100 and 300% strains, tensile strength, and strain at break of the composites with and without sepiolite filler, were determined at 500 mm/min according to ISO 37 (Type 2) using universal testing equipment, LR5K Plus (Lloyd Instruments, West Sussex, UK). The dumbbell-shaped test specimens with a thickness of

2 mm and an overall length of test specimens of 75 mm were used in this study.

2.3.5. Microstructural properties

Microstructural changes, *i.e.*, distribution of sepiolite filler in the cross-linked samples and crystallization during stretching, were investigated using small-/wide-angle X-ray scattering, SAXS/WAXS measurement. Moreover, SAXS and WAXS measurements were performed at the BL1.3W:SAXS/WAXS, Siam Photon Laboratory, Synchrotron Light Research Institute, Nakhon Ratchasima, Thailand. The WAXD and SAXS data were taken during continuous stretching at a 500 mm/min crosshead speed. The SAXSIT data processing program was employed to normalize and rectify all WAXD and SAXS data. The degree of crystallinity [%] corresponding to the (200) plane was estimated using the Equation (5) [12]:

$$\text{Crystallinity [\%]} = \frac{A_c}{A_c + A_a} \quad (5)$$

where A_c denotes the area below the 200 crystalline peaks and A_a denotes the amorphous halo area. The average crystallite sizes corresponding to (200) planes were estimated from the Scherrer equation [13] (Equation (6)):

$$\text{Crystalline size} = \frac{K\lambda}{\beta \cos \theta} \quad (6)$$

where K is equal to 0.89, λ is the wavelength, β is the half width at half height, and θ is the Bragg angle.

Structural changes, *e.g.*, dispersion of cross-link network structures in NR and distributions of the filler in the composites with different vulcanizing agents, were analyzed by using SAXS measurements. Two-dimensional (2D) SAXS images were background corrected and then integrated to obtain the scattering

intensity (I) as a function of the scattering vector (q). The q is defined as Equation (7):

$$q = \frac{4\pi \sin \theta}{\lambda} \quad (7)$$

where λ is the wavelength and 2θ is the scattering angle.

2.3.6. Morphological properties

Scanning electron microscopy (SEM) (Quanta 400, Thermo Fisher Scientific, Brno-Cernovice, Czech Republic) was used to analyze the dispersion of sepiolite clay filler in the NR matrix containing various vulcanizing agents. The samples were fractured in liquid nitrogen before sputter coating with gold to minimize electrostatic charge buildup during testing.

3. Results and discussion

3.1. Curing properties

The curing characteristics of NR and its composite compounds with various cross-link agents are displayed in Table 2. It was seen that the M_L , the indirect indicator of a compound viscosity, M_H , the modulus of fully cross-linked composites, and $M_H - M_L$, the distinction between the shear moduli of cross-linked and uncrosslinked composites, increased with the incorporation of sepiolite clay filler. Because the sepiolite has a high aspect ratio and surface area [9], the high surface area of the filler provides a more favorable surface for the filler to interact with the polymer chains for interacting with the rubber molecules. Physical interactions between rubber chain segments adsorbing on filler surfaces served as additional cross-links in composites, restricting the rubbery matrix chain mobility. Consequently, the stiffness of the composites has been enhanced [14]. Aside from the difference between the shear moduli before and after cross-linked and composites, $M_H - M_L$ can be

Table 2. Minimum torque (M_L), maximum torque (M_H), torque difference ($M_H - M_L$), scorch time (t_{S1}), and cure time (t_{90}) of NR and its composites with different vulcanizing agents.

Sample	Curing parameters				
	M_L [dN·m]	M_H [dN·m]	$M_H - M_L$ [dN·m]	t_{S1} [min]	t_{90} [min]
S	3.90±0.01	17.12±0.03	13.22±0.02	1.59±0.00	6.04±0.01
S-Sep 10	4.10±0.01	18.36±0.06	14.26±0.06	2.97±0.11	9.44±0.07
P	3.09±0.02	21.65±0.03	18.56±0.01	0.60±0.03	11.82±0.01
P-Sep 10	3.61±0.01	23.61±0.02	20.00±0.02	0.71±0.03	14.47±0.03
Ph	3.73±0.01	20.82±0.02	17.09±0.01	0.93±0.50	16.03±0.03
Ph-Sep 10	3.80±0.05	22.51±0.02	18.71±0.02	0.88±0.03	15.91±0.08

determined the relative cross-link density of rubber. The relative cross-link density of rubber composites increased with the incorporation of sepiolite filler. In the composite, the increase of cross-link density has resulted from good rubber–filler interactions [15, 16]. t_{S1} and t_{90} indicate the commencement of vulcanization and the time required to achieve 90% of the M_H value, respectively [17]. Except for the phenolic resin system, t_{S1} and t_{90} of NR composites cross-linked with sulfur and peroxide systems were longer than those of the neat cross-linked NR counterparts. Such observation can be attributed to the small fraction of chemical cross-links being absorbed in the structural tunnels of sepiolite [6, 18]. Considering the composite cross-linked with the phenolic resin system, both t_{S1} and t_{90} were slightly reduced, implying that the curing reaction occurred faster when the sepiolite was added. This decrease was probably attributed to

the competitive interaction between phenolic resin with rubber chains (cross-link reaction) and phenolic resin with sepiolite filler, as will be discussed later.

3.2. Fourier-transform infrared spectroscopy (FTIR)

Figure 2 depicts the FTIR spectra of pure sepiolite and NR/sepiolite composites with different vulcanizing agents in the wavenumber range of 400–4000 cm^{-1} (Figure 2a), 3000–4000 cm^{-1} (Figure 2b), and 400–1200 cm^{-1} (Figure 2c). For comparison, the spectra of their unfilled counterparts were also included. From Figure 2a, the characteristic peaks at approximately 428, 469, and 535 cm^{-1} in pure sepiolite were particularly assigned to Si–O–Si bending vibration, whereas the broadband centered at 1031 cm^{-1} corresponded to the stretching of Si–O [19]. The band at 3690 and 3627 cm^{-1} were ascribed to the

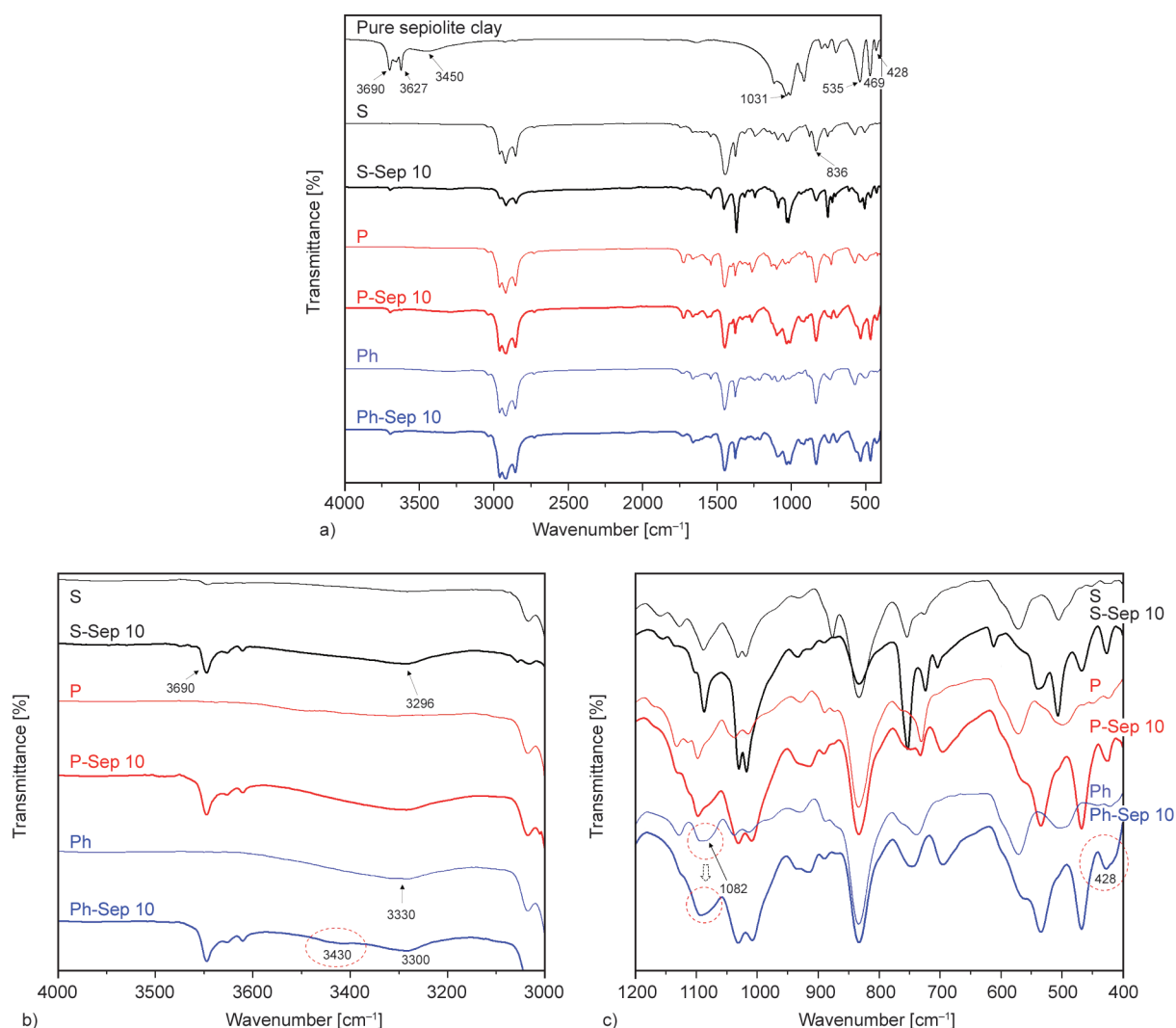


Figure 2. FTIR spectra of NR and its composites with different vulcanizing agents in the wavenumber range of a) 400–4000 cm^{-1} , b) 3000–4000 cm^{-1} , and c) 400–1200 cm^{-1} .

OH groups in the octahedral sheet and the OH stretching vibration in the external surface of sepiolite, and the broad peak centered at 3450 cm^{-1} in the range of $3600\text{--}3200\text{ cm}^{-1}$ was attributed to OH stretching of the zeolitic water in the sepiolite channels [19, 20]. For the NR cross-linked with sulfur (S), peroxide (P) and phenolic resin (Ph), the important characteristic peak of cross-linked NR was found at 837 cm^{-1} , which was associated with the out-of-plane bending vibration of C–H in the –CH=CH– group of cis-1,4-unit [6, 21]. With the exclusion of the Ph sample, all NR cross-linked with other systems did not exhibit a peak in the bands between 4000 and 3000 cm^{-1} (Figure 2b). The peak at 3330 cm^{-1} found in the Ph sample was attributed to –OH vibration of phenolic resin [22]. Up on the addition of sepiolite to the NR, the peak assigned to the OH stretching of sepiolite (3690 cm^{-1}) and –OH stretching from the zeolitic water (3296 cm^{-1}) were observed in all composites, indicating the presence of sepiolite dispersion in the rubber matrix. The phenolic resin cross-linked composites (Ph-Sep 10) caught the attention since they showed two peaks at 3430 and 3300 cm^{-1} , while these two peaks were not found in the composites cross-linked with peroxide (P-Sep 10) and sulfur (S-Sep 10) systems. When compared to those Ph, P, and S-Sep 10 samples, it was more likely that the –OH groups in Ph-Sep 10 had different chemical environments, indicating the probability of a hydrogen bonding (H-bond) between the –OH groups of the phenolic resin and the –OH groups of the sepiolite filler.

Considering the peak at 428 cm^{-1} in different composites (Figure 2c), a significant change was found in the spectrum of the Ph-Sep 10 compared to those of P-Sep 10 and S-Sep 10. The Ph-Sep 10 had a shoulder and broad peak at 428 cm^{-1} , whereas the others had simply a single sharp peak. Additionally, the broad peak at 1082 cm^{-1} due to C–O stretching in phenolic resin found in the Ph sample was also sharpened in Ph-Sep 10. These findings revealed that the O–Si–O and C–O present in the Ph-Sep 10 had different chemical environments when compared with those of P-Sep 10, S-Sep 10, Ph, and pure sepiolite. The OH group of phenolic resin (–CH₂OH) in the cross-linked precursor might chemically react with the silanol group (–SiOH) located at the edges surface of sepiolite. It is widely accepted that many silanol groups (–SiOH) are located along the margins of the sepiolite structure [8, 9], whereas the phenolic

resin contains a hydroxyl (–OH) as a functional group. These two groups can interact with one other at molding temperatures ($160\text{ }^\circ\text{C}$) via chemical bonding between silanol groups (–SiOH) located at the sepiolite edges and the OH group of phenolic resin, resulting in a Si–O–C bond, whereas hydrogen bonding is possible at low temperatures. According to the reports [22, 23], the peak for the Si–O–C bond appears at 1085 cm^{-1} , which may merge with the broad peak at 1082 cm^{-1} in this study. The presence of both the Si–O–C bond and the hydrogen bond was previously reported in composites composed of NR/clay nanocomposites [22], epoxidized natural rubber-(ENR-) silica [23], and ENR-sepiolite [24]. The presence of additional hydrogen bonding at low temperatures would result in the improvement of various properties. These hydrogen bonds would not affect the rheometer torque at vulcanization temperature because they exhibited temperature-dependent behavior, *i.e.*, they disintegrate at elevated temperatures [25]. As a result, the t_{90} of Ph and Ph-Sep 10 were almost comparable. Figure 3 depicts a possible interaction between the phenolic resin and sepiolite through the formation of hydrogen bonding and the Si–O–C bond. In addition to the cross-link reaction, these interactions would serve as an extra cross-linking point, resulting in faster scorch and cure times.

3.3. Thermomechanical properties and cross-link density

Figure 4 illustrates the normalized force curves of NR and its composites with different vulcanizing agents as a function of temperature obtained from temperature scanning stress relaxation (TSSR) measurement. At temperatures of $30\text{--}50\text{ }^\circ\text{C}$, the initial normalized force of all samples increased slightly due to the entropy effect [26, 27]. A slight reduction of force at $50\text{--}100\text{ }^\circ\text{C}$ was probably due to the detachment of physical bonding among rubber molecules or between rubber and filler. At temperatures above $100\text{ }^\circ\text{C}$, the force abruptly decreases toward zero due to chain scission, and cleavage of network bridges between rubber molecules caused by thermo-oxidative reaction occurs [28]. Depending on the cross-linked systems, the force at any given temperature of cross-linked NR was shifted to a higher temperature. In the case of sulfur cross-linked NR, the decrement of force was found at a lower temperature than those of peroxide and phenolic systems due to lower bonding dissociation energy of the cross-linked

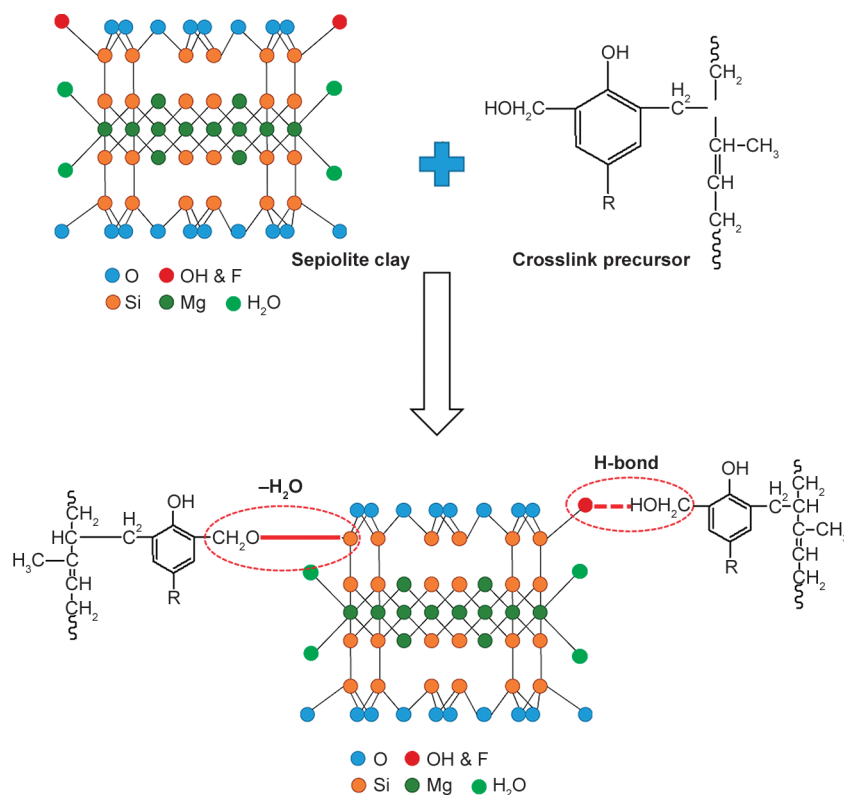


Figure 3. The probable mechanism of interactions between phenolic resin and sepiolite filler.

generated by the sulfur system, *i.e.*, monosulfidic (C–S–C; 285 kJ/mol), disulfidic (C–S–S–C; 268 kJ/mol), and polysulfidic (C–S–S_x–C; 252 kJ/mol) [29, 30]. In contrast, the C–C bonds generated from peroxide and phenolic systems provide a bear bonding energy of 344 kJ/mol, having higher dissociation energy than those of sulfidic cross-links [29, 31]. Therefore, the rubber cross-linked with the sulfur system had a more readily network bridge breakdown at elevated temperatures than peroxide and phenolic systems. Moreover, the incorporation of sepiolite slightly shifted the force reduction toward higher temperatures

compared to their unfilled counterparts at 120–170 °C. This was attributed to the sepiolite acting as a thermal insulator and as the mass transport barrier to the volatile products generated during decomposition [32]. The parameters obtained from TSSR measurement in terms of initial stress (σ_0) and the temperature at which the force ratio was reduced to 10, 50, and 90% (T_{10} , T_{50} , and T_{90}) concerning the initial force value [11], are shown in Table 3.

Table 3 shows that T_{10} , T_{50} , and T_{90} of the NR were enhanced by adding sepiolite due to the thermal insulator characteristic of the filler, as previously mentioned. Furthermore, the sepiolite filler may

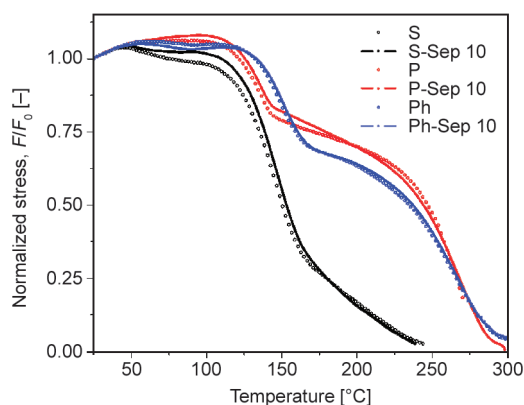


Figure 4. Normalized stress-temperature curves of NR and its composites with different vulcanizing agents.

Table 3. Initial stress (σ_0), the temperature at which the force ratio was reduced to 10, 50, and 90% with respect to the initial force value (T_{10} , T_{50} , and T_{90}), and cross-linked density (ν) of NR and its composites with different vulcanizing agents.

Sample	TSSR parameters				
	σ_0 [MPa]	T_{10} [°C]	T_{50} [°C]	T_{90} [°C]	ν [mol/m ³]
S	0.23	121.30	150.50	218.00	74.68
S-Sep 10	0.23	127.10	153.30	215.00	76.33
P	0.35	133.90	247.20	271.90	74.60
P-Sep 10	0.30	136.60	244.30	281.10	77.22
Ph	0.35	144.70	234.70	284.60	75.11
Ph-Sep 10	0.44	146.40	237.30	284.10	99.03

also adsorb some rubber chains, thereby retarding softening of the composites. It should be noted here that the T_{50} value in the P-Sep 10 was lower than in its unfilled sample, which was most likely due to poor dispersion and/or weak interaction between rubber and filler, as discussed later in the morphological properties section.

Considering σ_0 and cross-link density (ν) of various samples, a significant improvement of both σ_0 and ν was observed in the Ph-Sep 10. Compared to their counterparts, σ_0 and ν for the phenolic resin cross-linked NR/sepiolite composite were improved by about 25 and 30%, respectively, while other systems showed only a minor improvement. This vast improvement surely suggested the establishment of an additional bonding network between the phenolic and sepiolite fillers, retarding the motion of the rubber chains and strengthening the materials. It should be noted that the cross-link density of pure NR with various vulcanizing agents ranged from 74 to 75 mol/m³, which was extremely low. As a result, the initial cross-link density obtained from these three systems can be assumed to be comparable and worthy of further comparison.

Figure 5 shows the time-dependent normalized stress (F/F_0) of NR and its composites with different vulcanizing agents during isothermal stress relaxation. This is an alternative approach to evaluating the rubber–filler interaction. Moreover, strong interaction between filler particles and rubber chains usually retarded the stress relaxation rate [7, 33]. Figure 5 shows that all composite samples showed a linearly decreasing trend of stress over time. A decrease in steep stress was observed in the S-Sep 10 and P-Sep 10 samples, implying that the molecular relaxation was

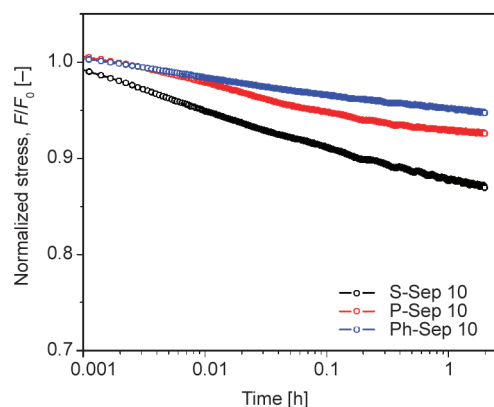


Figure 5. Normalized stress during isothermal stress relaxation of NR and its composites with different vulcanizing agents.

very fast in these two samples. A lower stress relaxation rate was observed in the Ph-Sep 10, implying the stronger interaction between rubber and filler presented in this sample. This could be due to the formation of physical/chemical bonding between phenolic resin-NR and sepiolite filler, as shown in Figure 3.

3.4. Tensile properties

Figure 6 illustrates a typical stress-strain relationship for the pure NR and NR composites with various curing processes. Comparing to their unfilled counterparts, incorporating sepiolite into the NR enhanced the stress at given strains, and the strain where the steep increase of stress occurred was found at much lower strains. This finding revealed that introducing sepiolite increased the stress of NR, lowering the point of strain at the stress upturn.

The tensile properties in terms of 100% modulus (M100), 300% modulus (M300), tensile strength (TS), and elongation at break (EB) are listed in Table 4. The incorporation of sepiolite filler enhances the M100 and M300, which could be due to the hydrodynamic effect arising from the inclusion of rigid particles. The incorporation of sepiolite filler reduced the mobility of the rubber chains, resulting in more rigid, stiffer, and harder composites [34]. Additionally, an increase in the cross-linking density created by rubber–filler interactions was also another reason for the increase of the modulus [15], as previously suggested by $M_H - M_L$.

Likewise, the TS of the NR was found to increase with the addition of sepiolite. Masa *et al.* [6] have ascribed this improvement to a needle-like shape of sepiolite with a high aspect ratio, which offered considerable

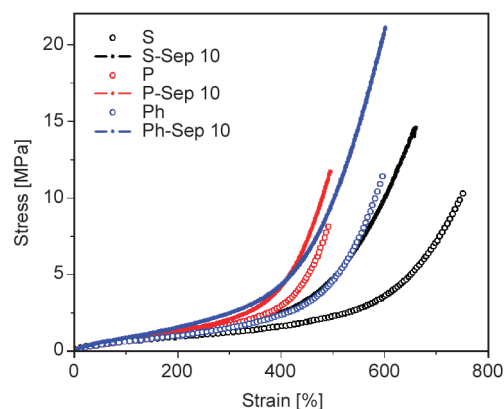


Figure 6. Representative stress-strain curves of NR and its composites with different vulcanizing agents.

Fsurface area to contact with the rubber, allowing for efficient stress transfer. Moreover, the rubber chains that possess linear chains can fit into the tight channels in the structure of sepiolite, causing a high interaction between sepiolite and NR [35].

It is worth highlighting that a massive increment in tensile modulus and TS was again noticed in the Ph-Sep 10 sample. The improvement of M100 and M300 in Ph-Sep 10 was about 43 and 69%, respectively, and the TS was about 78% compared to that of its unfilled sample, while the other vulcanizing agents (S-Sep 10 and P-Sep 10) showed only a slight improvement that was less than 35%. Such significant improvements noticed in the Ph-Sep 10 were attributed to a strong interaction between sepiolite and rubber due to the presence of phenolic resin, which resulted in improved stress transfer efficiency between the rubber matrix and the filler, resulting in greater modulus and TS. On the other hand, a slight improvement in the other vulcanizing agents could be attributed to the physical interaction between rubber and sepiolite filler. As a result of total cross-link density enhancement, the composites showed stiffer vulcanizates, limiting the deformation of the composites. Therefore, the EB of the composites was reduced.

3.5. Morphological properties

Scanning electron microscopic (SEM) analysis was performed to understand better the dispersion of sepiolite in an NR matrix comprising various vulcanizing agents. Figure 7 shows the micrographs of cryo-fractured surfaces of NR/sepiolite composites with various vulcanizing agents as observed through the SEM technique. The cross-link agents were discovered to have significantly impacted the dispersion of sepiolite filler (lighter dispersed phases) in the rubber

Table 4. Tensile properties in terms of 100 and 300% modulus (M100 and M300), tensile strength (TS), and elongation at break (EB).

Sample	Tensile properties			
	M100 [MPa]	M300 [MPa]	TS [MPa]	EB [%]
S	0.66±0.03	1.29±0.10	10.42±0.01	766±19
S-Sep 10	0.70±0.07	1.67±0.01	14.04±2.08	688±80
P	0.63±0.01	1.72±0.04	8.21±0.81	497±12
P-Sep 10	0.78±0.04	2.08±0.09	11.02±0.68	490±11
Ph	0.61±0.02	1.49±0.14	11.90±0.14	606±14
Ph-Sep 10	0.87±0.01	2.52±0.08	21.19±0.72	588±13

matrix (darker background). The smallest size, from 0.25 to 6.00 μm , with the most homogeneous dispersion, was observed in the Ph-Sep 10 sample (Figure 7c), which was slightly better than that of the S-Sep 10 (Figure 7a).

The use of phenolic resin was presumably advantageous because the OH group in the phenolic resin may interact with the silanol groups ($-\text{SiOH}$) found on the sepiolite edges filler, as revealed by FTIR, causing homogeneity in sepiolite dispersion throughout the rubber matrix. This would almost certainly result in a significant improvement in the thermomechanical properties and mechanical properties of Ph-Sep 10. Although the sepiolite dispersion in S-Sep 10 and Ph-Sep 10 was slightly different, the increase in TS of Ph-Sep 10 was nearly double that of S-Sep 10 compared to their unfilled counterparts. This significant improvement could only be achieved through strong interaction between filler and rubber. On the other hand, several agglomerates with the size of about 0.50–20.00 μm with the poorest dispersion were seen in the P-Sep 10 sample (Figure 7b). Such large aggregation found in the P-Sep 10 would surely destroy adhesion between rubber and filler, which may cause a reduction of mechanical properties, such

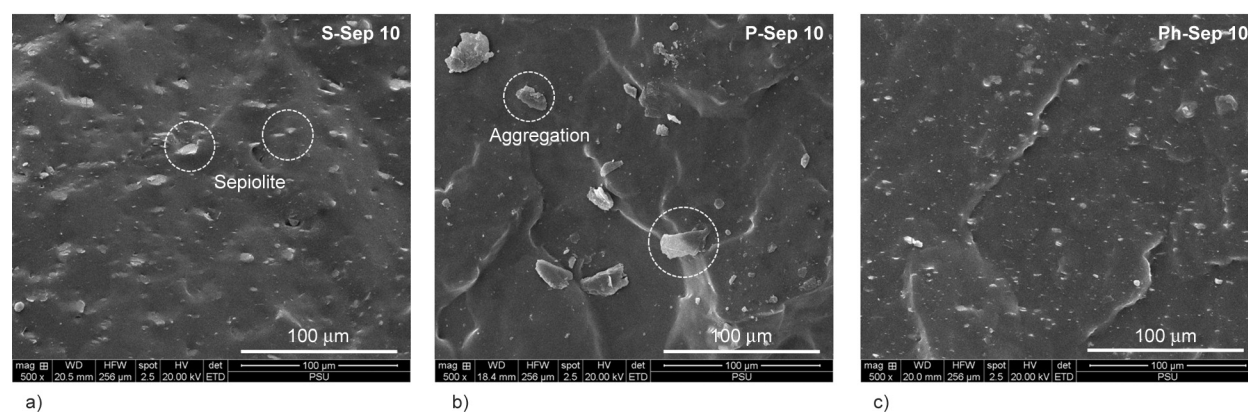


Figure 7. SEM micrographs of a) S-Sep 10, b) P-Sep 10, and c) Ph-Sep 10.

as TS and EB of the composite samples. Poor dispersion of sepiolite in P-Sep 10 was probably attributed to part of the sepiolites being reaggregated during the vulcanization process. The related mechanism of this reaggregation is not clear at the moment. To clarify the aggregation of sepiolite during vulcanization, further investigation is required. However, similar behavior has been found in sulfur-crosslinked rubber/clay nanocomposites, and it was suggested that because of some organic cations were being ejected because of a probable reaction between the intercalant and vulcanizing agents [36, 37].

3.6. Microstructural properties

Figure 8 shows representative two-dimensional (2D) wide-angle X-ray scattering (WAXS) photographs of the composite sample (Ph-Sep 10) before (0% strain) and after deformation to 400% strain. Since no strain-induced crystallization occurs, no reflection spot was found for the sample before stretching (Figure 8a). When the strain-induced crystallization took place while stretching, various reflection spots were noticed due to the highly oriented crystal of NR induced by the stretching (Figure 8b). The most intense spots corresponded to different planes, *i.e.*, (200), (201), and (120). Among various intense reflection spots, the variation in crystallography corresponding to the (200) plane was investigated to evaluate the influence of sepiolite addition and types of cross-link agents on the microstructures of NR.

Figure 9 shows the degrees of crystallinity corresponding to the (200) planes of various cross-linked NR and composites. The crystallinity of all samples increased with increasing strain, proving that the crystallization of the NR was caused by deformation-induced crystallization. It is also seen that incorporating sepiolite filler increased the crystallinity of NR in all cases, depending on their dispersion. A significant enhancement of crystallinity was observed when

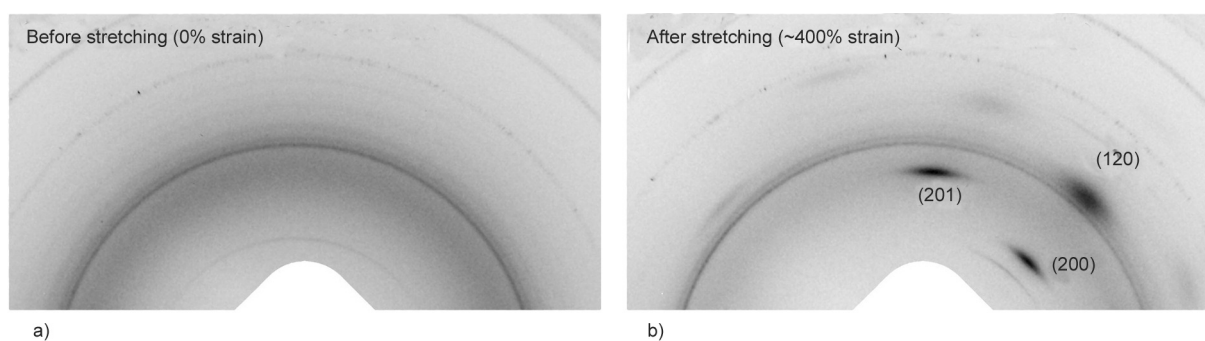


Figure 8. 2D WAXS images of the composite sample a) before and b) after stretching.

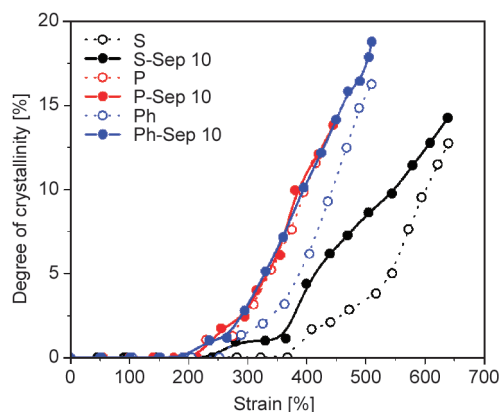


Figure 9. Degree of crystallinity at various strains in the NR and its composites with different vulcanizing agents.

the NR composites were cross-linked by sulfur and phenolic resin. As previously demonstrated in Figures 7a and 7c, good sepiolite filler dispersion in S-Sep 10 and Ph-Sep 10 significantly improved the crystallinity of NR due to high numbers of interfacial interactions (physical and/or chemical) between the NR chains and the filler. The presence of interfacial interactions would prevent the NR chain from moving, favoring alignment of the NR chains along the stretching direction, and resulting in more crystallinity [22, 38]. At the same strain, the crystallinity of Ph-Sep 10 was greater than that of S-Sep 10 due to the better interaction between rubber and filler phases. On the contrary, these interactions would be very limited in NR composites with poor filler dispersion (Figure 7b), preventing the rubber chains from aligning and crystallizing. Thus, the overall crystallinity of P-Sep 10 is not higher than that of unfilled rubbers. A reduction of crystallinity in NR composites with poor dispersion was also reported [38].

One may argue that less complexity in peroxide would provide a better change in crystallization compared to other systems. However, the addition of sepiolite makes the systems more complicated.

The introduction of filler in NR changes the stress field, increases the local strain of the chain, and leads to local heterogeneities [39]. Thus, the changes in various properties were more complicated even in a less complex peroxide system. In addition, the stain at which the crystallization took place was found at the lower strain in the composites, thus lowering the strain where the stress upturn occurred in the stress-strain curves when the unfilled samples were compared (Figure 6). This was probably attributed to the addition of the filler enhanced the network chain density, reducing then the distance between the cross-link points and shortening some rubber chains. These shorter chains are responsible for enhancing stain-induced crystallization at a small strain. Furthermore, the physical interaction between the filler and rubber chains is sufficient for improving the strain-induced crystallization of the NR [40]. The highest ability of strain-induced crystallization was observed in the Ph-Sep 10, where the highest TS was achieved. The strong rubber–filler interaction caused by the phenolic resin and sepiolite filler could clarify this phenomenon.

Considering the NR samples containing various vulcanizing agents, it was found that the type of cross-links formed in the rubber matrix has a significant effect on the crystallization process during stretching, although their cross-link densities (Table 3) were comparable. This suggested that the type of cross-link formation and distance between two cross-link points, as circled in Figure 10, could influence the strain-induced crystallization behavior. As previously suggested in the vulcanized NR with varied sulfur cross-link types (mono-, di- and polysulfidic) [41], short monosulfidic, or disulfidic linkages could better restrict the movement of the rubber chains compared to long polysulfidic linkages, accelerating, and enhancing the crystallization process. Therefore, the short and rigid structure of cross-links induced from the peroxide system (Figure 10b) may

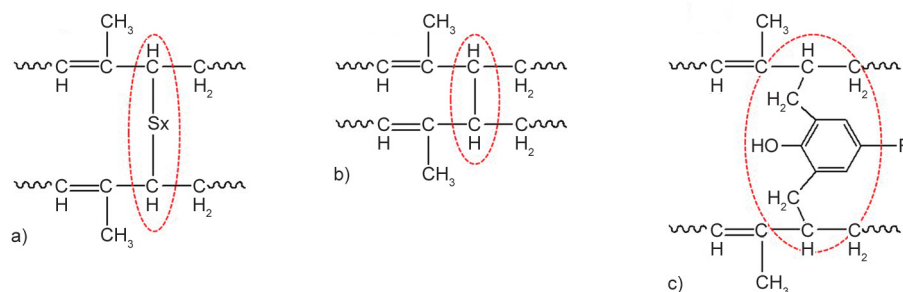


Figure 10. Cross-link formation from a) sulfur, b) peroxide and c) phenolic resin systems.

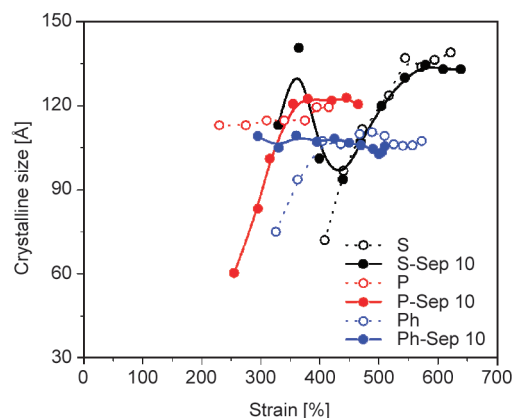


Figure 11. Variation of crystallite size at various strains in the NR and its composites with different vulcanizing agents.

better constrain the NR chain mobility, facilitating the orientation of the chains and thus enhancing the crystallization process during stretching. The highest crystallinity was found in the peroxide system, while the lowest crystallinity was observed in the sulfur system. It was reported that the NR cross-linked with peroxide exhibited a higher degree of crystallinity than the NR cross-linked with sulfur due to the peroxide system producing a more homogeneous network structure than the sulfur system [42].

Figure 11 displays the variation of crystalline size corresponding to the (200) plane at various strains in the NR and its composites with different vulcanizing agents. The crystallite size varied from approximately 60 to 130 Å, depending on the strains and vulcanizing agents. All the unfilled samples and composites showed a fluctuation in crystalline size with the variation in strains. It is believed that the strain-induced crystallization process involves two competing processes. Stretching, on the one hand, resulted in crystallite generation and crystallite growth, while on the other hand, declined crystallite formation and disappeared the generated crystallites. These events are thought to occur in a rubber matrix at random but more or less correlatively [42]. These two phenomena

may result in the fluctuation in crystallite size during stretching. However, the changes in crystalline size were very small in the Ph-Sep 10. Such observation was probably attributed to the homogeneity of filler dispersion with strong rubber–filler interaction. To prove the homogeneity of filler dispersion in various samples, the small-angle X-ray scattering technique was applied.

Small-angle X-ray scattering (SAXS) measurements of all samples were performed to investigate the

structures of the cross-link distribution and filler distributions [43]. A plot of the scattering intensity (I) against the scattering vector (q) of NR and its composites containing various vulcanizing agents is shown in Figure 12. Figure 12a shows that the scattering intensities of all unfilled NR with various vulcanizing agents showed a strong upturn in the low q region due to the heterogeneous network structures in the vulcanizates created by cross-linking network structures [44, 45]. Since the variation of scattering

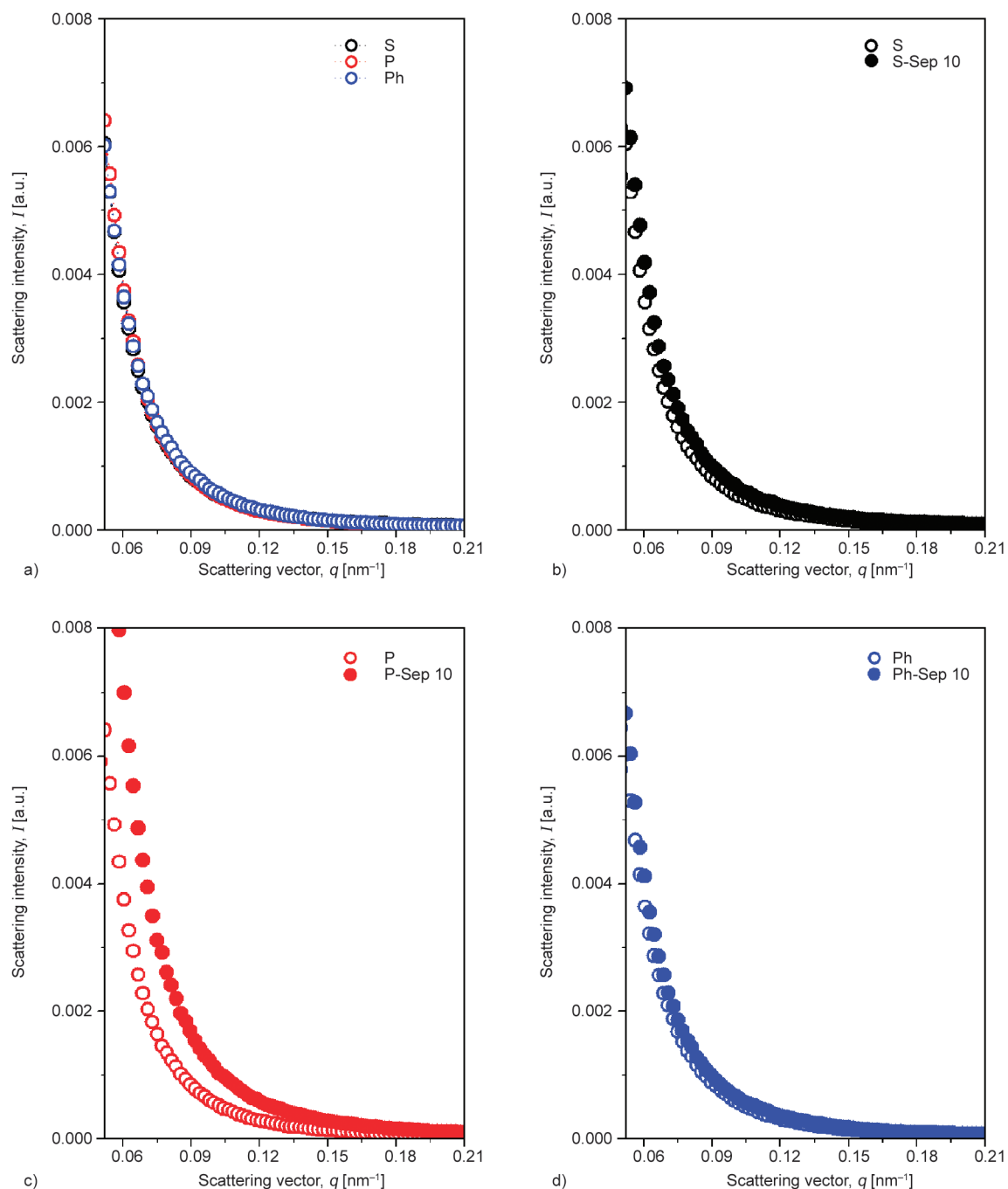


Figure 12. Correlation of the scattering intensity I with the scattering vector q for the a) unfilled NR samples and b) sulfur, c) peroxide, and d) phenolic resin cross-linked NR and their composites.

intensities of all unfilled samples were not significantly different, it can be assumed that the structure of cross-link networks with varied vulcanizing agents was almost similar. In the case of composites, there was a clear difference in scattering intensity between cross-linked NR and cross-linked composites. The SAXS intensity patterns for cross-linked composites displayed higher intensity than those of cross-linked counterparts (Figure 12b–12d). Therefore, the difference in the pattern of SAXS for cross-linked composites should be attributed to the presence of sepiolite filler. The presence of sepiolite altered the local electron density, which SAXS can detect. Notably, the scattering intensity of P-Sep 10 was substantially higher than that of the corresponding unfilled sample (Figure 12c), owing to poor sepiolite dispersion in the NR matrix, as evidenced by SEM (Figure 7), which causes high electron density fluctuation.

In contrast, the scattering intensity of the composites cross-linked with sulfur and phenolic resin (Figures 12b and 12d) remained nearly unaltered after the filler was added. Such phenomenon was attributed to the homogeneous dispersion with the smallest dimensions of sepiolite in the rubber matrix, as previously confirmed by SEM investigation. The SAXS results matched well with those obtained from the SEM observation.

4. Conclusions

In this study, composites of NR filled with sepiolite were prepared. The influence of several vulcanizing agents, including sulfur, peroxide, and phenolic resin, on the properties of the NR composites was investigated. Compared to other vulcanizing agents, the phenolic resin improved thermomechanical properties with the lowest stress relaxation rate. The highest tensile stress and TS were also achieved when the phenolic resin was used as a crosslinker. The enhancement was about 69% for tensile stress at 300% strains and about 78% for the TS. Such significant improvement was attributed to the homogeneity of small sepiolite dispersion with strong adhesion between rubber and filler through the assistance of phenolic resin, as suggested by FTIR. Such strong interaction facilitated the strain-induced crystallization process in the NR. The phenolic resin was the best vulcanizing agent for preparing NR composites containing sepiolite as filler.

Acknowledgements

This research was supported by Prince of Songkla University (Grant No. UIC6402030S).

References

- [1] Bokobza L.: Natural rubber nanocomposites: A review. *Nanomaterials*, **9**, 12 (2019). <https://doi.org/10.3390/nano9010012>
- [2] Roy K., Debnath S. C., Potiyaraj P.: A critical review on the utilization of various reinforcement modifiers in filled rubber composites. *Journal of Elastomers and Plastics*, **52**, 167–193 (2020). <https://doi.org/10.1177/0095244319835869>
- [3] Chang B. P. P., Gupta A., Muthuraj R., Mekonnen T.: Bioresourced fillers for rubber composite sustainability: Current development and future opportunities. *Green Chemistry*, **23**, 5337–5378 (2021). <https://doi.org/10.1039/D1GC01115D>
- [4] Maslowski M., Miedzianowska J., Strzelec K.: Natural rubber composites filled with crop residues as an alternative to vulcanizates with common fillers. *Polymers*, **11**, 972 (2019). <https://doi.org/10.3390/polym11060972>
- [5] Zaini N. A. M., Ismail H., Rusli A.: Tensile, thermal, flammability and morphological properties of sepiolite filled ethylene propylene diene monomer (EPDM) rubber composites. *Iranian Polymer Journal*, **27**, 287–296 (2018). <https://doi.org/10.1007/s13726-018-0609-6>
- [6] Masa A., Krem-ae A., Ismail H., Hayeemasae N.: Possible use of sepiolite as alternative filler for natural rubber. *Materials Research*, **23**, e20200100 (2020). <https://doi.org/10.1590/1980-5373-MR-2020-0100>
- [7] Hayeemasae N., Adair A., Rasidi M. S. M., Jitsopin P., Masa A.: Influence of sepiolite addition methods and contents on physical properties of natural rubber composites. *Science and Technology Indonesia*, **7**, 140–148 (2022). <https://doi.org/10.26554/sti.2022.7.2.140-148>
- [8] Kumar K. D., Tsou A. H., Bhowmick A. K.: Unique tackification behavior of needle-like sepiolite nanoclay in brominated isobutylene-co-p-methylstyrene (BIMS) rubber. *Macromolecules*, **43**, 4184–4193 (2010). <https://doi.org/10.1021/ma100472r>
- [9] Mohanty T. R., Neeraj P., Ramakrishnan S., Amarnath S., Lorenzetti D., Mohamed P., Tyres A.: Sepiolite nanoclay: A reinforcing filler in the natural rubber/butadiene rubber (NR/BR) matrix for tire tread compound application. *Rubber World*, **263**, 32–44 (2021).
- [10] Di Credico B., Tagliaro I., Cobani E., Conzatti L., D'Arienzo M., Giannini L., Mascotto S., Scotti R., Stagnaro P., Tadiello L.: A green approach for preparing high-loaded sepiolite/polymer biocomposites. *Nanomaterials*, **9**, 46 (2019). <https://doi.org/10.3390/nano9010046>

- [11] Vennemann N., Bökamp K., Bröker D.: Crosslink density of peroxide cured TPV. *Macromolecular Symposia*, **245–246**, 641–650 (2006).
<https://doi.org/10.1002/masy.200651391>
- [12] Hernández M., López-Manchado M. A., Sanz A., Nogales A., Ezquerro T. A.: Effects of strain-induced crystallization on the segmental dynamics of vulcanized natural rubber. *Macromolecules*, **44**, 6574–6580 (2011).
<https://doi.org/10.1021/ma201021q>
- [13] Tosaka M., Murakami S., Poompradub S., Kohjiya S., Ikeda Y., Toki S., Sics I., Hsiao B. S.: Orientation and crystallization of natural rubber network as revealed by WAXD using synchrotron radiation. *Macromolecules*, **37**, 3299–3309 (2004).
<https://doi.org/10.1021/ma0355608>
- [14] Hayemasae N., Adair A., Masa A.: Comparative study on viscosities, stress relaxation, curing and mechanical properties of sepiolite and silica filled natural rubber composites. *Malaysian Journal of Analytical Sciences*, **26**, 176–190 (2022).
- [15] Bokobza L., Chauvin J-P.: Reinforcement of natural rubber: Use of *in situ* generated silicas and nanofibres of sepiolite. *Polymer*, **46**, 4144–4151 (2005).
<https://doi.org/10.1016/j.polymer.2005.02.048>
- [16] Kim D. Y., Park J. W., Lee D. Y., Seo K. H.: Correlation between the crosslink characteristics and mechanical properties of natural rubber compound via accelerators and reinforcement. *Polymers*, **12**, 2020 (2020).
<https://doi.org/10.3390/polym12092020>
- [17] Kopal I., Labaj I., Vrškova J., Harničárová M., Valíček J., Ondrušová D., Krmela J., Palková Z.: A generalized regression neural network model for predicting the curing characteristics of carbon black-filled rubber blends. *Polymers*, **14**, 653 (2022).
<https://doi.org/10.3390/polym14040653>
- [18] Zadaka-Amir D., Bleiman N., Mishael Y. G.: Sepiolite as an effective natural porous adsorbent for surface oil-spill. *Microporous and Mesoporous Materials*, **169**, 153–159 (2013).
<https://doi.org/10.1016/j.micromeso.2012.11.002>
- [19] Frost R. L., Locos O. B., Ruan H., Klopogge J. T.: Near-infrared and mid-infrared spectroscopic study of sepiolites and palygorskites. *Vibrational Spectroscopy*, **27**, 1–13 (2001).
[https://doi.org/10.1016/S0924-2031\(01\)00110-2](https://doi.org/10.1016/S0924-2031(01)00110-2)
- [20] Alkan M., Tekin G., Namli H.: FTIR and zeta potential measurements of sepiolite treated with some organosilanes. *Microporous and Mesoporous Materials*, **84**, 75–83 (2005).
<https://doi.org/10.1016/j.micromeso.2005.05.016>
- [21] Chen D., Shao H., Yao W., Huang B.: Fourier transform infrared spectral analysis of polyisoprene of a different microstructure. *International Journal of Polymer Science*, **2013**, 937284 (2013).
<https://doi.org/10.1155/2013/937284>
- [22] Masa A., Saito R., Saito H., Sakai T., Kaesaman A., Lopattananon N.: Phenolic resin-crosslinked natural rubber/clay nanocomposites: Influence of clay loading and interfacial adhesion on strain-induced crystallization behavior. *Journal of Applied Polymer Science*, **133**, 43214 (2016).
<https://doi.org/10.1002/app.43214>
- [23] Manna A. K., De P. P., Tripathy D. K., De S. K., Peiffer D. G.: Bonding between precipitated silica and epoxidized natural rubber in the presence of silane coupling agent. *Journal of Applied Polymer Science*, **74**, 389–398 (1999).
[https://doi.org/10.1002/\(SICI\)1097-4628\(19991010\)74:2<389::AID-APP21>3.0.CO;2-L](https://doi.org/10.1002/(SICI)1097-4628(19991010)74:2<389::AID-APP21>3.0.CO;2-L)
- [24] Hayemasae N., Zakaria N. H., Ismai H.: Epoxidized natural rubber/modified sepiolite composites. *KGK Kautschuk Gummi Kunststoffe*, **70**, 18–25 (2017).
- [25] Wittenberg E., Meyer A., Eggers S., Abetz V.: Hydrogen bonding and thermoplastic elastomers – A nice couple with temperature-adjustable mechanical properties. *Soft Matter*, **14**, 2701–2711 (2018).
<https://doi.org/10.1039/C8SM00296G>
- [26] Vennemann N., Wu M.: Thermoelastic properties and relaxation behavior of S-SBR/silica vulcanizates. *Rubber World*, **246**, 18–23 (2012).
- [27] Matchawet S., Kaesaman A., Vennemann N., Kumerlöwe C., Nakason C.: Effects of imidazolium ionic liquid on cure characteristics, electrical conductivity and other related properties of epoxidized natural rubber vulcanizates. *European Polymer Journal*, **87**, 344–359 (2017).
<https://doi.org/10.1016/j.eurpolymj.2016.12.037>
- [28] Srinivasan N., Bokamp K., Vennemann N.: New test method for the characterisation of filled elastomers. *KGK Kautschuk Gummi Kunststoffe*, **58**, 650–655 (2005).
- [29] Bhowmick A. K., Mangaraj D.: Vulcanization and curing techniques. in ‘Rubber products manufacturing technology’ (eds.: Bhowmick A. K., Hall M. M., Benarey H. A.) Marcel Dekker, New York, 315–396 (1994).
- [30] Gopi Sathi S., Harea E., Machů A., Stoček R.: Facilitating high-temperature curing of natural rubber with a conventional accelerated-sulfur system using a synergistic combination of bismaleimides. *Express Polymer Letters*, **15**, 16–27 (2021).
<https://doi.org/10.3144/expresspolymlett.2021.3>
- [31] Kruželák J., Sýkora R., Hudec I.: Sulphur and peroxide vulcanisation of rubber compounds – Overview. *Chemical Papers*, **70**, 1533–1555 (2016).
<https://doi.org/10.1515/chempap-2016-0093>
- [32] Chen H., Zheng M., Sun H., Jia Q.: Characterization and properties of sepiolite/polyurethane nanocomposites. *Materials Science and Engineering: A*, **445**, 725–730 (2007).
<https://doi.org/10.1016/j.msea.2006.10.008>

- [33] Maria H. J., Lyczko N., Nzihou A., Joseph K., Mathew C., Thomas S.: Stress relaxation behavior of organically modified montmorillonite filled natural rubber/nitrile rubber nanocomposites. *Applied Clay Science*, **87**, 120–128 (2014).
<https://doi.org/10.1016/j.clay.2013.10.019>
- [34] Pasbakhsh P., Ismail H., Fauzi M. A., Bakar A. A.: Influence of maleic anhydride grafted ethylene propylene diene monomer (MAH-g-EPDM) on the properties of EPDM nanocomposites reinforced by halloysite nanotubes. *Polymer Testing*, **28**, 548–559 (2009).
<https://doi.org/10.1016/j.polymertesting.2009.04.004>
- [35] Bhattacharya M., Bhowmick A. K.: Polymer–filler interaction in nanocomposites: New interface area function to investigate swelling behavior and Young’s modulus. *Polymer*, **49**, 4808–4818 (2008).
<https://doi.org/10.1016/j.polymer.2008.09.002>
- [36] Wu Y-P., Ma Y., Wang Y-Q., Zhang L-Q.: Effects of characteristics of rubber, mixing and vulcanization on the structure and properties of rubber/clay nanocomposites by melt blending. *Macromolecular Materials and Engineering*, **289**, 890–894 (2004).
<https://doi.org/10.1002/mame.200400085>
- [37] Varghese S., Karger-Kocsis J., Gatos K. G.: Melt compounded epoxidized natural rubber/layered silicate nanocomposites: Structure-properties relationships. *Polymer*, **44**, 3977–3983 (2003).
[https://doi.org/10.1016/S0032-3861\(03\)00358-6](https://doi.org/10.1016/S0032-3861(03)00358-6)
- [38] Carretero-Gonzalez J., Retsos H., Verdejo R., Toki S., Hsiao B. S., Giannelis E. P., López-Manchado M. A.: Effect of nanoclay on natural rubber microstructure. *Macromolecules*, **41**, 6763–6772 (2008).
<https://doi.org/10.1021/ma800893x>
- [39] Chenal J-M., Gauthier C., Chazeau L., Guy L., Bomal Y.: Parameters governing strain induced crystallization in filled natural rubber. *Polymer*, **48**, 6893–6901 (2007).
<https://doi.org/10.1016/j.polymer.2007.09.023>
- [40] Masa A., Iimori S., Saito R., Saito H., Sakai T., Kaesaman A., Lopattananon N.: Strain induced crystallization behavior of phenolic resin crosslinked natural rubber/clay nanocomposites. *Journal of Applied Polymer Science*, **132**, 42580 (2015).
<https://doi.org/10.1002/app.42580>
- [41] Sainumsai W., Suchiva K., Toki S.: Influence of sulphur crosslink type on the strain-induced crystallization of natural rubber vulcanizates during uniaxial stretching by *in situ* WAXD using a synchrotron radiation. *Materials today: Proceedings*, **17**, 1539–1548 (2019).
<https://doi.org/10.1016/j.matpr.2019.06.179>
- [42] Ikeda Y., Yasuda Y., Hijikata K., Tosaka M., Kohjiya S.: Comparative study on strain-induced crystallization behavior of peroxide cross-linked and sulfur cross-linked natural rubber. *Macromolecules*, **41**, 5876–5884 (2008).
<https://doi.org/10.1021/ma800144u>
- [43] Takenaka M.: Analysis of structures of rubber-filler systems with combined scattering methods. *Polymer Journal*, **45**, 10–19 (2013).
<https://doi.org/10.1038/pj.2012.187>
- [44] Osaka N., Kato M., Saito H.: Mechanical properties and network structure of phenol resin crosslinked hydrogenated acrylonitrile-butadiene rubber. *Journal of Applied Polymer Science*, **129**, 3396–3403 (2013).
<https://doi.org/10.1002/app.39010>
- [45] Masa A., Soontaranon S., Hayemasae N.: Influence of sulfur/accelerator ratio on tensile properties and structural inhomogeneity of natural rubber. *Polymer (Korea)*, **44**, 519–526 (2020).
<https://doi.org/10.7317/pk.2020.44.4.519>

Research article

Valorization of nylon and viscose-rayon textile yarn wastes for fabricating nanocomposite films

Prince Kumar Mishra^{ID}, Arihant Ahuja^{ID}, Bhupender Kumar Mahur^{ID}, Vibhore Kumar Rastogi^{*ID}

Department of Paper Technology, Indian Institute of Technology Roorkee, 247667 Uttarakhand, India

Received: 7 July 2022 accepted in revised form 19 September 2022

Abstract. In this work, two types of pre-consumer textile waste, namely, viscose-rayon and nylon yarn, were utilized for nanocomposite filmmaking using the green solvent casting method. The nanocellulose was extracted from the viscose-rayon and incorporated as a filler in nylon films. The effects of nanocellulose on thermal, chemical, mechanical, structural, and barrier properties of films containing 0.1, 0.5, and 1 wt% nanocellulose were investigated in detail. The thermal study of films using differential scanning calorimetry (DSC) confirmed that adding nanocellulose into the nylon matrix does not act as a nucleating agent as nylon yarn waste already had ~5 wt% nucleating agents (thermogravimetric analysis, TGA). Rather, a decrease in the crystallinity of films was determined with the addition of nanocellulose. No significant changes in the mechanical properties were observed for nylon nanocomposite films. However, an increased hydrogen bonding was observed between the nanocellulose and nylon, along with the reorientation of hydrogen bonds (Fourier-transform infrared spectroscopy, FTIR). A dense cross-section and structured surface were observed in the scanning electronmicroscopic (SEM) images for nanocomposite films. The water vapor barrier of films increased as the concentration of nanocellulose increased in the nylon films and resulted in a 55% decrease in water vapor transmission rate (WVTR) compared to neat nylon film.

Keywords: nanocomposites, nylon yarn textile waste, viscose-rayon yarn waste, nanocellulose, waste valorization

1. Introduction

The textile industry generates a large amount of waste, leading to waste accumulation, greenhouse gas emissions, and environmental pollution. Textile wastes are often classified as pre-consumer (fibers, yarns, fabrics, and mixed fiber/yarn/fabric with chemicals), post-consumer (discarded garments), and industrial waste (technical textiles, carpets, durries, conveyor belts, industrial ropes, drive belts, medical textiles). Most of these discarded textiles can be recycled but are landfilled or incinerated due to the cost involved [1]. Textile waste can be valorized depending on its type, form, and usability. A recent review on the valorization potential of textile wastes is presented elsewhere [2]. Textile wastes could be valorized for numerous applications, including textile manufacturing, energy generation [3], building

materials [4], packaging film [5], paper [6], and composites [7]. Textile waste includes fiber/yarn/fabric of cotton, cellulose (viscose, flax, hemp, kapok, rami), wool, polyester (PET), nylon-6, acrylic, and polypropylene.

Recently, viscose-rayon has been gaining much attention as a raw material for green textiles [8]. It is a manmade regenerated cellulosic textile produced from the wet spinning process of natural sources like woods [9, 10] that are later converted into yarns. Yarns are further used in textile weaving, hand-knotted carpet weaving, home furnishing, and industrial textile applications [9, 10]. In the textile weaving processes, a huge amount of cut viscose-rayon yarns waste is generated [11, 12], which is either incinerated or landfilled [1, 13]. A few research articles have been reported on the valorization potential of

*Corresponding author, e-mail: vibhore.rastogi@pt.iitr.ac.in
© BME-PT

viscose-rayon for energy production [14], reinforcement in building materials [4], reinforcement in polymer composite [15], and extraction of nanocellulose (NC) [16]. Viscose-rayon consists of pure alpha-cellulose and hence possesses numerous surface hydroxyl groups, which are reactive and interact strongly with the polar polymer matrix; otherwise, the presence of lignin and hemicellulose as in native cellulose fibers resulted in weak interactions with a polar matrix like nylon [20].

Nylon-6 is a synthetic polymer extensively used in textile production [17], packaging [18], composites [19], and many other applications [3, 20–23] due to its excellent mechanical and thermal properties, transparency, and resistance to chemicals [24]. Consequently, an enormous amount of nylon waste is generated annually, which needs urgent attention. Packaging and composite waste of nylon often contain multi-layered components [25], which makes recycling or valorization cumbersome. However, a few research articles on nylon textile waste valorization are reported for applications like insulation material [21], building material [20], energy [23], and filtration membrane [22] due to the simplicity and purity of nylon-6 in textile waste. The industrial-grade of nylon-6 is often reinforced with cellulosic-based fibers like flax, hemp, hardwood [19], nano/micro-fibrillated cellulose (NFC/MFC) [26], and cellulose nanocrystals (CNC) [27] to enhance the mechanical properties of composites. The tensile strength increased by 23.82% with the addition of fibers, and lower crystallinity was observed with the addition of NFC/MFC and CNC. Apart from cellulosic fillers, graphene has been previously added to the recycled nylon-6 matrix to enhance the tensile strength of the films at a lower concentration of 2 wt% [28]. In another study impact strength of recycled nylon-6 was improved by 55.5% with the addition of Hytrel (elastomer) [29]. However, for packaging applications, both mechanical and barrier properties (like oxygen transmission rate, OTR, and water vapor transmission rate, WVTR) of pure nylon-6 were targeted by blending with nanoclays like montmorillonite [30] and Cloisite 30B [31], which increased oxygen barrier by 2.8 times. With the continuous trend of sustainability, green fillers are favored. In addition, waste management practices leading to waste-to-wealth and circular economy are the prime concern of many countries [32]. Nylon-6 is used as a packaging material where an oxygen barrier is required, but it absorbs

water and loses its barrier properties because it is hygroscopic. Therefore, it is a sandwiched layer for packaging applications [18]. Inorganic materials such as nanoclay have enhanced water and oxygen barrier properties of nylon-6 [30]. The barrier properties of nylon-6 textile waste can also be enhanced using bio-based nanomaterials like nanocellulose, but it is never reported and explored. Due to the presence of polar groups in nylon-6, it is expected to have higher compatibility with the hydroxyl groups of cellulose [20], along with good dispersion. Thus, compatibilizers or coupling reagents are not needed for composites.

In the present study, powdered nanocellulose was incorporated (derived from viscose-rayon textile waste) in the nylon-6 matrix (obtained from nylon textile yarn waste) to produce nanocomposite films. A detailed raw material analysis of nylon textile waste was conducted, revealing a few nucleating agents, plasticizers, and antioxidants in nylon textile yarn waste. Nanocomposite films containing a variable amount of nanocellulose were characterized for their morphological (field emission scanning electron microscopy, FESEM; atomic force microscopy AFM), chemical (FTIR), thermal (TGA, DSC), mechanical (universal testing machine, UTM), and barrier properties (WVTR, contact angle). This work emphasized the importance of nanocellulose extraction from viscose yarn waste and used it as a green filler for the nylon matrix. In addition, nylon yarn textile waste was proposed as a cheap alternative to expensive industrial-grade nylon-6 for various appropriate applications.

2. Materials and methods

2.1. Materials

Nylon scrap yarn waste was collected from Kusumgar Corporates Pvt. Ltd. (Textile Mill, Vapi, Gujrat, India), and the viscose-rayon yarn waste was obtained from a local yarn vendor (Bhadohi, Uttar Pradesh, India). Sulphuric acid (97% pure) and acetic acid (98% pure) were purchased from Avantor Performance Materials India Limited (India).

2.2. Sample preparation

2.2.1. Extraction of nanocellulose from viscose-rayon yarn waste

The acid hydrolysis technique was adopted from elsewhere [16] to extract nanocellulose from viscose yarn waste. First, the viscose yarn was cut into small

fibers, washed thoroughly with hot water, and dried. The 64 wt% H₂SO₄ solution was prepared and cooled in an ice bath. 1 g of viscose yarn was slowly added to 20 ml of cold 64 wt% H₂SO₄ solution under stirring to avoid the decomposition of viscose yarn. Further, heating was done at 40 °C in an oil bath placed over a hot plate magnetic stirrer. The hydrolyzed sample was collected after the reaction time of 30 minutes and appeared white, suggesting no over degradation of nanocellulose, which would otherwise turn dark yellowish [16]. The suspension was immediately cooled by adding 400 ml of cold deionized water to stop the reaction, and the pH was also increased from 1 to 3. A turbid supernatant of nanocellulose suspension was formed and kept for settling down for over 48 hours that was later drained and collected. To eliminate the free excess acid from the nanocellulose, a semi-permeable membrane was used for dialysis against deionized water for 72 hours until a neutral pH was attained. Finally, the nanocellulose sample was ultrasonicated, refrigerated at –40 °C, and further lyophilized at –70 °C to obtain nanocellulose powder.

2.2.2. Fabrication of neat nylon and nylon nanocomposite films

Nylon yarn waste was washed thoroughly with hot water to remove any surface impurities and later dried and stored at 23 °C and 50% RH. Neat nylon and nanocomposite films were developed using acetic acid as a green solvent by the solution casting method. 0.4 g of nylon yarn was dissolved in 27 ml of acetic acid (1.5% w/v). The stirring was done for 45 minutes at 80 °C using a temperature-controlled hot plate magnetic stirrer. The nanocellulose powder derived from viscose yarn waste was dispersed into nylon acetic acid solution under continuous stirring for 5 minutes with a concentration of 0% (neat, control), 0.1, 0.5, 1, and 2 wt%. The resulting solution was then cast into 90 mm diameter glass Petri dishes using a surface leveler to obtain films of uniform thickness. The solvent was evaporated in a hot air oven at 50±3 °C for 12 hours, and films were peeled off from the Petri dishes. Before physical, chemical, and mechanical testing, the prepared nylon nanocomposite films were stored at 23 °C and 50% RH in a regulated environment [33]. All prepared films will be denoted as Neat Nylon (nylon film with 0% nanocellulose), Nylon-0.1% (nylon film with 0.1% nanocellulose), Nylon-0.5% (nylon film with 0.5%

nanocellulose), Nylon-1% (nylon film with 1% nanocellulose), and Nylon-2% (nylon film with 2% nanocellulose) throughout the text.

2.3. Characterization

2.3.1. Fourier transform infrared spectroscopy (FTIR)

Attenuated total reflection Fourier-transform infrared spectroscopy or ATR-FTIR was conducted to determine the chemical composition of nylon yarn waste, viscose yarn waste, nanocellulose, and nanocomposite films, using Perkin Elmer, C91158 spectrophotometer (Chicago, USA). FTIR spectra were collected between 4000 and 500 cm⁻¹ wavenumbers with a resolution of 4 cm⁻¹ and averaged over 16 scans. The spectra were baseline corrected and normalized for comparative analysis to determine the changes in chemical content.

2.3.2. Field emission-scanning electron microscopy (FESEM)

The variation in surface and cross-section morphologies of nylon yarn waste, viscose yarn waste, nanocellulose, and nanocomposite films was inspected by Field Emission Scanning Electron Microscopy (MIRA3 LMH Tescan, USA), operating at an accelerating voltage of 5 kV. The cross-sections were obtained by cryo-fracturing in liquid nitrogen. Each sample was sputter-coated with a thin gold layer (2–10 nm) using glow discharge plasma to improve conductivity and picture clarity [34].

2.3.3. Atomic force microscopy (AFM)

The nanoscale's topography of nanocellulose produced from viscose waste was further studied with atomic force microscopy (AFM, Bruker Dimension Icon AFM, USA). A dilute suspension of nanocellulose was probe sonicated and drop cast over a glass slide. The glass slide was dried overnight at ambient conditions, and images were obtained in Scan Assist mode using silicon nitride tips. The diameters of nanocellulose were analyzed using Nanoscope analysis software.

2.3.4. Differential scanning calorimetry (DSC)

The thermal behavior of nylon yarn waste and all fabricated nylon-based nanocomposite films was studied using differential scanning calorimetry (TA Instruments, New Castle, DE, USA, DSC 25) under a constant nitrogen gas flow. Double heating cycles

with an intermediate cooling cycle were performed on each 5 mg weight sample (sealed in aluminum pans). To erase the thermal history, samples were heated from 0 to 250 °C at 10 °C/min during the first heating cycle and maintained at 250 °C for 2 minutes before being cooled to 0 °C at 10 °C/min. The sample was then heated a second time at 10 °C/min from 0 to 250 °C. Three measurements were taken for each sample. The thermogram's second heating cycle was used to determine the glass transition (T_g), melting point (T_m), and melting enthalpy (H_m). The cooling cycle was used to measure the temperature of melt crystallization (T_{mc}). Equation (1) was used to calculate the total crystallinity (X_c) of nylon yarn waste and nylon-based nanocomposite:

$$X_c = \frac{\Delta H_m}{\Delta H_m^0 (1 - \alpha)} \cdot 100 \quad (1)$$

where the melting enthalpy of the generated crystals in the nylon-6 is ΔH_m , while the theoretical enthalpy value for a 100% crystalline nylon-6 is ΔH_m^0 (190 J/g) [35], and α is the weight fraction of nanocellulose content in nanocomposite films.

2.3.5. Thermogravimetry analysis (TGA)

The thermal degradation behavior of samples was studied using thermogravimetric (TA Instruments, New Castle, DE, USA, TGA 55). The sample weight of around 5 mg was heated from 25 to 600 °C at 10 °C/min (ASTM E1131). The testing was conducted in a nitrogen gas atmosphere with a 20 ml/min gas flow rate.

2.3.6. Thickness and mechanical properties of films

A digital micrometer (Lorentzen & Wettres, Stockholm, Sweden) was used to measure the thickness of the neat nylon and nanocomposite films. Each sample was measured at five different locations and reported as a mean with a standard deviation.

Mechanical properties such as tensile strength and percentage elongation at break were determined using the Universal Testing Machine (INSTRON 3365, Integrated System Solutions, Bengaluru, India). Rectangular strips of dimension 10×40 mm² were cut by a cutting die and tested with a primary grip separation of 20 mm at a 1 mm/min crosshead speed. Each sample was replicated three times.

2.3.7. Water contact angle and water vapor transmission rate (WVTR) of films

The surface wettability of films was measured by the sessile drop test method using a contact angle analyzer (DSA25 KRÜSS GmbH, Germany). A droplet volume of 5 µl was placed on films using a microsyringe. The measurements were repeated three times per sample.

As described in ASTM E96/E96M-16, the desiccant method was used to calculate the WVTR of all samples. Around 10 g of dried silica gel was placed in glass vials with an opening mouth area of 2.27 cm². The developed films were securely sealed on top of the glass vials. The glass vials were then placed in a desiccator with a saturated sodium chloride solution to maintain a relative humidity of 75%. The desiccators were then sealed with paraffin wax and kept in a 25 °C oven. The weights of the cups were taken at the start and every 24 hours for a total of 10 days. Each sample was replicated three times. The slope [g/day] of the curve drawn between weight and days, divided by transfer area, *i.e.*, 2.27 cm², was used to calculate WVTR [g/(m²·day)].

2.4. Statistical analysis

With the help of statistical software SPSS ver. 26, the experimental data were statistically analyzed to estimate the analysis of variance (IBM Corporation, Armonk, USA). The Tukey *post hoc* test ($p < 0.05$) was used to see if there were any significant changes. Small alphabets in superscripts were assigned next to the values. Different letters in the respective column indicate a significant difference in values considering a 95% confidence level.

3. Results and discussion

3.1. The threshold concentration of nanocellulose in nylon films

The nylon films with varying concentrations of nanocellulose were prepared and placed over the printed white logo on black paper, presented in Figure 1. All films appeared to be transparent, smooth, and without cracks. As the concentration of nanocellulose increased, the films became slightly cloudier. At 2 wt% nanocellulose, the film appeared white, brittle, and developed cracks. The brittle nature of the film might be due to increased bonding between the hydroxyl groups of nanocellulose and amine group of nylon, leading to arresting of nylon's crystallization

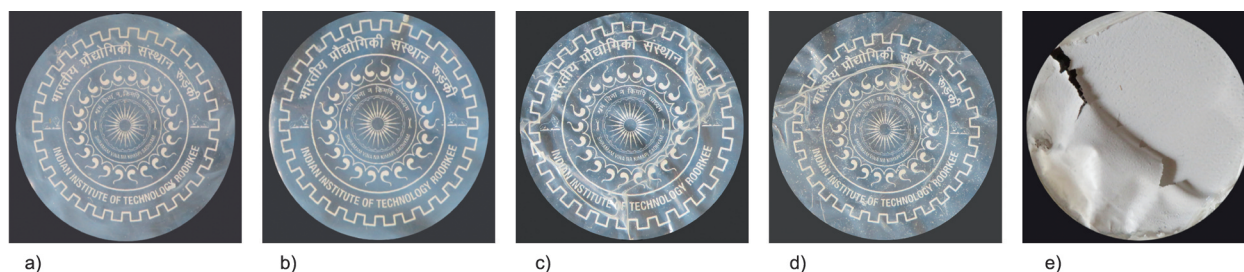


Figure 1. Photographs of solvent cast nylon-nanocellulose films showing (a) neat Nylon film, (b) Nylon-0.1% film, (c) Nylon-0.5% film, (d) Nylon-1% film, and (e) Nylon-2% film.

into the amorphous form and thus resulting in disrupted internal bonding between the nylon polymeric chains leading to cracks [36]. Therefore, nanocellulose up to 1 wt% was selected as a threshold concentration of filler in nylon films, and Nylon-2% was not characterized further.

3.2. The thickness of the films

The thickness plays a crucial role in a polymer's physical and functional properties. Table 1 indicates the thickness of the nanocomposite films. It can be observed that all films were uniform and varied in

Table 1. The thickness of neat nylon and nylon nanocomposite films.

Sample	Thickness [μm]
Neat nylon	48 \pm 2.74 ^a
Nylon-0.1%	54 \pm 5.48 ^a
Nylon-0.5%	49 \pm 4.18 ^a
Nylon-1%	53 \pm 2.71 ^a

The mean and standard deviation are used to express the data. ^aDifferent letters in the same column indicate significant differences ($p < 0.05$). (There are no significant differences.)

thickness in the range of 48–53 μm . No significant differences in thickness were determined for all films. The thickness of the films was also aligned with the thickness observed in the FESEM images performed on the cross-section of the films (will be shown later).

3.3. Fourier transform infrared spectroscopy

FTIR was used to analyze raw fiber waste, fabricated nanocellulose, and nanocomposite films. Figure 2a shows the absorption bands for viscose-rayon yarn waste and extracted nanocellulose; a broad peak around 3400 cm^{-1} (–OH stretching), 2920 cm^{-1} (CH_2 symmetrical and asymmetrical stretching), 1642 cm^{-1} (C=O stretching), 1432 cm^{-1} (CH_2 symmetric bending), 1372 cm^{-1} (C–H bending), 1150 cm^{-1} (C–O–C asymmetric stretching), 1020 cm^{-1} (C–O stretching), 895 cm^{-1} (C–O–C stretching) and 670 cm^{-1} (C–H bending), as described previously [16, 37–43]. Similarly, the characteristics peaks of nylon yarn waste (Figure 3a) shows a broad peak around 3400 cm^{-1} (–OH stretching), 3291 cm^{-1} (N–H stretching bond), 2925 cm^{-1} (CH_2 asymmetric stretching), 2853 cm^{-1}

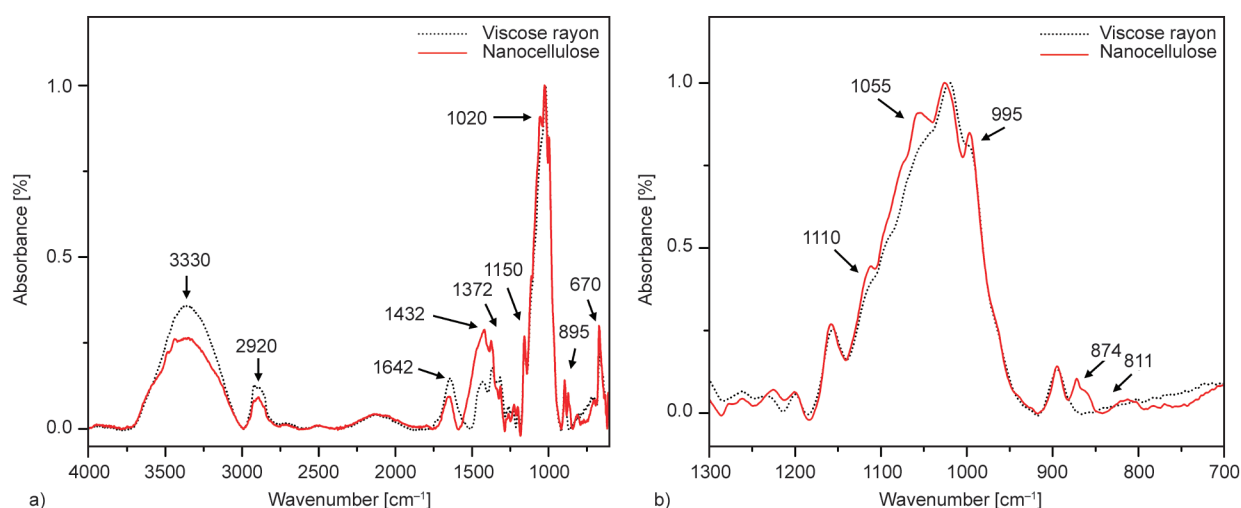


Figure 2. FTIR plots of viscose yarn and nanocellulose in the wavenumber of (a) 4000 to 600 cm^{-1} and (b) magnified at 1300 to 700 cm^{-1} .

(C–H stretching), 1633 cm^{-1} (C=O (amide-I) stretching), 1534 cm^{-1} (N–H (amide-II) deformation), 1367 cm^{-1} (CH_2 wagging), and 1261 cm^{-1} (CH_3 bending), 1025 cm^{-1} (C–O stretching) and 695 cm^{-1} (C–H bending), as reported in previous literature [44]. From Figure 2a, the appearance of new peaks at 874 and 811 cm^{-1} was only observed in the nanocellulose sample representing C–O– SO_3 group vibration, attributed to the presence of sulfonate esters on the nanocellulose surface during sulphuric acid hydrolysis [45, 46]. Several other bands related to sulfonate esters were also reported in the literature ranging from 1350 to 750 cm^{-1} [45]. Due to the increase in the surface area of nanocellulose compared to viscose, it was expected that the peak intensity around 3330 cm^{-1} should be higher for nanocellulose because of more free hydroxyls (–OH) at the surface. Rather a decrease in the 3330 cm^{-1} peak was visible in the nanocellulose sample. A similar observation was noted qualitatively in the case of nanocellulose extracted using sulphuric acid [16]. This decrease in peak intensity results from converting a few surface hydroxyls of nanocellulose with sulfonyl groups, thereby reducing the overall hydroxyls present on the surface. Moreover, the intensity of several nanocellulose peaks (1432 and 1371 cm^{-1}) was higher than viscose. The higher peak at 1110 , 1055 , and 995 cm^{-1} might be due to higher C–O–C ether linkages that were developed after acid hydrolysis and thereby resulted in an increased crystallinity of nanocellulose [47] (Figure 2b). The spectra were normalized on cellulose ring-related bands (1200 to 850 cm^{-1}). The crystallinity index was calculated for viscose-rayon and nanocellulose from the peak intensity

ratio of $1373/2900\text{ cm}^{-1}$ [48]. The crystallinity index for viscose and nanocellulose was 1.48 and 2.82 , respectively. The increased crystallinity of nanocellulose compared to viscose fiber is in line with the previous studies [16], as sulphuric acid degrades the amorphous part of cellulose and thus increases the crystallinity of cellulose.

To compare the chemical composition of nylon yarn waste and nylon films, the spectra were normalized at 1168 cm^{-1} [49, 50]. From Figure 3a, a broad peak around 3460 cm^{-1} (–OH stretching) was observed in nylon yarn waste, which is usually absent or very weak in the spectrum of industrial-grade nylon pellets [51]. It indicates the presence of additives like talc powder (as a nucleating agent) or phenols (antioxidant) in the nylon yarn that is usually added to enhance the mechanical properties and thermal stability, respectively, during the manufacturing process of nylon fibers for textile application [52]. The presence of phenols in nylon yarn waste was further confirmed by a peak at 750 cm^{-1} . Hot water washing of nylon yarn before film formation might remove the extra talc on the surface of the yarn and lead to a reduction in the peak of 3400 cm^{-1} in the neat nylon film. Similarly, solvent processing of nylon yarn at 80°C completely oxidized the antioxidant present, and hence peak at 750 cm^{-1} was absent in films. Peaks at 17201 and 1740 cm^{-1} (C=O stretching) in nylon yarn indicated the presence of plasticizers that are often added to nylon during the processing of nylon yarn to avoid runnability issues and to provide elasticity to yarn [17]. It is also observed that peak intensity at 3300 cm^{-1} (hydrogen-bonded N–H stretching) increased for neat nylon film compared to nylon

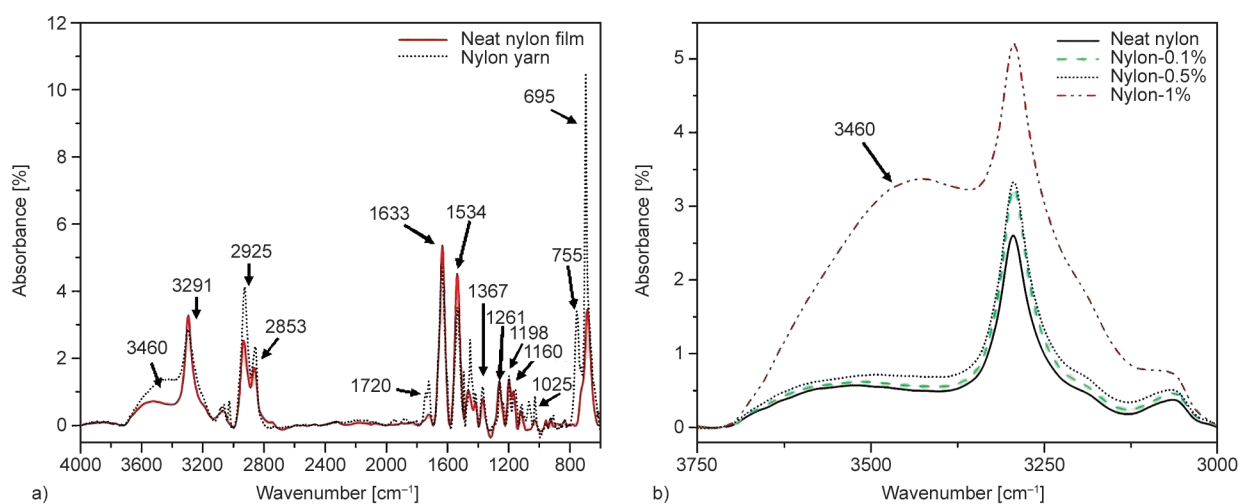


Figure 3. FTIR spectra of (a) nylon yarn and neat nylon film and (b) neat nylon and nylon nanocomposite films containing nanocellulose.

yarn, which is attributed to solvent processing providing easy mobility to polymeric chains leading to new hydrogen bond formation. In contrast, a reduction in the peak intensity at 695, 1198, 1367, 1418, 2925, and 2850 cm^{-1} for neat nylon film was evident compared to the nylon yarn waste. This observation is attributed to the conversion of α -crystalline form (stable) of nylon to γ -crystalline form (metastable) that was mediated through solvent processing [51]. As the concentration of nanocellulose in the films was very low ($\leq 1\%$) and the limitations of FTIR to sense the material up to a few microns deep inside the film [53], the prominent characteristic peak of nanocellulose (1200 to 900 cm^{-1}) was not visible in the nanocomposite films (data not shown). From Figure 3b, with the addition of nanocellulose in the nylon films, a continuous increase of broad peak at 3460 cm^{-1} was observed, attributed to the formation of new hydrogen bonds with the OH groups of cellulose and amide groups of nylon [51]. At the maximum concentration of nanocellulose in the film (1%), the peak intensity at 3460 cm^{-1} increased abruptly, possibly due to the increased hydrogen bonding between the nanocellulose and the nylon that reoriented the original hydrogen bonding in the nylon polymeric chain [51].

3.4. Field emissions-scanning electron microscopy

FESEM was used to analyze the surface morphology and cross-section of fiber waste, nanocellulose, and prepared nylon nanocomposite films. Figure 4a and Figure 4c illustrate the surface of the viscose and nylon yarn waste (as received), respectively. From the surface of viscose yarn, fine longitudinal lines or striations of a single viscose fiber are visible. The flower-like surface of viscose fiber is due to the shape of the spinneret used in the wet spinning of viscose fibers. In contrast, the nylon yarn waste showed a uniform rod-like surface appearance with few impurities at the surface that might be talc powder (Figure 4d), which were absent from the viscose yarn (Figure 4b). The diameter from FESEM images was observed as $35.71 \pm 9.42 \mu\text{m}$ for nylon yarn and $11.47 \pm 4.01 \mu\text{m}$ for viscose-rayon yarn.

Nanocellulose was extracted using viscose-rayon yarn waste by acid hydrolysis. The FESEM of nanocellulose was performed by drop-casting the nanocellulose water suspension onto the glass plate. The nanocellulose appeared as small aggregates

(Figure 5a) with irregular shapes (Figure 5b). The irregular shapes of nanocellulose were due to strong swelling treatments by NaOH in the wet spinning process of viscose-rayon fiber from wood and had already been reported in past research [16]. At higher magnification, nanocellulose aggregates' diameter appeared to be less than 100 nm (Figure 5b).

The FESEM images of all the nylon films are shown in Figure 6. The surface image of the neat nylon film (Figure 6a) was smooth and had a uniform structure without any visible impurities, cracks, or agglomeration. With the addition of nanocellulose, the structuring of the surface (Figure 6b–6d) was observed when compared to neat nylon. This surface structuring could be due to the reorientation of hydrogen bonds in nylon polymeric chains due to the formation of new hydrogen bonds between nylon and nanocellulose (as seen previously) [51]. In the FESEM of cryo-fractured cross-section images, the thickness of all the films was around 50 μm (Figure 6e–6h). At higher magnification (Figure 6i), minute pores were observed in the neat nylon film due to solvent evaporation during the casting process. A few nanocellulose clusters were visible (marked with arrows) in the nanocomposite film at a low concentration of nanocellulose (0.1 and 0.5 wt%) (Figure 6j–6k), showing a better dispersion of nanocellulose in the nylon matrix. As the concentration of nanocellulose was increased to 1 wt% in the films, the pores were not visible (Figure 6l). These pores were closed due to the hydrogen bonding between nanocellulose and nylon and nanocellulose as a filler material that filled the pores, thus forming a denser structure required for high-barrier packaging applications.

3.5. Atomic force microscopy

The AFM micrograph of nanocellulose extracted from viscose-rayon yarn waste after 30 min of the hydrolysis reaction was performed on a $2 \times 2 \mu\text{m}^2$ sample size. It was observed that nanoparticles of irregular shape were present (Figure 7) and had an average diameter size of $65.03 \pm 10.15 \text{ nm}$. As previously reported in the literature, due to the many hydroxyl groups and high surface area [1, 54, 55], the drying process leads to agglomeration of nanocellulose during the AFM analysis, hence diminishing the specific surfaces by forming strong hydrogen bonds [56]. The TEM has seen similar fragmented forms in the literature [57].

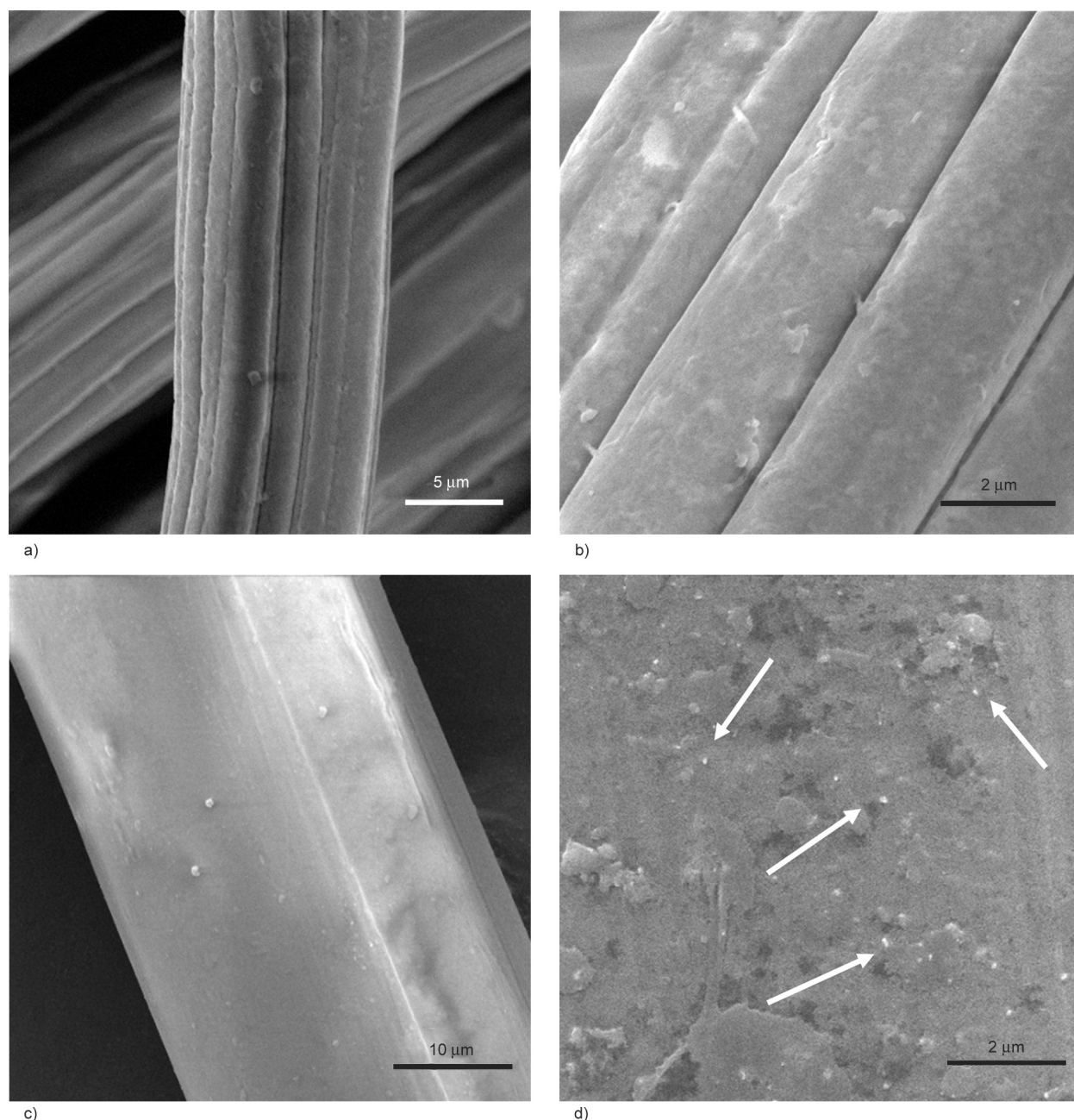


Figure 4. FESEM image of (a) viscose-rayon yarn waste, (b) viscose-rayon yarn waste magnified, (c) nylon yarn waste, and (d) nylon yarn waste magnified.

3.6. Differential scanning calorimetry

The crystallization behavior of nylon yarn waste and nylon films was investigated by DSC with first cooling and second heating curves, as shown in Figure 8. For nylon yarn waste, T_m close to 219 °C signifies the presence of nylon-6 in the yarn waste [51]. The higher T_{mc} of nylon yarn waste (186 °C) than the pure nylon-6 (180 °C) [58] might be attributed to the presence of nucleating agents in the yarn like talc powder, boron nitride, or any organic phosphates (as seen previously). From Figure 8a, fully developed melt crystalliza-

tion peaks (T_{mc}) were observed for different samples during the cooling cycle. Clearly, the crystallization of nylon yarn occurred in a broad temperature range ($T_{onset} = 193.75$ °C, $T_{endset} = 176.17$ °C), whereas the crystallization of neat nylon and other films occurred in a narrow temperature regime ($T_{onset} = 191.94$ – 193.38 °C, $T_{endset} = 178.5$ – 177.16 °C), which signifies the effect of solvent processing favoring the crystallization of nylon by providing more mobility to the polymeric chains. A similar observation reported the effect of solvent processing on crystallization [36].

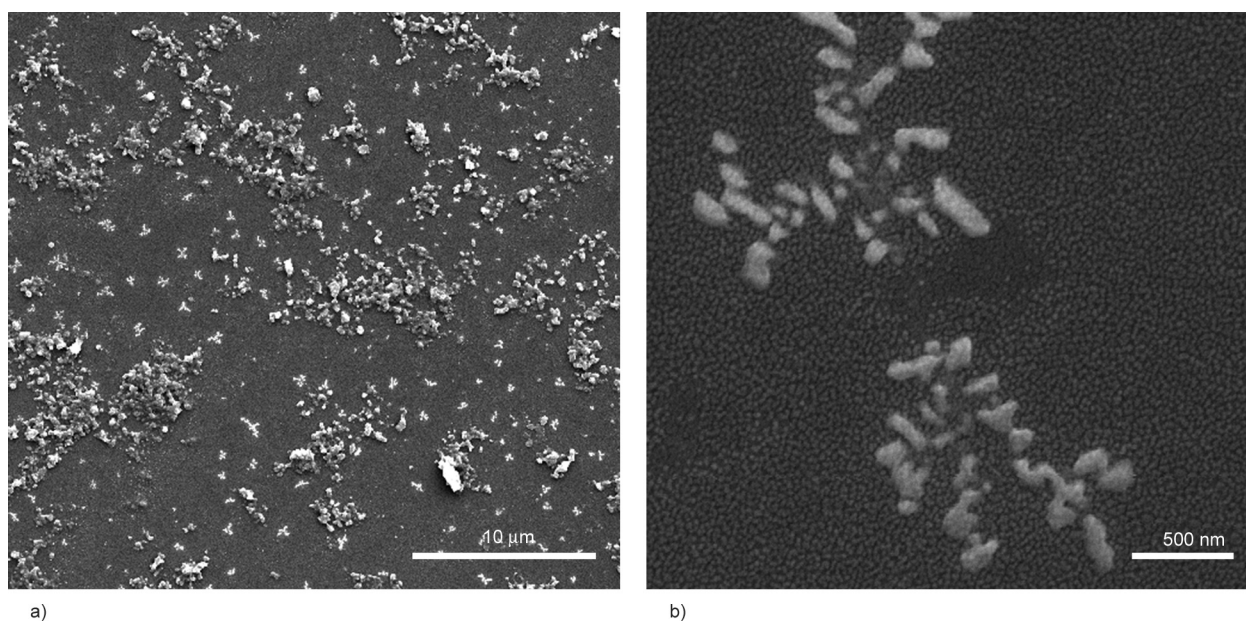


Figure 5. FESEM image of (a) nanocellulose and (b) magnified image of nanocellulose.

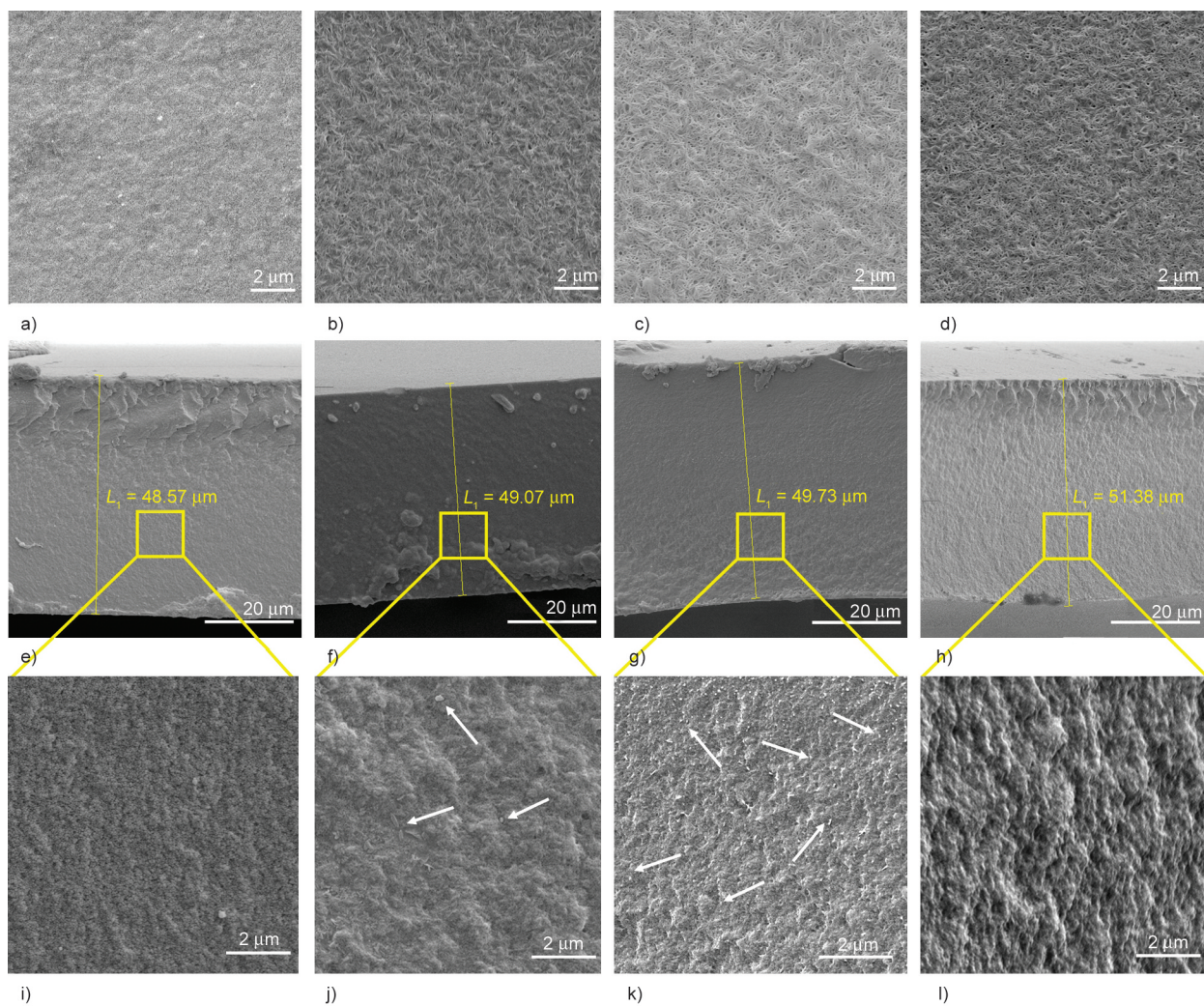


Figure 6. FESEM images of nylon- nanocellulose composite films illustrating the surface morphology of (a) neat nylon film, (b) Nylon-0.1% film, (c) Nylon-0.5% film, (d) Nylon-1% and cross-section morphology of (e) neat nylon film, (f) Nylon-0.1% film, (g) Nylon-0.5% film, (h) Nylon-1% film, and magnified cross-section of (i) neat nylon film, (j) Nylon-0.1% film, (k) Nylon-0.5% film, (l) Nylon-1% film.

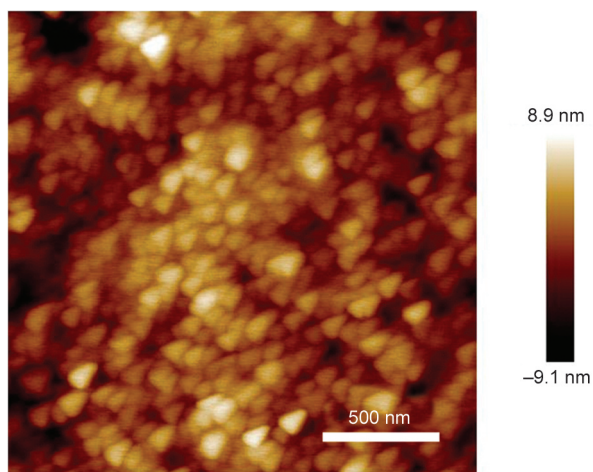


Figure 7. AFM image of nanocellulose extracted from viscose-rayon yarn waste.

Figure 8b reflects the glass transition temperature and melting peaks of nylon yarn and nylon nanocomposite films. Two melting peaks were observed, indicating γ -crystalline form and α -crystalline form, which were in line with previous DSC studies of nylon yarns [59]. Various thermal characteristics are summarized in **Table 2**. With the increasing concentrations of nanocellulose in nylon films, a slight decrease in T_{mc}

was observed, whereas the T_g of films increased. Consequently, the crystallinity of films was also decreased with the increasing nanocellulose. Similar observations were reported when CNFs were incorporated into the nylon-6 matrix [51]. These effects are attributed to the strong interactions between hydroxyl groups of nanocellulose and the polar amide groups of nylon, which restricted the movement of nylon polymeric chains due to increased hydrogen bonding [51, 60] (seen previously from FTIR).

3.7. Thermogravimetric analysis

Figure 9 shows the weight loss curve of nylon yarn waste, neat nylon film, and nylon nanocomposite film (Nylon-1%). A 5 wt% residue was obtained for nylon yarn waste at 600 °C, confirming the presence of inorganic substances like talc in the nylon yarn (mentioned previously). In contrast, the residues for neat nylon film and Nylon-1% film were less than 1.5 wt%, confirming the removal of talc from the yarn’s surface during the washing of the fibers. Some fluctuations were also visualized in the temperature range of 150–200 °C for nylon waste (marked with

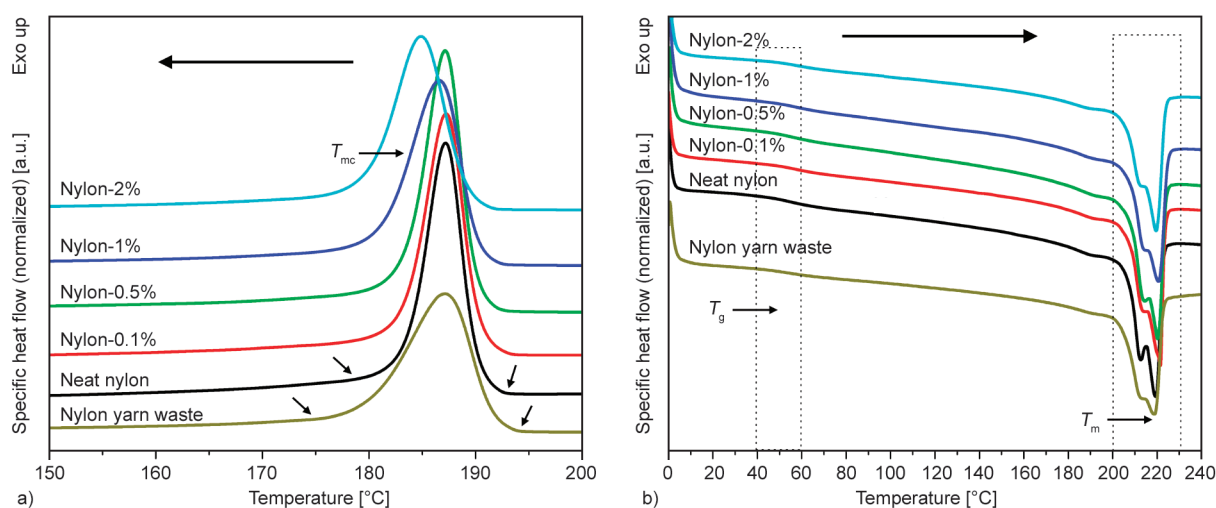


Figure 8. DSC curves of nylon yarn and nylon films during (a) first cooling and (b) second heating.

Table 2. DSC analysis for nylon yarn and nylon nanocomposite films.

Sample	T_{mc} [°C]	T_g [°C]	T_m [°C]	ΔH_m [J/g]	X_c [%]
Nylon yarn waste	186.17±0.76 ^b	54.00±0.30 ^a	219.50±0.50 ^b	60.17±0.76 ^d	31.67±0.38 ^c
Neat nylon	187.54±0.13 ^c	53.68±0.25 ^a	222.19±0.18 ^d	62.33±0.72 ^c	32.80±0.24 ^d
Nylon-0.1%	187.47±0.13 ^c	54.70±0.31 ^{a,b}	221.49±0.25 ^d	59.73±0.45 ^{c,d}	31.47±0.21 ^{b,c}
Nylon-0.5%	187.13±0.12 ^{b,c}	55.73±0.14 ^{b,c}	220.36±0.14 ^c	58.39±0.43 ^c	30.78±0.35 ^b
Nylon-1%	186.71±0.52 ^{b,c}	56.48±0.11 ^{c,d}	219.77±0.18 ^{b,c}	55.32±0.66 ^b	29.41±0.23 ^a
Nylon-2%	185.08±0.22 ^a	57.39±0.16 ^d	218.76±0.13 ^a	53.39±0.43 ^a	28.68±0.40 ^a

The mean and standard deviation are used to express the data.

^{a,b,c,d} Different letters in the same column indicate significant differences ($p < 0.05$).

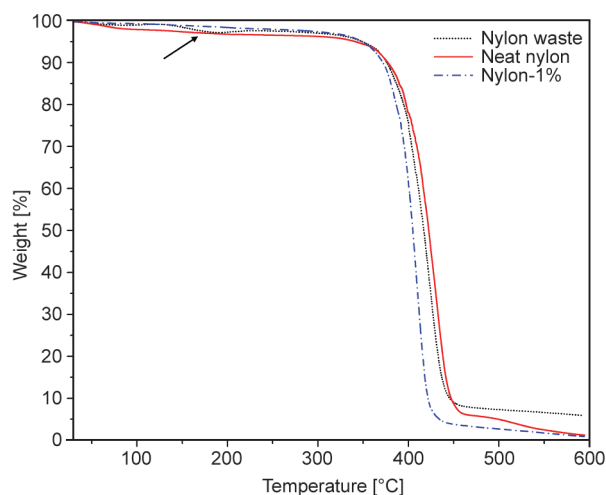


Figure 9. TGA curve for nylon yarn waste and nylon films.

arrow), which might be due to the release of some plasticizers from the nylon yarn. The film with nanocellulose showed an early degradation compared to neat nylon, which might be due to less thermal stability of cellulose when compared to nylon-6 [51]. In addition, a higher concentration of nanocellulose (1 wt%) might lead to an increased reorientation of hydrogen bonds, which result in the conversion of a fraction of α -crystalline form (stable) to γ -crystalline form (metastable) and consequently became less thermally stable.

3.8. Thickness and mechanical properties of films

The effect of nanocellulose on the film's mechanical properties, like tensile strength and elongation at break, was determined and presented in Table 2. With the addition of nanocellulose in the nylon films (up to 0.5 wt%), tensile strength decreased compared to neat film. However, the tensile strength remained similar to neat film at a maximum concentration of nanocellulose (1 wt%). The decrease in tensile strength (at low filler content) might be attributed to a few aggregates of nanocellulose in the nylon matrix, which were unable to disperse in the matrix due to the lower shear generated in response to the lower viscosity of the suspension. Although nanocellulose powder was freeze-dried to avoid the formation of aggregates and produce a porous, weakly bonded material [61], a few agglomerates might still be present in the powder. A similar case was observed where large agglomerates of microcrystalline cellulose (MCC) in PLA (polylactic acid) reduced the tensile strength of the composite [62]. Whereas, at higher filler concentration (1 wt%),

Table 3. Mechanical properties of neat and nanocomposite films.

Sample	Tensile strength [MPa]	Elongation at break [%]	Modulus [MPa]
Neat nylon	20.43±2.03 ^a	10.81±5.45 ^a	1411±34 ^a
Nylon-0.1%	13.79±4.43 ^a	17.93±5.70 ^a	1040±25 ^a
Nylon-0.5%	13.95±1.67 ^a	11.81±2.13 ^a	976±128 ^a
Nylon-1%	19.05±1.89 ^a	10.82±1.09 ^a	1121±151 ^a

The mean and standard deviation are used to express the data. ^aDifferent letters in the same column indicate significant differences ($p < 0.05$). (There are no significant differences.)

higher suspension viscosity was achieved, leading to higher shear required to break the nanocellulose aggregates and disperse them uniformly in the matrix. In addition, for Nylon-1% film, the higher hydrogen bonding between cellulose and nylon, as observed from FTIR, might also be the reason for maintaining the higher tensile strength, similar to neat film. When comparing modulus (stiffness), the modulus decreased with the addition of nanocellulose when the concentration was 0.1 and 0.5 wt%. A decrease in stiffness of about 30.78% was observed, however, the modulus increased drastically to 1121 MPa when the concentration of nanocellulose was 1 wt% in nylon-6 matrix. This high modulus was in-line with the tensile strength observed at 1 wt% of nanocellulose. It can be seen that by adding a small amount of nanocellulose, the film's elasticity increased, and the strength and stiffness decreased, showing ductile behavior. However, at high nanocellulose content (1 wt%), the elongation, tensile, and modulus were like that of the neat nylon film. Although, it should be noted that the differences in tensile strength, elongation at break, and modulus for films were insignificant when considering standard deviation (Table 3).

3.9. Barrier properties: water contact angle and water vapor transmission rate of films

The water contact angles of the films were determined and presented in Figure 10. The contact angle decreased from 60.38° to 48.38° with the addition of nanocellulose. The nanocellulose being hydrophilic [63] has increased the surface wettability of the nylon films. One more reason for the decrease in contact angle could be the reorientation of the hydrogen bond at the surface of the nanocomposite films, as previously discussed in FTIR; and hydrogen bonding being highly polar [64] can have a lower contact angle

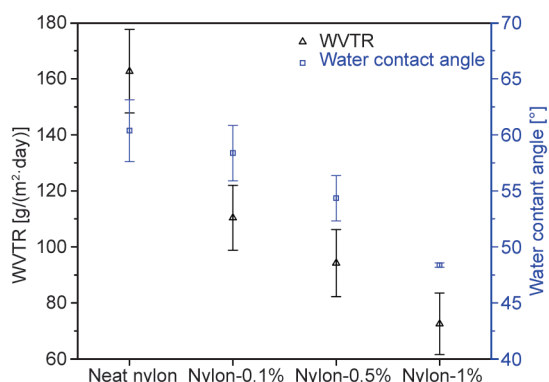


Figure 10. Water contact angle and WVTR of nanocomposite films.

with the water; hence the affinity of films towards water also increased.

The WVTR of the nylon films incorporated nanocelluloses were determined and presented in Figure 10. WVTR of the nanocomposite films significantly decreased compared to neat film. WVTR was decreased from 162.72 for neat films to 72.54 g/(m²·day) for Nylon-1% films. Similar results were achieved when nanoclay was added to the nylon matrix [58]. The decrease in WVTR of films is attributed to the increased surface structuring and dense cross-section of films (from FESEM images), leading to higher tortuosity for water vapors. The tortuous path created for moisture transfer by nanocellulose inside the nylon polymer matrix delays the transfer rate of water vapors. A similar observation was observed when CNC was incorporated in PLA [65] and PHB (polyhydroxybutyrate) [66] films. The nanocomposite film from textile yarn waste might create a new opportunity for application in packaging where a high barrier is required. Nevertheless, due to the water-sensitive nature of nylon-6 [18], the nanocomposite films should be sandwiched between the layers of water-insensitive polyolefins (PP or PE) for preparing multi-layered packaging [18] in order to take complete advantage of the engineered properties of developed films.

4. Conclusions

A high-water vapor barrier nylon nanocomposite films were successfully prepared using the solvent casting method utilizing acetic acid as a green solvent. Nanocellulose powder as a green nanofiller was extracted from the viscose-rayon textile yarn waste by acid hydrolysis and later introduced into the nylon matrix obtained from nylon textile yarn waste.

Nanocellulose strongly interacted with the nylon matrix by forming new hydrogen bonds. In addition, nanocellulose also reoriented a few existing hydrogen bonds of nylon, as determined through FTIR and DSC. Consequently, nanocomposite films appeared dense with structuring at the surface (from FESEM), which increased the tortuosity for water vapors, and hence a maximum of 55% reduction in WVTR was noted for nylon films containing 1 wt% nanocellulose. However, the surface wettability of films was increased with the incorporation of nanocellulose. The tensile strength and elongation at break of nanocomposite films were changed with the addition of nanocellulose. The tensile strength decreased by 32.5%, elongation at break increased by 65.86%, and modulus decreased by 30.78% when 0.1 wt% of nanocellulose was added. However, at higher concentrations (1 wt%), the mechanical properties were similar to that of neat nylon films. The raw material analysis of nylon textile waste revealed the presence of around 5 wt% inorganic matter (TGA) that acted as a nucleating agent for nylon matrix (DSC). Nanocellulose did not act as a nucleating agent for the nylon matrix; rather, the crystallinity of nylon films decreased with the introduction of nanocellulose (DSC). The presence of plasticizers and antioxidants in nylon textile yarn waste was also evident from FTIR. Nevertheless, with nearly the same thermal properties as industrial-grade nylon-6, the pre-consumer nylon textile yarn waste could be a cheap alternative to expensive nylon-6 for various applications. Finally, the developed high-barrier nylon nanocomposite films may find an application where a low WVTR is required for packaging. More rigorous studies on the barrier properties of multi-layered packaging materials incorporating the developed nanocomposite film as a sandwich layer will be conducted in our future research.

Acknowledgements

Prince Kumar Mishra would like to thank the Ministry of Education (MoE), Government of India, for providing resources and financial support to carry out this research work during his Master's study.

References

- [1] Wang Z., Yao Z., Zhou J., Zhang Y.: Reuse of waste cotton cloth for the extraction of cellulose nanocrystals. *Carbohydrate Polymers*, **157**, 945–952 (2017). <https://doi.org/10.1016/j.carbpol.2016.10.044>



- [2] Mishra P. K., Izrayeel A. M. D., Mahur B. K., Ahuja A., Rastogi V. K.: A comprehensive review on textile waste valorization techniques and their applications. *Environmental Science and Pollution Research*, **29**, 65962–65977 (2022).
<https://doi.org/10.1007/s11356-022-22222-6>
- [3] Ozger O. B., Girardi F., Giannuzzi G. M., Salomoni V. A., Majorana C. E., Fambri L., Baldassino N., Di Maggio R.: Effect of nylon fibres on mechanical and thermal properties of hardened concrete for energy storage systems. *Materials and Design*, **51**, 989–997 (2013).
<https://doi.org/10.1016/j.matdes.2013.04.085>
- [4] Echeverria C. A., Handoko W., Pahlevani F., Sahajwalla V.: Cascading use of textile waste for the advancement of fibre reinforced composites for building applications. *Journal of Cleaner Production*, **208**, 1524–1536 (2019).
<https://doi.org/10.1016/j.jclepro.2018.10.227>
- [5] Zhong X., Li R., Wang Z., Wang Y., Wang W., Yu D.: Highly flexible, transparent film prepared by upcycle of wasted jute fabrics with functional properties. *Process Safety and Environmental Protection*, **146**, 718–725 (2021).
<https://doi.org/10.1016/j.psep.2020.12.013>
- [6] Aishwariya S.: Waste management technologies in textile industry. *Innovative Energy and Research*, **7**, 211 (2018).
<https://doi.org/10.4172/2576-1463.1000211>
- [7] To M. H., Uisan K., Ok Y. S., Pleissner D., Lin C. S. K.: Recent trends in green and sustainable chemistry: Rethinking textile waste in a circular economy. *Current Opinion in Green and Sustainable Chemistry*, **20**, 1–10 (2019).
<https://doi.org/10.1016/J.COGLSC.2019.06.002>
- [8] Haslinger S., Ye Y., Rissanen M., Hummel M., Sixta H.: Cellulose fibers for high-performance textiles functionalized with incorporated gold and silver nanoparticles. *ACS Sustainable Chemistry and Engineering*, **8**, 649–658 (2020).
<https://doi.org/10.1021/acssuschemeng.9b06385>
- [9] Colom X., Carrillo F.: Crystallinity changes in lyocell and viscose-type fibres by caustic treatment. *European Polymer Journal*, **38**, 2225–2230 (2002).
[https://doi.org/10.1016/S0014-3057\(02\)00132-5](https://doi.org/10.1016/S0014-3057(02)00132-5)
- [10] Zeng H., Tang R-C.: Adsorption properties of direct dyes on viscose/chitin bicomponent fiber: Evaluation and comparison with viscose fiber. *RSC Advances*, **4**, 38064–38072 (2014).
<https://doi.org/10.1039/C4RA05874G>
- [11] Chen H-L., Burns L. D.: Environmental analysis of textile products. *Clothing and Textiles Research Journal*, **24**, 248–261 (2006).
<https://doi.org/10.1177/0887302X06293065>
- [12] Babu B. R., Parande A. K., Raghu S., Kumar T. P.: Cotton textile processing: Waste generation and effluent treatment. *The Journal of Cotton Science*, **11**, 141–153 (2007).
- [13] Wang Y.: Fiber and textile waste utilization. *Waste and Biomass Valorization*, **1**, 135–143 (2010).
<https://doi.org/10.1007/s12649-009-9005-y>
- [14] Stanescu M. D.: State of the art of post-consumer textile waste upcycling to reach the zero waste milestone. *Environmental Science and Pollution Research*, **28**, 14253–14270 (2021).
<https://doi.org/10.1007/s11356-021-12416-9>
- [15] Montava-Jordà S., Torres-Giner S., Ferrandiz-Bou S., Quiles-Carrillo L., Montanes N.: Development of sustainable and cost-competitive injection-molded pieces of partially bio-based polyethylene terephthalate through the valorization of cotton textile waste. *International Journal of Molecular Sciences*, **20**, 1378 (2019).
<https://doi.org/10.3390/ijms20061378>
- [16] Prado K. S., Gonzales D., Spinacé M. A. S.: Recycling of viscose yarn waste through one-step extraction of nanocellulose. *International Journal of Biological Macromolecules*, **136**, 729–737 (2019).
<https://doi.org/10.1016/j.ijbiomac.2019.06.124>
- [17] Hufenus R., Yan Y., Dauner M., Kikutani T.: Melt-spun fibers for textile applications. *Materials*, **13**, 4298 (2020).
<https://doi.org/10.3390/ma13194298>
- [18] Ammala A.: Nylon-MXD6 resins for food packaging. in ‘Multifunctional and nanoreinforced polymers for food packaging’ (ed.: Lagarón J-M.) Elsevier, Cambridge, Vol. 1, 243–260 (2011).
<https://doi.org/10.1533/9780857092786.1.243>
- [19] Alonso-Montemayor F. J., Tarrés Q., Oliver-Ortega H., Espinach F. X., Narro-Céspedes R. I., Castañeda-Facio A. O., Delgado-Aguilar M.: Enhancing the mechanical performance of bleached hemp fibers reinforced polyamide 6 composites: A competitive alternative to commodity composites. *Polymers*, **12**, 1041 (2020).
<https://doi.org/10.3390/polym12051041>
- [20] Shakiba M., Ghomi R. E., Khosravi F., Jouybar S., Bigham A., Zare M., Abdouss M., Moaref R., Ramakrishna S.: Nylon – A material introduction and overview for biomedical applications. *Polymers for Advanced Technologies*, **32**, 3368–3383 (2021).
<https://doi.org/10.1002/pat.5372>
- [21] Dissanayake D. G. K., Weerasinghe D. U., Wijesinghe K. A. P., Kalpage K. M. D. M. P.: Developing a compression moulded thermal insulation panel using post-industrial textile waste. *Waste Management*, **79**, 356–361 (2018).
<https://doi.org/10.1016/j.wasman.2018.08.001>
- [22] Šišková A. O., Pleva P., Hříza J., Frajová J., Sedlářiková J., Peer P., Kleinová A., Janalíková M.: Reuse of textile waste to production of the fibrous antibacterial membrane with filtration potential. *Nanomaterials*, **12**, 50 (2021).
<https://doi.org/10.3390/nano12010050>
- [23] Lee S., Jung S., Lin K-Y. A., Tsang Y. F., Kwon E. E.: Use of CO₂ and nylon as the raw materials for flammable gas production through a catalytic thermo-chemical process. *Green Chemistry*, **23**, 8922–8931 (2021).
<https://doi.org/10.1039/D1GC02540F>
- [24] Cai Y., Li Q., Wei Q., Wu Y., Song L., Hu Y.: Structures, thermal stability, and crystalline properties of polyamide 6/organic-modified Fe-montmorillonite composite nanofibers by electrospinning. *Journal of Materials Science*, **43**, 6132–6138 (2008).
<https://doi.org/10.1007/s10853-008-2921-6>

- [25] Bauer A. S., Tacker M., Uysal-Unalan I., Cruz R. M. S., Varzakas T., Krauter V.: Recyclability and redesign challenges in multilayer flexible food packaging – A review. *Foods*, **2021**, 2702 (2021).
<https://doi.org/10.3390/FOODS10112702>
- [26] Kiziltas A., Nazari B., Gardner D. J., Bousfield D. W.: Polyamide 6-cellulose composites: Effect of cellulose composition on melt rheology and crystallization behavior. *Polymer Engineering and Science*, **54**, 739–746 (2014).
<https://doi.org/10.1002/pen.23603>
- [27] Rahimi S. K., Otaigbe J. U.: The role of particle surface functionality and microstructure development in isothermal and non-isothermal crystallization behavior of polyamide 6/cellulose nanocrystals nanocomposites. *Polymer*, **107**, 316–331 (2016).
<https://doi.org/10.1016/j.polymer.2016.11.023>
- [28] Korkees F., Aldrees A., Barsoum I., Alshammari D.: Functionalised graphene effect on the mechanical and thermal properties of recycled PA6/PA6,6 blends. *Journal of Composite Materials*, **55**, 2211–2224 (2021).
<https://doi.org/10.1177/0021998320987897>
- [29] Janchai K., Boonmahitthisud A., Chaiwutthinan P., Chuayjuljit S., Hongrattanavichit I.: Property improvement of recycled nylon 6 by thermoplastic poly(ether-ester) elastomer and wollastonite. *Materials Science Forum*, **1053**, 47–51 (2022).
<https://doi.org/10.4028/p-ns1103>
- [30] Agarwal A., Raheja A., Natarajan T. S., Chandra T. S.: Effect of electrospun montmorillonite-nylon 6 nanofibrous membrane coated packaging on potato chips and bread. *Innovative Food Science and Emerging Technologies*, **26**, 424–430 (2014).
<https://doi.org/10.1016/J.IFSET.2014.09.012>
- [31] Purkayastha S., Dutta A., Ghosh A. K., Saha N. C.: Processability and performance property correlation for LDPE/PA6-based nanocomposite and its monolayer blown film for packaging application. *Bulletin of Materials Science*, **45**, 47 (2022).
<https://doi.org/10.1007/s12034-021-02627-8>
- [32] Paliwal R.: From waste to wealth: Stepping toward sustainability through circular economy. in ‘Handbook of solid waste management’ (eds.: Baskar C., Ramakrishna S., Baskar S., Sharma R., Chinnappan A., Sehrawat R.) Springer, Singapore, Vol. 1, 441–463 (2021).
- [33] Tanwar R., Gupta V., Kumar P., Kumar A., Singh S., Gaikwad K. K.: Development and characterization of PVA-starch incorporated with coconut shell extract and sepiolite clay as an antioxidant film for active food packaging applications. *International Journal of Biological Macromolecules*, **185**, 451–461 (2021).
<https://doi.org/10.1016/j.ijbiomac.2021.06.179>
- [34] Mahmood S., Mandal U. K., Chatterjee B., Taher M.: Advanced characterizations of nanoparticles for drug delivery: Investigating their properties through the techniques used in their evaluations. *Nanotechnology Reviews*, **6**, 355–372 (2017).
<https://doi.org/10.1515/ntrev-2016-0050>
- [35] Liu K., Li Y., Tao L., Xiao R.: Preparation and characterization of polyamide 6 fibre based on a phosphorus-containing flame retardant. *RSC Advances*, **8**, 9261–9271 (2018).
<https://doi.org/10.1039/C7RA13228J>
- [36] Rastogi V. K., Samyn P.: Novel processing of polyhydroxybutyrate with micro- to nanofibrillated cellulose and effect of fiber morphology on crystallization behaviour of composites. *Express Polymer Letters*, **14**, 115–133 (2020).
<https://doi.org/10.3144/expresspolymlett.2020.11>
- [37] Li Y., Li G., Zou Y., Zhou Q., Lian X.: Preparation and characterization of cellulose nanofibers from partly mercerized cotton by mixed acid hydrolysis. *Cellulose*, **21**, 301–309 (2014).
<https://doi.org/10.1007/s10570-013-0146-6>
- [38] Alemdar A., Sain M.: Isolation and characterization of nanofibers from agricultural residues – Wheat straw and soy hulls. *Bioresource Technology*, **99**, 1664–1671 (2008).
<https://doi.org/10.1016/j.biortech.2007.04.029>
- [39] Carrillo F., Colom X., Suñol J., Saurina J.: Structural FTIR analysis and thermal characterisation of lyocell and viscose-type fibres. *European Polymer Journal*, **40**, 2229–2234 (2004).
<https://doi.org/10.1016/j.eurpolymj.2004.05.003>
- [40] Nelson M. L., O’Connor R. T.: Relation of certain infrared bands to cellulose crystallinity and crystal latticed type. Part I. Spectra of lattice types I, II, III and of amorphous cellulose. *Journal of Applied Polymer Science*, **8**, 1311–1324 (1964).
<https://doi.org/10.1002/APP.1964.070080322>
- [41] Rizal S., Olaiya F. G., Saharudin N. I., Abdullah C. K., Olaiya N. G., Haafiz M. K., M., Yahya E. B., Sabaruddin F. A., Ikramullah, Khalil H. P. S. A.: Isolation of textile waste cellulose nanofibrillated fibre reinforced in polylactic acid-chitin biodegradable composite for green packaging application. *Polymers*, **13**, 325 (2021).
<https://doi.org/10.3390/polym13030325>
- [42] Oh S. Y., Yoo D. I., Shin Y., Kim H. C., Kim H. Y., Chung Y. S., Park W. H., Youk J. H.: Crystalline structure analysis of cellulose treated with sodium hydroxide and carbon dioxide by means of X-ray diffraction and FTIR spectroscopy. *Carbohydrate Research*, **340**, 2376–2391 (2005).
<https://doi.org/10.1016/j.carres.2005.08.007>
- [43] Popescu C-M., Singurel G., Popescu M-C., Vasile C., Argyropoulos D. S., Willför S.: Vibrational spectroscopy and X-ray diffraction methods to establish the differences between hardwood and softwood. *Carbohydrate Polymers*, **77**, 851–857 (2009).
<https://doi.org/10.1016/j.carbpol.2009.03.011>
- [44] Tegginamata P., Ravindrachary V., Mahantesha B. K., Sahanakumari R., Ramani R., Kotresh T. M., Ananth S.: CdO nano-particles induced structural, thermal, surface morphological and electrical properties of Nylon-6. in ‘AIP Conference Proceedings. Manglore, India’ Vol. 2244, 070022 (2020).
<https://doi.org/10.1063/5.0009367>

- [45] Yu X., Jiang Y., Wu Q., Wei Z., Lin X., Chen Y.: Preparation and characterization of cellulose nanocrystal extraction from pennisetum hybridum fertilized by municipal sewage sludge *via* sulfuric acid hydrolysis. *Frontiers in Energy Research*, **9**, 653 (2021).
<https://doi.org/10.3389/fenrg.2021.774783>
- [46] Kusmono, Listyanda R. F., Wildan M. W., Ilman M. N.: Preparation and characterization of cellulose nanocrystal extracted from ramie fibers by sulfuric acid hydrolysis. *Heliyon*, **6**, e05486 (2020).
<https://doi.org/10.1016/j.heliyon.2020.e05486>
- [47] Segal L., Creely J. J., Martin A. E., Conrad C. M.: An empirical method for estimating the degree of crystallinity of native cellulose using the X-ray diffractometer. *Textile Research Journal*, **29**, 786–794 (1959).
<https://doi.org/10.1177/004051755902901003>
- [48] Kruer-Zerhusen N., Cantero-Tubilla B., Wilson D. B.: Characterization of cellulose crystallinity after enzymatic treatment using fourier transform infrared spectroscopy (FTIR). *Cellulose*, **25**, 37–48 (2018).
<https://doi.org/10.1007/s10570-017-1542-0>
- [49] Giller C. B., Chase D. B., Rabolt J. F., Snively C. M.: Effect of solvent evaporation rate on the crystalline state of electrospun nylon 6. *Polymer*, **51**, 4225–4230 (2010).
<https://doi.org/10.1016/j.polymer.2010.06.057>
- [50] Sallem-Idrissi N., Sclavons M., Debecker D. P., Devaux J.: Miscible raw lignin/nylon 6 blends: Thermal and mechanical performances. *Journal of Applied Polymer Science*, **133**, 42963 (2016).
<https://doi.org/10.1002/app.42963>
- [51] Sridhara P. K., Masso F., Olsén P., Vilaseca F.: Strong polyamide-6 nanocomposites with cellulose nanofibers mediated by green solvent mixtures. *Nanomaterials*, **11**, 2127 (2021).
<https://doi.org/10.3390/nano11082127>
- [52] Ossman M., Fatah M. A., Ossman M. E., Mansour M. S., Fattah M. A., Taha N., Kiros Y.: Peanut shells and talc powder for removal of hexavalent chromium from aqueous solutions. *Bulgarian Chemical Communications*, **46**, 629–639 (2014).
- [53] Sharma P., Ahuja A., Dilsad Izrayeel A. M., Samyn P., Rastogi V. K.: Physicochemical and thermal characterization of poly(3-hydroxybutyrate-co-4-hydroxybutyrate) films incorporating thyme essential oil for active packaging of white bread. *Food Control*, **133**, 108688 (2022).
<https://doi.org/10.1016/j.foodcont.2021.108688>
- [54] Yue Y., Zhou C., French A. D., Xia G., Han G., Wang Q., Wu Q.: Comparative properties of cellulose nanocrystals from native and mercerized cotton fibers. *Cellulose*, **19**, 1173–1187 (2012).
<https://doi.org/10.1007/s10570-012-9714-4>
- [55] Xiong R., Zhang X., Tian D., Zhou Z., Lu C.: Comparing microcrystalline with spherical nanocrystalline cellulose from waste cotton fabrics. *Cellulose*, **19**, 1189–1198 (2012).
<https://doi.org/10.1007/s10570-012-9730-4>
- [56] Lu P., Hsieh Y-L.: Cellulose isolation and core-shell nanostructures of cellulose nanocrystals from chardonnay grape skins. *Carbohydrate Polymers*, **87**, 2546–2553 (2012).
<https://doi.org/10.1016/j.carbpol.2011.11.023>
- [57] Chen G-Y., Yu H-Y., Zhang C-H., Zhou Y., Yao J-M.: A universal route for the simultaneous extraction and functionalization of cellulose nanocrystals from industrial and agricultural celluloses. *Journal of Nanoparticle Research*, **18**, 48 (2016).
<https://doi.org/10.1007/s11051-016-3355-8>
- [58] Allafi A. R., Pascall M. A.: The effect of different percent loadings of nanoparticles on the barrier and thermal properties of nylon 6 films. *Innovative Food Science and Emerging Technologies*, **20**, 276–280 (2013).
<https://doi.org/10.1016/j.ifset.2013.08.009>
- [59] Klata E., van de Velde K., Krucińska I.: DSC investigations of polyamide 6 in hybrid GF/PA6 yarns and composites. *Polymer Testing*, **22**, 929–937 (2003).
[https://doi.org/10.1016/S0142-9418\(03\)00043-6](https://doi.org/10.1016/S0142-9418(03)00043-6)
- [60] Sunday D. F., Green D. L.: Thermal and rheological behavior of polymer grafted nanoparticles. *Macromolecules*, **48**, 8651–8659 (2015).
<https://doi.org/10.1021/acs.macromol.5b00987>
- [61] Dufresne A.: Cellulose nanomaterials as green nanoreinforcements for polymer nanocomposites. *Philosophical Transactions of the Royal Society A: Mathematical, Physical and Engineering Sciences*, **376**, 20170040 (2018).
<https://doi.org/10.1098/rsta.2017.0040>
- [62] dos Santos F. A., Iulianelli G. C. V., Tavares M. I. B.: Effect of microcrystalline and nanocrystals cellulose fillers in materials based on PLA matrix. *Polymer Testing*, **61**, 280–288 (2017).
<https://doi.org/10.1016/j.polymertesting.2017.05.028>
- [63] Seoane I. T., Cerrutti P., Vazquez A., Manfredi L. B., Cyrus V. P.: Polyhydroxybutyrate-based nanocomposites with cellulose nanocrystals and bacterial cellulose. *Journal of Polymers and the Environment*, **25**, 586–598 (2017).
<https://doi.org/10.1007/s10924-016-0838-8>
- [64] Yamabe S., Morokuma K.: Molecular orbital studies of hydrogen bonds. IX. Electron distribution analysis. *Journal of the American Chemical Society*, **97**, 4458–4465 (1975).
<https://doi.org/10.1021/ja00849a003>
- [65] Fortunati E., Peltzer M., Armentano I., Torre L., Jiménez A., Kenny J. M.: Effects of modified cellulose nanocrystals on the barrier and migration properties of PLA nano-biocomposites. *Carbohydrate Polymers*, **90**, 948–956 (2012).
<https://doi.org/10.1016/J.CARBPOL.2012.06.025>
- [66] Dhar P., Bhardwaj U., Kumar A., Katiyar V.: Poly(3-hydroxybutyrate)/cellulose nanocrystal films for food packaging applications: Barrier and migration studies. *Polymer Engineering and Science*, **55**, 2388–2395 (2015).
<https://doi.org/10.1002/PEN.24127>

Research article

Size dependence of the elastic modulus of thin polymer fibers – modeling

Andrei V. Subbotin^{1,2}, Alexander Ya. Malkin^{1*}, Andrei V. Andrianov³,
Valerii G. Kulichikhin¹

¹A. V. Topchiev Institute of Petrochemical Synthesis, Russian Academy of Science, Leninskii prospect, 29, 119991 Moscow, Russia

²A. N. Frumkin Institute of Physical Chemistry and Electrochemistry, Russian Academy of Sciences, Leninskii prospect, 31, 119991 Moscow, Russia

³M. V. Lomonosov, Moscow State University, Physical Faculty, Leninskii Gory, 1, 119991 Moscow, Russia

Received 14 June 2022; accepted in revised form 21 September 19

Abstract. The problem of the size dependence of physical properties is one of the most intriguing when we transit to the nano-level. Experiments have shown that this effect is characteristic of the elastic modulus of many polymeric nanofibers obtained by electrospinning. Existing explanations of this effect did not offer a general understanding of the physical nature of this phenomenon. In this study, we propose a universal model of this phenomenon. We consider the structure of fibers within the framework of the core-shell model, in which the shell is approximated by a thin elastic surface. The analysis of deformation is based on the fundamental laws of the mechanics of deformation of twisted thin shells and, unlike the theories proposed earlier, does not require any additional artificial arguments. This approach made it possible to obtain a simple analytical expression for the size dependence of the elastic modulus, which represents it as the sum of the bulk modulus of the core and two additional moduli proportional to D^{-1} and D^{-3} , respectively. The resulting model corresponds to all available (from published sources) experimental data, related to polymer of very different chemical structure, and therefore can be considered as universal.

Keywords: *nanomaterials, polymer electrospinning, elasticity, surface tension, surface curvature*

1. Introduction

The problem of the size dependence of the fundamental mechanical properties of materials does not exist in physics and technical applications. However, when we move into the nanoscale world. We see that many important characteristics of the products do depend on their size. One of the intriguing phenomena of this kind is the size dependence of the elastic modulus of polymeric nanofibers obtained by electrospinning from polymer solutions [1–3]. This effect is especially important for the use of nanofibers as a reinforcing component in critical applications in modern technology. This behavior is similar to the

analogous effect known for metal and oxide nanowires. For these objects, it was assumed that the concept of surface tension is the dominating mechanism of increasing the modulus [4, 5]. Structure analysis has shown that nanowires can be really treated as a composite of a core-shell structure with cover layers, which penetrate deep into the bulk of a wire depends on its size [6, 7]. This is also applied to polymer fibers, which have a different structure of the volume and outer shell [8–10], which is mainly due to the diffusion process of evaporation of a solvent during their formation from a polymer solution [11]. Indeed, evaporation of the solvent leads to the formation of

*Corresponding author, e-mail: alex_malkin@mig.phys.msu.ru

© BME-PT

a thin glassy [12] or gel-like [13] film skin on the free surface of the polymer solution, which ensures the formation of the fiber shell.

The primary explanation for the increase in the elastic modulus of ultrathin fibers seems obvious due to their very large relative surface area. However, this approach was rejected [14] due to the fact that a quantitative estimation based on real values of surface tension did not give a reasonable agreement with the experimental data. Meanwhile, in these calculations, the surface tension was considered as a single characteristic of a surface, like in different liquids. However, it is well known that surfaces demonstrate viscoelastic properties [15], and this is especially important for nanoscale objects [16]. Surface elasticity was considered in continuum mechanics of surface/interface layers [17] and was used in constructing the core-shell model of nanowires [18] since nano-size fibers are important not only for organic but also for inorganic objects. In the latter publication, the numerical results have demonstrated the applicability of this model (including two fitting factors related to the surface – the inhomogeneity degree constant and the surface layer thickness) for the elastic modulus of ZnO and Si nanowires in bending and tension loading modes.

The core-shell model has also been used to explain the increase in the elastic modulus for thin fibers due to the deformation and orientation of molecular aggregates within the fiber [19]. This approach shifted the responsibility for the increase in the elastic modulus to the structure of the central part of the fiber.

The purpose of this work is to formulate a simple phenomenological theory based on the two-cylinder core-shell model for fitting experimental data obtained for various polymer nanofibers and explaining the dependence of the total elastic modulus of ultra-fine fibers on their diameter due to the elastic properties of the surface layer associated with its curvature.

2. Theory

Let's start with the simplest model and imagine a fiber in the form of a cylindrical core of the diameter d and the elastic (Young) modulus of E_d , and a shell with an elastic modulus of E_D and a thickness $\delta = 0.5(D - d)$ (D is the total fiber diameter as shown in Figure 1). The core and shell are believed to obey Hooke's law and $E_D \gg E_d$.

The apparent modulus of the core-shell fiber E is defined by the Equation (1):

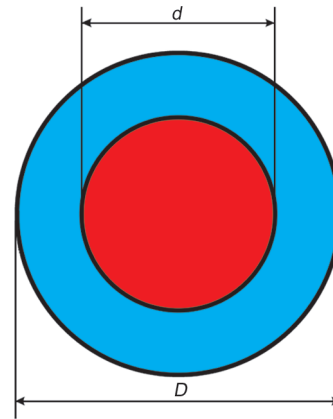


Figure 1. Two-component core-shell model of the cross-section of a fiber.

$$E = \frac{4F}{\pi D^2 \epsilon} \quad (1)$$

where $\epsilon = \text{const}$ is the deformation and the force, F , is the sum of the forces acting in at the core and the shell (Equation (2)):

$$F = \frac{\pi(D^2 - d^2)}{4} E_D \epsilon + \frac{\pi d^2}{4} E_d \epsilon \quad (2)$$

Substituting Equation (2) into Equation (1), we arrive at the Equation (3):

$$E = E_D \frac{D^2 - d^2}{D^2} + E_d \left(\frac{d}{D}\right)^2 \quad (3)$$

which can be written as Equation (4):

$$E = E_D \left[1 - \left(\frac{d}{D}\right)^2\right] + E_d \left(\frac{d}{D}\right)^2 \quad (4)$$

Then, as a first approximation, we assume that the shell thickness weakly depends on the fiber diameter, *i.e.* $\delta = \text{const}$, and $\delta/D \ll 1$. In this case, the $E(D)$ dependence is expected to be Equation (5):

$$E = E_d + (E_D - E_d) \frac{4\delta}{D} \quad (5)$$

The results of comparing the curve calculated by Equation (5) with experimental data for various polymer nanofibers are included in Figure 2 (blue dots line), which presents the general picture of our approach. (A more detailed analysis of the experimental data is given below.) Despite the fact that formula (5) indicates an increase in the elastic modulus with decreasing fiber size, the predicted effect is rather weak and does not allow one to describe the experimental data (except poly(vinyl alcohol) (PVA), Figure 2d).

The model considered above does not fully take into account the structure of the shell and, in particular, its anisotropy: macromolecules in the shell have a higher orientation than in bulk since in the process of spinning the fiber and evaporation of the solvent, a polymer-enriched surface layer with more pronounced viscoelastic properties is formed. In addition, side groups attached to the polymer backbone can also be ordered due to the surface effect. Therefore, the elasticity of the shell must be characterized by several elastic moduli, and this complicates the consideration of the core-shell model in the general case. To simplify further consideration, we replace the shell with an elastic surface and use the phenomenological approach based on the analysis of the general expression for the surface energy. At the same time, we continue to assume that the elasticity of the core is described by Hooke's law.

Consider again a thin cylinder having an elastic surface. The cross-section of fiber was shown in Figure 1. The elastic properties of the shell (surface layer) will be determined based on the surface energy. The initial length of the cylinder is L , and its deformation is $\varepsilon = \Delta L/L$, where ΔL is the elongation of the cylinder. Accordingly, the radius of the cylinder $R = D/2$ decreases and is equal to $R - \Delta R$, $\Delta R > 0$. The volume of the cylinder is assumed to be constant. Then ΔR is found from the volume conservation equation $V = \pi R^2 L = \pi (R - \Delta R)^2 L (1 + \varepsilon)$, (Equation (6)):

$$\Delta R = R \left(1 - \frac{1}{\sqrt{1 + \varepsilon}} \right) \cong \frac{1}{2} R \left(\varepsilon - \frac{3}{4} \varepsilon^2 \right) \quad (6)$$

Change in the surface area of the cylinder in extension is Equation (7):

$$\begin{aligned} \Delta A &= 2\pi(R - \Delta R)(L + \Delta L) - 2\pi RL = \\ &= A_0(\sqrt{1 + \varepsilon} - 1) \cong \frac{1}{2} A_0 \left(\varepsilon - \frac{1}{4} \varepsilon^2 \right) \end{aligned} \quad (7)$$

where $A_0 = 2\pi RL$ is the initial surface area of the cylinder.

Let us accept that the bulk elastic modulus of the cylinder is E_d . The change of the elastic energy in extension therefore is Equation (8):

$$\Delta F_{\text{core}} = \frac{1}{2} E_d \varepsilon^2 V \quad (8)$$

Then we write the energy of the shell by analogy with the energy of the lipid layer as the sum of two terms [22–24], Equation (9):

$$F_{\text{shell}} = F_{\text{surf}}[A] + F_{\text{curve}}[C_1, C_2] \quad (9)$$

Here the first term depends only on the area of the surface and is associated with a change in the energy due to its stretching, and the second term reflects the curvature of the surface and depends on the principal curvature values, C_1 and C_2 . For a straight cylinder of radius R , $C_1 = 1/R$, $C_2 = 0$.

Upon small elongation of the cylinder, the change of the surface term in Equation (9) is written in the following form (Equation 10):

$$\begin{aligned} \Delta F_{\text{surf}} &= F_{\text{surf}}[A_0 + \Delta A] - F_{\text{surf}}[A_0] = \\ &= A_0 \left(\gamma \frac{\Delta A}{A_0} + \frac{1}{2} \mu \left(\frac{\Delta A}{A_0} \right)^2 \right) \cong \\ &\cong \frac{1}{2} A_0 \left(\gamma \varepsilon + \frac{1}{4} (\mu - \gamma) \varepsilon^2 \right) \end{aligned} \quad (10)$$

where γ is the surface tension and μ is the elastic modulus of stretching of the surface. Since the radius of curvature of the shell is much larger than the width of the shell, the expression for the second term in Equation (9) can be expanded in a series with respect to the curvature (Equation (11)):

$$\begin{aligned} F_{\text{curve}}[C_1, C_2] &= \\ &= -\kappa \int C \, dA + \frac{1}{2} K \int C^2 \, dA + K_G \int C_1 C_2 \, dA \end{aligned} \quad (11)$$

where $C = C_1 + C_2$ is the total curvature of the surface. Here we introduce additional moduli κ , K and K_G , resulting from the change of curvature [20–22]. Obviously, in our case of uniaxial tension, the last term in Equation (11) is equal to zero ($C_2 = 0$) and $C = C_1$.

Now consider the change in the energy F_{curve} , Equation (11), due to extension. The total curvature after deformation is $C = 1/(R - \Delta R)$, therefore Equation (12):

$$\Delta F_{\text{curve}} = -A_0 \varepsilon \frac{\kappa}{R} + \frac{3A_0}{4} \frac{K}{R^3} \left(\varepsilon + \frac{1}{4} \varepsilon^2 \right) \quad (12)$$

The total change in the energy ΔF_{tot} , of the cylinder due to extension is determined by the sum Equation (13):

$$\Delta F_{\text{tot}} = \Delta F_{\text{core}} + \Delta F_{\text{surf}} + \Delta F_{\text{curve}} \quad (13)$$

Finally, we can find the effective modulus of elasticity as Equation (14):

$$E = \frac{1}{V} \frac{\partial^2 \Delta F_{\text{tot}}}{\partial \epsilon^2} = E_d + \frac{\mu - \gamma}{2R} + \frac{3K}{4R^3} \quad (14)$$

Thus, when a straight cylinder is stretched, the effective modulus does not depend on the curvature moduli κ and K_G . It is interesting to note that surface tension makes a negative contribution to the elastic modulus. Comparing the formula of Equation (14) with Equation (5) we can conclude that when $\gamma = 0$ and $K = 0$ we come to our previous model with $\mu = 4\delta(E_D - E_d)$. Thereby, the additional input into the elastic modulus of the nanofibers includes two terms proportional to $1/R$ and $1/R^3$, respectively. Besides, it is reasonable to assume that $\mu - \gamma > 0$. The final fitting can be presented as Equation (15):

$$E = E_d + \frac{K_1}{D} + \frac{K_2}{D^3} \quad (15)$$

where the coefficients K_1 and K_2 , in accordance with Equation (9), have the following physical sense (Equations (16) and (17)):

$$K_1 = \mu - \gamma \quad (16)$$

$$K_2 = 6K \quad (17)$$

i.e. K_1 is mainly determined by the stretching modulus of the surface and K_2 – by the curvature elastic modulus.

3. Experimental and discussion

We examined five available sets of experimental data for the $E(D)$ dependences, which were found in current publications. The size dependences of the elastic modulus $E(D)$ were described for: poly(2-acrylamido-2-methyl-1-propanesulfonic acid) (PAMPS) [23], Nylon-66 (PA66) [24], polypyrrol (PPy) [25], poly(vinyl alcohol) (PVA) [26], polyacrylonitrile (PAN) [27]. The nanofibers were obtained by the electrospinning technique using different polymer-solvent systems.

Experimental data on the $E(D)$ dependencies are always obtained and presented in original publications with a wide scatter. We have shown the fields of experimental data and usually have used averaged points for calculations unless otherwise stated. Fitting equation constants will be found by the standard RMS procedure after presenting them in linearized log-log coordinates. In some cases, we presented fitting lying in the experimental field but not as the averaged

curves (that will be noted separately). For comparison, we also presented the results of calculations for the simplest two-cylinder model, which included only elastic stretching moduli.

Figure 2 demonstrates the results of the comparison of the dependences calculated by Equation (15) with the experimental data for various polymer nanofibers (red dash lines), and Table 1 collects the obtained values of the constants K_1 and K_2 .

The analysis of Figure 2 shows that Equation (5) does not give satisfactory results, except for one case of PVA (Figure 2d). In the latter case, the increase in the modulus of this polymer occurs rather smoothly. Indeed, the $E(D)$ dependence for this polymer is approximated by a power law with the power is -0.7 , which is much less than in other cases. This result can be explained by a very pronounced core-shell structure of the PVA crystalline fibers with a rigid anisotropic outer layer, observed in the original publication [26]. Thus, this structure is the most equivalent to a scheme in Figure 1, and the influence of surface curvature elasticity does not appear. It leads to the zero-value of the $1/D^3$ term in Equation (15). Then the latter equation also fits these data. The difference in the lines in this figure is explained by the fact that when calculating according to Equation (5), we took into account the free term.

For three polymers - PAMPS (Figure 2a), Nylon 66 (Figure 2b), and PPy (Figure 2c), the developed two-term model (Equation (15)) provides quite a fairly good quantitative agreement with experimental data. The agreement of the theoretical model with experimental data for PAN (Figure 2e) should be treated as qualitative. The increase in the modulus with a decrease in the fiber diameter occurs more sharply than $1/D^3$. Perhaps this indicates the need to take into account the higher terms in the expansion (Equation (10)).

Based on the results obtained, we assume that the core-shell model and the concept of the outer surface elasticity is a reasonable assumption about the strong

Table 1. Values of the parameters used for fitting.

Polymer	$4\delta(E_D - E_d)$ [nm·GPa]	K_1 [nm·GPa]	$K_2 \cdot 10^{-6}$ [nm ³ ·GPa]
PAMPS	11	30	0.26
Nylon	185	200	8.5
PPy	110	250	2.0
PVA	800	1100	0
PAN	100	800	20

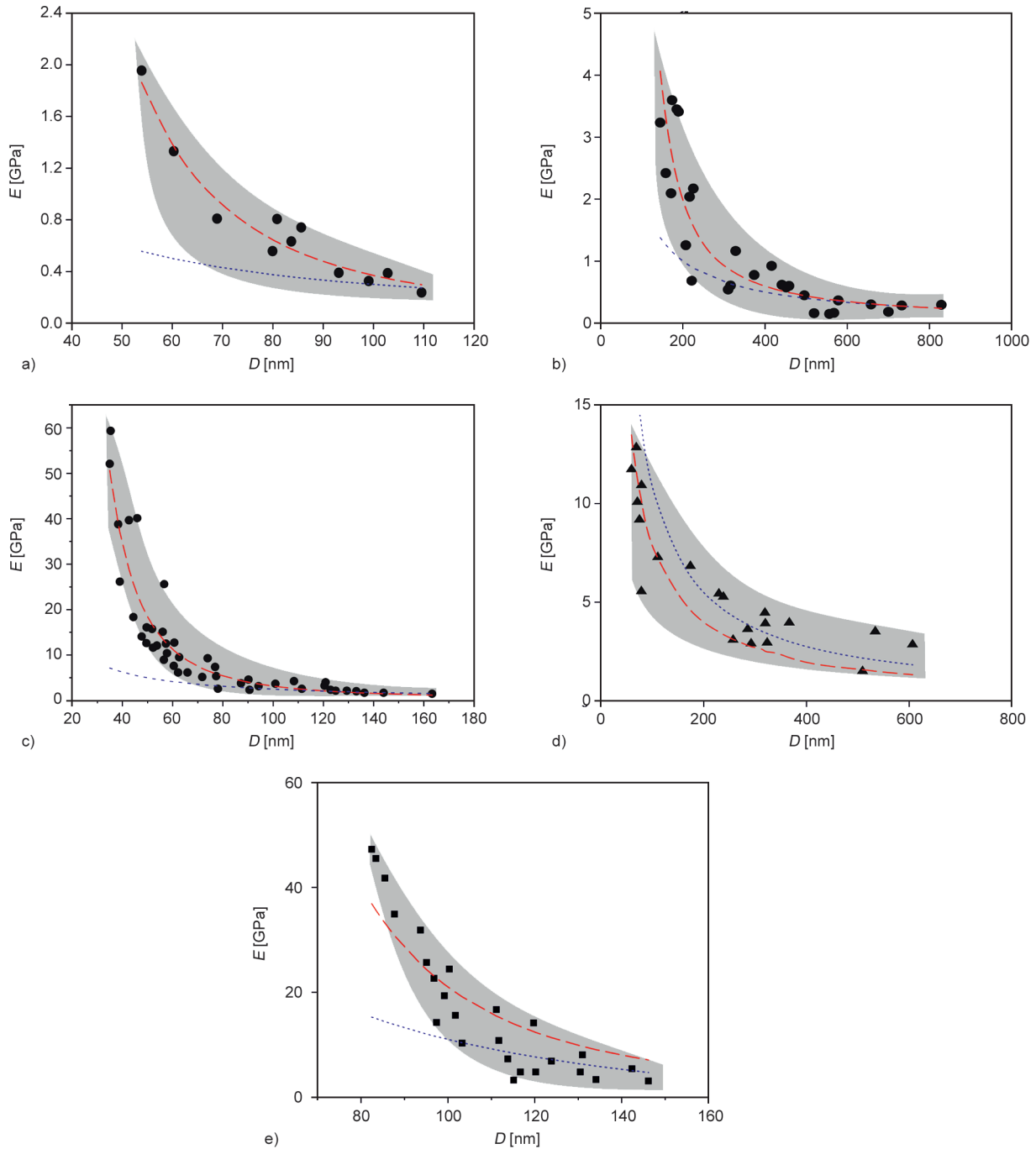


Figure 2. Comparison of the results of fitting by Equations (5) (blue dots) and (15) (red dash lines) with experimental data for various polymers: a) PAMPS [23]; b) Nylon 66 [24]; c) PPy [25]; d) PVA [26]; e) PAN [27]. Grey fields are areas of spreading experimental results. All experimental data were reproduced with permission.

increase in the elastic modulus of electrospun nanosize polymer fibers with a decrease in their diameter. Of course, more experimental evidence would be welcome.

4. Conclusions

In summary, we showed that the size dependence of the elastic modulus of electrospun nanoscale fibers from various polymers in all cases could be

quantitatively described in terms of a core-shell model with a shell characterized by the stretching and curvature elasticity. This model turns out to be applicable to various polymer nanofibers and can be considered as a universal physical explanation of the phenomenon under discussion. The role of the shell (surface layer) was estimated on the base of a phenomenological consideration of the change in the surface free energy due to elastic deformation. This

approach leads to a two-term equation describing the size dependence of the elastic modulus of nanofiber. The fitting parameters used in theory are reduced to the surface stretching modulus and the surface curvature elastic modulus.

The shell-core morphology is characteristic of all fibers spun from polymer solutions by the wet or dry-wet methods. The main reason for the difference in the structure of the shell and core is the mutual diffusion of the coagulant inside and the solvent outside the spinning jet/fiber. According to X-ray diffraction data in transmission and reflection modes [28], the shell is more ordered than the core, and the final fibers show the dependence of mechanical properties on diameter, increasing with decreasing thickness.

Acknowledgements

We acknowledge funding from Ministry of Science and Higher Education of the RF (Agreement # 175-15-2020-794). The authors are grateful for permission to use experimental data from Ref. [23, 24] to APS, from Ref. [25] to AIP, from Ref. [26] to Elsevier., and from [27] to ACS.








References

- [1] Reneker D. H., Yarin A. L.: Electrospinning jets and polymer nanofibers. *Polymer*, **49**, 2387–2425 (2008). <https://doi.org/10.1016/j.polymer.2008.02.002>
- [2] Xue J., Wu T., Dai Y., Xia Y.: Electrospinning and electrospun nanofibers: Methods, materials, and applications. *Chemical Reviews*, **119**, 5298–5415 (2019). <https://doi.org/10.1021/acs.chemrev.8b00593>
- [3] Arinstein A., Burman M., Gendelman O., Zussman E.: Effect of supramolecular structure on polymer nanofibre elasticity. *Nature Nanotechnology*, **2**, 59–62 (2007). <https://doi.org/10.1038/nnano.2006.172>
- [4] Cuenot S., Frétiigny C., Demoustier-Champagne S., Nysten B.: Surface tension effect on the mechanical properties of nanomaterials measured by atomic force microscopy. *Physical Review B*, **69**, 165410 (2004). <https://doi.org/10.1103/PhysRevB.69.165410>
- [5] Chen C. Q., Shi Y. S. Zhang J., Zhu Y., Yan J.: Size dependence of Young's modulus in ZnO nanowires. *Physical Review Letters*, **96**, 075505 (2006). <https://doi.org/10.1103/PhysRevLett.96.075505>
- [6] He J., Lilley C. M.: Surface effect on the elastic behavior of static bending nanowires. *Nano Letters*, **8**, 1798–1802 (2008). <https://doi.org/10.1021/nl0733233>
- [7] Megelski S., Stephens J. S., Chase D. B., Rabolt J. F.: Micro- and nanostructured surface morphology on electrospun polymer fibers. *Macromolecules*, **35**, 8456–8466 (2002). <https://doi.org/10.1021/ma020444a>
- [8] Wang X., Xu Y., Jiang Y., Jiang J., Turng L-S., Li Q.: Core/shell structure of electrospun polycarbonate nanofibers. *Polymer Testing*, **70**, 498–502 (2018). <https://doi.org/10.1016/j.polymertesting.2018.08.009>
- [9] Arinstein A., Zussman E.: Electrospun polymer nanofibers: Mechanical and thermodynamic perspectives. *Journal of Polymer Science Part B: Polymer Physics* **49**, 691–707 (2011). <https://doi.org/10.1002/polb.22247>
- [10] Stockdale T. A., Cole D. P., Staniszewski J. M., Roenbeck M. R., Papkov D., Lustig S. R., Dzenis Y. A., Strawhecker K. E.: Hierarchical mechanisms of lateral interactions in high-performance fibers. *ACS Applied Materials and Interfaces*, **12**, 22256–22267 (2020). <https://doi.org/10.1021/acsami.9b23459>
- [11] Dayal P., Liu J., Kumar S., Kyu T.: Experimental and theoretical investigations of porous structure formation in electrospun fibers. *Macromolecules*, **40**, 7689–7694 (2007). <https://doi.org/10.1021/ma071418l>
- [12] de Gennes P. G.: Solvent evaporation of spin cast films: 'Crust' effects. *The European Physical Journal E*, **7**, 31–34 (2002). <https://doi.org/10.1140/epje/i200101169>
- [13] Okuzono T., Ozawa K., Doi M.: Simple model of skin formation caused by solvent evaporation in polymer solutions. *Physical Review Letters*, **97**, 136103 (2006). <https://doi.org/10.1103/PhysRevLett.97.136103>
- [14] Burman M., Arinstein A., Zussman E.: Do surface effects explain the unique elasticity of polymer nanofibers? *Europhysics Letters*, **96**, 16006 (2011). <https://doi.org/10.1209/0295-5075/96/16006>
- [15] Miller R., Liggieri L.: *Interfacial rheology*. CRC Press, Boca Raton (2019).
- [16] Hamilton J. C., Wolfer W. G.: Theories of surface elasticity for nanoscale objects. *Surface Science*, **603**, 1284–1291 (2009). <https://doi.org/10.1016/j.susc.2009.03.017>
- [17] Ojaghnezhad F. H. Shodja M.: Surface elasticity revisited in the context of second strain gradient theory. *Mechanics of Materials*, **93**, 220–237 (2016). <https://doi.org/10.1016/j.mechmat.2015.11.003>
- [18] Yao H., Yun G., Bai N., Li J.: Surface elasticity effect on the size-dependent elastic property of nanowires. *Journal of Applied Physics*, **111**, 083506 (2012). <https://doi.org/10.1063/1.3703671>
- [19] Arinstein A.: Confinement mechanism of electrospun polymer nanofiber reinforcement. *Journal of Polymer Science Part B: Polymer Physics*, **51**, 756–763 (2013). <https://doi.org/10.1002/polb.23246>
- [20] Helfrich W.: Elastic properties of lipid bilayers: Theory and possible experiments. *Zeitschrift Für Naturforschung C*, **28**, 693–703 (1973). <https://doi.org/10.1515/znc-1973-11-1209>
- [21] Khokhlov A. R., Semenov A. N., Subbotin A. V.: Shape transformations of protein-like copolymer globules. *The European Physical Journal E*, **17**, 283–306 (2005). <https://doi.org/10.1140/epje/i2005-10011-1>

- [22] Subbotin A. V., Semenov A. N.: Spatial self-organization of comb macromolecules. *Polymer Science Series A*, **49**, 1328–1357 (2007).
<https://doi.org/10.1134/S0965545X07120085>
- [23] Shin M. K., Kim S. I., Kim S. J.: Size-dependent elastic modulus of single electroactive polymer nanofibers. *Applied Physics Letters*, **89**, 231929 (2006).
<https://doi.org/10.1063/1.2402941>
- [24] Burman M., Arinstein A., Zussman E.: Free flight of an oscillated string pendulum as a tool for the mechanical characterization of an individual polymer nanofiber. *Applied Physics Letters*, **93**, 193118 (2008).
<https://doi.org/10.1063/1.3000016>
- [25] Cuenot S., Demoustier-Champagne S., Nysten B.: Elastic modulus of polypyrrole nanotubes. *Physical Review Letters*, **85**, 1690 (2000).
<https://doi.org/10.1103/PhysRevLett.85.1690>
- [26] Stachewcz U., Bailey R. J., Wang W., Barber A. H.: Size dependent mechanical properties of electrospun polymer fibers from a composite structure. *Polymer*, **53**, 5132–5137 (2012).
<https://doi.org/10.1016/j.polymer.2012.08.064>
- [27] Papkov D., Zou Y., Andalib M. A., Goponenko A., Cheng S. Z. D., Dzenis Y. A.: Simultaneously strong and tough ultrafine continuous nanofibers. *ACS Nano*, **7**, 3327–3331 (2013).
<https://doi.org/10.1021/nn400028p>
- [28] Makarov I. S., Golova L. K., Vinogradov M. I., Levin I. S., Gromovykh T. I., Arkharova N. A., Kulichikhin V. G.: Cellulose fibers from solutions of bacterial cellulose in N-methylmorpholine N-oxide. *Fibre Chemistry*, **51**, 175–181 (2019).
<https://doi.org/10.1007/s10692-019-10069-6>

Research article

Evaluation of the use of carbon nanotubes recovered from a biodegradation process in the production of new biodegradable polymer nanocomposites

Ana Paula Bernardo da Silva¹, Cássia Costa Giroto¹, Thaís Larissa Amaral Montanheiro^{1,2},
Marcelo Alexandre de Farias³, Larissa Stieven Montagna¹, Dayane Batista Tada⁴,
Fernando Henrique Cristovan⁵, Ana Paula Lemes^{1*}

¹Laboratory of Polymer and Biopolymer Technology (TecPBio), Universidade Federal de São Paulo, Talim, 330, São José dos Campos, 12231-280 São Paulo, Brazil

²Laboratory of Nanotechnology, Division of Fundamental Sciences, Instituto Tecnológico de Aeronáutica, Praça Marechal Eduardo Gomes, 50, São José dos Campos, 12228-900 São Paulo, Brazil

³Brazilian Nanotechnology National Laboratory (LNNano), Brazilian Center for Research in Energy and Materials (CNPEM), Campinas, 113083-970 São Paulo, Brazil

⁴Nanomaterials and Nanotoxicology Laboratory, Universidade Federal de São Paulo, Talim, 330, São José dos Campos, 12231-280 São Paulo, Brazil

⁵Universidade Federal de Jataí, Instituto de Ciência Exatas e Tecnologia, Câmpus Jatobá, BR 364, km 195, 3800, 75801-615 Jataí, GO, Brazil

Received 13 July 2022; accepted in revised form 23 September 2022

Abstract. The present study carried out the characterization of carbon nanotubes (CNT) recovered from the biodegradation process of poly(3-hydroxybutyrate-co-3-hydroxyvalerate) (PHBV)/CNT nanocomposites and the use of this recovered CNT (CNT-rec) in the production of new PHBV nanocomposites. The results obtained by characterization of CNT-rec were very similar to the CNT. Therefore, it was possible to state that CNT properties were preserved during the biodegradation process; however, CNT-rec contained impurities such as proteins and residual PHBV. Regarding the performance as nanofillers, although both CNT and CNT-rec decreased the thermal stability of nanocomposites compared to neat PHBV, this effect was less intense in the CNT-rec nanocomposites. It is expected that both nanofillers acted as nucleating agents in the PHBV matrix crystallization process but with different effectiveness. There was no significant difference between the electrical conductivity comparing PHBV/CNT 2% and PHBV/CNT-rec 2% nanocomposites. Therefore, the recovery and use of CNT-rec is a feasible process.

Keywords: nanocomposites, biodegradable polymers, carbon nanotubes recovered, poly(3-hydroxybutyrate-co-3-hydroxyvalerate), biopolymers

1. Introduction

The search for environmentally friendly materials has motivated a lot of investigations in academia and industry. In this regard, biodegradable polymers have stood out as an alternative material mainly to replace synthetic polymers and in the production of materials

from renewable resources [1, 2]. However, with the advancement in the production and use of biodegradable polymers, new questions have arisen in the literature. The effective biodegradation of these materials when disposed of in a conducive environment. The possibility of recycling increases their useful life

*Corresponding author, e-mail: aplemess@gmail.com

© BME-PT

in the market since many have a higher production cost than conventional materials. And whether contaminants are generated during the biodegradation process since many of them are processed with other materials and additives.

Therefore, studying the biodegradation of both biodegradable polymers from renewable and synthetic sources is extremely important [3, 4]. These studies have proven that these polymers are indeed biodegraded, but there is still a lack of information regarding methods that allow ensuring the complete biodegradation of the majority of the biopolymers and that they are suitable for disposal in certain biodegradation media [5]. Siracusa [6] pointed out the difficulty of ensuring that all synthetic biodegradable polymers are suitable for composting, noting the possible contamination of the environment by polymer fragments. The author also highlighted the importance of having the polymer entirely biodegraded. Other polymers already in commercial use (in plastic bags) and reported as 100% biodegradable did not show the same results in biodegradation studies performed in the laboratory and at home-composting conditions. The polymers did not suffer total decomposition, mainly at home-composting conditions, thus alerting them to the unbridled use of this material that is reported as suitable for biodegradation [7].

In this context, the concerns regarding the waste of biodegradable polymers have to be the same raised by the waste of petroleum-based thermoplastic polymers. Considering the current limitations of the biodegradation process and the higher production cost in comparison with those derived from petroleum, recycling biopolymers has emerged as a prominent research field. Despite being still little explored, recycling biopolymers has been proven to be economically, ecologically, and technologically advantageous. Some biodegradable polymers may present more viable recycling steps than petroleum-based polymers, making their use even more attractive [8]. However, it is noted that recycling is more beneficial for biodegradable polymers with thickness above 1 mm, and when the polymer is thinner, it is more profitable to recover it (proper collection) before it is disposed of by composting rather than recycling because thinner polymers degrade more easily [8, 9]. Although numerous works that reported on recovery by recycling, biodegradation test, or even toxicity (such as ecotoxicity with plants) of biodegradable polymers are observed [1, 4, 10–12], the composites

or nanocomposites produced with these polymers have been very little considered [13, 14]. Commonly, biodegradable polymers are processed with other polymers (polymer blends) or reinforced with filler or nanofiller, generating composites or nanocomposites with enhanced properties [2, 15–25]. Few studies address the effect of the addition of the nanofiller on the polymer biodegradation property [4, 21, 26–32], and even fewer studies have investigated what happens to the nanofillers after polymer biodegradation [26]. Since most parts of the inserted nanofillers are not biodegradable, studies about their destination should be considered in the research of nanocomposites. Just as important, strategies for reusing these nanocomposites or a part of them, such as the nanoparticles themselves, should also be considered.

Among the biodegradable polymers produced from renewable resources and synthesized from microbial fermentation is the family of polyhydroxyalkanoates (PHAs). Poly(3-hydroxybutyrate-co-3-hydroxyvalerate) (PHBV) is one of the copolymers of this family with great prominence in the production of composites and nanocomposites [33–40]. Some of our previous studies have focused on the analysis of the effect of the introduction of filler and nanofiller on the biodegradation of PHBV. Titanium dioxide (TiO₂) nanoparticles or glassy carbon (GC) were shown to not affect the biodegradation of PHBV nanocomposites [31, 41]. Nevertheless, the introduction of CNT or graphite nanosheets (GNS) decreased the biodegradation rate with increasing nanofiller content [26, 30, 42, 43]. The lower biodegradation rate was associated with changes caused on the material surface, hydrophilicity, and exposure of the nanofiller to the biodegradable material. Added to this, in our previous study [26], it was observed that with the biodegradation of the nanocomposite films, the CNTs were exposed and released into the reaction medium as part of the biodegradation residues. PHBV/CNT 2% nanocomposite films were biodegraded in a liquid medium on a large scale for 20 was analyzed by field emission scanning electron microscope. It was observed that CNT was intact after the test, reinforcing the importance of an adequate treatment of the waste and indicating the possibility of recovery of these CNT after the biodegradation process.

CNT used as reinforcement in biodegradable polymeric matrices has been largely reported in the scientific literature [17, 22, 44–51]. However, the characterization and reuse of the CNT after the process

of biodegradation of these matrices have not been investigated yet. Due to the chemical and structural properties of CNT, it is expected that these properties will be unchanged in the biodegradation process, encouraging their recovery for reuse in the same material or in the production of other nanocomposites and products. This process would close the life cycle of this material and meet the principles of sustainability in the development of products. Thus, the present study carried out the characterization of CNT recovered in a biodegradation process of PHBV/CNT nanocomposites to evaluate the preservation of their properties and consequently provide crucial information to evaluate their reuse. Furthermore, the recovered CNT was used in the production of PHBV nanocomposites. The as-prepared PHBV nanocomposites with recovered CNT (PHBV/CNT-rec) were characterized regarding thermal, morphological, and electrical properties. The comparison with the properties of PHBV nanocomposite prepared with CNT and CNT-rec pointed out the successful recovery process of CNT and the use of these CNT to obtain nanocomposites with similar properties.

2. Experimental

2.1. Materials

Multiwalled carbon nanotubes (CNT) were supplied by CNT CO. Ltd. (Incheon, Korea). The CNT were produced by chemical vapor deposition with a purity of 93% (weight), diameter in the range of 10 to 40 nm, and length in the range of 5 to 20 μm . Poly(3-hydroxybutyrate-co-3-hydroxyvalerate) was supplied by PHB Industrial Ltd. (São Paulo, Brazil), with 15 mol% of hydroxyvalerate units and average molecular weight (M_w) of 230.000 $\text{g}\cdot\text{mol}^{-1}$. To prepare the films, chloroform (CHCl_3) from LabSynth (Diadema, Brazil) was used as a solvent.

2.2. Nanocomposites films preparation

Films of PHBV/CNT nanocomposites were prepared by solution-casting according to the methodology determined in previous works [25, 26, 52, 53]. PHBV was solubilized in chloroform under heating, with 8% (w/v). A suspension of CNT in chloroform was previously sonicated in an ultrasonic processor (VCX 750 Sonics, 750 W; 20 kHz) for 2 min. The solution and suspension, PHBV and CNT in chloroform, were sonicated for 1 min and then poured onto Petri plates. The films were formed after the evaporation of the chloroform overnight. PHBV nanocomposite films

were produced with 0, 1, and 2 wt% CNT and labeled as PHBV, PHBV/CNT 1%, and PHBV/CNT 2%.

2.3. CNT recovery

The CNT recovered (CNT-rec) were obtained from the biodegradation of films from the PHBV/CNT 2% nanocomposites following the methodology developed by our research group and previously reported [26]. The films were incubated in a mineral solution with a microorganisms consortium previously extracted from the soil at 32 °C with the agitation of 130 rpm for 20 days until complete biodegradation of the polymer. The CNT released in the solution was recovered in a centrifugation process and later washed again (four times). After each centrifugation step, the supernatant was discarded, and a volume of deionized water was added to the suspension with the CNT-rec. Aliquots containing the final mass of CNT-rec with deionized water were frozen and then lyophilized at -84 °C for 24 h in a Labconco Free Zone 2.5 Plus Lyophilizer (Missouri, USA). CNT-rec was used to produce new films, following the same methodology of preparation of the nanocomposites (Section 2.2). Nanocomposites films were produced with 1, and 2 wt% CNT-rec labeled as PHBV/CNT-rec 1% and PHBV/CNT-rec 2%.

2.4. Characterization of CNT

Pristine CNT and CNT-rec were analyzed in a field emission gun scanning electron microscope (FEG-SEM) model MIRA 3 (TESCAN, Brno, Czech Republic) operating at 20 kV. A transmission electron microscope (TEM) JEOL JEM 1400Plus (JEOL, Japan) was used to obtain images of the pristine CNT and CNT-rec, operating at 80 kV. The nanofillers were placed on carbon-coated copper grids.

Fourier transform infrared (FT-IR) spectroscopy was performed using a Shimadzu IR Affinity-1 (Kyoto, Japan), with 2 cm^{-1} resolution, to confirm the presence of impurities remaining or molecules adhering to the CNT-rec surface. Pristine CNT and CNT-rec were prepared onto potassium bromide (KBr) crystals. Pristine CNT and CNT-rec were analyzed by Raman Renishaw 2000 spectrometer (Renishaw, Old Town, Gloucestershire, UK), coupled to an optical microscope with an argon laser (514 nm).

The samples were submitted to X-ray diffraction in a high-resolution X-ray diffractometer Philips X-Pert MRD (Eindhoven, Netherlands), with $K_{\alpha 1}$ (1542 Å) of a copper tube operating under 45 kV and 40 mA.

The data were collected over a range of scattering angles (2θ) of 10–40°, time per step of 20 s, and step size of 0.02°.

2.5. Characterization of nanocomposites films

Differential scanning calorimeter (DSC) measurements of PHBV/CNT and PHBV/CNT-rec nanocomposites were performed using a Netzsch model DSC 204 Phoenix (Selb, Germany). Samples were sealed in an aluminum DSC pan and heated from room temperature to 200 °C at 10 °C·min⁻¹, and they were kept at this temperature for 2 min. Posteriorly, samples were cooled to -20 °C at 10 °C·min⁻¹, held at this temperature for 1 min, and again heated to 200 °C at 10 °C·min⁻¹. Measurements were performed under a nitrogen atmosphere with a flow rate of 50 ml·min⁻¹. The degree of crystallinity, X_c [%], was calculated according to Equation (1):

$$X_c [\%] = \frac{\Delta H_m}{\phi_{\text{PHBV}} \cdot \Delta H_m^0} \cdot 100 \quad (1)$$

where ΔH_m is the total melting enthalpy on second heating, ϕ_{PHBV} is the weight fraction of PHBV in the nanocomposite, and ΔH_m^0 is the theoretical melting-heat value of 100% crystalline PHBV, which was taken as 109 J·g⁻¹ [54]. ϕ_{PHBV} was considered equal to 0.99 and 0.98 for nanocomposites with 1 and 2 wt% nanofiller, respectively.

Thermogravimetric analyses (TGA) of PHBV/CNT and PHBV/CNT-rec nanocomposites were performed using Netzsch TG 209 F1 Iris[®] equipment (Selb, Germany). Samples were heated at a rate of 20 °C·min⁻¹, starting from 50 to 800 °C, under nitrogen flow.

DC conductivity of the nanocomposites was measured using the two probe method and equipment of Keithley 2400 SourceMeter (Keithley Instruments, Inc., Cleveland, OH, USA). The films had an average thickness of 40 μm, and the electrical contact was gold/palladium thin film deposited by a Sputter Coater SCD 050 Baltec (Scotia, NY, USA) on both sides of the sample producing a metal–nanocomposite–metal structure. The values were calculated using Equation (2):

$$\sigma = \frac{iL}{VA} \quad (2)$$

where σ is the electrical conductivity [S·cm⁻¹]; i is the electric current [A]; L is the sample thickness [cm]; V is the voltage [V], and A is the electrical contact area [cm²].

The cryogenically fractured surfaces of nanocomposite films were analyzed by FEG-SEM in TESCAN (model MIRA 3) equipment (Brno, Czech Republic). The samples were fractured in liquid nitrogen, fixed in aluminum stubs with carbon tape, and covered with a thin layer of gold deposited by a Sputter Coater SCD 050 BalTec (Scotia, NY, USA).

3. Results and discussion

3.1. Characterization of CNT

3.1.1. Morphology: FEG-SEM and TEM

FEG-SEM analyzes were performed to evaluate CNT morphology and possible changes resulting from the biodegradation process. The long length (Figure 1a), homogeneity in diameter size, and surface integrity of the nanotubes (Figure 1b) can be observed in the micrographs of the pristine CNT.

In the same way, in Figure 1c, it is possible to observe the presence of CNT-rec in large quantities in the residual recovered after the biodegradation test. However, the residual still presents some regions of CNT-rec with the PHBV matrix that had not been fully degraded in the biodegradation process (indicated in Figure 1c with arrows). In our previous work, Silva *et al.* [26] also showed the great presence of CNT in the final residue of the biodegradation of PHBV/CNT 2% films, and in some regions, the presence of the PHBV matrix that has not been fully degraded. An area with several CNT-rec with part of its length completely free from the matrix can be observed in Figure 1c, whereas in Figure 1d, regions of its length adhere to the polymer matrix (indicated by arrows). In Figure 1d, free CNT-rec with diameters similar to those of pristine CNTs (in the 30 nm range) can be observed, indicating that despite the biodegradation process, the structure of the CNT is preserved. In this micrograph, one can also notice the presence of CNT-rec with parts completely inserted inside the matrix, as indicated by the white arrows. The morphology of CNT-rec due to the biodegradation process was further investigated by TEM. Figure 2a–2c shows the TEM micrographs of the original CNT, where it is possible to see CNT with different lengths and diameters and the presence of amorphous carbon (Figure 2a). These structures are already expected since they are known to be formed during thermochemical vapor deposition (TCVD). It is also noted black spherical particles that correspond to the metallic catalyst particles, which are the main impurity arising from the process of obtaining

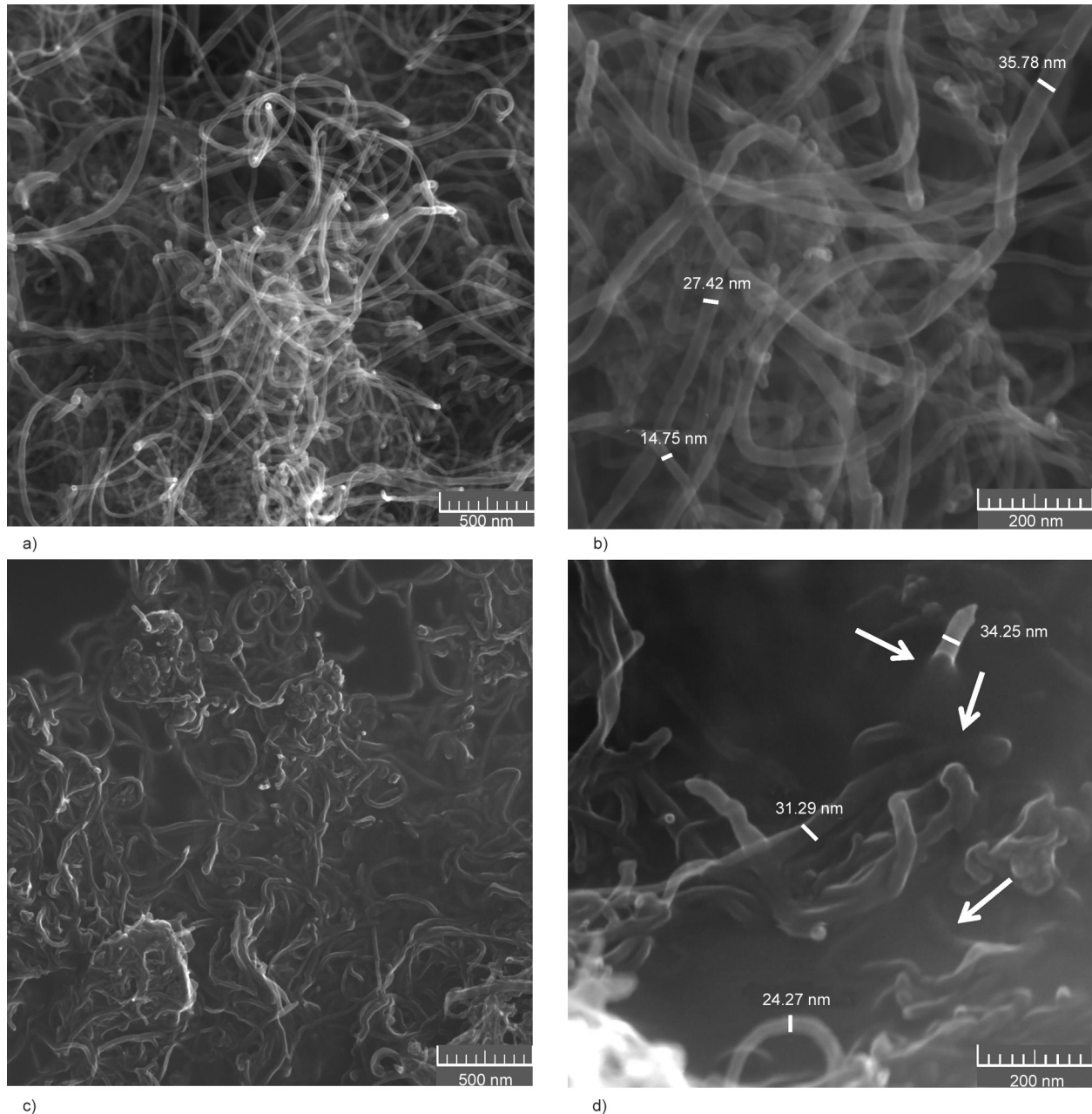


Figure 1. FEG-SEM images of (a, b) pristine CNT; (c, d) CNT-rec.

the CNT. CNT agglomerates can also be observed (indicated by arrows in [Figure 2b](#)). The presence of CNT agglomerate (darker region), amorphous carbon, and metallic catalyst particles have already been identified in our previous work [25]. In addition, the micrograph with the highest magnification ([Figure 2c](#)) shows some conical closed ends (indicated by the arrows) that are typical of not oxidized CNT, and it is believed that the formation occurs due to the presence of pentagonal rings inserted between the hexagonal rings that make up the graphite sheet [55].

In the micrographs, it is possible to notice the presence of residues from the biodegradation process around the CNT-rec (indicated in [Figure 2d](#) with

arrows), probably the non-biodegraded PHBV and residue from the biodegradation test, confirming what was observed in the SEM micrographs ([Figure 1](#)). Two factors may have caused the non-biodegradation of the PHBV still present in the CNT-rec: A possible antimicrobial activity of the CNT [56–59], which hindered the biodegradation process of the PHBV chains that were physically attached to the CNTs; The period of time in which the test was performed (20 days), which may not have been enough to complete the action of the microorganisms.

In the analysis of the CNT-rec, black spherical particles are noted, which are also observed in the pristine CNT, where they refer to the presence of the

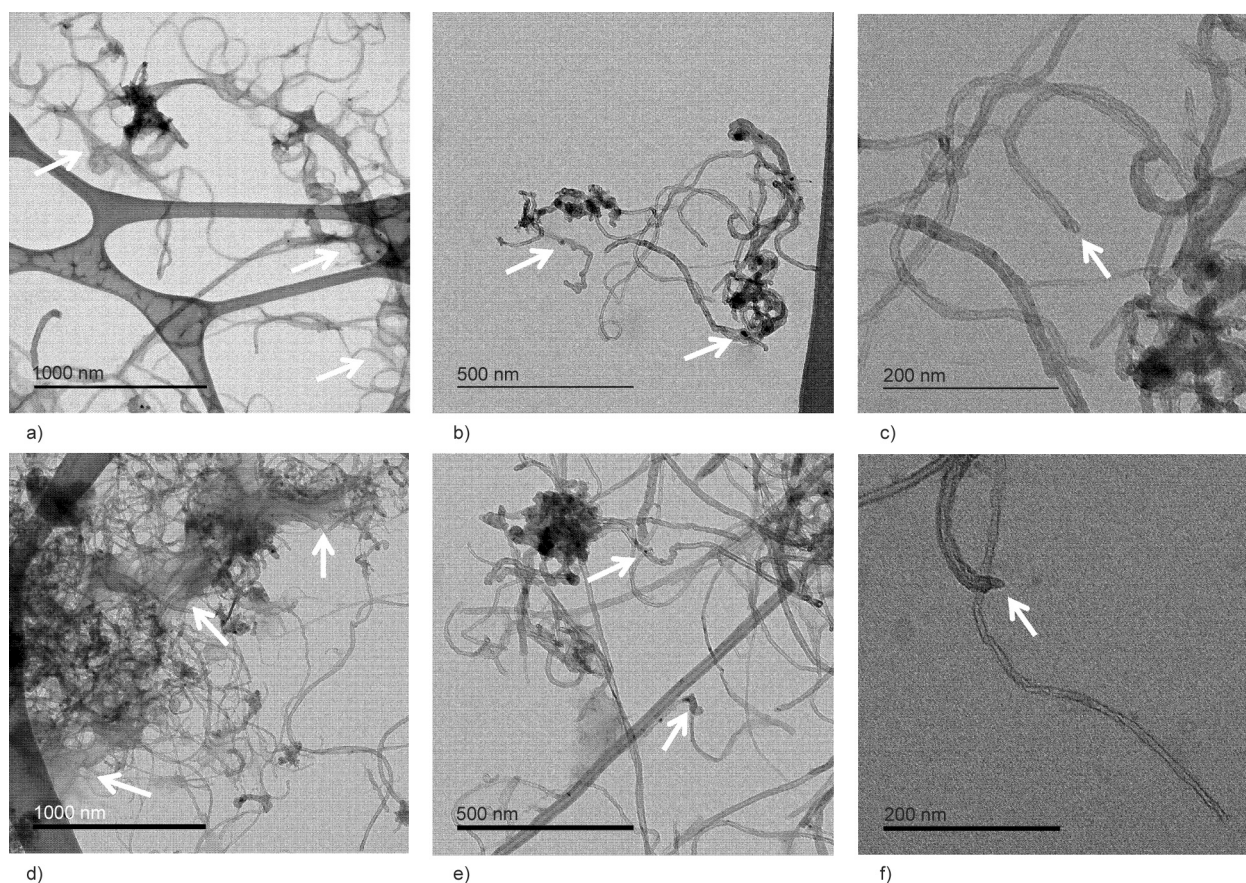


Figure 2. TEM images of (a–c) pristine CNT and (d–f) CNT-rec.

metallic catalyst particles used in the CNT production method (Figure 2e). The arrow (Figure 2f) indicates that the tip of the CNT-rec is closed; that is, it has not been oxidized in the biodegradation process, indicating that the structure of the CNT-rec has not been damaged.

3.1.2. FT-IR spectroscopy

Figure 3 shows spectra of PHBV, CNT-rec, and pristine CNT. In the PHBV spectra, the characteristic bands of this neat polymer are verified, which are present in other works in the literature [33, 60, 61]. FT-IR was used to characterize structural changes in the CNT-rec from the biodegradation process compared to the pristine CNT.

In the spectrum of CNT-rec, the broad band at 3450 cm^{-1} is more intense compared with pristine CNT. This band is assigned to the OH stretching of carboxylic groups ($\text{O}=\text{C}-\text{OH}$), and is related to the water molecules that the impurities present in the CNT-rec may have absorbed during storage [62]. Spectrum bands at 2926 and 2870 cm^{-1} , observed in pristine CNT and CNT-rec, are assigned to the asymmetric and symmetric stretching of the methylene present in the hexagonal structure of CNT. The

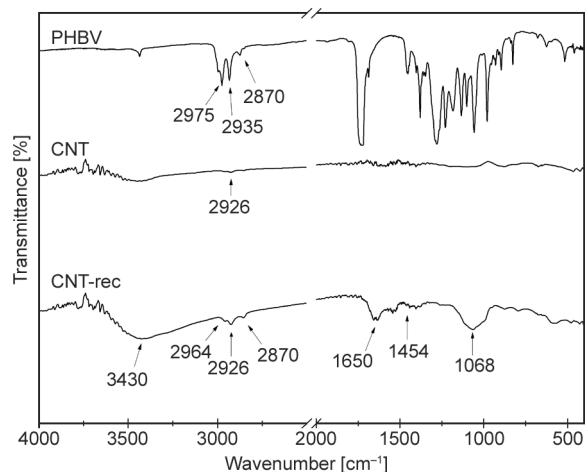


Figure 3. FT-IR spectra of the neat PHBV, pristine CNT, and CNT-rec.

identification of these bands in the CNT is related to defects in the sidewalls of the nanotubes [63]. In the spectrum of CNT-rec, some bands from the remaining PHBV are observed, indicating the presence of PHBV chains in this CNT after the biodegradation process. In addition, another band characteristic of PHBV is observed in the CNT-rec at 1454 cm^{-1} that is assigned to asymmetric angular deformation of methyl groups in the polymeric chain of PHBV [12,

33, 60]. The remaining bands of PHBV in the spectrum of CNT-rec are in accordance with the results from FEG-SEM and TEM, confirming the presence of small amounts of non-degraded PHBV.

The FT-IR spectrum of CNT-rec also shows the bands at 1650 and 1068 cm^{-1} that are characteristic of the amide functional group I and can be assigned to the presence of proteins since proteins have intense transmittance bands at those wavenumbers. The band at 1650 cm^{-1} refers to C=O stretching vibration with a small participation of the C–C–N deformation, out-of-phase C–N stretching vibration, and NH in-plane bend. And the band at 1068 cm^{-1} refers to NH_2 deformation vibration [64, 65]. These bands are additional indications of the presence of protein adhered to the surface of the CNT-rec, being a remnant of the biodegradation process. These proteins are expected to be produced by the microorganisms and released into the reaction medium. Therefore, as observed in the morphological characterizations, the existence of impurities adhered to the CNT-rec is noted (as observed in TEM images, Figure 2), which in this case indicates that the PHBV did not biodegrade completely, remaining attached to the CNT-rec, and also the residues of the biodegradation process, which in this case, maybe protein molecules.

3.1.3. Raman spectroscopy

Information about the degree of disorder of the crystal structure can be obtained through Raman spectroscopy, an analysis widely used to characterize carbon materials [66]. All graphitic materials, including CNT, exhibit a strong peak at 1580 cm^{-1} (G band), which is the first-order mode attributed to symmetry vibrations, known as E_{2g} , associated with perfect graphite [67–70]. Since most carbonaceous materials exhibit significant disorders, other bands are observed. A band near 1350 cm^{-1} called the defect band (D1 band) is attributed to the A_{1g} symmetry vibration mode of the graphite lattice, being caused by structural defects and the presence of heteroatoms. The band at 1620 cm^{-1} (D2 band) is assigned to lattice vibration analogous to the G band, but this

vibration is from the graphene layers that are not sandwiched between two graphene layers. The band near 1530 cm^{-1} (D3 band) is assigned to the amorphous sp^2 -bonded carbon species, and this band is presented in poorly ordered materials, organic molecules, fragments, or functional groups. The band at 1150 cm^{-1} (D4 band) is assigned to sp^3 - sp^2 mixed sites at the edges of crystallites or C–C and C=C stretching vibrations of polyene-like structures [68–70]. Figure 4 presents Raman spectra (experimental curve), their respective deconvolutions (fit peak curve), and the cumulative peak curve for pristine CNT and CNT-rec. The methodology used for deconvolutions is described by Sadezky *et al.* [68]. The combination of bands generated an R -square greater than 0.99, being close to 1, which characterizes an adequate fit (the theoretical curves and the values were obtained using OriginPro 8.5 software.). The bands discussed (G, D1, D2, D3, and D4) are detected in both samples, pristine CNT and CNT-rec.

To determine the degree of disorder in the structure of CNT, the ratio between the relative intensities of the D1 and G bands (ID_1/IG) is usually calculated, which is presented in Table 1. The ID_1/IG ratio tends to be higher for materials with higher defect density. For the analyzed samples, the ID_1/IG ratios are 1.25 for pristine CNT and 1.03 for CNT-rec, which suggests that CNT-rec has fewer defects in its structure compared with pristine CNT. However, since the

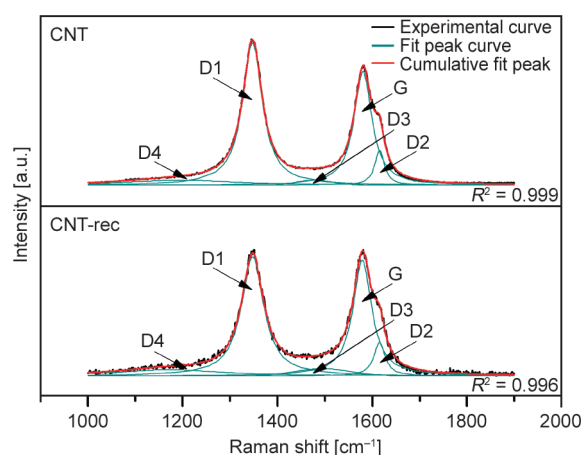


Figure 4. Raman spectra and deconvolution for pristine CNT and CNT-rec.

Table 1. Raman parameters calculated for pristine CNT and CNT-rec.

Sample	Intensity			Area ratio				
	D1	G	ID1/IG	D1/All	D2/All	D3/All	D4/All	G/All
CNT	0.98	0.78	1.25	0.49	0.06	0.02	0.08	0.35
CNT-rec	0.82	0.79	1.03	0.44	0.06	0.05	0.09	0.36

presence of mineral salts is observed in the XRD results of CNT-rec, this impurity can have caused the change in the D1 band intensity of CNT-rec (Table 1). Therefore, the ratios between the areas of each band and the total area (sum of all areas) are calculated to correlate the organization of this CNT structure and possible defects or impurities (Table 1). Thus, it can be seen that the other bands that are also attributed to defects and impurities (D2, D3, and D4) do not have a significant decrease between CNT-rec and pristine CNT; on the contrary, the ratio between D3/all-area and D4/all area have an increase. This result indicates that in the case of the D3/all area ratio of the CNT-rec (which is higher when compared to the ratio of pristine CNT), there is a great number of defects and/or impurities that can be attributed to the presence of organic molecules, fragments or functional groups [68, 69], and the presence of minerals [71]. Bar-Ziv *et al.* [71] relate the band's appearance around 1500 cm^{-1} to the presence of mineral matter observed in mineral-rich coal samples. The increase in the D3/all area ratio indicates the presence of $\text{sp}^3\text{-sp}^2$ bonds or C–C and C=C stretching vibrations characteristic of polyene-like structures [68, 69] and the presence of ionic impurities [68]. This result can indicate the presence of parts of the PHBV chain in the CNT-rec. Cuesta *et al.* [72] attribute the presence of this band to impurities and thus would not be linked to the degree of disorder of the material, which in this case is not a disorder of graphite. That being so, in the Raman analysis, as in the previous analyses, the presence of mineral salts and PHBV as impurities in the CNT-rec are also observed, but it is also observed that the biodegradation process does not affect the CNT structure of the CNT-rec, thus enabling its recovery after this process.

3.1.4. X-ray diffraction (XRD)

CNT X-ray diffractograms are characteristic of crystalline solids, which provide information regarding structural changes and/or the presence of impurities. Figure 5 shows the diffractograms of the pristine CNT and CNT-rec. As can be seen, both curves show peaks at approximately $2\theta = 26.1^\circ$, which is characteristic of graphitic structure on the walls of the carbon nanotubes, reflection from the 002 planes of graphite [73, 74]. However, the intensity of this peak in the CNT-rec curve is lower when compared with that observed for the pristine CNT. This can indicate that CNT-rec still has residues from the PHBV

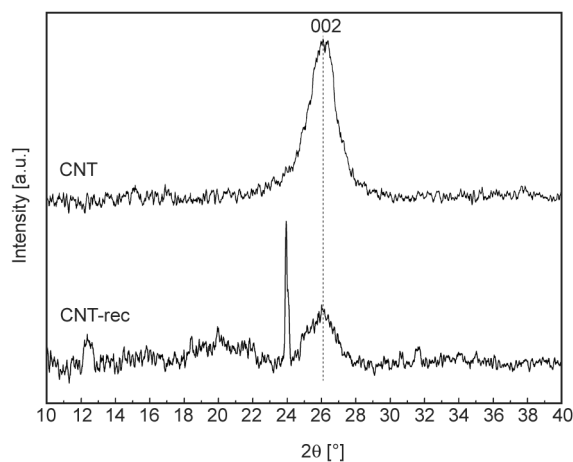


Figure 5. XRD diffractometer curves of CNT and CNT-rec.

matrix and the biodegradation process, as observed in morphological analyses (Figure 1 and Figure 2) and results of FT-IR.

CNT-rec diffractogram presents an unexpected peak at $2\theta = 24^\circ$, which can be associated with possible residues from the biodegradation test, such as mineral salts. This peak is characteristic of potassium dihydrogen phosphate (KH_2PO_4) [75, 76], one of the mineral salts used in the biodegradation test [26]. Even with the washings by centrifugation, some remnant of this salt remained in the CNT-rec or in the PHBV mass, which is observed in the micrographs, and thus detected in the XRD.

The presence of PHBV can also be noted in the X-ray diffractogram of CNT-rec, where small elevations in the curve can be observed exactly in the characteristic regions of the PHBV planes, which are: $2\theta = 13^\circ$ referring to the 020 plane, a slight elevation between $19\text{--}23^\circ$ where it contains the 021, 101, and 11 planes, and a slight displacement, shoulder, at 26° that may be due to the 121 plane at $2\theta = 25^\circ$. All these planes are presented and discussed in our previous work [17]. These plans are characteristic of the orthorhombic structure of PHBV [16, 53, 77]. Since PHBV appears as an impurity in CNT-rec, these peaks do not appear as evident as when observed in an XRD of its nanocomposite, but comparing CNT-rec to pristine CNT may indicate the presence of PHBV.

3.2. Characterization of nanocomposites films

3.2.1. Differential scanning calorimeter (DSC)

DSC analyses are performed to determine the crystallization and melting behaviors of PHBV and its nanocomposites with CNT and CNT-rec. Figure 6

shows the DSC curves for the cooling (after the first heating to eliminate the thermal history) and the second heating of the PHBV, PHBV/CNT, and PHBV/CNT-rec nanocomposites. The values of crystallization temperature (T_c) obtained in the cooling and the melting temperature (T_m), melting enthalpy (ΔH_m), and degree of crystallinity (X_c) obtained in the second heating of PHBV and nanocomposites can be observed in Table 2.

In the cooling curves (Figure 6a and Figure 6c), it can be seen that for pure PHBV, the crystallization peak occurs at a lower temperature than nanocomposites with CNT and CNT-rec. This result suggests that both the pristine CNT and the CNT-rec acted as nucleating agents, providing the previous crystallization of the PHBV matrix. The effect of the CNT nucleating agent on the PHBV matrix is also observed in the DSC results of the PHBV/CNT films with the addition of 1 to 10% CNT [25, 52, 54]. When well dispersed, CNTs increase the number of nucleation sites and, consequently, increase the polymer crystallization rate [54,

78]. In the case of CNT-rec (T_c at $\sim 75^\circ\text{C}$), this effect is less pronounced than the pristine CNT (T_c at $90\text{--}98^\circ\text{C}$), probably due to the lower actual concentration of CNT-rec. The characterizations of the CNT (Section 3.1) reveal that the CNT-rec contained impurities from the biodegradation process; therefore, the actual concentration of CNT in the PHBV/CNT-rec may be lower than the added mass of CNT in the PHBV/CNT nanocomposites.

In the curves of the second heating of pure PHBV (Figure 6b and Figure 6d), a melting peak of 170°C and a small shoulder in the curve of 157°C are observed. For the PHBV/CNT and PHBV/CNT-rec nanocomposites, it is possible to observe two melting peaks related to different lamella sizes of the crystalline phase, related to the homogeneous and heterogeneous PHBV nucleation [39, 79]. The introduction of CNT and CNT-rec intensifies this bimodal distribution due to its influence on the nucleation of the crystals that can occur both in heterogeneous and homogeneous nucleation, as already observed for the

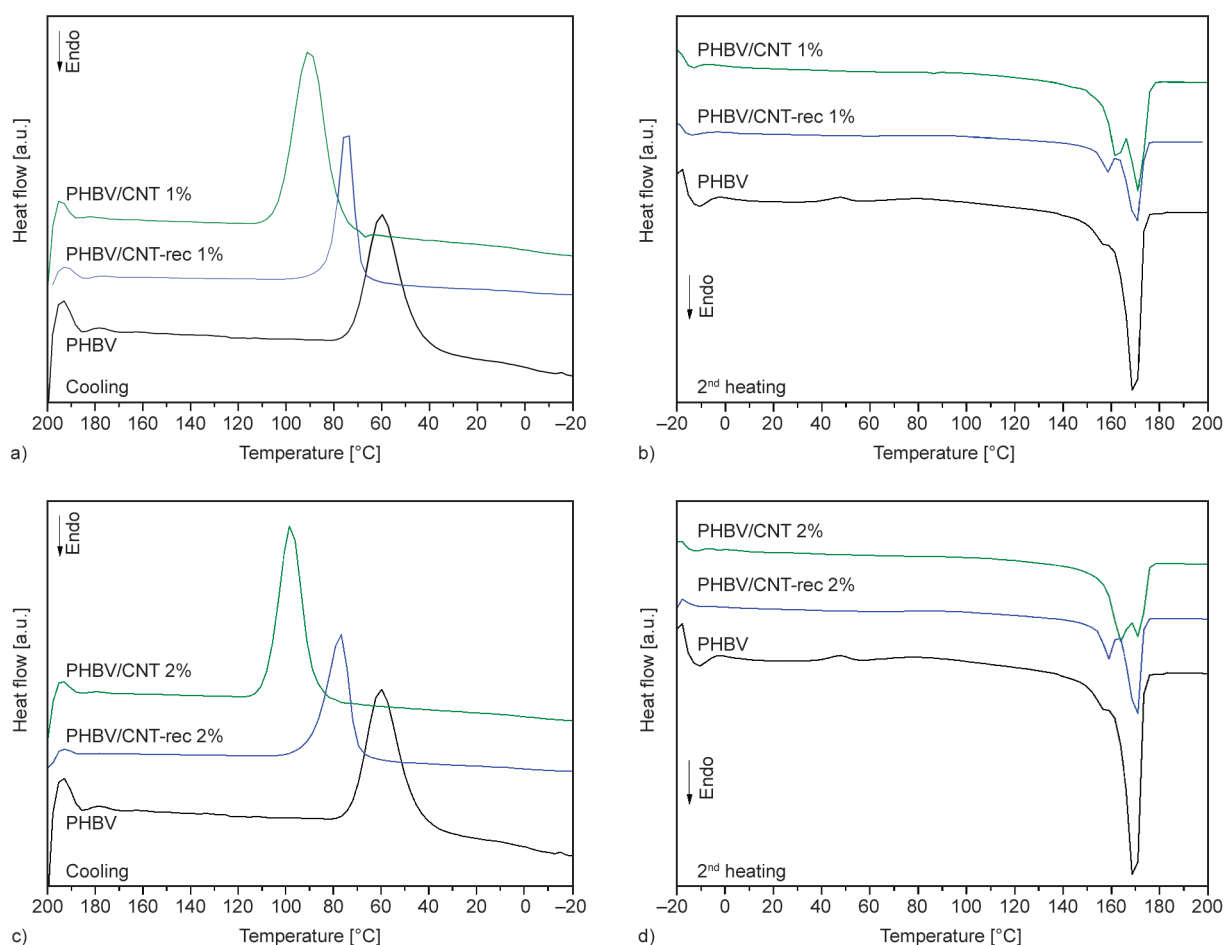


Figure 6. DSC curves of neat PHBV, PHBV/CNT 1%, and PHBV/CNT-rec 1%: (a) cooling and (b) second heating. Neat PHBV, PHBV/CNT 2% and PHBV/CNT-rec 2%: (c) cooling and (d) second heating.

introduction of CNT and other nanoparticles in the PHBV matrix [16, 39, 41, 54, 80]. Still, for the CNT-rec nanocomposite, this first peak appears with lower intensity when compared to the CNT pristine nanocomposite, which again indicates a lower actual nanofiller concentration in these films. The variations in the melting temperatures (T_{m1} and T_{m2}) are not significant when comparing all samples.

Table 2 also shows a decrease in the degree of crystallinity with the addition and increase of CNT concentration. Although CNT acts as a nucleating agent, when homogeneously dispersed in polymeric matrices and higher concentrations, they can act as a physical barrier, due to their length, for the growth of crystallites, hindering the crystallization of the polymer [17, 81]. The PHBV/CNT nanocomposite has a higher degree of crystallinity than PHBV/CNT-rec, which may be related to the better distribution of CNT in the matrix and the more real content of CNT in the final material. The most significant decrease in the degree of crystallinity (~40%) in PHBV/CNT-rec nanocomposites compared to pure PHBV may be related to impurities from the biodegradation process, as proven in other analyzes (morphology, FT-IR, Raman, and XRD). The contaminants, such as salts and protein, present in CNT-rec act as a barrier to the diffusion and folding of polymeric chains in the crystalline phase during crystallization. In this way, the PHBV matrix crystallization process is hampered since the mobility of the chains is restricted, and the PHBV/CNT-rec nanocomposites show a lower degree of crystallinity [36]. Furthermore, in the case of PHBV/CNT-rec nanocomposites, no significant difference is observed between the different concentrations, as in the case of PHBV/CNT nanocomposites, probably because the 2% mass of CNT-rec does not correspond solely to CNT, but also impurities.

Table 2. Thermal parameters evaluated from DSC for PHBV, nanocomposites PHBV/CNT and nanocomposites PHBV/CNT-rec.

Sample	T_c [°C]	T_{m1} [°C]	T_{m2} [°C]	ΔH_m [J/g]	X_c [%]
PHBV	60	N/D	170	87.07	79.9
PHBV/CNT 1%	90	163	171	72.71	67.4
PHBV/CNT-rec 1%	75	158	170	40.64	37.7
PHBV/CNT 2%	98	164	172	55.16	51.6
PHBV/CNT-rec 2%	77	159	171	42.47	39.8

N/D = not determined

3.2.2. Thermogravimetric analysis (TGA)

Thermogravimetric analysis (TGA) determined the thermal degradation behavior of neat PHBV and its nanocomposites with CNT and CNT-rec in an inert atmosphere (N_2) (Figure 7). In the TGA curves of all samples (Figure 7a and Figure 7b), it is found that the thermal degradation occurred in a single step, related to the thermal degradation of the PHBV matrix, which is proven by the curves of the first derivative (DTG) (Figure 7c and Figure 7d). The thermal degradation of the PHBV occurs by transesterification and cis-elimination [82]. To determine the effect of the introduction of the CNT and CNT-rec in the thermal degradation of the PHBV matrix, the temperature at 1% weight loss ($T_{1\%}$), the onset temperature (T_{onset}), the temperature at the maximum weight loss (T_{max}), and the residual mass (RM) are shown in Table 3.

In the $T_{1\%}$, an increase in the thermal stability in all nanocomposites is observed after the introduction of CNT. The increase in $T_{1\%}$ is more evident for nanocomposites with 1 and 2% of pristine CNT. This increase can be related to the decrease in the transport of combustion gas during the polymer decomposition with the addition of CNT and causing the absorption of free radicals produced in the degradation of the carbon surface [83]. A similar result is also reported in our previous work [52] in PHBV/MWCNT and PHBV/functionalized MWCNT nanocomposites and by Lai *et al.* [83] with the addition of MWCNT in PHBV nanocomposites.

However, the onset degradation temperature (Table 3) does not show the same trend. The T_{onset} of PHBV/CNT 1%, PHBV/CNT-rec 1%, and PHBV/CNT-rec 2% nanocomposites are almost the same as PHBV. But a small decrease of 7 °C in the T_{onset} of PHBV/CNT 2% nanocomposite is observed. The difficulty of CNT dispersion can have caused this effect on this concentration in the PHBV matrix. In the production of PHBV/MWCNT nanocomposites, Lemes *et al.* [25] observed that the increase of MWCNT concentration does not improve the thermal stability in the same proportion, and they attribute this result to the difficulty of nanofiller dispersion. Although, in other words, the increase in the thermal stability is observed in PHBV nanocomposites with 0.5 wt% of MWCNT, where the nanofiller act as a barrier to the permeation of combustion gas in nanocomposites with good dispersion of the MWCNT [52].

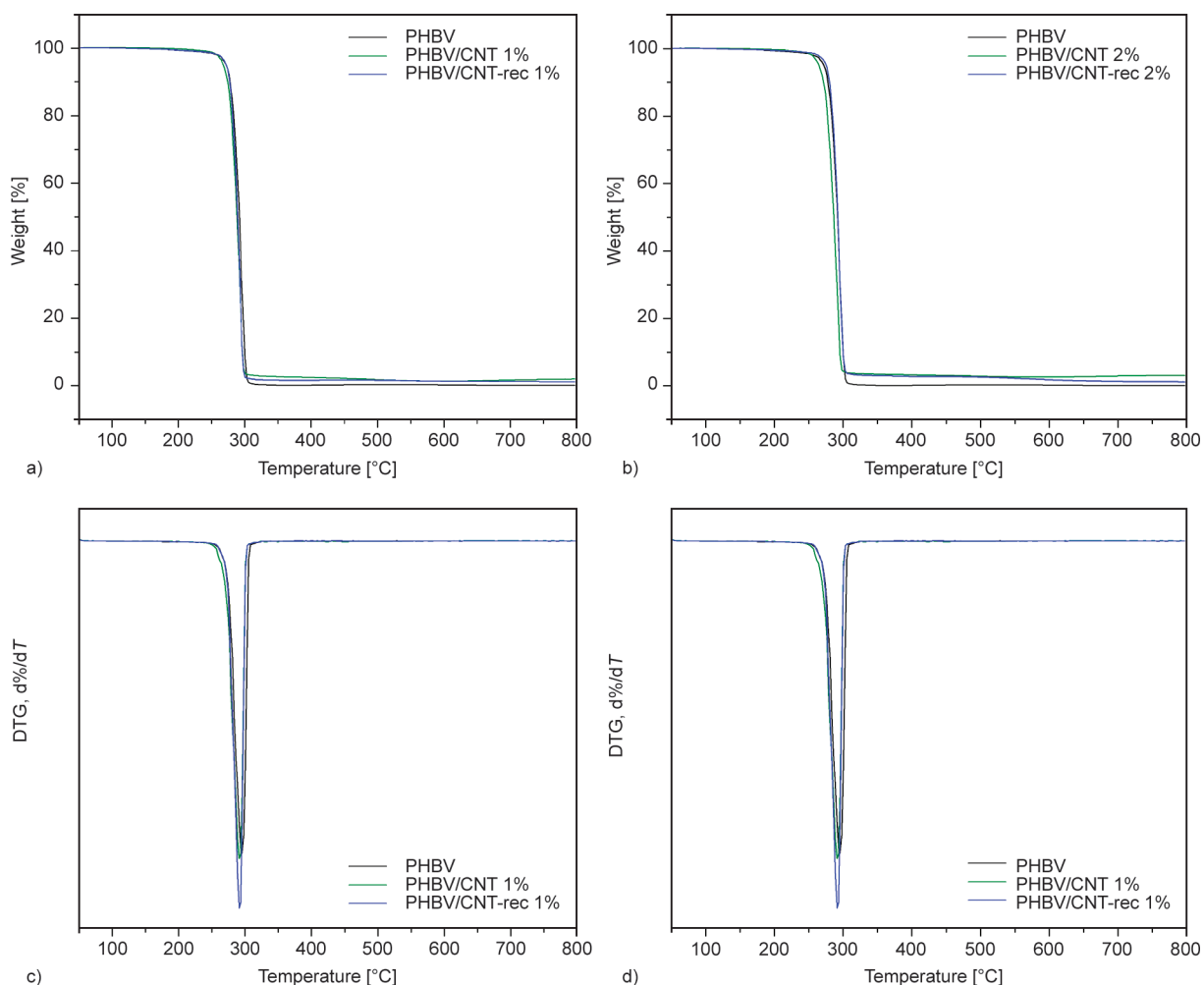


Figure 7. Thermogravimetric curves of PHBV, nanocomposites PHBV/CNT and nanocomposites PHBV/CNT-rec. a) and b) thermogravimetric curves; c) and d) first derivative curves.

Comparing the two nanocomposites with the content of 2%, PHBV/CNT 2%, and PHBV/CNT-rec 2%, the same behavior of decreased thermal stability is not observed. PHBV/CNT-rec 2% may have maintained the same temperature range as PHBV due to the actual content of CNT inserted being smaller in this nanocomposite since, as previously observed, CNT-rec contained not only CNT but also impurities. Thus, in the case of PHBV/CNT-rec nanocomposites, the

Table 3. Temperature at 1% weight loss ($T_{1\%}$), onset temperature (T_{onset}), temperature of maximum weight-loss rate (T_{max}), and residual mass (RM) for PHBV, PHBV/CNT, and PHBV/CNT-rec nanocomposites.

Sample	$T_{1\%}$ [°C]	T_{onset} [°C]	T_{max} [°C]	RM [%]
PHBV	225	282	303	0,02
PHBV/CNT 1%	245	280	297	1,97
PHBV/CNT-rec 1%	230	280	297	1,08
PHBV/CNT 2%	242	275	299	3,11
PHBV/CNT-rec 2%	240	283	302	1,16

non-variation of thermal stability may be related to the presence of impurities from the biodegradation process, such as the polymer itself.

In the T_{max} results (Table 3), the addition of 1% CNT causes a small decrease of 6 °C in the temperature value for the nanocomposites with pristine CNT and CNT-rec and of 4 °C for the PHBV/CNT 2%. This small decrease can be associated with CNT dispersion in the polymer; since not being well dispersed, the nanofiller does not act as a transport barrier for combustion gases, as was expected [83]. With the addition of 2% CNT-rec, no significant variation is observed compared to PHBV, which may also be associated with nanofiller dispersion in the matrix. In addition, the presence of PHBV in the CNT-rec may have collaborated in not affecting more expressively (impairing) the thermal stability of the nanocomposite. Lai *et al.* [83] observe an increase of 16 °C in T_{max} for PHBV nanocomposites with 2% of MWCNT and relate this increase to the

effective dispersion of the MWCNT, that act as a barrier to thermal degradation of the polymer.

As expected, the *RM* value obtained for the PHBV films is very close to 0% since, at this temperature, it is expected that the entire polymer has already degraded. The *RM* of nanocomposite with 1 and 2% pristine CNT show values well above the expected value, close to the added CNT content for each nanocomposite, since this is supposed to be the residue from the thermal degradation of the nanocomposites. However, this value is proportional for both nanocomposites. In the previous work of this research group [52], it was also observed an increase in *RM* value compared to the content of CNT in PHBV/MWCNT nanocomposites, being justified by the more active surface of the pristine CNT, which prevented the degradation of a small part of the polymer. Meanwhile, for the PHBV/CNT-rec 1% and PHBV/CNT-rec 2% nanocomposites, lower *RM* values are noticed compared to the content of CNT in the PHBV/CNT-rec nanocomposites. The difference in the *RM* value of the PHBV/CNT-rec 2% is even greater. This effect may be associated with the real content of CNT-rec that was added being lower since the CNT-rec still contained impurities arising from the biodegradation process as observed in the characterization of CNT-rec and which may have suffered thermal degradation.

Results obtained from the TGA analysis show that even with impurities in the CNT-rec, the PHBV/CNT-rec nanocomposites present suitable thermal stability, and under some conditions, it is even better than the thermal stability obtained by the addition of pristine CNT. These results further support our claim that the recovery and reuse of these carbon materials after the biodegradation process of the films is a feasible strategy.

3.2.3. Morphology

Cryogenically fracture surfaces of PHBV/CNT, and PHBV/CNT-rec nanocomposites were analyzed by FEG-SEM micrographs (Figure 8). The PHBV/CNT 1% (Figure 8a) shows a smooth fracture surface typical of a brittle and hard material; in addition, it is possible to observe the presence of CNT in the PHBV matrix (white arrows). On the other hand, PHBV/CNT-rec 1% (Figure 8c) presents a slightly rougher surface, characteristic of a material that suffered some deformation before rupture. But in this region of the micrograph, it is impossible to observe

the presence of CNTs, only possible impurities (white arrows), which may be linked to a smaller amount of nanofiller than the added content and the nanofiller not being well dispersed in the polymer matrix, due to the agglomerates.

PHBV/CNT 2% (Figure 8b) presents a rougher surface than other nanocomposites, indicating that it suffered a greater deformation before rupture. In comparison with the PHBV/CNT 1% nanocomposite, the increase in the content of CNT may also have contributed to the increase in roughness. CNT is present in the PHBV matrix (white arrows) with good interaction between nanofiller and polymer. However, in other works with this same CNT content, it is possible to observe the presence of a greater amount of CNT well dispersed in the polymer [83] or to identify the nanofiller's poor dispersion in large areas agglomerates [25]. Therefore, the micrograph of PHBV/CNT 2% (Figure 8b) may indicate the heterogeneity of the nanocomposite and thus may not represent regions that may contain the CNT poorly dispersed in the polymer matrix. This would be in agreement with the results observed in TGA, that the poor dispersion impaired the improvement of the thermal degradation temperatures of the nanocomposites.

A single CNT (white arrow) is observed on the fracture surface of PHBV/CNT-rec 2% (Figure 8d), in addition to a smooth surface, characteristic of a brittle and hard material, and the presence of impurities (white circles). Similar to the PHBV/CNT-rec 1% nanocomposite, this result indicates that the amount of CNT in the nanocomposite is lower. This is also in agreement with the other characterizations that stated the non-real content (being 2% in this nanocomposite) of the CNT and the presence of impurities (white circles).

3.2.4. Electrical conductivity

Electrical conductivity measurements are performed to verify the influence of the addition of CNT (pristine CNT and CNT-rec) to the PHBV matrix and the possible consequences of the biodegradation process on the electrical properties of CNT-rec. The values were calculated using Equation (2) through the linear portion of the *I-V* curves obtained from the equipment and are shown in Table 4. The PHBV shows the behavior of an insulating polymer, as observed by the electrical conductivity value ($5.1 \cdot 10^{-13} \text{ S} \cdot \text{cm}^{-1}$) [52]. The addition of CNT can turn the nanocomposite

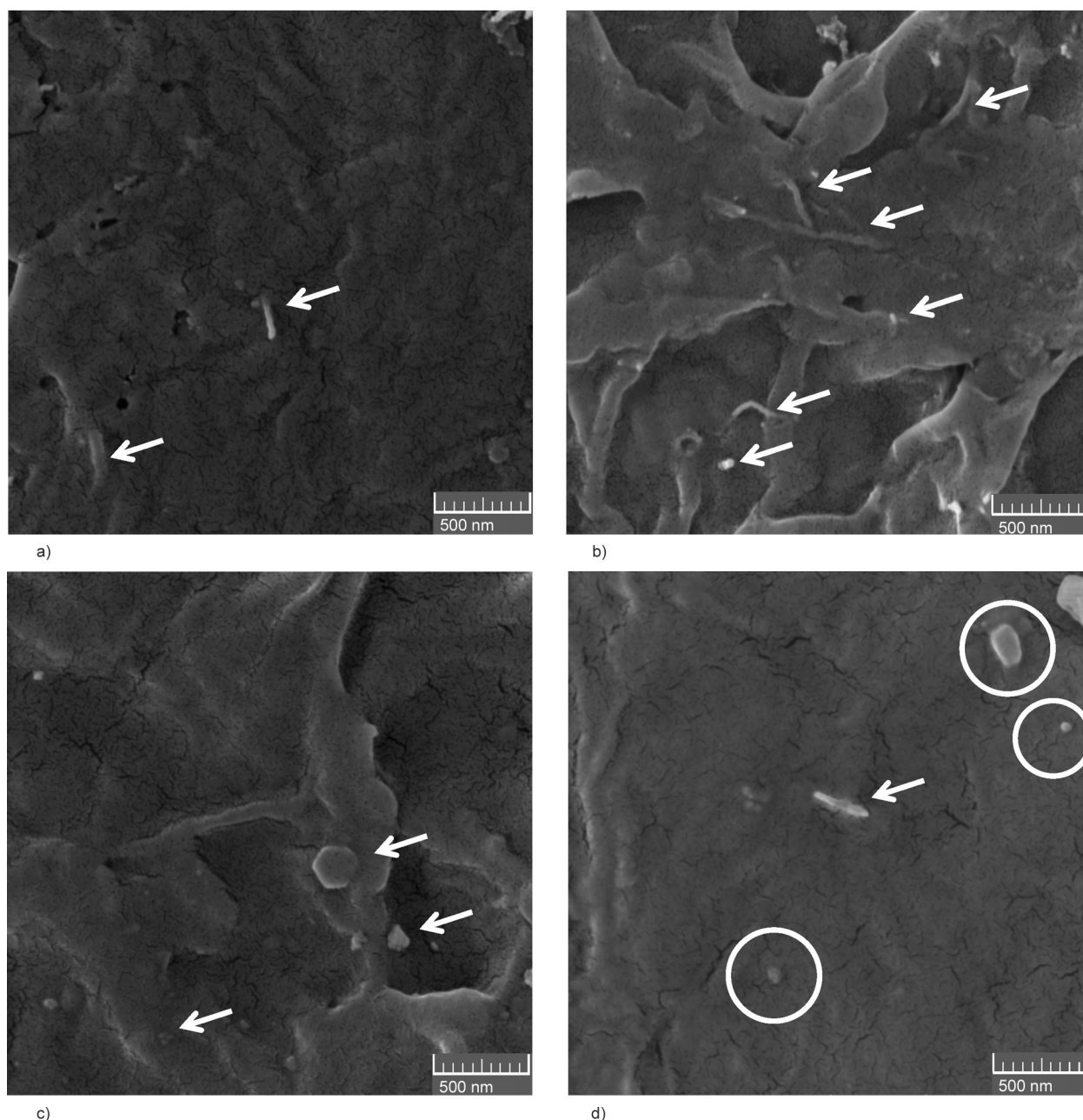


Figure 8. FEG-SEM micrographs of (a) PHBV/CNT 1%, (b) PHBV/CNT 2%, (c) PHBV/CNT-rec 1%, and, (d) PHBV/CNT-rec 2% nanocomposites.

into a semiconductor or conductive material up to a certain value (percolation threshold). The percentage

Table 4. Electrical conductivity values of PHBV, nanocomposites PHBV/CNT, and nanocomposites PHBV/CNT-rec.

Sample	Conductivity [S·cm ⁻¹]
PHBV*	$5.10 \cdot 10^{-13}$
PHBV/CNT 1%	$5.77 \cdot 10^{-4}$
PHBV/CNT-rec 1%	$4.18 \cdot 10^{-11}$
PHBV/CNT 2%	$1.42 \cdot 10^{-2}$
PHBV/CNT-rec 2%	$1.41 \cdot 10^{-2}$

*Value of the reference [52]

of CNT greatly influences the electrical conductivity of the nanocomposite, so this property tends to increase according to the increase in the percentage of the nanofiller [84, 85].

As expected, the addition of 1% CNT to the PHBV provides a significant improvement in the electrical conductivity of the nanocomposite, an increase of 9 orders of magnitude, when compared to the values of pure PHBV. The improvement in the electrical property supposes that a conductive network of CNT is formed in the polymeric matrix, thus allowing the transport of electrons in the nanocomposite [85]. The electrical conductivity of PHBV/CNT-rec 1%

nanocomposite ($4.18 \cdot 10^{-11} \text{ S} \cdot \text{cm}^{-1}$) is lower by 7 orders of magnitude compared to PHBV/CNT 1% ($5.77 \cdot 10^{-4} \text{ S} \cdot \text{cm}^{-1}$) and an increase of 2 orders of magnitude compared of pure PHBV. This result can be justified due to the amount of residual PHBV and impurities present in the CNT-rec, making the actual mass of CNT-rec in nanocomposite less than that mentioned, as already discussed and presented in other analyses.

Within this context, it would be expected that the electrical conductivity in the case of PHBV/CNT-rec 2% nanocomposite would also be lower compared to that of PHBV/CNT 2% nanocomposite due to the lower real concentration of CNT-rec. Surprisingly, there is no significant difference between the electrical conductivity of the PHBV/CNT 2% nanocomposite ($1.42 \cdot 10^{-2} \text{ S} \cdot \text{cm}^{-1}$) and the PHBV/CNT-rec 2% ($1.41 \cdot 10^{-2} \text{ S} \cdot \text{cm}^{-1}$). This result indicates that even with a concentration of less than 2% CNT, this amount can be sufficient to reach the percolation threshold in the PHBV/CNT-rec 2% film and thus result in a conductivity value close to the film with 2% CNT. The increase compared to pure PHBV is 11 orders of magnitude for both PHBV/CNT-rec 2% and PHBV/CNT 2%.

Therefore, electrical conductivity measurements of PHBV nanocomposite reveal that the biodegradation process does not compromise the electrical properties of CNT-rec, which corroborates with the results of previous analyses that observed the integrity of CNT-rec after the biodegradation process. Therefore, it is possible to state that it is possible to obtain nanocomposites with the same electrical properties when using pristine CNT or CNT-rec.

4. Conclusions

The use of carbon nanotubes recovered (CNT-rec) from the biodegradation of PHBV/CNT nanocomposites films to produce new nanocomposites with PHBV matrix is viable and very promising. Since the life cycle of this material can be closed in a relatively short period, it is full of sustainable principles of new material development. The methodology applied in this work shows that it is possible to recover the CNT from the biodegradation of PHBV/CNT nanocomposites; however, the CNT-rec still contained impurities such as proteins, mineral salts, and the PHBV matrix that were not fully biodegraded, thus indicating that the CNT recovery process needs to be improved. Despite that, it is found that CNT-rec

maintains its main structural characteristics. Comparing the properties of PHBV/CNT and PHBV/CNT-rec nanocomposites, it is noted that the effect of these nanofillers on the matrix is very close, mainly concerning the thermal and electrical properties of the nanocomposites. In some cases, despite observing the same trend, the changes of the PHBV properties are less evident in the PHBV/CNT-rec, probably due to the lower accurate content of CNT-rec in the nanocomposite since the nanofiller contains impurities arising from the biodegradation process. Regarding electrical conductivity, which can be considered a key property of the final application of the nanocomposite, there is no significant difference between the PHBV/CNT and PHBV/CNT-rec nanocomposites. Therefore, the results reported herein show that the recovery of the CNT from a nanocomposite is a feasible process that results in CNT with similar properties to the original ones and that the CNT recovered can be applied to produce new samples of the PHBV nanocomposite also with similar properties of the original nanocomposite.

Acknowledgements

The authors would like to thank the Instituto Nacional de Pesquisas Espaciais (INPE) for Raman measurements, DRX analyses, and SEM-FEG images and the Centro Nacional de Pesquisa em Energia e Materiais (CNPEM) for TEM images. The authors are grateful to João Paulo Barros Machado for the help in the Raman measurements and DRX analyses.

This work was supported by the Coordenação de Aperfeiçoamento de Pessoal de Nível Superior (CAPES) – Finance Code-001. The authors acknowledge the financial support received from Fundação de Amparo à Pesquisa do Estado de São Paulo (FAPESP 2019/15976-0 and 2017/24873-4) and Conselho Nacional de Desenvolvimento Científico e Tecnológico (CNPq 313989/2018-4).

References

- [1] Zhong Y., Godwin P., Jin Y., Xiao H.: Biodegradable polymers and green-based antimicrobial packaging materials: A mini-review. *Advanced Industrial and Engineering Polymer Research*, **3**, 27–35 (2020).
<https://doi.org/10.1016/j.aiepr.2019.11.002>
- [2] Armentano I., Puglia D., Luzi F., Arciola C. R., Morena F., Martino S., Torre L.: Nanocomposites based on biodegradable polymers. *Materials*, **11**, 795 (2018).
<https://doi.org/10.3390/ma11050795>
- [3] Kliem S., Kreutzbruck M., Bonten C.: Review on the biological degradation of polymers in various environments. *Materials*, **13**, 4586 (2020).
<https://doi.org/10.3390/ma13204586>

- [4] Meereboer K. W., Misra M., Mohanty A. K.: Review of recent advances in the biodegradability of polyhydroxyalkanoate (PHA) bioplastics and their composites. *Green Chemistry*, **22**, 5519–5558 (2020).
<https://doi.org/10.1039/d0gc01647k>
- [5] Lamparelli R. C. B. C., Montagna L. S., da Silva A. P. B., do Amaral Montanheiro T. L., Lemes A. P.: Study of the biodegradation of PLA/PBAT films after biodegradation tests in soil and the aqueous medium. *Biointerface Research in Applied Chemistry*, **12**, 833–846 (2022).
<https://doi.org/10.33263/BRIAC121.833846>
- [6] Siracusa V.: Microbial degradation of synthetic biopolymers waste. *Polymers*, **11**, 1066 (2019).
<https://doi.org/10.3390/polym11061066>
- [7] Adamcová D., Zloch J., Brtnický M., Vaverková M. D.: Biodegradation/disintegration of selected range of polymers: Impact on the compost quality. *Journal of Polymers and the Environment*, **27**, 892–899 (2019).
<https://doi.org/10.1007/s10924-019-01393-3>
- [8] Stachowiak T., Łukasik K.: The management of polymer and biodegradable composite waste in relation to petroleum-based thermoplastic polymer waste – In terms of energy consumption and processability. *Sustainability*, **13**, 3701 (2021).
<https://doi.org/10.3390/su13073701>
- [9] Scaffaro R., Maio A., Sutera F., Gulino E. F., Morreale M.: Degradation and recycling of films based on biodegradable polymers: A short review. *Polymers*, **11**, 651 (2019).
<https://doi.org/10.3390/polym11040651>
- [10] Weng Y-X., Wang X-L., Wang Y-Z.: Biodegradation behavior of PHAs with different chemical structures under controlled composting conditions. *Polymer Testing*, **30**, 372–380 (2011).
<https://doi.org/10.1016/j.polymertesting.2011.02.001>
- [11] Alshehrei F.: Biodegradation of synthetic and natural plastic by microorganisms. *Journal of Applied & Environmental Microbiology*, **5**, 8–19 (2017).
<https://doi.org/10.12691/jaem-5-1-2>
- [12] Wei L., McDonald A. G.: Accelerated weathering studies on the bioplastic, poly(3-hydroxybutyrate-co-3-hydroxyvalerate). *Polymer Degradation and Stability*, **126**, 93–100 (2016).
<https://doi.org/10.1016/j.polymdegradstab.2016.01.023>
- [13] Kumar V., Sehgal R., Gupta R.: Blends and composites of polyhydroxyalkanoates (PHAs) and their applications. *European Polymer Journal*, **161**, 110824 (2021).
<https://doi.org/10.1016/j.eurpolymj.2021.110824>
- [14] Eraslan K., Aversa C., Nofar M., Barletta M., Gisario A., Salehiyan R., Goksu Y. A.: Poly(3-hydroxybutyrate-co-3-hydroxyhexanoate) (PHBH): Synthesis, properties, and applications - A review. *European Polymer Journal*, **167**, 111044 (2022).
<https://doi.org/10.1016/j.eurpolymj.2022.111044>
- [15] Lizundia E., Sarasua J. R., D'Angelo F., Orlacchio A., Martino S., Kenny J. M., Armentano I.: Biocompatible poly(L-lactide)/MWCNT nanocomposites: Morphological characterization, electrical properties, and stem cell interaction. *Macromolecular Bioscience*, **12**, 870–881 (2012).
<https://doi.org/10.1002/mabi.201200008>
- [16] Montagna L. S., do Amaral Montanheiro T. L., Machado J. P. B., Passador F. R., Lemes A. P., Rezende M. C.: Effect of graphite nanosheets on properties of poly(3-hydroxybutyrate-co-3-hydroxyvalerate). *International Journal of Polymer Science*, **2017**, 9316761 (2017).
<https://doi.org/10.1155/2017/9316761>
- [17] do Amaral Montanheiro T. L., Campos T. M. B., Montagna L. S., da Silva A. P., Ribas R. G., de Menezes B. R. C., Passador F. R., Thim G. P.: Influence of CNT pre-dispersion into PHBV/CNT nanocomposites and evaluation of morphological, mechanical and crystallographic features. *Materials Research Express*, **6**, 105375 (2019).
<https://doi.org/10.1088/2053-1591/ab42ed>
- [18] Backes E. H., Pires L. D. N., Beatrice C. A. G., Costa L. C., Passador F. R., Pessan L. A.: Fabrication of biocompatible composites of poly(lactic acid)/hydroxyapatite envisioning medical applications. *Polymer Engineering and Science*, **60**, 636–644 (2020).
<https://doi.org/10.1002/pen.25322>
- [19] da Silva T. F., Menezes F., Montagna L. S., Lemes A. P., Passador F. R.: Preparation and characterization of antistatic packaging for electronic components based on poly(lactic acid)/carbon black composites. *Journal of Applied Polymer Science*, **136**, 47273 (2019).
<https://doi.org/10.1002/app.47273>
- [20] Terzopoulou Z., Papageorgiou D. G., Papageorgiou G. Z., Bikiaris D. N.: Effect of surface functionalization of halloysite nanotubes on synthesis and thermal properties of poly(ϵ -caprolactone). *Journal of Materials Science*, **53**, 6519–6541 (2018).
<https://doi.org/10.1007/s10853-018-1993-1>
- [21] Zaidi Z., Mawad D., Crosky A.: Soil biodegradation of unidirectional polyhydroxybutyrate-co-valerate (PHBV) biocomposites toughened with polybutylene-adipate-co-terephthalate (PBAT) and epoxidized natural rubber (ENR). *Frontiers in Materials*, **6**, 275 (2019).
<https://doi.org/10.3389/fmats.2019.00275>
- [22] Verginio G. E. A., do Amaral Montanheiro T. L., Montagna L. S., Marini J., Passador F. R.: Effectiveness of the preparation of maleic anhydride grafted poly(lactic acid) by reactive processing for poly(lactic acid)/carbon nanotubes nanocomposites. *Journal of Applied Polymer Science*, **138**, 50087 (2020).
<https://doi.org/10.1002/app.50087>
- [23] de Oliveira Ferreira S. O., do Amaral Montanheiro T. L., Montagna L. S., Guerrini L. M., Lemes A. P.: Study of cellulose nanocrystals and zinc nitrate hexahydrate addition in chitosan hydrogels. *Materials Research*, **22**, e20180760 (2019).
<https://doi.org/10.1590/1980-5373-MR-2018-0760>

- [24] do Amaral Montanheiro T. L., Montagna L. S., Patrulea V., Jordan O., Borchard G., Ribas R. G., Campos T. M. B., Thim G. P., Lemes A. P.: Enhanced water uptake of PHBV scaffolds with functionalized cellulose nanocrystals. *Polymer Testing*, **79**, 106079 (2019).
<https://doi.org/10.1016/j.polymertesting.2019.106079>
- [25] Lemes A. P., do Amaral Montanheiro T. L., da Silva A. P., Durán N.: PHBV/MWCNT films: Hydrophobicity, thermal and mechanical properties as a function of MWCNT concentration. *Journal of Composites Science*, **3**, 12 (2019).
<https://doi.org/10.3390/jcs3010012>
- [26] da Silva A. P., do Amaral Montanheiro T. L., Montagna L. S., Andrade P. F., Durán, N., Lemes A. P.: Effect of carbon nanotubes on the biodegradability of poly(3-hydroxybutyrate-co-3-hydroxyvalerate) nanocomposites. *Journal of Applied Polymer Science*, **136**, 48020 (2019).
<https://doi.org/10.1002/app.48020>
- [27] da Silva A. P., Pereira M. P., Passador F. R., Montagna L. S.: PLA/coffee grounds composites: A study of photodegradation and biodegradation in soil. *Macromolecular Symposia*, **394**, 2000091 (2020).
<https://doi.org/10.1002/masy.202000091>
- [28] Goodwin D. G., Boyer I., Devahif T., Gao C., Frank B. P., Lu X., Kuwama L., Gordon T. B., Wang J., Ranville J. F., Bouwer E. J., Fairbrother D. H.: Biodegradation of carbon nanotube/polymer nanocomposites using a monoculture. *Environmental Science & Technology*, **52**, 40–51 (2018).
<https://doi.org/10.1021/acs.est.7b02062>
- [29] da Silva T. F., Menezes F., Montagna L. S., Lemes A. P., Passador F. R.: Effect of lignin as accelerator of the biodegradation process of poly(lactic acid)/lignin composites. *Materials Science & Engineering B*, **251**, 114441 (2019).
<https://doi.org/10.1016/j.mseb.2019.114441>
- [30] Montagna L. S., do Amaral Montanheiro T. L., Borges A. C., Koga-Ito C. Y., Lemes A. P., Rezende M. C.: Biodegradation of PHBV/GNS nanocomposites by *Penicillium funiculosum*. *Journal of Applied Polymer Science*, **134**, 44234 (2016).
<https://doi.org/10.1002/app.44234>
- [31] de Souza Vieira L., Montagna L. S., da Silva A. P. B., Verginio G. E. A., Passador F. R.: Effect of glassy carbon addition and photodegradation on the biodegradation in aqueous medium of poly(3-hydroxybutyrate-co-3-hydroxyvalerate)/glassy carbon green composites. *Journal of Applied Polymer Science*, **138**, 50821 (2021).
<https://doi.org/10.1002/app.50821>
- [32] Masood F., Aziz M., Haider H., Shakil O., Yasin T., Hameed A.: Biodegradation of gamma irradiated poly-3-hydroxybutyrate/sepiolite nanocomposites. *International Biodeterioration and Biodegradation*, **126**, 1–9 (2018).
<https://doi.org/10.1016/j.ibiod.2017.09.012>
- [33] Antunes A., Popelka A., Aljarod O., Hassan M. K., Kasak P., Luyt A. S.: Accelerated weathering effects on poly(3-hydroxybutyrate-co-3-hydroxyvalerate) (PHBV) and PHBV/TiO₂ nanocomposites. *Polymers*, **12**, 1743 (2020).
<https://doi.org/10.3390/polym12081743>
- [34] de Souza Vieira L., Montagna L. S., Marini J., Passador F. R.: Influence of particle size and glassy carbon content on the thermal, mechanical, and electrical properties of PHBV/glassy carbon composites. *Journal of Applied Polymer Science*, **138**, 49740 (2020).
<https://doi.org/10.1002/app.49740>
- [35] Rivera-Briso A. L., Serrano-Aroca Á.: Poly(3-hydroxybutyrate-co-3-hydroxyvalerate): Enhancement strategies for advanced applications. *Polymers*, **10**, 732 (2018).
<https://doi.org/10.3390/polym10070732>
- [36] Malmir S., Barral L., Bouza R., Esperanza M., Seoane M., Feijoo-Bandín S., Lago F.: Poly(3-hydroxybutyrate-co-3-hydroxyvalerate)/cellulose nanocrystal films: Artificial weathering, humidity absorption, water vapor transmission rate, antimicrobial activity and biocompatibility. *Cellulose*, **26**, 2333–2348 (2019).
<https://doi.org/10.1007/s10570-018-2216-2>
- [37] Arroyo J., Ryan C.: Incorporation of carbon nanofillers tunes mechanical and electrical percolation in PHBV:PLA blends. *Polymers*, **10**, 1371 (2018).
<https://doi.org/10.3390/polym10121371>
- [38] Dasan Y. K., Bhat A. H., Faiz A.: Polymer blend of PLA/PHBV based bionanocomposites reinforced with nanocrystalline cellulose for potential application as packaging material. *Carbohydrate Polymers*, **157**, 1323–1332 (2017).
<https://doi.org/10.1016/j.carbpol.2016.11.012>
- [39] Sridhar V., Lee I., Chun H. H., Park H.: Graphene reinforced biodegradable poly(3-hydroxybutyrate-co-4-hydroxybutyrate) nano-composites. *Express Polymer Letters*, **7**, 320–328 (2013).
<https://doi.org/10.3144/expresspolymlett.2013.29>
- [40] Bledzki A. K., Jaszkwicz A.: Mechanical performance of biocomposites based on PLA and PHBV reinforced with natural fibres – A comparative study to PP. *Composites Science and Technology*, **70**, 1687–1696 (2010).
<https://doi.org/10.1016/j.compscitech.2010.06.005>
- [41] Braga N. F., da Silva A. P., Arantes T. M., Lemes A. P., Cristovan F. H.: Physical–chemical properties of nanocomposites based on poly(3-hydroxybutyrate-co-3-hydroxyvalerate) and titanium dioxide nanoparticles. *Materials Research Express*, **5**, 15303–15317 (2018).
<https://doi.org/10.1088/2053-1591/aa9f7a>
- [42] Montagna L. S., Oyama I. C., Lamparelli R. C. B. C., Silva A. P., do Amaral Montanheiro T. L., Lemes A. P.: Evaluation of biodegradation in aqueous medium of poly(hydroxybutyrate-co-hydroxyvalerate)/carbon nanotubes films in respirometric system. *Journal of Renewable Materials*, **7**, 117–128 (2019).
<https://doi.org/10.32604/jrm.2019.00036>

- [43] Lemes A. P., do Amaral Montanheiro T. L., Passador F. R., Durán N.: Nanocomposites of polyhydroxyalkanoates reinforced with carbon nanotubes: Chemical and biological properties. in 'Eco-friendly polymer nanocomposites, advanced structured materials' (eds.: Thakur V., Thakur M.) Springer, New Delhi, 79–108 (2015).
https://doi.org/10.1007/978-81-322-2470-9_3
- [44] Singh N. K., Singh S. K., Dash D., Gonugunta P., Misra M., Maiti P.: CNT induced β -phase in polylactide: Unique crystallization, biodegradation, and biocompatibility. *The Journal of Physical Chemistry C*, **117**, 10163–10174 (2013).
<https://doi.org/10.1021/jp4009042>
- [45] Qiu Z., Wang H., Xu C.: Crystallization, mechanical properties, and controlled enzymatic degradation of biodegradable poly(ϵ -caprolactone)/multi-walled carbon nanotubes nanocomposites. *Journal of Nanoscience and Nanotechnology*, **11**, 7884–7893 (2011).
<https://doi.org/10.1166/jnn.2011.4714>
- [46] Yu H.-Y., Qin Z.-Y., Sun B., Yang X.-G., Yao J.-M.: Reinforcement of transparent poly(3-hydroxybutyrate-co-3-hydroxyvalerate) by incorporation of functionalized carbon nanotubes as a novel bionanocomposite for food packaging. *Composites Science and Technology*, **94**, 96–104 (2014).
<https://doi.org/10.1016/j.compscitech.2014.01.018>
- [47] Silva A. P. B., Montagna L. S., Passador F. R., Rezende M. C., Lemes A. P.: Biodegradable nanocomposites based on PLA/PHBV blend reinforced with carbon nanotubes with potential for electrical and electromagnetic applications. *Express Polymer Letters*, **15**, 987–1003 (2021).
<https://doi.org/10.3144/expresspolymlett.2021.79>
- [48] Russell R. A., Foster L. J. R., Holden P. J.: Carbon nanotube mediated miscibility of polyhydroxyalkanoate blends and chemical imaging using deuterium-labelled poly(3-hydroxyoctanoate). *European Polymer Journal*, **105**, 150–157 (2018).
<https://doi.org/10.1016/j.eurpolymj.2018.05.031>
- [49] Kim S., Zare Y., Garmabi H., Rhee K. Y.: Variations of tunneling properties in poly (lactic acid) (PLA)/poly (ethylene oxide) (PEO)/carbon nanotubes (CNT) nanocomposites during hydrolytic degradation. *Sensors and Actuators A: Physical*, **274**, 28–36 (2018).
<https://doi.org/10.1016/j.sna.2018.03.004>
- [50] Zare Y., Rhee K. Y.: Following the morphological and thermal properties of PLA/PEO blends containing carbon nanotubes (CNTs) during hydrolytic degradation. *Composites Part B: Engineering*, **175**, 107132 (2019).
<https://doi.org/10.1016/j.compositesb.2019.107132>
- [51] Zare Y., Rhee K. Y.: Expression of normal stress difference and relaxation modulus for ternary nanocomposites containing biodegradable polymers and carbon nanotubes by storage and loss modulus data. *Composites Part B: Engineering*, **158**, 162–168 (2019).
<https://doi.org/10.1016/j.compositesb.2018.09.076>
- [52] do Amaral Montanheiro T. L., Cristóvan F. H., Machado J. P. B., Tada D. B., Durán N., Lemes A. P.: Effect of MWCNT functionalization on thermal and electrical properties of PHBV/MWCNT nanocomposites. *Journal of Materials Research*, **30**, 55–65 (2014).
<https://doi.org/10.1557/jmr.2014.303>
- [53] do Amaral Montanheiro T. L., Montagna L. S., Machado J. P. B., Lemes A. P.: Covalent functionalization of MWCNT with PHBV chains: Evaluation of the functionalization and production of nanocomposites. *Polymer Composites*, **40**, 288–295 (2017).
<https://doi.org/10.1002/pc.24644>
- [54] Vidhate S., Innocentini-Mei L., D'Souza N. A.: Mechanical and electrical multifunctional poly(3-hydroxybutyrate-co-3-hydroxyvalerate)-multiwall carbon nanotube nanocomposites. *Polymer Engineering & Science*, **52**, 1367–1374 (2012).
<https://doi.org/10.1002/pen.23084>
- [55] Endo M., Takeuchi K., Kobori K., Takahashi K., Kroto H. W., Sarkar A.: Pyrolytic carbon nanotubes from vapor-grown carbon fibers. *Carbon*, **33**, 873–881 (1995).
[https://doi.org/10.1016/0008-6223\(95\)00016-7](https://doi.org/10.1016/0008-6223(95)00016-7)
- [56] Chung H., Son Y., Yoon T. K., Kim S., Kim W.: The effect of multi-walled carbon nanotubes on soil microbial activity. *Ecotoxicology and Environmental Safety*, **74**, 569–575 (2011).
<https://doi.org/10.1016/j.ecoenv.2011.01.004>
- [57] Kang S., Herzberg M., Rodrigues D. F., Elimelech M.: Antibacterial effects of carbon nanotubes: Size does matter! *Langmuir*, **24**, 6409–6413 (2008).
<https://doi.org/10.1021/la800951v>
- [58] Mocan T., Matea C. T., Pop T., Mosteanu O., Buzoianu A. D., Suciú S., Puia C., Zdrehus C., Iancu C., Mocan L.: Carbon nanotubes as anti-bacterial agents. *Cellular and Molecular Life Sciences*, **74**, 3467–3479 (2017).
<https://doi.org/10.1007/s00018-017-2532-y>
- [59] You Y., Das K., Guo H., Chang C.-W., Navas-Moreno M., Chan J. W., Verburg P., Poulson S. R., Wang X., Xing B., Yang Y.: Microbial transformation of multiwalled carbon nanotubes by *Mycobacterium vanbaalenii* PYR-1. *Environmental Science and Technology*, **51**, 2068–2076 (2017).
<https://doi.org/10.1021/acs.est.6b04523>
- [60] Antunes A., Luyt A. S., Popelka A., Mahmoud A., Aljarod O., Hassan M. K., Kasak P.: Influence of accelerated weathering on the physical and structural properties of poly(lactic-acid)/poly(3-hydroxybutyrate-co-3-hydroxyvalerate) (PLA/PHBV) blends. *Express Polymer Letters*, **15**, 687–707 (2021).
<https://doi.org/10.3144/expresspolymlett.2021.58>
- [61] Kann Y., Shurgalin M., Krishnaswamy R. K.: FTIR spectroscopy for analysis of crystallinity of poly(3-hydroxybutyrate-co-4-hydroxybutyrate) polymers and its utilization in evaluation of aging, orientation and composition. *Polymer Testing*, **40**, 218–224 (2014).
<https://doi.org/10.1016/j.polymertesting.2014.09.009>
- [62] Țucureanu V., Matei A., Avram A. M.: FTIR spectroscopy for carbon family study. *Critical Reviews in Analytical Chemistry*, **46**, 502–520 (2016).
<https://doi.org/10.1080/10408347.2016.1157013>

- [63] Scheibe B., Borowiak-Palen E., Kalenczuk R. J.: Oxidation and reduction of multiwalled carbon nanotubes - Preparation and characterization. *Materials Characterization*, **61**, 185–191 (2010).
<https://doi.org/10.1016/j.matchar.2009.11.008>
- [64] Barth A.: Infrared spectroscopy of proteins. *Biochimica et Biophysica Acta – Bioenergetics*, **1767**, 1073–1101 (2007).
<https://doi.org/10.1016/j.bbabi.2007.06.004>
- [65] Pretsch E., Buhlmann P., Affolter C.: *Structure determination of organic compounds: Tables of spectral data*. Springer, New York (2000).
- [66] Belin T., Epron F.: Characterization methods of carbon nanotubes: A review. *Materials Science and Engineering B: Solid-State Materials for Advanced Technology*, **119**, 105–118 (2005).
<https://doi.org/10.1016/j.mseb.2005.02.046>
- [67] Beyssac O., Goffé B., Petitot J-P., Froigneux E., Moreau M., Rouzaud J-N.: On the characterization of disordered and heterogeneous carbonaceous materials by Raman spectroscopy. *Spectrochimica Acta Part A: Molecular and Biomolecular Spectroscopy*, **59**, 2267–2276 (2003).
[https://doi.org/10.1016/S1386-1425\(03\)00070-2](https://doi.org/10.1016/S1386-1425(03)00070-2)
- [68] Sadezky A., Muckenhuber H., Grothe H., Niessner R., Pöschl U.: Raman microspectroscopy of soot and related carbonaceous materials: Spectral analysis and structural information. *Carbon*, **43**, 1731–1742 (2005).
<https://doi.org/10.1016/j.carbon.2005.02.018>
- [69] Sheng C.: Char structure characterised by Raman spectroscopy and its correlations with combustion reactivity. *Fuel*, **86**, 2316–2324 (2007).
<https://doi.org/10.1016/j.fuel.2007.01.029>
- [70] Tomaszewicz M., Mianowski A.: Char structure dependence on formation enthalpy of parent coal. *Fuel*, **199**, 380–393 (2017).
<https://doi.org/10.1016/j.fuel.2017.02.081>
- [71] Bar-Ziv E., Zaida A., Salatino P., Senneca O.: Diagnostics of carbon gasification by Raman microprobe spectroscopy. *Proceedings of the Combustion Institute*, **28**, 2369–2374 (2000).
[https://doi.org/10.1016/S0082-0784\(00\)80649-9](https://doi.org/10.1016/S0082-0784(00)80649-9)
- [72] Cuesta A., Dhamelincourt P., Laureyns J., Martínez-Alonso A., Tascón J. M. D.: Raman microprobe studies on carbon materials. *Carbon*, **32**, 1523–1532 (1994).
[https://doi.org/10.1016/0008-6223\(94\)90148-1](https://doi.org/10.1016/0008-6223(94)90148-1)
- [73] Wu F. Y., Cheng H. M.: Structure and thermal expansion of multi-walled carbon nanotubes before and after high temperature treatment. *Journal of Physics D: Applied Physics*, **38**, 4302–4307 (2005).
<https://doi.org/10.1088/0022-3727/38/24/006>
- [74] Peng Y., Liu H.: Effects of oxidation by hydrogen peroxide on the structures of multiwalled carbon nanotubes. *Industrial and Engineering Chemistry Research*, **45**, 6483–6488 (2006).
<https://doi.org/10.1021/ie0604627>
- [75] Jančaitienė K., Šlinkšienė R.: KH₂PO₄ crystallisation from potassium chloride and ammonium dihydrogen phosphate. *Polish Journal of Chemical Technology*, **18**, 1–8 (2016).
<https://doi.org/10.1515/pjct-2016-0001>
- [76] Vorontsov D., Filonenko S., Kanak A., Okrepka G., Khalavka Y.: Charge directed assembly of CdTe/CdS nanoparticles inside monocrystalline KH₂PO₄. *CrystrEngComm*, **19**, 6804–6810 (2017).
<https://doi.org/10.1039/c7ce01688c>
- [77] Öner M., Çöl A. A., Pochat-Bohatier C., Bechelany M.: Effect of incorporation of boron nitride nanoparticles on the oxygen barrier and thermal properties of poly(3-hydroxybutyrate-co-hydroxyvalerate). *RSC Advances*, **6**, 90973–90981 (2016).
<https://doi.org/10.1039/c6ra19198c>
- [78] do Amaral Montanheiro T. L., de Menezes B. R. C., Montagna L. S., Beatrice C. A. G., Marini J., Lemes A. P., Thim, G. P.: Non-isothermal crystallization kinetics of injection grade PHBV and PHBV/carbon nanotubes nanocomposites using isoconversional method. *Journal of Composites Science*, **4**, 52 (2020).
<https://doi.org/10.3390/jcs4020052>
- [79] Gunaratne L. M. W. K., Shanks R. A., Amarasinghe G.: Thermal history effects on crystallisation and melting of poly(3-hydroxybutyrate). *Thermochimica Acta*, **423**, 127–135 (2004).
<https://doi.org/10.1016/j.tca.2004.05.003>
- [80] Wang K., Wang Y., Zhang R., Li Q., Shen C.: Preparation and characterization of microbial biodegradable poly(3-hydroxybutyrate-co-4-hydroxybutyrate)/organoclay nanocomposites. *Polymer Composites*, **33**, 838–842 (2012).
<https://doi.org/10.1002/pc.22220>
- [81] da Silva B. C., dos Santos C. M., de Oliveira Couto C. A., Backes E. H., Passador F. R.: Evaluation of aging resistance in UHMWPE/LLDPE blend-based carbon nanotubes nanocomposites. *Macromolecular Symposia*, **383**, 1700079 (2019).
<https://doi.org/10.1002/masy.201700079>
- [82] Aoyagi Y., Yamashita K., Doi Y.: Thermal degradation of poly[(R)-3-hydroxybutyrate], poly[ε-caprolactone], and poly[(S)-lactide]. *Polymer Degradation and Stability*, **76**, 53–59 (2002).
[https://doi.org/10.1016/S0141-3910\(01\)00265-8](https://doi.org/10.1016/S0141-3910(01)00265-8)
- [83] Lai M., Li J., Yang J., Liu J., Tong X., Cheng H.: The morphology and thermal properties of multi-walled carbon nanotube and poly(hydroxybutyrate-co-hydroxyvalerate) composite. *Polymer International*, **53**, 1479–1484 (2004).
<https://doi.org/10.1002/pi.1566>
- [84] Sanchez-Garcia M. D., Lagaron J. M., Hoa S. V.: Effect of addition of carbon nanofibers and carbon nanotubes on properties of thermoplastic biopolymers. *Composites Science and Technology*, **70**, 1095–1105 (2010).
<https://doi.org/10.1016/j.compscitech.2010.02.015>
- [85] Aguilar J. O., Bautista-Quijano J. R., Avilés F.: Influence of carbon nanotube clustering on the electrical conductivity of polymer composite films. *Express Polymer Letters*, **4**, 292–299 (2010).
<https://doi.org/10.3144/expresspolymlett.2010.37>